ROYAUME DU MAROC
Université Mohammed V - RABAT -
جامعة محمد الخامس – الرباط –
Faculté des sciences
كلية العلوم
CENTRE D'ETUDES DOCTORALES - SCIENCES ET TECHNOLOGIES

N° d'ordre 3422

THESE

En vue de l'obtention du : **DOCTORAT**

Structure de Recherche : Laboratoire de la Matière Condensée et Sciences Interdisciplinaires
Discipline : Physique
Spécialité : Energétique et Sciences des Matériaux

Présentée et soutenue le : 23/01/2021 par :

Aicha El BOUKILI

Active Magnetic Refrigerator Modeling and Magnetocaloric effect in: Manganites oxides materials "$(La\text{-}Ca)MnO_3$" and intermetallic compound "$AlFe_2B_2$"

JURY

Abdelilah BENYOUSSEF	PES, Académie Hassan II des Sciences et Techniques-Rabat	Président
Abdallah EL KENZ	PES, Université Mohammed V-Rabat, Faculté des Sciences	Rapporteur/Examinateur
Noureddine MASAIF	PES, Université Ibn Tofail –Kénitra, Faculté des Sciences	Rapporteur/Examinateur
Lahoucine BAHMAD	PES, Université Mohammed V-Rabat, Faculté des Sciences	Rapporteur/Examinateur
Mohamed BALLI	PES, Université internationale de Rabat	Examinateur
Mohammed HAMEDOUN	Ancien PES, Université sidi Mohamed ben Abdellah-Fès, Faculté des Sciences	Invité
Omar MOUNKACHI	PA, Université Mohammed V-Rabat, Faculté des Sciences	Invité
Hamid EZ-ZAHRAOUY	PES, Université Mohammed V-Rabat, Faculté des Sciences	Directeur de Thèse

Année Universitaire : 2020/2021

Acknowledgements

First and foremost, praise and thank be to **Allah SWT** , the almighty, for giving me the blessing, the strength, the chance and endurance to complete my thesis.

The work presented in this thesis was carried out at the laboratory of Condensed Matter and Interdisciplinary Sciences (LaMCScI) at the Faculty of Sciences (Mohammed V University in Rabat) under the supervision of professor **Hamid EZ-ZAHRAOUY**, in collaboration with "Materials and Nanomaterials" Center at Moroccan Foundation for Advanced Science, Innovation and Research (MAScIR), Rabat, Morocco.

I want first of all to express my deep gratitude to my supervisor prof. **Hamid EZ-ZAHRAOUY**, Professor at the Faculty of Sciences, Mohammed V University, who accepted me to his laboratory and directed my research, who has been since the beginning of my Master thesis an inspiring mentor and honest scientist. I also would like to thank him for his trust, availability, passion for research and numerous debates which we had during all period of preparation of this thesis.

A huge thank to prof. **Abdelilah BENYOUSSEF**, Resident member of the Hassan II Academy of Science and Technology in Rabat, who brought me a lot during this thesis. Your valuable suggestions, constructive advice and your pedagogy have served me well. Thank you for honoring me and accepting to be the president of the jury members of this thesis.

I would like to thank the thesis committee for reviewing my work and giving their insightful and useful comments. It is an honor for me that they agreed to judge this work.

I would like to thank prof. **Abdallah EL KENZ** from Mohammed V University in Rabat, Faculty of Sciences, for reporting and reviewing this thesis.

I would like to thank prof. **Noureddine MASAIF** from University Ibn Tofail-Kénitra, Faculty of Sciences, for reporting and reviewing this thesis.

I would like to thank prof. **Lahoucine BAHMAD** from Mohammed V University in

Rabat, Faculty of Sciences, for reporting and reviewing this thesis.

My sincere thanks also go to prof. **Mohamed BALLI** from International University of Rabat, for his availability and the time he devoted to this thesis. His immense knowledge and rigorous attitude have inspired me to pursue high-quality research. I thank him for accepting to examine this thesis and giving valuable remarks and perceptive comments.

I also want to express my deep recognition to prof. **Mohammed HAMEDOUN**, to have received me within the laboratory of Materials and nanomaterials at MAScIR foundation and for all that he taught me in experimental part of my thesis. This work could not have been accomplished without his respective contributions. I thank him for accepting to be a jury member and giving valuable remarks and perceptive comments.

I would like to express my sincere gratitude to Mr. **Omar MOUNKACHI**, Assistant Professor at Mohammed V University in Rabat, Faculty of Sciences for having trusted me throughout the thesis and given me the opportunity to work on his project. I thank him for accepting to be a jury member and giving valuable remarks and perceptive comments.

I would like to thank Mr. **Najim TAHIRI**, from Mohammed V University in Rabat, Faculty of Sciences, Mr. **El Mehdi SALMANI** from Mohammed V University in Rabat, Mr. **Rafik M'NASSRI**, from Higher Institute of Applied Sciences and Technology of Kasserine, Kairouan University, Tunisia, Dr. **Khadija EL MAALAM** from MAScIR foundation and Dr. **Wasim JAMSHED** from Capital University of Science and Technology, Islamabad Pakistan, for their collaboration.

My thanks go to Dr. **Badr KAOUI** and Dr. **Ramael BRUNO** from BMBI laboratory of UTC University, France. I wish to thank you for the encouragements during my thesis, the interesting discussions and for your kindness during my stay at UTC University, I would like to salute **Mouna AOUICHAOUI** for all the fun we have had.

I would like to acknowledge the financing of my PhD. I therefore thank the support of Ministry of Higher Education, Scientific Research, and Professional Training, Morocco and the National Center for Scientific and Technological Research (CNRST) for the financial support and giving me facilities to do my research works in the Framework of the national program PPR under contract no. PPR/2015/57 and MAScIR Foundation.

I would like to express my recognition to every member of MAScIR Foundation especially to the administration personnel and to all the platform personnel for their help and availability. Thank you Mme. **Nawal CHRAIBI**, General Director of MAScIR. Thank you Mme. **Hanane BAYAHIA**, Human resources manager at MAScIR. Thank you Mr. **Chakib TILSAGHANI**, Director, technology platform at MAScIR and all the members of MAScIR platform who have helped me a lot with the measurements.

I am thankful to my friends. Firstly, to my best friend **Hajar ZAROUAL**, to always cheering me up. To my great friends Dr. **Rachida LAMOURI**, **Hafssa BOULANOIR**, Dr. **Siham DIFI**, **Somia MAAZI**, **Youssra BOUASSRIA**, Dr. **Hamid BENBIH**. I would like to salute my collegues **Faissal AL MANJLI**, Dr. **ABRAIME Ibrahim**, Dr. **FKHAR Lahcen**, **Mohamed TADOUT**, Dr. **Ghassane TIOUITCHI** , who have left their mark on the good atmosphere of life in the laboratory.

Finally, the most important thanks of all, will carry to all my family. I thank from the bottom of my heart my beloved mom (**Lala Fatima GHIATI**) and my father (**Sidi Mohammed EL BOUKILI**) for their love and support. Without them, this day would not have been possible. My husband **Simohamed EL ALAOUI**, thank you for being mine and for your patience with me, I love you, the most. I thank my sweet and adorable sisters **Latifa** and **Aziza**, my dear brother **Ssi Hicham** for the good times in my life. It belongs to them that I devote this thesis.

EL BOUKILI Aicha, Rabat, December 02,2020

Abstract

Magnetocaloric energy conversion is a cooling technology based on the magnetocaloric effect (MCE). The latter is a physical phenomenon which results in the cooling or heating of certain materials under the action of a magnetic field. The objective of the present thesis aims to estimate the potential of application of this phenomenon in magnetic refrigeration technology.

This work is divided in two parts. The first part involved the study of the MCE physics and the experimental and theoretical results obtained for two different material families. Thus, compounds with a giant magnetocaloric effect with the formula $AlFe_2B_2$ and manganite $La_{1-x}A_xCa_{0.4}MnO_3$ were explored in regard to their structural, magnetic and magnetocaloric effect properties, as well as for use as the energy source in magnetic refrigeration devices. The thermomagnetic properties of the solid refrigerant have been determined by using the Mean field theory and Monte Carlo simulations as well as by experimental measurements. The second part is focused on developing a 1D numerical model to optimize the active magnetic regenerator system. This model is used to calculate and simulate the operation of active magnetic refrigeration cycle (AMR) in order to predict thermal performances of the cycle and consequently to contribute to the comprehension of the complex magneto-thermal coupling between the carrier fluid and the magnetocaloric effect of solid refrigerant in the magnetic device.

Keywords: Magnetic refrigeration, Magnetocaloric effect, Permanent magnets field source, Active magnetic regenerative regenerator system (AMRR).

Résumé

La conversion d'énergie magnétocalorique est une technologie de production de froid basée sur l'effet magnétocalorique (EMC). Ce dernier est un phénomène physique qui se traduit par le refroidissement ou l'échauffement de certains matériaux sous l'action d'un champ magnétique. L'objectif de la présente thèse vise à estimer le potentiel d'application de ce phénomène dans la technologie de la réfrigération magnétique.

Ce travail est divisé en deux parties. La première partie concernait l'étude de la physique de l'(EMC) et les résultats expérimentaux et théoriques obtenus pour deux familles de matériaux. Ainsi, des composés à effet magnétocalorique géant de formule $AlFe_2B_2$ et des oxydes de type manganite $La_{1-x}A_xCa_{0.4}MnO_3$ ont été explorés en ce qui concerne leurs propriétés structurales, magnétiques et magnétocalorique, ainsi que leur utilisation comme source d'énergie dans les dispositifs de réfrigération magnétique. Les propriétés thermomagnétiques du réfrigérant solide ont été déterminées en utilisant la théorie du champ moléculaire et des simulations de Monte Carlo ainsi que par des mesures expérimentales. La deuxième partie est axée sur le développement d'un modèle numérique 1D pour optimiser le système de régénérateur magnétique actif. Ce modèle permet de calculer et simuler le fonctionnement du cycle de réfrigération magnétique actif (AMR) afin de prédire les performances thermiques du cycle et par conséquent de contribuer à la compréhension du couplage magnétothermique complexe entre le fluide caloporteur et l'effet magnétocalorique de réfrigérant solide dans un dispositif magnétique.

Mots clés: Réfrigération magnétique, Effet magnétocalorique, Source de champ à aimants permanents, Réfrigération magnétique à régénération active (AMRR).

Résumé détaillé

L'énergie thermique provenant des techniques conventionnelles telles que les systèmes basés sur la compression/détente d'un gaz n'est plus souhaitable en raison de leurs effets néfastes sur l'environnement, par conséquent, l'orientation vers des technologies efficaces semble nécessaire. Dans ce contexte, la réfrigération magnétique basée sur l'effet magnétocalorique (MCE) est considérée comme une technique de refroidissement prometteuse qui permet d'éliminer complètement le réfrigérant synthétique nocif, généralement utilisé par les réfrigérateurs standard tels que les chlorofluorocarbures (CFC), les hydrofluorocarbures (HFC) ou les hydro chlorofluorocarbures (HCFC).

Les matériaux magnétocaloriques et les systèmes de refroidissement magnétique ont fait l'objet de nombreuses études, dans le but de découvrir de nouveaux matériaux magnétocaloriques présentant des niveaux d'effet magnétocalorique (MCE) élevés. Au départ, les matériaux magnétocaloriques utilisés dans l'étude des systèmes de réfrigération magnétique basés sur le principe du cycle AMR étaient le Gd et certains alliages connexes tels que GdTb, GdDy et GdEr. Cependant, l'utilisation de tels réfrigérants magnétiques est limitée en raison de leur cout élevé et de leur faible stabilité chimique. Il est à noter que d'un point de vue pratique, le matériau magnétocalorique approprié doit présenter un grand EMC (Effet magnétocalorique) sous des champs magnétiques relativement faibles ($\leq$2 T) qui peuvent être atteints via des aimants permanents disponibles sur le marché. La magnétisation, la chaleur spécifique, le changement d'entropie magnétique isotherme et le changement de température adiabatique sont les principaux paramètres qui caractérisent les matériaux magnétocaloriques, pour déterminer ces paramètres nous avons utilisées des méthodes théoriques (à savoir la théorie du champ moléculaire et la simulation Monte Carlo) et la méthode expérimentale de mesure de l'EMC (Méthode indirecte-Mésures magnétiques) afin de les exploiter ultérieurement dans une étude thermo fluidique à l'aide d'un modèle basé sur un cycle magnétothermique spécifique appelé cycle a régénération AMRR (Active Magnetic Regenerative Refrigeration). Cela nous permettrait d'avoir une meilleure idée sur la performance de différents matériaux dans les réfrigérateurs magnétiques fonctionnels.

Nous avons commencé notre thèse par l'élaboration d'un modèle numérique 1D du régénérateur magnétique actif basé sur le cycle AMR qui utilise le Gd comme réfrigérant. Le modèle permet l'évaluation des performances de refroidissement de différents MCMs (Magneto-Caloric Materials). Le régénérateur magnétique actif est considéré composé d'un régénérateur, deux réservoirs chauds et froids, un fluide de transfert de chaleur. Le régénérateur est constitué d'un matériau magnétocalorique (MCM) qui se réchauffe lors de l'application d'un champ magnétique, H, et se refroidit lorsque le champ est retiré, ce qui en fait la partie la plus essentielle du cycle AMR. Le modèle prend les données théoriquement ou expérimentalement mesurées ΔT_{ad}(H, T) et Cp(H,T) comme données d'entrée et fournit comme résultats des mesures de performance quantitatives du système de refroidissement magnétique, à savoir la différence de température entre la source chaude et froide (T_{span}), et la puissance de refroidissement(Q_c). Avec ce modèle, il est possible d'évaluer plusieurs matériaux magnétocaloriques (MCMs) dans un cycle AMR.

Trois différents MCMs ont été étudiés à l'aide de ce modèle en termes de leur T_span et la puissance de refroidissement, Gd, $AlFe_2B_2$ et $La_{1-x}Ca_{0.4}MnO_3$. En effet, pour la partie qui concerne les matériaux magnétocaloriques de la présente thèse. Nous avons commencé notre travail par une étude théorique par MFT (Théorie du champ moléculaire) du matériau Gd considéré comme le matériau référence de la technologie de réfrigération magnétique, ses propriétés magnétocaloriques ont été déterminé, et par la suite nous avons évalués ses performances de refroidissement à l'aide de notre modèle numérique du cycle AMR-1D. Après avoir validé les résultats de notre modèle AMR-1D, nous avons travaillés sur la famille des matériaux intermétallique, nous avons choisis le matériau $AlFe_2B_2$ car ces composées sont constituées d'éléments légers et abondants. Nous avons calculé les valeurs ΔS_m et ΔT_{ad} pour le matériau intermétallique $AlFe_2B_2$ à l'aide de l'approche Monte Carlo qui ont été introduites dans le modèle numérique 1D-AMR. Cependant, l'utilisation de tels réfrigérants magnétiques à base d'alliage métallique est limitée parce qu'ils présentent l'inconvénient d'oxydation en contact avec l'eau. Pour surmonter ce problème, les manganites pérovskites de formule générale $La_{1-x}A_xMnO_3$, avec A = Sr, Ba, Ca ... ont attiré beaucoup d'attention pour utilisation comme réfrigérants dans la

technologie de réfrigération magnétique en raison de leurs nombreux avantages tels que, leurs faible coût, préparation facile, contrôle de la granulométrie par traitement thermique et une stabilité chimique élevée. Dans ce contexte, nous avons étudiés expérimentalement les manganites (La-Ca)MnO_3 en calculant leurs propriétés magnétocaloriques. D'autre part, nous avons exploré l'impact de la phase secondaire Mn_2O_3 sur la morphologie, la structure et les propriétés magnétiques du matériau $La_{1-x}A_xCa_{0.4}MnO_3$
. Les caractéristiques magnétocaloriques sont également analysées en termes d'aimantation et de mesures de chaleur spécifique.

Lors de l'examen des MCMs, toutes les conditions de fonctionnement importantes d'un système de réfrigération magnétique linière ont été fixées, telles que le débit du fluide, la température ambiante, la durée du cycle, l'intensité du champ magnétique. Nos résultats indiquent que Gd présente le T_{span} maximum avec une charge de refroidissement respectable, tandis que $La_{1-x}Ca_{0.4}MnO_3$ génère un span de température faible. D'autre part même si le composé $AlFe_2B_2$ ne fonctionnait pas aussi bien que Gd, il pourrait être le choix de MCM pour la réalisation de la réfrigération magnétique en raison de son coût beaucoup plus faible. En plus de la possibilité d'évaluer divers matériaux magnétocaloriques, notre modèle suggère une optimisation des paramètres de fonctionnement en termes de débit et fréquence du cycle, on note que ces paramètres dépendent des conditions de fonctionnement du système (par ex. géométrie du régénérateur, masse des matériaux magnétocaloriques, etc.).

Scientific production

Accepted papers

[1]: **A. El Boukili**, N. Tahiri, E. Salmani, H. Ez-Zahraouy, M. Hamedoun, A. Benyoussef, M. Balli, O. Mounkachi "Magnetocaloric and cooling properties of the intermetallic compound $AlFe_2B_2$ in an AMR cycle system,". Intermetallics journal, 104, 84–89, 2019.

---

[2]: **A. El Boukili**, H. Ez-Zahraouy, M. Hamedoun, A. Benyoussef, M. Balli, O. Mounkachi, "Numerical investigation of cooling properties of $La_{1-x}Ca_{0.4}MnO_3$ in an active magnetic regenerator system, " Refrigeration science and technology journal, DOI: 10.18462/iir.icr.2019.1768

---

[3]: **A. El Boukili**, O. Mounkachi, M. Hamedoun, P. Lachkar, E. K. Hlil, A. Benyoussef, M. Balli and H. Ez-Zahraouy"A study of structural, magnetic and magnetocaloric properties of (1-x)$La_{0.6}Ca_{0.4}MnO_3$/xMn_2O_3 composite materials ,". Journal of alloys and compounds, DOI: 10.1016/j.jallcom.2020.158392

---

[4]: **A. El Boukili**, H. Ez-zahraouy, M. Hamedoun, A. Benyoussef, M. Balli, O. Mounkachi,, ""Numerical Optimization of the Energetic Performance of a Near Room Temperature Magnetic Refrigerator,". IEEE, Oct. 2018, DOI: 10.1109/IRSEC.2017.8477431.

Submitted papers

[5]: **A. El Boukili**, K. El Maalam, M. Hamedoun, A. Benyoussef, M. Balli, O. Mounkachi, H. Ez-Zahraouy, Magnetic, magnetocaloric and transport properties of rare earth doped perovskite manganites $La_{0.5}R_{0.1}Ca_{0.4}MnO_3$ (R=La, Eu, Pr), Submitted to Powder technology Journal.

---

[6]: L. Fkhar, **A. El Boukili**, M. Ait Ali, O. Mounkachi, M. Dietze, S. Habouti, M. Es-Souni, M. Hamedoun, A. El Kenz, A. Benyoussef, E.-K. Hlil, H. Ez-Zahraouy, K. El Maalam,"Effect of Mn-site doping on the magnetic and magnetocaloric properties of $(La_{0.6}Pr_{0.1})Sr_{0.3}Mn(Fe/Cr)O_3$,", Submitted to Journal of alloys and compounds,

---

Patents

[1]: A. El Boukili, Abdelilah Benyoussef, Mohammed Hamedoun, Matériau composite à base de pérovskite et ses applications dans le domaine de la réfrigération magnétique (OMPIC): N° Dépôt : 46675 et 47008.

Oral Communications in International Conferences

[1]: A. El Boukili et al., "DeMESYs 2017": International Conference on Development and Manufacturing of Electronic Systems, Rabat, Morocco.

[2]: A. El Boukili et al., "IMSEGEC 2017": 1st International Materials Science and Engineering for Green Energy Conference, Ifrane, Morocco.

[3]: A. El Boukili et al., "IRSEC 2017": International Renewable and Sustainable Energy Conference, Tanger, Morocco.

[4]: A. El Boukili et al., "Nano-TN 2018" Conference –February 19-22, 2018, Marrakech, Morocco.

[5]: A. El Boukili et al.,"EMCMRE 2019": 5th Euro Mediterranean conference on materials and renewable energies, Marrakech, Morocco.

[6]: A. El Boukili et al., "IRSEC 2019" International Renewable and Sustainable

Energy Conference–December 05-08, 2019,Agadir, Morocco.

[7]: A. El Boukili et al., "ICR 2019": 25th International congress of Refrigeration, in Montreal (Canada).

Poster communications in International Conferences

[8]: A. El Boukili et al.,"IMSEGEC 2018": 2nd International Materials Science and Engineering for Green Energy Conference, Rabat, Morocco.

[9]: A. El Boukili et al., "Nano-TN 2020" Conference –February 19-22, 2020, Marrakech, Morocco.

[10]: A. El Boukili et al., "THERMAG 2018": International Conference on Caloric Cooling, Darmstadt, Germany.

[11]: A. El Boukili et al., "IMSEGEC 2018": 2nd International Materials Science and Engineering for Green Energy Conference, Rabat, Morocco.

Contents

Acknowledgements **i**

Abstract **iv**

Résumé **v**

Résumé détaillé **vi**

Scientific production **ix**

List of Tables **xviii**

List of Figures **xix**

List of abbreviations **xxiv**

General introduction **1**

I Fundamentals and State of the art **5**

1 Magnetism and magnetocaloric effect **6**

1.1 Introduction 6

1.2 Magnetic materials 7

1.2.1 Introduction to magnetic materials 7

1.2.1.1 Diamagnetic materials 7

1.2.1.2 Paramagnetic materials 8

1.2.1.3 Antiferromagnetic materials 9
1.2.1.4 Ferromagnetic materials 10
1.2.1.5 Ferrimagnetic materials 12
1.2.2 Classification of ferromagnetic materials 12
1.2.2.1 Domain structure and hysteresis 12
1.2.2.2 Hard magnetic materials 16
1.2.2.3 Soft magnetic materials 17
1.2.3 The Curie temperature 17
1.2.3.1 Measurement of Curie temperature of ferromagnetic materials 18
1.3 The Magnetocaloric effect (MCE) 21
1.3.1 Introduction to the magnetocaloric effect 21
1.3.2 The Thermodynamics of the MCE 24
1.3.3 Methods of magnetocaloric properties investigation 27
1.3.3.1 Direct methods 27
1.3.3.2 Indirect methods 28
1.4 From the magnetocaloric effect to magnetic refrigeration 29
1.4.1 Thermodynamic cycles 30
1.4.1.1 Carnot cycle 30
1.4.1.2 Brayton cycle 30
1.4.1.3 Ericsson cycle 30
1.4.1.4 Stirling cycle 30
1.4.1.5 The AMR Thermodynamic Cycle 31
1.4.2 Magnetocaloric Materials 34
1.4.2.1 General Criteria for the Selection of the magnetocaloric material 34
1.4.2.2 Magnetocaloric effect in oxides 37
1.4.3 Magnetic cooling systems 49
1.4.3.1 Magnetic field sources 50

1.5 Conclusion 51

2 Computational methods and Experimental techniques 52

2.1 Introduction 52

2.2 Density Functional Theory 52

2.2.1 Introduction to Density Functional Theory 52

2.2.1.1 Schrödinger equation 53

2.2.1.2 Born-Oppenheimer approximation 54

2.2.1.3 Hartree-Fock approximation 55

2.2.2 Principle of Density Functional Theory 55

2.2.2.1 Hohenberg-Kohn theorems 55

2.2.2.2 Kohn-Sham equations 56

2.3 Monte Carlo simulation 58

2.3.1 Introduction 58

2.3.2 Basic concepts of Monte Carlo simulation 59

2.4 Theoretical Approach for MCE: Molecular Field Theory 59

2.4.1 Weiss mean field model 59

2.4.2 Debye model for phonons 61

2.5 Synthesis methods 62

2.5.1 Solid state reaction (SSR) method 62

2.5.2 Wet Chemistry methods 63

2.5.2.1 Sol-Gel method 63

2.5.2.2 Modified Pechini sol gel 64

2.6 Characterization techniques 65

2.6.1 Thermogravimetric analysis (TGA) 65

2.6.2 X-Ray diffraction (XRD) 66

2.6.3 Scanning Electron Microscopy (SEM) 68

2.6.4 Transmission Electron Microscope (TEM) 70

2.6.5 Magnetic properties measurements system (SQUID-MPMS-XL7 magnetometer): 71

2.7 Conclusion 72

II Contribution and results 74

3 Magnetocaloric and Cooling Properties of the Intermetallic Compound $AlFe_2B_2$ in an AMR Cycle System 75

3.1 Introduction 75

3.2 Computational details 77

3.2.1 First principles calculation (DFT) 77

3.2.2 Monte Carlo simulation (MCs) 77

3.2.3 AMR cycle model 79

3.3 Results and discussion 80

3.3.1 Crystal structure and density of states 80

3.3.2 Magnetic and magnetocaloric properties 81

3.3.3 Cooling properties 84

3.4 Conclusions 88

4 A study of structural, magnetic, magnetocaloric and cooling properties of (1-x)$La_{0.6}Ca_{0.4}MnO_3$/xMn_2O_3 composite materials 91

4.1 Introduction 91

4.2 Experimental details 94

4.3 Computational details 95

4.3.1 AMR cycle model 95

4.3.2 Description of the regenerator and working cycle 96

4.3.2.1 Governing equations 97

4.4 Results and discussion 98

4.4.1 Structural properties 98

4.4.2 Magnetic and magnetocaloric properties 103

4.4.3 Cooling properties 118

4.5 Conclusion 123

5 The magnetic refrigeration test device 125

5.1 Introduction . . . 125

5.2 Magnetic field source . . . 126

5.3 Regenerator (Active material) . . . 127

5.4 The Heat Transfer Fluid System . . . 128

5.5 Measuring Instruments . . . 128

5.6 Practical realization of the reciprocating prototype . . . 129

5.7 Computational details . . . 130

5.7.1 Magnetic study by finite elements . . . 130

5.7.1.1 Conditions for simulation . . . 131

5.7.2 The numerical AMR model . . . 132

5.7.2.1 Description of the regenerator and working cycle . . . 133

5.7.2.2 Governing equations . . . 134

5.7.2.3 Initial and boundary condition . . . 138

5.8 Results and discussion . . . 139

5.8.1 Magnetic field analysis . . . 139

5.8.2 Cooling performance . . . 140

5.8.3 conclusion . . . 144

General conclusion 146

Appendices 148

A The Effect of PEG additive on the morphology and magnetocaloric properties in $La_{0.6}Ca_{0.4}MnO_3$. 148

A.0.1 Material preparation structural Characterization . . . 149

A.0.2 Structural Characterization: Morphology and composition . . . 149

A.0.3 Magnetic and magnetocaloric properties . . . 150

A.0.4 Conclusion . . . 152

Appendices 153

B Magnetic, magnetocaloric of rare earth (R= Eu, Pr) doped perovskite manganites $La_{0.5}R_{0.1}Ca_{0.4}MnO_3$ 153

Bibliography 156

List of Tables

1.1 MCE parameters of different materials based La manganite family. 40

3.1 Magnetic and magnetocaloric properties of the intermetallic $AlFe_2B_2$ in comparison with experimental results reported by (Tan et al., 2013). 86

3.2 MCE parameters reported for $AlFe_2B_2$. 89

4.1 Geometrical and thermo-physical parameters of water and $La_{0.6}Ca_{0.4}MnO_3$ used in simulations. 95

4.2 Rietveld refined lattice parameters, unit cell volume and crystallite size for (1-x)$La_{0.6}Ca_{0.4}MnO_3$/xMn_2O_3, (x = 0, 5, 10, 15 and 20 %) calculated using Topas software 99

4.3 Rietveld refined lattice parameters, unit cell volume and crystallite size for (1-x)$La_{0.6}Ca_{0.4}MnO_3$/xMn_2O_3, (x = 0, 5, 10, 15 and 20 %) calculated using Topas software 101

4.4 Magnetic and magnetocaloric properties of (1-x)$La_{0.6}Ca_{0.4}MnO_3$/xMn_2O_3 compared with those reported in recent published works. 117

5.1 Geometrical and thermo-physical parameters of water and Gadolinium used in simulation. 133

5.2 empirical constants C and M. 138

List of Figures

1.1 The influence of the core material on the inductance 7

1.2 (a) The atomic dipole configuration for a diamagnetic material with and without a magnetic field. (b) Atomic dipole configuration with and without an external magnetic field for a paramagnetic material 9

1.3 The crystal structure of MnO consists of alternating layers of 111 type planes of oxygen and manganese ions. 10

1.4 Schematic illustration of the mutual alignment of atomic dipoles for a ferromagnetic material. 11

1.5 A qualitative Schematic of magnetic domains in a polycrystalline material. 13

1.6 The B-versus-H behavior for a ferromagnetic or ferrimagnetic material that was initially unmagnetized 15

1.7 Magnetic flux density B versus the magnetic field strength H for a ferromagnetic material that is subjected to forward and reverse saturations (points S and S'). 16

1.8 Comparison of magnetization curves (hysteresis loops) for soft and hard magnetic material 17

1.9 The effect of temperature on (a) the hysteresis loop and (b) the remanance. 18

1.10 Inflection point method used for determining T_C 19

1.11 The Arrott plot technique used for determining T_C 20

1.12 Magnetocaloric effect used for determining T_C 21

1.13 The entropy-temperature (S-T) diagram illustrating the isothermal and adiabatic magnetization processes 23

1.14 Analogy between magnetocaloric refrigeration and gas refrigeration. 29
1.15 S–T diagram of thermodynamic cycles used for magnetic refrigeration.[1] . 31
1.16 AMR cycle and the temperature profile along the AMR during all four operational phases [2]. 33
1.17 Illustration of the different challenges for magnetic refrigeration with respect to applications [3]. 36
1.18 Schematic general distinctions between second-order and first-order materials via magnetization (a and b) and specific heat (c and d) in relation to temperature and magnetic field 37
1.19 Ideal cubic Perovskite $AMnO_3$ structure. 39

2.1 The solid state reaction route. 63
2.2 Sol-Gel process steps. 64
2.3 Thermogravimetric analysis apparatus. 65
2.4 Bruker D8 X-ray diffractometer. 67
2.5 Schematic diagram of an x-ray diffractometer 68
2.6 The diffraction pattern obtained from a sample of gold powder 68
2.7 FEI Scanning Electron Microscope, Quanta FEG 450 69
2.8 Transmission Electron Microscopy (TECNAI G^2 Series). 71
2.9 MPMS-XL7 magnetometer. 72

3.1 Crystalline structure of the $AlFe_2B_2$ compound. 81
3.2 Total and partial densities of state (DOS) for $AlFe_2B_2$. 82
3.3 The temperature dependence of the magnetization, susceptibility, and the specific heat of $AlFe_2B_2$ compound, for a zero-external magnetic field, using MCs. 83
3.4 The magnetic entropy changes for the intermetallic $AlFe_2B_2$ as a function of temperature calculated under 1, 3 and 5 T, magnetic fields. 83
3.5 The relative cooling power as a function of field. 84

3.6 Temperature dependence of the adiabatic temperature change for $AlFe_2B_2$ compound under magnetic fields of 1T, 3T and 5T using Monte Carlo simulations. 85

3.7 Temperature changes at the hot and the cold ends versus number of cycles for a 1 T-AMR-unit operation with both Gd and $AlFe_2B_2$ plates at the ambient temperature at a cycling frequency of f=0.5 Hz. 87

3.8 Cooling power vs. temperature span. 88

4.1 Parallel plates of MCM stacked in the regenerator. The MCM is in gray and the fluid channels in blue 96

4.2 XRD patterns of $LCMO/\ Mn_2O_3$ composite. Blue asterisk indicate peaks of Mn_2O_3 for $x = 0.1, 0.2$ samples. 100

4.3 Reitveld refined XRD patterns of the $LCMO/\ Mn_2O_3$ for x=0.2 using Topas software. 101

4.4 SEM images and EDAX analyses of (1-x)$La_{0.6}Ca_{0.4}MnO_3$/xMn_2O_3 for $x = 0, 0.05, 0.1$ and 0.2. 102

4.5 Scanning electron micrographs of (1-x)$La_{0.6}Ca_{0.4}MnO_3$/xMn_2O_3 showing the cations distribution for x=0.1. 103

4.6 Temperature dependence of magnetization measured at $\mu_0 H$=0.05T for (1-x)$La_{0.6}Ca_{0.4}MnO_3$/xMn_2O_3 ($0 \leq x \leq 0.2$) samples. The inset shows the dM/dT curves for $x = 0, 0.1, 0.2$. 104

4.7 Scanning electron micrographs of (1-x)$La_{0.6}Ca_{0.4}MnO_3$/xMn_2O_3 showing the cations distribution for x=0.1 108

4.8 M^2 versus $\mu_0 H/M$ isotherms (Arrot's curves). The inset is the temperature dependence of the spontaneous magnetization Msp and $\frac{1}{\chi}$ for (1-x)$La_{0.6}Ca_{0.4}MnO_3$/xMn_2O_3 composites (a) $x = 0$, (b) $x = 0.1$, (c) $x = 0.2$. 110

4.9 The magnetic entropy change as a function of temperature for different applied magnetic fields for (1-x)$La_{0.6}Ca_{0.4}MnO_3$/xMn_2O_3 composites (a) $x = 0, (b)x = 0.1, (c)x = 0.2$. 113

4.10 Magnetic field dependence of RCP reported for $LCMO/Mn_2O_3$composites. 114

4.11 Enhanced RCP for $x = 0.1$ and 0.2. 115
4.12 The specific heat of some selected $La_{0.6}Ca_{0.4}MnO_3/Mn_2O_3$ composites as a function of temperature measured under zero magnetic field. 116
4.13 Temperature dependence of adiabatic temperature change for (1-x)$La_{0.6}Ca_{0.4}MnO_3$/xMn_2O_3 (with $x = 0$ and 0.1) under $1T$ magnetic field. 117
4.14 Temperature span between hot and cold sides of the regenerator 119
4.15 Temperature span between hot and cold sides of the regenerator 120
4.16 Cooling power vs. temperature span 122
4.17 COP vs. temperature span 123

5.1 AMR cycle 128
5.2 Thermocouple type T used in the experimental setup. 129
5.3 General view of the linear magnetic refrigeration prototype. 129
5.4 Geometry of Halbach cylinder of 8 permanent magnets used for magnetic simulations. 131
5.5 Photograph of the Halbach cylinder used in the developped prototype . . . 131
5.6 View of the mesh performed for finite element modeling of the Halbach . . 132
5.7 Parallel plate regenerator. The MCM is in gray and the fluid channels in blue. 134
5.8 Heat capacity of Gadolinium used for the one-dimensional model 136
5.9 Adiabatic temperature change deducated from the heat capacity 137
5.10 (a) Geometry of Halbach cylinder of 8 permanent magnets, (b) distribution of magnetic flux simulated by COMSOL 139
5.11 No-Load temperature gradient along the solid material 140
5.12 Time evolution of Temperature of both sides within the regenerator 141
5.13 temperature evolution versus number of cycles 142
5.14 Effect of the thickness of the fluid on the difference of T. 143
5.15 Profile of the energy produced by the magnetocaloric material. 144

A.1 Material preparation Structural Characterization 149

A.2 SEM and TEM micrographs of particles at different magnifications synthesized using PEG 4000. 149
A.3 M-T curve for the synthesized LCMO at 500 Oe applied field 150
A.4 Isothermal magnetization (M–H) measured from 100 to 300 K, LCMO-PEG 4000 150
A.5 Temperature dependence of the magnetic entropy change change for LCMO-PEG4000 calculated at various external field 151
A.6 The calculated RCP values for LCMO-PEG4000. 152

B.1 XRD patterns LECMO 153
B.2 XRD patterns LPCMO 154
B.3 Isothermal magnetization (M–H) measured from 100 to 300 K for LECMO (R=Eu) and LPCMO (R=Pr) 154
B.4 Magnetic entropy change for LECMO (R=Eu) and LPCMO (R=Pr) . . . 155

List of abbreviations

Ms	Saturation magnetization
Mr	Remanent magnetization
DFT	Density Functional Theory
GGA	Generalized Gradient Approximation
KS	Khon Sham
MT	Muffin-Tin
APW	Augmented-Plane-Wave
LAPW	Linearized-Augmented-Plane-Wave
FP-LAPW	Full Potential Linearized-Augmented-Plane-Wave
MCS	Monte Carlo simulation
MAE	Magneto-crystalline anisotropy energy
K_B	Boltzmann constant
SSR	Solid-State reaction
SG	Sol-gel
XRD	X-ray diffraction
SEM	Scanning Electron Microscopy
TEM	Transmission Electron Microscopy
SQUID	Superconducting Quantum Interference Device
MPMS	Magnetic Properties Measurement System
AMRR	Active magnetic regenerative refrigeration
MCE	Magnetocaloric effect
ΔT_{ad}	Adiabatic temperature change (MCE) (K)
MCMs	Magnetocaloric materials
ΔS	Entropy change (J/Kg.K)
PDE	partial differential equations

General introduction

Refrigeration process is in continuous development. But until today, the traditional technique based on the refrigerant compression, remains the dominant technique with high yield as a second biggest source of greenhouse gas emissions after electricity, and significant responsible of huge increase of energy consumption. As stated by the international energy agency (IEA), the overall world electricity consumption of 2016 is estimated at 23816 TWh, of which 67% is produced from fossil fuels.

In the current context of a shortage of energy resources and an increase in emissions of greenhouse gases into the atmosphere, reducing the use of synthetic refrigerants and energy consumption are major challenges for the refrigeration industry. Measures have been adopted internationally. Some States have implemented them through regulations. In addition, intensive research activities are conducted by laboratories to address these challenges.

In this spirit, we noticed the enhanced interest of the researchers to innovate new clean technologies for cold production, such as: Thermoelectric refrigeration named the Peltier effect [4],Thermoacoustic [5], Adsorption cooling system [6], and caloric cooling technologies including electrocaloric [7], mechanocaloric [8] and magnetocaloric effects [2]. We mention that a material that displays more than one of these effects is considered as a multicaloric material (multiferroic) with multicaloric effects [9]. These solid state technologies which are still in the phase of research and development, are the most promising cooling techniques that allows to fully eliminate the harmful synthetic refrigerant for the future [10].

Magnetic refrigeration, which is the subject of the thesis work presented here, is a cold production technology based on a physical phenomenon called the magnetocaloric effect (MCE) taking place in solid state refrigerants. This technology operates without CFC or HCFC neither compressor is considered as one of the serious alternatives to conventional refrigeration systems. The interest generated by magnetic refrigeration is mainly due to its high energy efficiency and the absence of harmful refrigerants for the environment. However, the main disadvantage of such systems is the low magnetocaloric properties of

materials. Consequently, the choice of the optimal working conditions, as well as, the optimal material is essential for the development of this technology.

The magnetocaloric effect at the base results in the cooling or heating of certain materials under adiabatic conditions through the application or removal of an external magnetic field. Simply put, when you approach a magnetocaloric material from a magnet, it heats up. When you move it away, it cools down.

The magnetocaloric effect being present in all magnetic substances, this gives a large field of research activity to find active materials suitable for each application. Gadolinium is the reference material for magnetic refrigeration at ambient temperature (Tc=294 K). This element also has the advantage of being an easy compound to obtain due to its purity. It finds its technological development thanks to the ease of implementation reflected by its high ductility and malleability. This is why it is used in the most current magnetic refrigeration devices at room temperature. However, its prohibitive price (up to 3500 /kg) and its limited reserves exclude it from possible magnetocaloric materials for consumer applications. It is therefore important to find another magnetocaloric material. Aiming to replace the gadolinium metal in prototypes, research has turned mainly to two families of magnetocaloric materials after the discovery of giant MCE in: $Gd_5(Si_xGe_{1-x})_4$ by Pecharsky and Gschnieder in 1997 [11] and those based on manganese such as $MnFeP_{1-x}As_x$ [12] and $MnAs_{1-x}Sb_x$ [13] compounds. Since then, a wide variety of advanced magnetocalorics with a giant magnetocaloric effect such as La(Fe, Mn,Co, $Mn)_{13-x}Si_x$(H,N, C)$_y$ [14–18], Ni-Mn-based Heusler [19] and $La_{1-x}Ca_xMnO_3$ manganites [20] was reported in the literature. Following that, a parallel effort was paid to design new types of efficient magnetic refrigerators, giving rise to preindustrial systems.

The work required to make the magnetic refrigeration a technology that can replace the conventional technology covers many areas: Fundamental aspects of magnetic and thermal phenomena coupling, on research, development, characterization and the optimization of active materials that have the appropriate properties, on how to best exploit them in a refrigeration machine by specific thermodynamic cycles, on how to produce a magnetic field and a suitable magnetic field variation, on the general optimization of devices. These

tasks make it possible to address all the problems related to this field of research and to study the three main components of magnetic refrigeration which are the magnetocaloric material considered as the energy source of this technology, the magnetic field source and its interaction with the material and the used thermodynamic cycle named active magnetic regenerative regenerator cycle (AMRR).

This thesis work is in the field of the study of magnetocaloric materials and magnetic refrigeration devices with permanent magnets over a wide temperature range. In this way, the present manuscript is a contribution to the study of the structural, magnetic and magnetocaloric properties of manganites. We attempted to study the elaboration, structural characterization by X-rays diffraction, morphological characterization, magnetic and magnetocaloric characterization of mixed valence perovskite manganite oxides of formulas ($La_{0.6}Ca_{0.4}MnO_3$), ($La_{0.6}Ca_{0.4}MnO_3$/ Mn_2O_3), ($La_{0.5}Eu_{0.1}Ca_{0.4}MnO_3$) and ($La_{0.5}Pr_{0.1}Ca_{0.4}MnO_3$). In addition, a 1D numerical model of the AMR cycle has been developed in order to understand the magnetothermal mechanism of the magnetic regenerator and to investigate the cooling performance of different MCMs implemented in the the magnetic regenerator based on the AMR cycle.

This thesis report is structured in two main parts: The first part concerns the state of the art and basic concepts, which contains two chapters:

* Chapter 1: A general introduction to magnetism and the necessary guidelines that are linked to this thesis are presented in this chapter in order to understand the magnetocaloric effect phenomena and how to exploit this effect in cold production.

* Chapter 2: This chapter focuses, in the first part, on the needed background of the computational methods, especially, Density Functional Theory, Molecular field theory, Monte Carlo Simulation, Finite difference method for the calculations of the structural, magnetic and magnetocaloric properties as well as for resolving differential equations. The second part of this chapter focuses on the experimental techniques used for the synthesis and the characterization of the studied $La_{1-x}A_xCa_{0.4}MnO_3$ compounds.

The second part concerns the obtained experimental and theoretical results, presented in three chapters:

* Chapter 3: We report in chapter 3 a detailed theoretical study dealing with the magnetic and thermal features of the intermetallic compound $AlFe_2B_2$ close to room temperature. The magnetocaloric properties in terms of both adiabatic temperature (ΔT_{ad}) and magnetic entropy (ΔS_{mag}) changes were determined using the Monte Carlo approach, while the thermodynamic performances were simulated according to the active magnetic refrigeration (AMR) model.

* Chapter 4: Deals with the study of manganite based La-Ca materials. Compounds (1-x)$La_{0.6}Ca_{0.4}MnO_3$/xMn_2O_3 ($x = 0, 0.05, 0.1, 0.15, 0.20$) composites were prepared by solid state reaction method. X-ray diffraction measurements were used to confirm the crystal structure and the average crystallite size of samples. Their magnetic, magnetocaloric and heat capacity properties display a second order magnetic phase transition at $260K$. In addition we performed a numerical analysis and performance parameters of $La_{0.6}Ca_{0.4}MnO_3$ perovskite manganite as active magnetocaloric material (MCM) in an active magnetic refrigeration cycle (AMR).

* Chapter 5: The third chapter of this part outline the work carried out on the study of magnetic refrigeration systems. To make the link with research on magnetocaloric materials, this system will make it possible to test the elaborated materials in real conditions and to study the influencing parameters. It is a linear system whose field is created by permanent magnet in the form of a halbach cylinder.

Part I

Fundamentals and State of the art

Chapter 1

Magnetism and magnetocaloric effect

1.1 Introduction

Strictly speaking, there is no such thing as a "nonmagnetic" material. Every material is made up of atoms; Atoms are made up of electrons spinning around them, similar to an electric current that carries a loop that generates a magnetic field. Therefore, every material responds to a magnetic field. The way in which this response of atoms and electrons in a material determines whether a material will be strongly or weakly magnetic.

This chapter presents the necessary guidelines to discuss the different categories of materials and their applications. The types of magnetism include diamagnetism, paramagnetism, and ferromagnetism. Furthermore, antiferromagnetism and ferrimagnetism are considered to be subcategories of ferromagnetism. All materials exhibit at least one of these types, and their behavior depends on the response of electrons and atomic magnetic dipoles to an externally applied magnetic fields. The term "nonmagnetic," generally means that the material is neither ferrimagnetic nor ferromagnetic. These "nonmagnetic" materials are further classified as diamagnetic (e.g., superconductors) or paramagnetic.

Ferromagnetic and ferrimagnetic materials are generally further classified into soft or hard magnetic materials. Hard magnetic materials or permanent magnets maintain their magnetization (high resistance to demagnetization). In soft materials, they can become magnetized, but when the magnetizing source of magnetization is removed, these materials lose their magnetism. The last part of this chapter will specifically introduce soft magnetic

materials for magnetocaloric energy conversion.

1.2 Magnetic materials

1.2.1 Introduction to magnetic materials

As mentioned earlier, there is no "non-magnetic" material. All materials respond to magnetic fields. We mention that several types of behavior are observed when a magnetic field is applied to the material, (See, Figure 1.1).

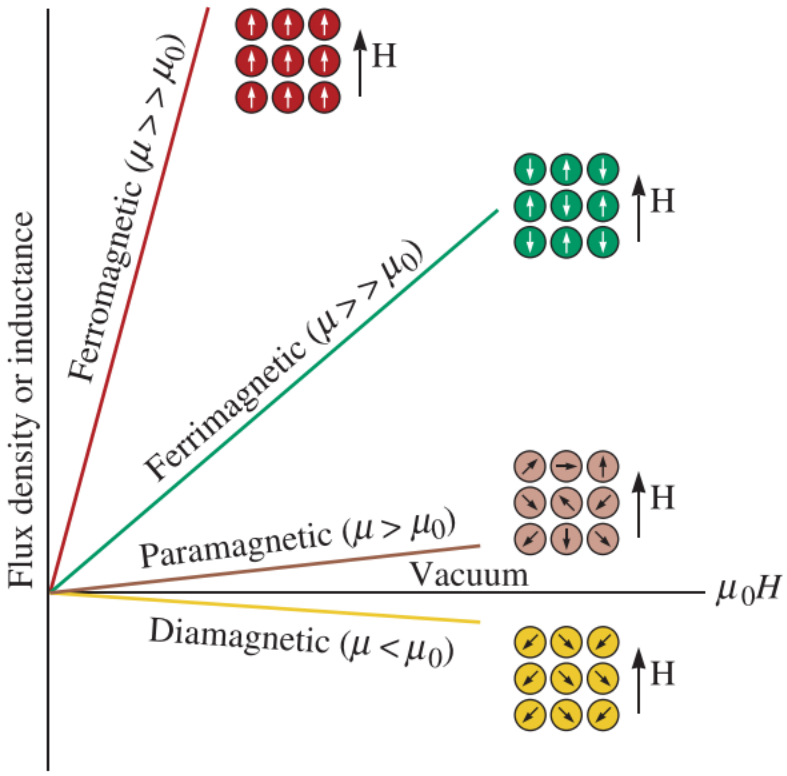

Figure 1.1: The influence of the core material on the inductance. The magnetic moment opposes the applied magnetic field in the diamagnetic material. For the same applied field, paramagnetic, ferrimagnetic and ferromagnetic materials show greater moments [21].

1.2.1.1 Diamagnetic materials

It is caused by a change in the orbital motion of electrons due to an applied magnetic field, the magnet and the material repeal each other. This is called "diamagnetism". Dia-

magnetic materials are materials that contain only non-magnetic atoms, such as, copper, silver, silicon, gold, and alumina are diamagnetic at room temperature. Diamagnetism is a very weak form of magnetism that is nonpermanent and only lasts when an external magnetic field is applied. In a diamagnetic material, the magnetization (M) direction is opposite to the direction of applied field (H) (see fig 1.2(a)).

1.2.1.2 Paramagnetic materials

When materials have unpaired electrons, a net magnetic moment due to the electron spin is related with each atom. In the presence of an external magnetic field, the dipoles line up with the field, causing a positive magnetization. Since the inter-atomic or inter-molecular distances are larger enough that the moments do not interact with each other, high magnetic fields are necessary to align all of the dipoles. In addition, the effect disappears once the magnetic field is removed. This effect, known as paramagnetism, is found in metals such as titanium, aluminum, and copper alloys. As we can see in figure 1.2(b). In the absence of an external field, paramagnetic materials are only subjected to thermal agitation and the overall magnetization is zero. presence of a magnetic field, the average orientation of the moments changes under the effect of the torque that brings them back according to both direction and orientation of the field. Thus, appearance of induced magnetization parallel to the magnetic field. Either paramagnetic or diamagnetic materials are considered nonmagnetic since they exhibit magnetization only in the presence of an external field. We mention that ferromagnetic and ferrimagnetic materials above the Curie temperature also display paramagnetic behavior.

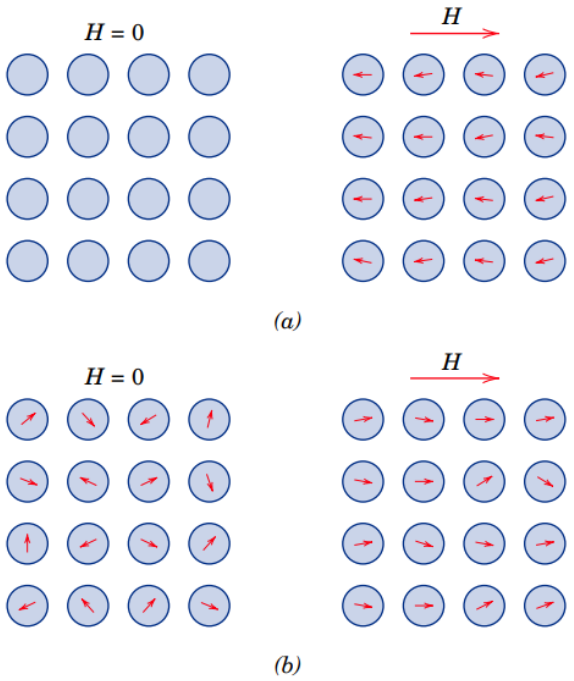

Figure 1.2: (a) The atomic dipole configuration for a diamagnetic material with and without a magnetic field. In the absence of an external field, no dipoles exist; in the presence of a field, dipoles are induced that are aligned opposite to the field direction. (b) Atomic dipole configuration with and without an external magnetic field for a paramagnetic material [22].

1.2.1.3 Antiferromagnetic materials

Antiferromagnetic materials are materials that spontaneously align their magnetic moments antiparallel when an external magnetic field is applied, or temperatures below a critical temperature called "Néel Temperature T_N" [23]. At temperatures above this point, antiferromagnetic materials also become paramagnetic.

In materials such as manganese, chromium, NiO and MnO, in the presence of an external magnetic field, the magnetic moments created in neighboring dipoles line up in exactly opposite directions, although the strength of each dipole is very high. Manganese oxide (MnO) is one material that exhibits this behavior as shown in Figure 1.3. These materials are antiferromagnetic and have zero magnetization. The magnetic susceptibility is positive and small. Furthermore, $MnCl_2$, CoO are examples of antiferromagnetic

materials.

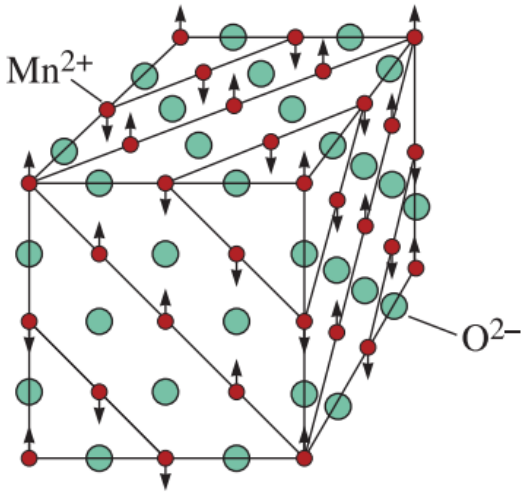

Figure 1.3: The crystal structure of MnO consists of alternating layers of 111 type planes of oxygen and manganese ions. The magnetic moments of the manganese ions in every other (111) plane are oppositely aligned. Consequently, MnO is antiferromagnetic [21].

1.2.1.4 Ferromagnetic materials

Ferromagnetic materials is resulted by the empty energy levels in the 3d level of iron nickel and cobalt. Similar behavior is found in some other materials, including gadolinium (Gd). In ferromagnetic materials the permanent individual magnetic moments simply align with the applied magnetic field caused by the exchange interaction or mutual reinforcement

Significant magnetizations are achieved even for low magnetic fields giving huge susceptibilities approaching 10^6 [21]. Above the temperature of transition (T_c) ferromagnetic materials acts like paramagnetic materials and their susceptibility known as the Curie-Weiss law and expressed as follows:

$$\chi_m = \frac{C}{T - T_c} \tag{1.1}$$

In this equation, C is a constant that depends upon the material, T_C is the Curie temperature, and T is the temperature above T_C. Identical to ferroelectrics ferromagnetic

materials show the creation of hystereis loop domains and magnetic domains. These materials will be discussed in the next section.

Permanent magnetic moments in ferromagnetic materials result from atomic magnetic moments due to uncancelled electron spins caused by the electron structure. Also, there is the contribution of the orbital magnetic moment that is minor compared to the spin moment. Moreover, in a ferromagnetic material, coupling interactions induce net spin magnetic moments of neighbors atoms to align with one another, even if the external field is removed. This is schematically illustrated in Figure 1.4.

The cause of these coupling forces is not fully understood, but it is thought to be caused by the electronic structure of the metal. This mutual spin arrangement exists over relatively large regions of the crystal, called domains. The maximum possible magnetization or saturation magnetization Ms, of a ferromagnetic material indicates the magnetization generated when all the magnetic dipoles in a solid are aligned with the external magnetic field; there is also a corresponding saturation magnetic flux density Bs. The saturation magnetization is calculated by the product of the net magnetic moment of each atom and the number of present atoms. For each of Nickel, Cobalt, Iron, the net magnetic moment of each atom is 0.60 1 72 and 2.22 bohr magnetons respectively.

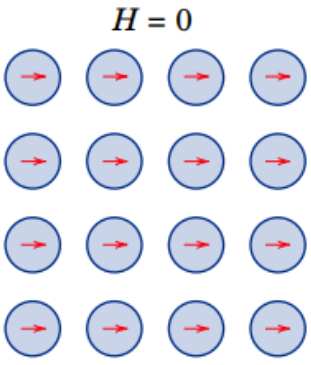

Figure 1.4: Schematic illustration of the mutual alignment of atomic dipoles for a ferromagnetic material, which will exist even in the absence of an external magnetic field [22].

1.2.1.5 Ferrimagnetic materials

Ferrimagnetism is the magnetic property of materials having unequal atomic moments aligned in opposite directions like antiferromagnetic materials.

In ceramic materials, different ions have unequal magnetic moments. In a magnetic field the dipoles of cation A can align with the field, unlike of the cation B dipoles that oppose the field. Because the strength of dipoles is not equal, a net magnetization results. These materials show a large, magnetic-field dependent magnetic susceptibility similar to ferromagnetic materials. They also show Curie-Weiss behavior (similar to ferromagnetic materials) at temperatures above the Curie temperature.

Most ferrimagnetic materials are ceramics and are good electrical insulators. Therefore, in these materials, electrical losses (known as eddy current losses) are much weaker compared to those in ferromagnetic metallic materials. Therefore, ferrites are used in many high-frequency applications [21].

1.2.2 Classification of ferromagnetic materials

On the basis of their hysteresis characteristics. Both ferromagnetic and ferrimagnetic materials are classified as either hard or soft. Hard magnetic materials or permanent magnets maintain their magnetization (high resistance to demagnetization). In soft materials, they can become magnetized, but when the magnetizing source of magnetization is removed, these materials lose their magnetism. In this section, we will discuss the basic concepts and definitions of domain structure and magnetic hysteresis, as well as we will look at some applications for magnetic materials [21, 22].

1.2.2.1 Domain structure and hysteresis

Within the single crystal or polycrystalline structure of a ferromagnetic or ferrimagnetic material that is at a below its curie temperature, a substructure composed of small volume regions, in which all of the magnetic dipole moments are aligned in a certain direction, even in the absence of an external field as shown in figure 1.5. Similar to ferroelectrics, application of a magnetic field (poling) will coerce many of the magnetic domains to

align with the magnetic field direction, and each one is magnetized to its saturation magnetization.

Domain boundaries, called Bloch walls, separate adjacent domains. The boundaries are adjacent zones in which the the magnetic moment direction changes gradually and continuously from that of one domain to that of the next (see figure 1.5(b)). Normally, domains are typically very small (microscopic in size), about 0.005 cm or less, while the Bloch walls are about 100 nm thick. We mention that, for a polycrystalline structure each grain may consist of more than a single domain with different magnetization orientations. The magnitude of the M field for the entire solid is the vector sum of the magnetizations of all the domains, each domain contribution being weighted by its volume fraction. For an unmagnetized ferromagnetic or ferrimagnetic specimen, the net magnetization off all the domains is zero.

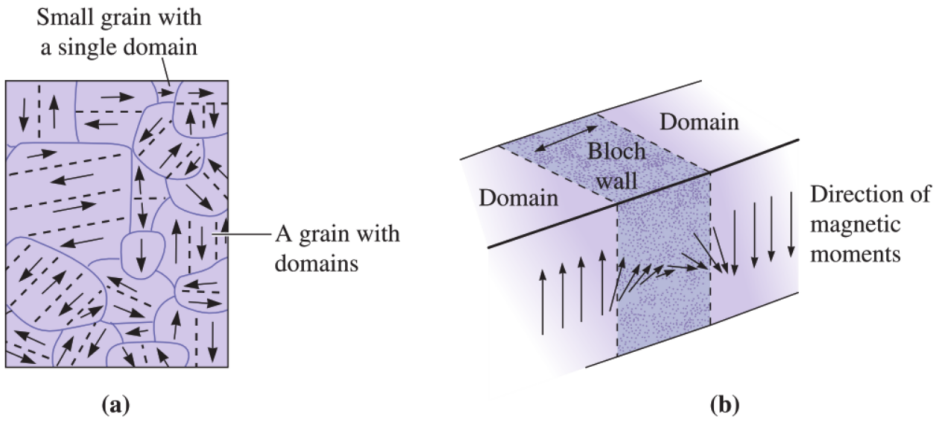

Figure 1.5: (a) qualitative Schematic of magnetic domains in a polycrystalline material. The dashed lines show demarcation between different magnetic domains; arrows represent atomic magnetic dipoles. Within each domain, all dipoles are aligned, whereas the direction of alignment varies from one domain to another. the dark curves show the grain boundaries. (b) The magnetic moments change direction continuously across the boundary between domains [21].

In the case of ferromagnets and ferrimagnets, flux density B and field intensity H are not proportional. If the material is initially unmagnetized, then B varies as a function of H, as presented in figure 1.6. When a magnetic field is first applied to a magnetic material,

magnetization initially increases slowly, then more rapidly as the domains begin to grow. Later, magnetization slows, as domains must eventually rotate to reach saturation. The curve starts from the origin, and as H is increases, the B field begins to increase slowly, then more rapidly, finally leveling off and becoming independent of H. This maximum value of B is the saturation flux density B_s, and the corresponding magnetization is the saturation magnetization M_s, mentioned previously.

When the H field is applied, the domain changes its shape and size through the movement of the domain boundary. The schematic structure of the domain is shown in the insets (marked U to Z) at several points along the curve B versus H in figure 1.6. Initially, the moments of the constituent domains are randomly oriented such that there is no net B (or M) field (inset U). When applying an external field, the domains oriented according to the favorable directions (or nearly aligned with) the applied field grow at the expense of those that are unfavorably oriented (insets V through X). This process continues as the field strength increases until the macroscopic specimen becomes a single domain nearly aligned with the field (inset Y). When this domain, by means of rotation, becomes oriented with the H field (inset Z) Saturation is achieved.

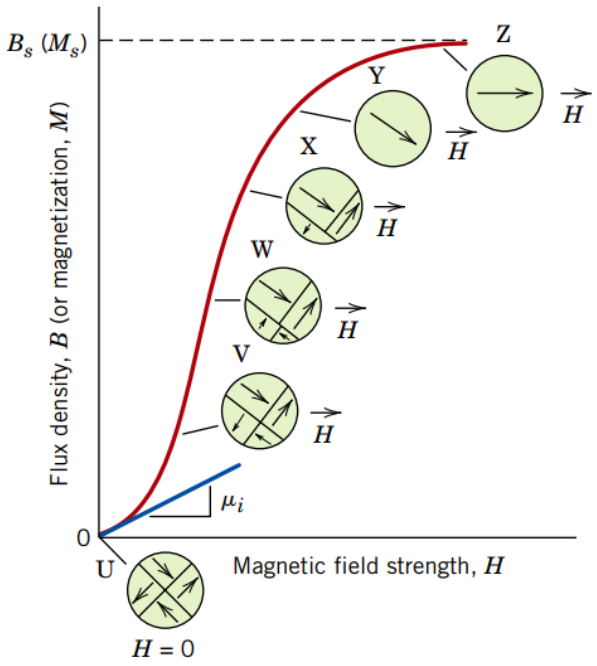

Figure 1.6: The B-versus-H behavior for a ferromagnetic or ferrimagnetic material that was initially unmagnetized. Domain configurations during several stages of magnetization are represented. Saturation flux density B_s, magnetization M_s, and initial permeability μ_i are also indicated [22].

The B-versus-H curve in figure 1.7 represents a hysteresis loop taken to saturation $B(H)$. From saturation, point S in figure 1.7, as the H field is decreased through field direction reversing, the curve does not retrace its original path. The hysteresis loop is the response curve of magnetic materials, through which they keep the memory of all their previous magnetization states through the elementary domains [24]. At zero H field point (R on the curve) there exists a residual B field that is called the remanence, or remanent flux density B_r, since the displacement of the Bloch walls is not instantaneous due to the magnetic anisotropy; a non-zero induction B_r occurs in the material in the absence of an external H field. Hysteresis behavior and permanent magnetization depends on the mobility of the Bloch walls. Upon reversal of the field direction from saturation (point S in figure 1.7), the process by which the domain structure changes is reversed.

To decrease the B field within the specimen to zero (point C on figure 1.7), an H field of magnitude $-H_C$ is required with an opposite direction to that of the original field; the

term H_c is called coercivity. Upon continuation of the applied field in this reverse direction, as indicated in the figure, saturation is achieved in the opposite sense, corresponding to point S'. Finally, a second reversal of the field to the point of the initial saturation point S completes the hysteresis loop symmetricaly and also yields both a negative remanence $-B_r$ and a positive coercivity $+H_C$.

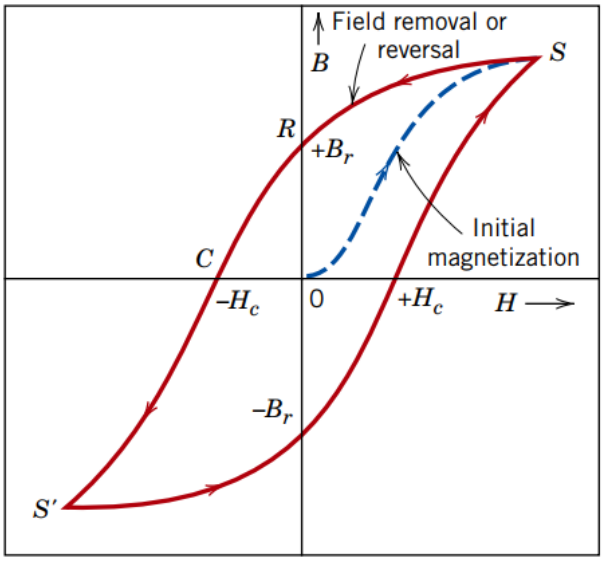

Figure 1.7: Magnetic flux density B versus the magnetic field strength H for a ferromagnetic material that is subjected to forward and reverse saturations (points S and S'). The hysteresis loop is represented by the solid curve; the dashed curve indicates the initial magnetization. The remanence B_r and the coercive force H_c are also shown [22].

1.2.2.2 Hard magnetic materials

Hard magnetic materials are used in permanent magnets, which must have a high resistance to demagnetization. In terms of hysteresis behavior, a hard magnetic material has a high coercivity (generally above 10 kA/m), high remanent induction, saturation flux density and a large hysteresis loop, as well as high hysteresis energy losses and a low initial permeability [25]. We mention that, the two most important characteristics relative to applications for these materials are the coercivity and the energy product designated as $(BH)_{max}$. The hysteresis characteristics for hard and soft magnetic materials are compared in figure 1.8.

1.2.2.3 Soft magnetic materials

Soft magnetic materials are materials in which the coercive field is low (usually less than 1000 A/m) [26]. The relative area within the hysteresis loop must be small; it is characteristically thin and narrow, as represented in figure 1.8. Therefore, a soft magnetic material should have a low coercivity and a high initial permeability. The magnetization saturation for these materials can be reached under relatively low applied field (i.e., is easily magnetized and demagnetized) and still exhibit low hysteresis energy losses. In addition, soft magnetic materials are used in generators, motors, dynamos, and switching circuits and many other applications.

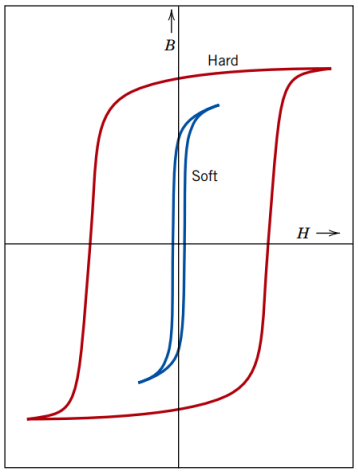

Figure 1.8: Comparison of magnetization curves (hysteresis loops) for soft and hard magnetic materials [22].

1.2.3 The Curie temperature

With rising the temperature of a ferromagnetic or ferrimagnetic material, the added thermal energy increases the thermal vibrations of the domains, making it easier for them to become aligned, but also preventing them from remaining aligned when the field is eliminated. Consequently, the saturation magnetization, remanance, and the coercive field drops with temperature, up to the Curie temperature, at which point it fall to near zero (figure 1.9). Above the Curie temperature (T_c), ferromagnetic or ferrimagnetic behavior is no longer observed. Instead, the material behaves as a paramagnetic material.

The curie temperature which is an intrinsic material characteristic can be changed by alloying elements. French scientists Marie and Pierre Curie (the only husband and wife to win a Nobel prize; Marie Curie actually won two Nobel prizes) performed research on magnets, and the Curie temperature refers to their name. The magnetic dipoles still can be aligned in a magnetic field above the curie temperature but they become randomly aligned in the absence of the field [21].

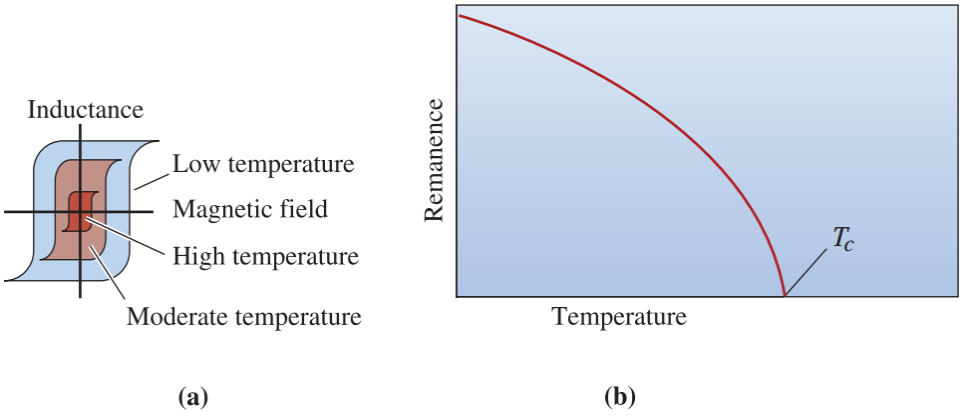

Figure 1.9: The effect of temperature on (a) the hysteresis loop and (b) the remanance. Ferromagnetic behavior disappears above the Curie temperature [21].

1.2.3.1 Measurement of Curie temperature of ferromagnetic materials

There are several techniques to determine the Curie temperature of ferromagnetic materials, the temperature at which the material change its magnetic state (example from paramagnetic to ferromagnetic). The Curie temperature can be influenced by several factors (magnetic fields, size effect, internal stresses, etc.). For perovskites-type materials, studied in the present thesis, the determination of the Curie temperature is essential. As the temperature transition of perovskites depend on several factors, it is important to determine it precisely. In this sense, we mention three different methods of analyzing experimental data to determine the Curie temperature in bulk samples, of which three have been chosen:

Inflection point method

The most widely used method is the inflection point method. This method consists of measuring, under a small applied field, the magnetization M of a substance as a function

of temperature T. Once M vs T curve is obtained, the Curie temperature is approximated by its inflection point. An inflection point is a point on a curve where the first derivative reaches an extrema (maximum or minimum) while the second derivative is zero [27].

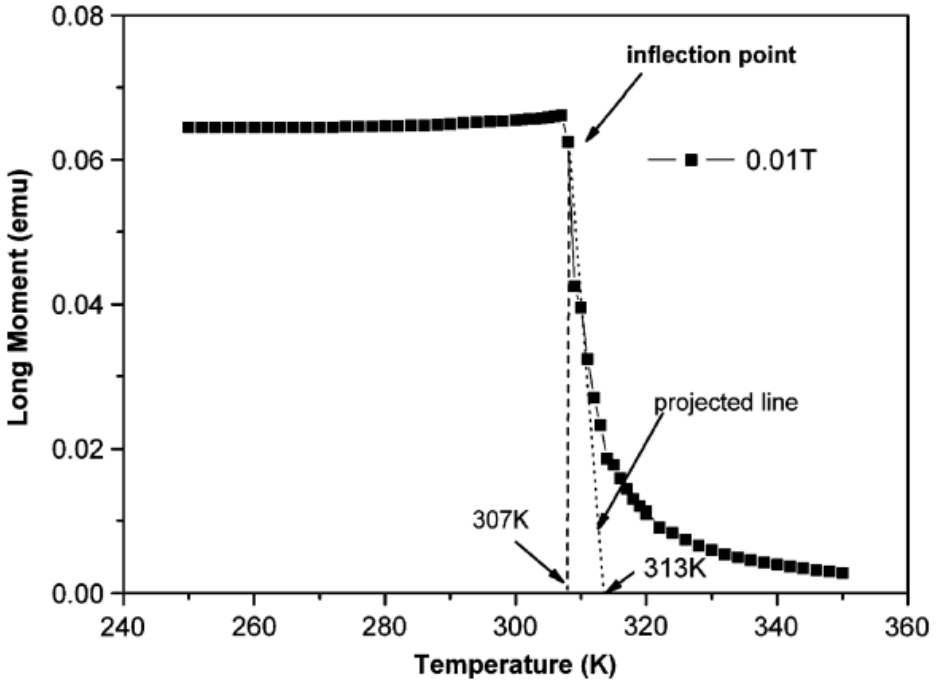

Figure 1.10: Inflection point method used for determining T_C. [27].

The Arrott plot method

Arrott plot technique is based on the Weiss–Brillouin treatment of molecular field theory [28]. Arrott's method attempts to exploit the behavior of isotherms as a function of the magnetic field μ_0H around the Curie point and proposes an extrapolation to better understand this critical point [29]. This technique Criterion, states that isotherms with linear behavior for M^3 as a function of μ_0H around T_C. The isotherm at the Curie point should not have its end curved as it should be a straight line passing through the origin (See figure 1.11) [30].

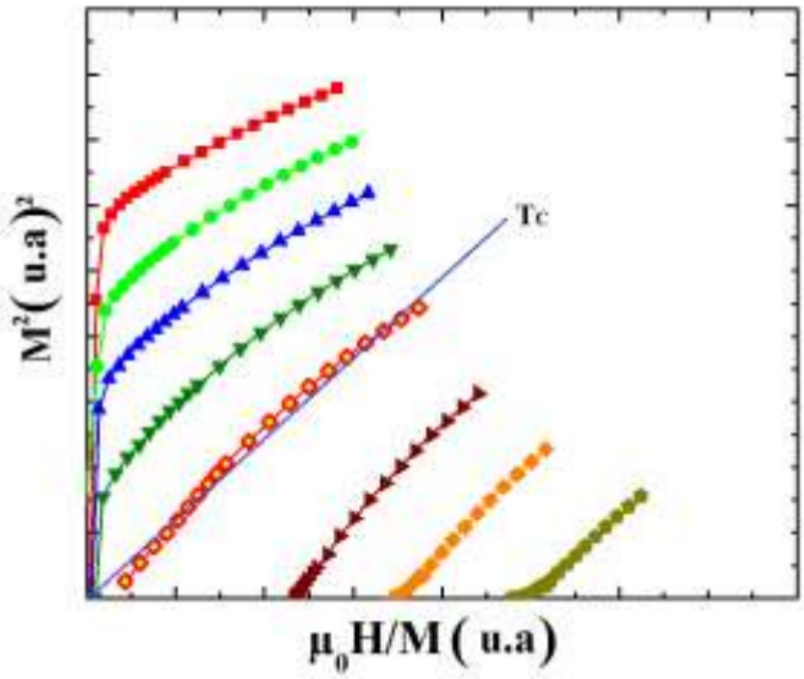

Figure 1.11: The Arrott plot technique used for determining T_C) [30].

Magnetocaloric effect method

This method is not a direct measurement of the Curie temperature, but rather it consists of determining the magnetic entropy change (ΔS_m) under an applied magnetic field μ_{0H}. The latter reaches its maximum value near the temperature of transition. Therefore, makes it possible to indirectly determine the Curie temperature. It is important to point out when using this method that the maximum external magnetic field applied to the substance should not exceed the maximum magnetic field that could be used in the inflection point method ($\leq$ 0.05T) [30]. Therefore, the measurement of the magnetization as a function of several magnetic fields allows to obtain the value of T_C as shown in figure 1.12:

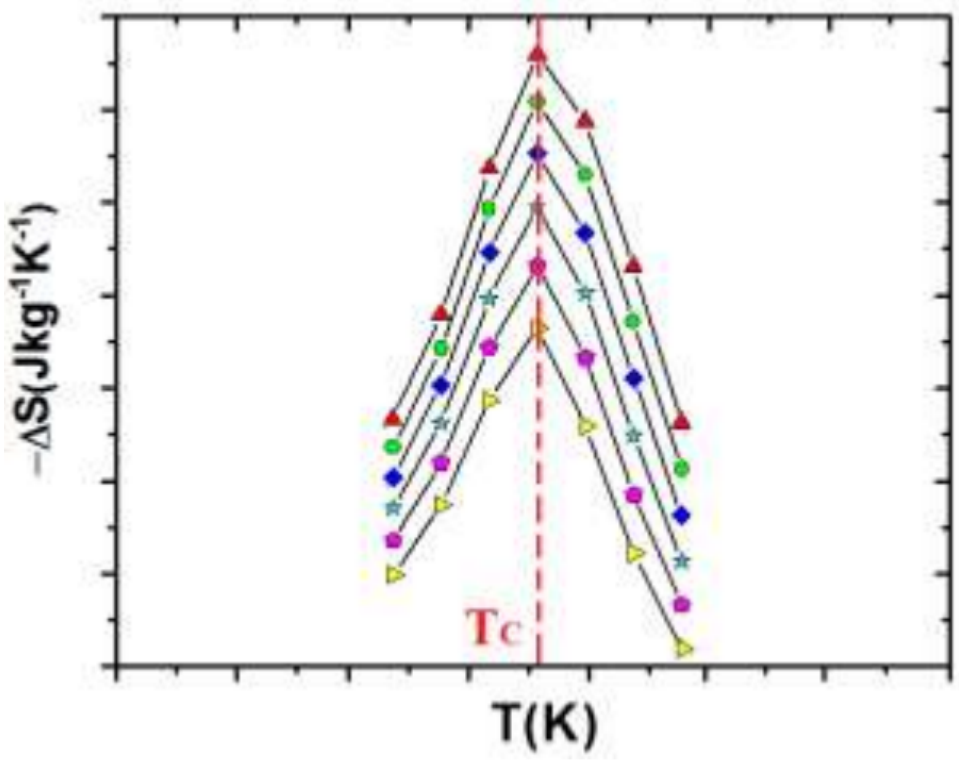

Figure 1.12: Magnetocaloric effect used for determining T_C).[30].

1.3 The Magnetocaloric effect (MCE)

1.3.1 Introduction to the magnetocaloric effect

Magnetocaloric energy conversion is a technology that consist of exploiting the magnetocaloric effect (MCE). The first experimental measurement of the MCE was done by Weiss and Piccard in 1917 [31]. In 1881, Warburg measured the magnetization of iron wire in increasing and decreasing magnetic field around the room-temperature, which is equivalent to a hysteresis cycle. Accordingly, he found that the magnetic irreversibility induces the heat dissipation in the ferromagnetic material [32].

Magnetocaloric effect results in the heating or cooling of magnetized or demagnetized magnetic material. It is generally expressed as the adiabatic temperature change or isothermal total entropy change $\delta S_{(T,H)}$ of a material due to the couplings between the magnetic moments and the atomic network under the action of an external magnetic field. The total magnetic entropy of a magnetic substance consists of magnetic (S_m),

lattice (S_{lat}), and electronic (S_{el}) contributions and is expressed as follows:

$$S(T,H) = S_m(T,H) + S_{lat}(T) + S_{el}(T) \tag{1.2}$$

Where T represent the material temperature and H is the applied magnetic field. Unlike magnetic entropy which depends heavily on the magnetic field, the electronic entropy and atomic entropy are independent of the applied field except for a few materials that exhibit a first-order magnetic transition.

For typical magnetocaloric materials, when the external magnetic flux density is varied and increased from H_I to H_F tends to orient the magnetic moments along the field direction (see figure 1.13), making the magnetic material more ordered. The obtained MCE can be determined in terms of the two thermodynamic process presented in the temperature-specific entropy (T-s) diagram in figure 1.13. This decreases the magnetic entropy and consequently the full entropy is given by the following equation:

$$\Delta S(T, H_I \rightarrow H_F) = S_F(T, H_F) - S_I(T, H_I) \tag{1.3}$$

with $H_F > H_I$ and $S_F < S_I$. In adiabatic conditions, the full entropy is conserved. Thus, the diminution of magnetic entropy is compensated by the change of the quantity S_{Lat} + S_{el} in the opposite way. Therefore, increase the material temperature (Fig. 2) by ΔT_{ad}:

$$\Delta T_{ad}(T_I, H_I \rightarrow H_F) = T_F(S_F) - T_I(S_I), \tag{1.4}$$

with $S_F = S_I$.

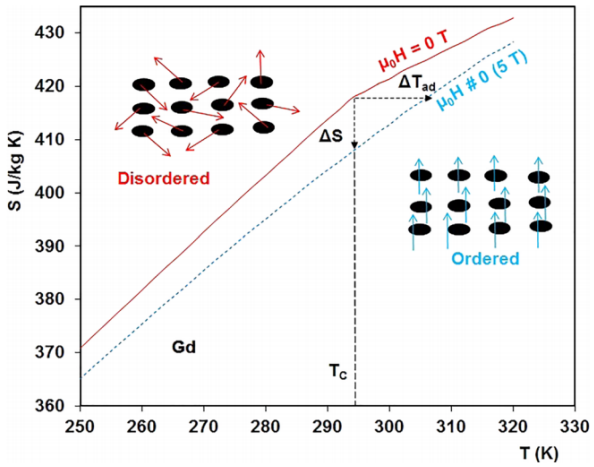

Figure 1.13: The entropy temperature (S-T) diagram Illustrating the isothermal and adiabatic magnetization processes[18].

The application of a high magnetic field makes it possible to align the magnetic moments thus creating a form of order in the solid. This change from a disordered magnetic state to an orderly state is accompanied by an isothermal reduction in magnetic entropy of S_m. In adiabatic conditions, total entropy remains constant. Thus, the decrease in magnetic entropy is compensated by the increase in atomic entropy in the opposite direction causing the increase in the intensity of atomic vibrations increasing the temperature of the material. This temperature change is known as the adiabatic temperature variation ΔT_{ad}. When the magnetic field is removed, the opposite occurs: an increase in the magnetic entropy is observed and the temperature drops. On this basis, the energy conversion cycles is possible by applying different thermodynamic processes.

In this section, the principle of magnetocaloric thermodynamic potentials are presented and described. In addition, an overview of the existing theoretical and experimental approaches to magnetocaloric thermodynamic cycles is given. Different magnetic thermodynamic cycles are described. Besides, thermodynamic cycles with conventional simple cycles, with emphasis on the AMR cycle principle, since most of the existing devices apply the AMR principle.

1.3.2 The Thermodynamics of the MCE

For the description of the magnetocaloric effect of a magnetocaloric material subjected to a magnetic field, it is necessary to define certain functions which characterize the thermodynamic properties [33]. The internal energy of a system according to the first principle of thermodynamics is described by the relation:

$$dU = \delta Q + \delta W \tag{1.5}$$

where δQ and δW respectively represent the quantity of heat exchanged and the work provided by the system. Introducing the following equations:

$$\delta Q = TdS \tag{1.6}$$

$$\delta W = -MdB = -BdM \tag{1.7}$$

l'équation (1.4) devient

$$dU = TdS - MdB = TdS - BdM \tag{1.8}$$

The free energy of a system is expressed by the relation:

$$F = U - TS \tag{1.9}$$

The total derivative of free energy can be written according to the equation:

$$dF = SdT - MdB \tag{1.10}$$

The free enthalpy of a system is expressed by the relation:

$$G = H - TS \tag{1.11}$$

where the enthalpy can be expressed by the expression:

$$H = U + pV \tag{1.12}$$

The derivative of enthalpy and free enthalpy are given as follows: For the case of the solid:

$$dH = dU \tag{1.13}$$

The use of relations (1,4), (1,7) and (1,9) gives:

$$dG = dH - TdS - SdT = SdT - MdB = SdT - BdM \tag{1.14}$$

Entropy, magnetic moment, pressure and volume can be written as a function of the partial derivatives of free energy and free enthalpy as follows:

$$S(T, B, V) = -\left(\frac{\delta F}{\delta T}\right)_{B,V} \tag{1.15}$$

$$M(T, B, V) = -\left(\frac{\delta F}{\delta B}\right)_{T,V} \tag{1.16}$$

$$p(T, B, V) = -\left(\frac{\delta F}{\delta V}\right)_{T,B} \tag{1.17}$$

$$S(T, B, p) = -\left(\frac{\delta G}{\delta T}\right)_{B,p} \tag{1.18}$$

$$M(T, B, p) = -\left(\frac{\delta G}{\delta B}\right)_{T,p} \tag{1.19}$$

$$V(T, B, p) = -\left(\frac{\delta G}{\delta p}\right)_{T,B} \tag{1.20}$$

$$B = -\left(\frac{\delta G}{\delta M}\right)_{T,p} \tag{1.21}$$

The combination of equations (1.17) and (1.15), (1.16) and (1.20) allows to define Maxwell's equations

$$\left(\frac{\delta S}{\delta B}\right)_{T,p} = \left(\frac{\delta M}{\delta T}\right)_{B,p} \tag{1.22}$$

$$\left(\frac{\delta S}{\delta M}\right)_{T,p} = \left(\frac{\delta B}{\delta T}\right)_{M,p} \tag{1.23}$$

The specific heat of a substance can be written according to the relation:

$$C = T\left(\frac{\delta S}{\delta T}\right) \tag{1.24}$$

The total derivative of entropy as a function of the temperature, field and pressure parameters is defined as follows:

$$dS = \left(\frac{\delta S}{\delta T}\right)_B dT + \left(\frac{\delta S}{\delta B}\right)_T dB \tag{1.25}$$

For an isentropic transformation equation (1.24) becomes

$$\frac{C_B}{T} dT = -\left(\frac{\delta M}{\delta T}\right)_B dB \tag{1.26}$$

The total derivative of temperature gives;

$$dT = -\frac{T}{c_B}\left(\frac{\delta M}{\delta T}\right)_B dB \tag{1.27}$$

Integration of equation (1.26) defines the magnetocaloric effect:

$$\Delta T_{ad} = -\int \frac{T}{c_B}\left(\frac{\delta M}{\delta T}\right)_B dB \tag{1.28}$$

1.3.3 Methods of magnetocaloric properties investigation

The main parameter that characterizes a magnetocaloric material is the adiabatic temperature change ΔT_{ad}. In most cases, methods of MCE measurements can be divided into two main groups: direct and indirect techniques. In the case of direct methods the material is subjected to a magnetic field change and its temperature change is directly measured by some technique. In the indirect methods the MCE and magnetic entropy change is determined on the basis of magnetization and / or heat capacity data.

1.3.3.1 Direct methods

In direct methods the initial sample temperature $T_i(H_i)$ and the final one $T_f(H_f)$ at the end of the magnetization are measured by using a temperature sensor in direct contact with the sample, the experiments are usually done in adiabatic conditions. The corresponding adiabatic temperature change is then measured as the difference $\Delta T_{ad} = T_F - T_I$. The field application to or removal from the sample is usually accomplished using pulsed or ramped magnetic fields changing with a rate of about 10 kOe/s [34]. This principle only allows measurements at a fixed temperature and for relatively weak magnetic fields (around 1T). To overcome these limitations and use this method to fully characterize the MCE, more sophisticated devices have been developed. Regarding the applied magnetic field, there are two techniques: pulsed techniques (Kurt, 1985) mainly used for intense fields (3T) and static techniques (Tishin, 1988). In these systems, the thermal insulation of the sample has been improved to ensure adiabatic conditions and differential temperature measurements using thermocouples with high quality have been implemented to increase accuracy. In addition, electronic circuits were introduced to compensate for the effect of magnetic field variation on the response of the temperature sensors.

1.3.3.2 Indirect methods

Magnetization measurements

The change in magnetic entropy is related to the magnetization by equation (1.29).

$$\Delta S_m = \int_0^H \left(\frac{\delta M}{\delta T}\right)_H dH \tag{1.29}$$

The numerical integration of the latter gives the values of ΔS_m at different field and temperature values through the numerical form of the Maxwell relation:

$$\Delta S_m(T, \Delta H) = \sum_i \frac{M_{i+1}(T_{i+1,H}) - M_i(T_i, H)}{T_{i+1} - T_i} \Delta H \tag{1.30}$$

This method is widely used, especially around room temperature; it allows a rapid evaluation of the magnetocaloric performances of materials. The study on the accuracy of the method performed by Pecharsky and Gschneidner [35] shows that it is better than the calorimetric method in the range of temperatures close to ambient (3 to 10% relative error).

Calorimetric measurements (heat capacity)

MCE can also be evaluated indirectly from specific heat measurements as a function of temperature in several constant magnetic fields $Cp(T, \mu_0 H)$ also called calorimetric measurements. This technique enables us to characterize the magnetocaloric effect in terms of both ΔS and ΔT_{ad} with the help of the following Equations [18].

$$S(T, \mu_{0H}) = S_0 + \int_0^T \frac{Cp(T, \mu_{0H})}{T} dT \tag{1.31}$$

where S_0 is the entropy at $T = 0K$ (zero temperature entropy), which is usually assumed to be zero (Foldeaki et al 1997a, Pecharsky and Gschneidner 1999a).

$$\Delta S_m(T, \mu_{0H}) = \Delta S(T, \mu_{0H}) = S(T, \mu_{0H}) - S(T, 0) \tag{1.32}$$

$$\Delta T_{ad} = -\frac{T}{Cp}\Delta S \tag{1.33}$$

1.4 From the magnetocaloric effect to magnetic refrigeration

As it is already presented in magnetocaloric energy conversion section, Cold production is very crucial for modern society. Knowing the basic effect, magnetization induce heating, while demagnetization induce cooling, we present here an analogy with the classic gas compression/ expansion refrigeration. This analogy is illustrated in figure 1.14. It's worth noting that the MCE refrigeration technology present many advantages compared to conventional technique, such as, free greenhouse gas, high energy efficiency, more compact cooling systems, and absence of the compressor (Low vibrations).The MCE is utilized in magnetic refrigeration machines. Therefore, the optimization of such a refrigeration system requires the study of three issues:

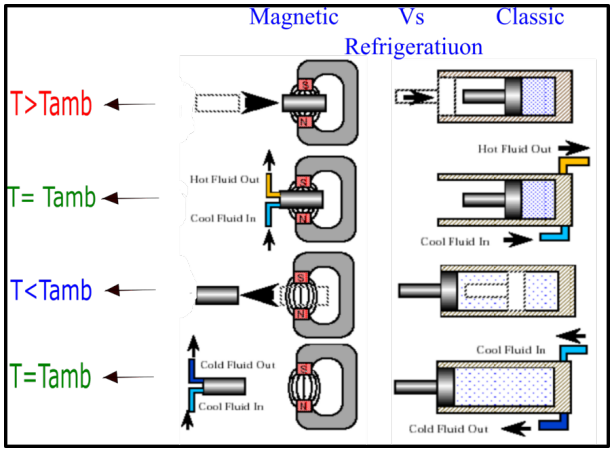

Figure 1.14: Analogy between magnetocaloric refrigeration and gas refrigeration.

- The thermodynamic cycle
- The magnetorefrigerant material
- The magnetic field source

1.4.1 Thermodynamic cycles

There are different thermodynamic cycles considered for magnetic refrigeration [2]. Here we will present the most known thermodynamic cycles, such as, Carnot cycle, Brayton cycle, Ericsson cycle, Stirling cycle and recently the AMR cycle. Figure 1.15 illustrates the main thermodynamic cycles used for magnetic refrigeration.

1.4.1.1 Carnot cycle

The Carnot cycle is the ideal cycle used to quantify the efficiency of all other cycles. It is composed of four processes: adiabatic magnetization (partial), isothermal magnetization (partial), adiabatic demagnetization (partial) and isothermal demagnetization (partial).

1.4.1.2 Brayton cycle

which is one of the most basic cycles of magnetic refrigeration. A machine based

on this cycle operates between two isofields (constant magnetic fields H_0) and two isentropic curves (constant total specific entropy S).

1.4.1.3 Ericsson cycle

A machine based on the Ericsson cycle operates along two isotherms and two isomagnetic field lines. This process requires heat regeneration.

1.4.1.4 Stirling cycle

The Stirling cycle is similar to Ericsson's one except that the exchanges with the outside are iso-magnetization instead of isofield.

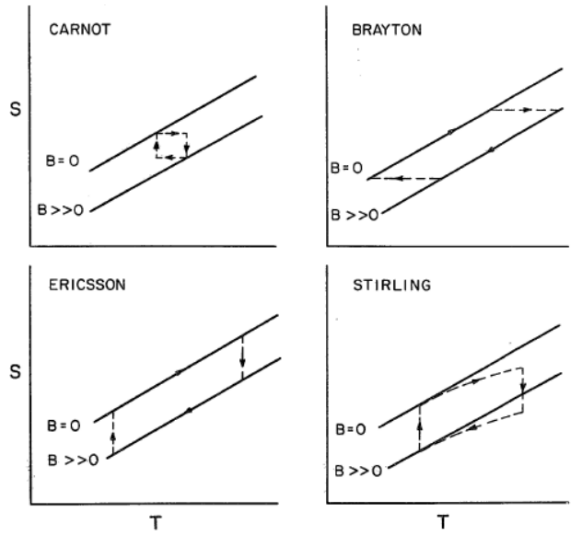

Figure 1.15: S–T diagram of thermodynamic cycles used for magnetic refrigeration.[1]

1.4.1.5 The AMR Thermodynamic Cycle

Most of the applications of magnetic refrigeration at room temperature use permanent magnets as the magnetic field source. The direct use of the magnetocaloric effect to cool in the vicinity of the ambient temperature does not allow to reach significant temperature span between the hot and cold sources, especially with systems using permanent magnets. For refrigeration and heat pump applications, EMC can be amplified through specific magnetothermal cycles called AMRR regeneration cycles. The majority of magnetic refrigerators designed in recent years use this type of cycle.

Significant research studies, both experimental and theoretical, has been carried out on the use of magnetocaloric effect for refrigeration after 1917 [31] when Weiss and Picard discovered a reversible heating of a nickel sample observed near its curie temperature of $(354°C)$ when the sample was exposed to a magnetic field, this discovery is called a "novel magnetocaloric phenomenon". On theoretical works, we found Tishin [36, 36] who used the molecular field theory (MFT) to quantify the crucial thermo-physical properties C_P, ΔT_{ad}, ΔS of magnetocaloric materials, that exhibit both first and second order magnetic phase transitions (Gd, Tb, Dy, Ho, Er, Tm, Fe, Ni, Co) used as a refrigerant by magnetic cooling devices. It should be noted that One of the problems of existing MCMs is the

adiabatic temperature change (ΔT_{ad}) or magnetocaloric effect (MCE) limit. ΔT_{ad} of gadolinium under 1 Tesla magnetic field is around 3 K and 9 K under 5 Tesla magnetic field, for this reason research orients itself to find new magnetic materials which exhibits a giant magnetocaloric effect, with large MCE chiefly at induction fields close to $2T$ and close to room temperature [37], with large entropy change as well as large adiabatic temperature change that offers the promise to surmount the gadolinium powders used in the current rotary refrigerator as Gd_5SiGe_2 [38].

A 1D and 2D numerical models of active magnetic regenerative refrigerator have been reported in multiple papers [39–45]. Engelbrecht et al. have concluded in [46] that the 2D and 1D models are in good agreement while the thermal fluid channels and solid plates are thin (in the case of a parallel plates regenerator), therefore the vertical internal thermal gradients are very low that they can be neglected compared to the thermal gradients in the direction of the fluid flow. Also, a review concerned the different models of (AMR) for room temperature applications was developed in [47].

On experimental works, several studies have treated the analysis of active magnetic regenerators. Among them, one can mention Legait et al. [48] who have examined four magnetocaloric regenerators using three different materials ($Pr_{0.65}Sr_{0.35}MnO_3$, $La(FeCo)_{13-x}Si_x$ and Gd). Tusek et al. have examined a detailed experimental analysis of six different gadolinium AMRs, three with parallel plate AMRs (with different porosities and different orientations of the plates to the magnetic field) as well as three with packed bed AMRs filled with (spheres, powders and with cylinders), they have found that the best cooling characteristics are reached for the parallel plates AMR with the smallest porosity (25%) and with parallel orientations of plates to the magnetic field [49]. A detailed review about various design of refrigerators investigated, both linear reciprocating and rotary magnetic refrigerator up to 2013 [50]. In this work, we were interested to study numerically the AMR cycle (Active magnetic refrigerator) for near room temperature applications.

The AMRR cycle of a magnetic refrigeration system consists of two adiabatic processes and two isofields presented by four following steps.

1. Magnetization of the magnetocaloric material magnetocaloric leads to its warming.

Under adiabatic conditions each point of the magnetocaloric material increases its temperature by T following the application of the magnetic field (Figure 1.16 a).

2. In the second step, the coolant flows from the cold tank to the hot tank to drain the heat-energy generated by the magnetocaloric material (Figure 1.16 b).

3. Adiabatic demagnetization of magnetocaloric material leading to its cooling (Figure 1.16 c).

4. Flow of hot coolant to drain cold energy towards the cold reservoir. Thus, the temperatures of the hot end and the cold end gradually evolve until equilibrium state of temperature after a certain number of cycles. This creates a temperature gradient in the magnetocaloric material (Figure 1.16 d).

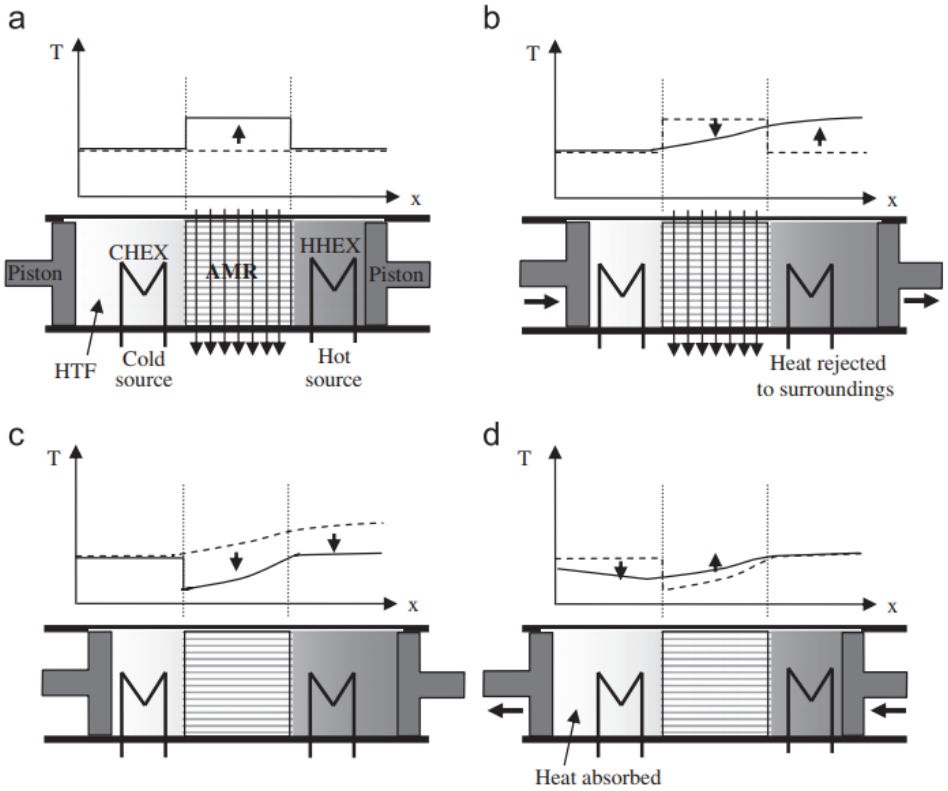

Figure 1.16: AMR cycle and the temperature profile along the AMR during all four operational phases [2].

1.4.2 Magnetocaloric Materials

Magnetocaloric material is the heart of the magnetic refrigerator. It is a critical component that greatly influences the thermodynamic performance of the machine. Implementation and use of efficient magnetocaloric materials are of great importance for the development of magnetic refrigeration in the vicinity of ambient temperature.

Currently gadolinium (Gd), a rare earth with an important EMC near ambient temperature, is the material used in the majority of magnetic refrigeration demonstrators and prototypes. However, despite its magnetocaloric power, gadolinium is not suitable for market applications due to its very high price. In addition, gadolinium has other disadvantages such as its limited refrigeration capacity and its easy oxidation like most rare earths. However, the use of gadolinium in refrigeration systems is preferred over other magnetocaloric materials due to its easy machining and availability on the market. New magnetocaloric materials have been developed to replace gadolinium in magnetic refrigeration systems. Among these materials, large magnetocaloric effect can be observed in $LaFe_{13-x}Si_x$ type, $Gd_5(Si_xGe_{1-x})_4$, Heusler compounds and transition-metal oxides.

1.4.2.1 General Criteria for the Selection of the magnetocaloric material

As the magnetocaloric material is the energy source of magnetic refrigeration, it must have certain characteristics to be good candidate for application as refrigerant. Recently Tino Gottschall et al., [3] have gathered a number of challenges need to be meet in order to develop magnetic cooling, from the fundamental science to the application, figure 1.17 illustrates schematically the different requirements necessary to develop this technology.

We mention here some essential conditions to take into account when selecting the material:

- Magnetic phase transition temperature close to the temperature of a targeted application.
- The Intensity of the magnetocaloric effect $\Delta S_m(T)$ and ΔT_{ad} must be high. Magnetic entropy variation $\Delta S_m(T)$, is linked to the magnetic moment of the material.

While, an adiabatic temperature variation ΔT_{ad} over a broad temperature range allows large cooling power and temperature span, with low sensitivity to heat rejection and low heat capacity C_P. These two parameters are closely related to the nature of the magnetic transition depending on whether it is first order or second order.

- The wide temperature range of the magnetocaloric effect, in other words large relative cooling power (RCP).
- High Thermal Conductivity and diffusivity to increase the heat transfer efficiency.
- High electrical resistance to reduce eddy current losses.
- The absence of magnetic hysteresis for the efficiency of the magnetization process.
- The absence of thermal hysteresis for the reversibility of the thermodynamic cycle.
- Good mechanical properties in order to simplify the manufacturing processes,
- Good chemical stability.
- low material roughness and low fluid viscosity to reduce pressure drops in the bed regenerator.
- Low cost of elaboration and ease of synthesis are important points for commercial applications.
- Good Corrosion Properties.

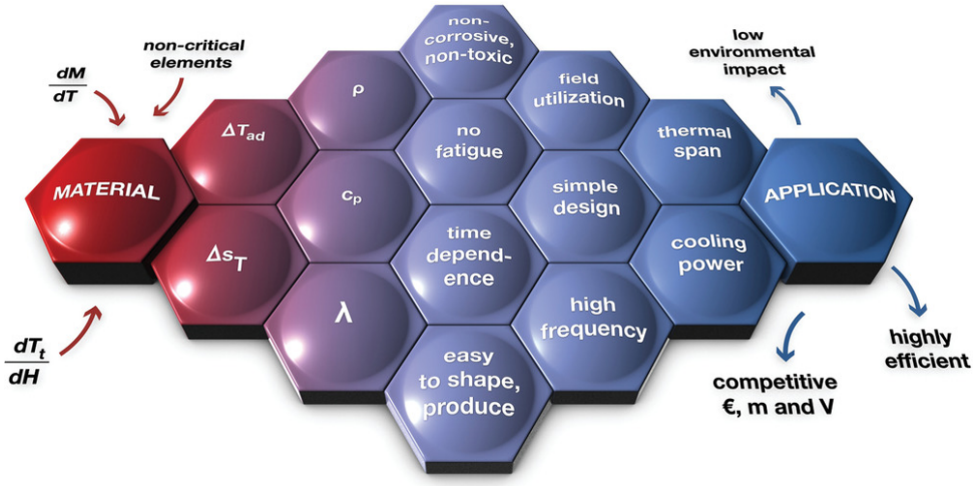

Figure 1.17: Illustration of the different challenges for magnetic refrigeration with respect to applications [3].

In general, MCMs can be divided into two groups based on the order of their phase transition from the ferromagnetic to paramagnetic state, thus calling them second-order or first-order materials [2]. The phase transition happens at the certain temperature, referred to as the Curie temperature (T_c). Above (T_c) the spontaneous magnetization disappears and the material becomes paramagnetic. Furthermore, the MCE is most noticeable at this phase transition. The difference between first-order and second-order materials is how this transition takes place (Fig. 1.18). The characteristic of the so-called "first order" materials, is the discontinuous change of the magnetization at some temperature (Fig. 2.1b) with associated structural-deformation and showing strong variations in the magnetic entropy $\Delta S_m(T)$ and in the adiabatic temperature ΔT_{ad} over a weak temperature range $\delta\ T_{FWHM}$. However, the entropy change only increases drastically to a certain value of magnetic field. These materials present a giant magnetocaloric effect. Indeed, the Maxwell's relation can only be used in the case of a system with equilibrium, its application out of equilibrium can lead to overestimates the $\Delta S_m(T)$. On the other hand, The characteristic of a second-order phase transition is the continuous change of the magnetization around the Curie temperature. Regarding the magnetic entropy change increases with a larger magnetic field and over a wider temperature range (see figure 1.18).

Currently, first order phase transition materials seem impractical for magnetic refrig-

eration even if they display a very large MCE. This may be due to hysteresis in the phase transformation and narrow MCE curves in the Curie temperature vicinity.

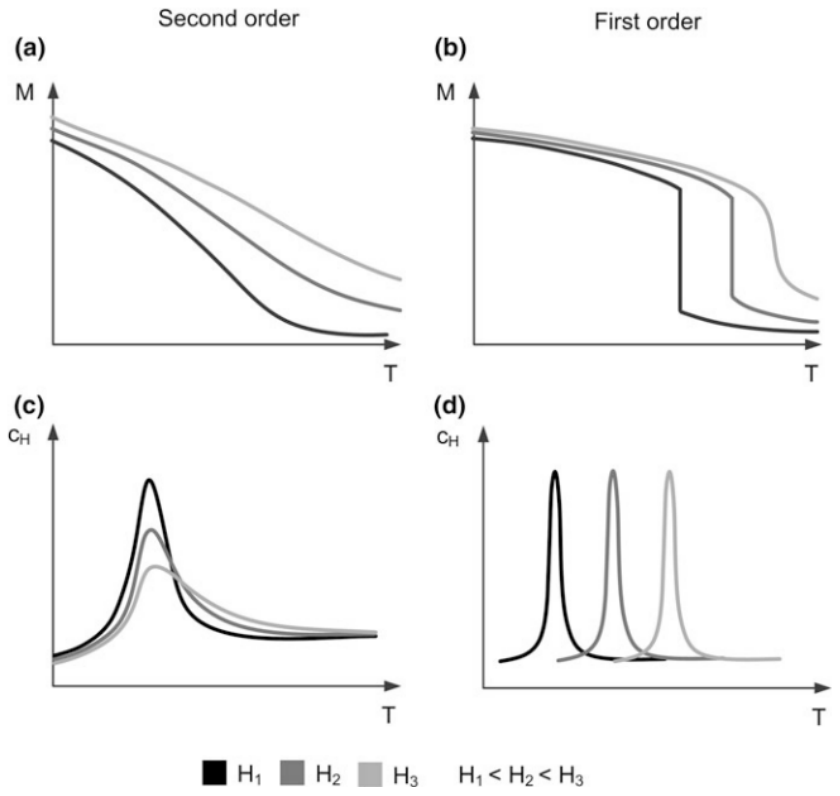

Figure 1.18: Schematic general distinctions between second-order and first-order materials via magnetization (a and b) and specific heat (c and d) in relation to temperature and magnetic field [2]

1.4.2.2 Magnetocaloric effect in oxides

Magnetothermal and magnetocaloric properties were investigated in various oxide compounds: garnets, orthoaluminates, vanadites, manganites and ferrites. perovskites based manganese known as manganites ($RMnO_3$) attract a major interest because of their interesting and complex magnetic and electrical properties, such as colossal magnetoresistance effect, charge and orbital ordering and electronic phase separation. Such compounds can reveal first-order magnetic phase transitions with a sharp change of magnetization and, because of that, high magnetocaloric properties. This circumstance, together with the ability to change in wide range the magnetic phase transition temperatures by variation of their composition (Curie temperatures of some compositions lie in room temperature

range), makes the manganites attractive for applications in magnetic refrigerators. These manganites with perovskite structure and general formulation $RE_{1-x}AE_xMnO_3$ where RE is a trivalent rare earth cation (La^{3+}, Pr^{3+}, Nd^{3+}, Sm^{3+}, Y^{3+}, etc.) and AE is a divalent alkaline earth metal (Ca^{2+}, Ba^{2+}, Sr^{2+}, etc. .). It is certainly possible to obtain complete solid solutions ($0 \leq x \leq 1$) as in the case of $La_{1-x}Ca_xMnO_3$ [51] or $La_{1-x}Sr_xMnO_3$ (under certain processing conditions). These manganites with unsubstituted stoichiometric compositions of $REMnO_3$ or $AEMnO_3$ type contain only manganese in the trivalent Mn^{3+} and tetravalent Mn^{4+} state, respectively. Substitution of RE by AE (and vice versa) leads to hole doping (or electron doping) and generates a mixed valence Mn^{4+}/ Mn^{3+} which is at the origin of the spectacular properties of manganites such as magnetoresistance. The latter is one of the fundamental characteristics of manganites which results in the strong correlations between structure, electronic and magnetic properties. The manganites oxides in which we are interested crystallize in a perovskite structure with general formula ABO_3. For this structure, the Bravais lattice of B sites is simple cubic. The cation A occupies the center of the cube and the oxygen ions occupy the midpoints of the edges. Site A hosts an alkaline earth: Ca, Sr, Ba or Pb and / or a trivalent element like (La, Pr, Nd..). The site B, can be occupied by a metal transition like manganese in the case of manganites. The ideal perovskite is cubic adopting a symmetry Pm3m (figure 1.19) and thanks to its ability to deform, this structure accommodates a wide variety of atoms to various valences. This allows for a wide variety of compositions resulting from insertion of a parent compound $AMnO_3$ with an alkaline earth atom, which gives the following balance of charges:

$A^{3+}Mn^{3+}O_3^{2-} \Rightarrow A_{1-x}^{3+}\ A_x^{2+}Mn_{1-x}^{3+}Mn_x^{4+}O_3^{2-}$

According to the equation above and in the case where there are no oxygen vacancies or vacancies at site A, the percentage x controls the ionization level of manganese. Indeed, the introduction of an atom divalent in the parent compound generates additional percentages of Mn^{4+} ions and Mn^{3+}. These ions characterized by their different electronic structures have a strong contribution on the mechanisms of structural, electronic and magnetic transitions by the the double exchange mechanism and the Jahn-Teller

distortion.

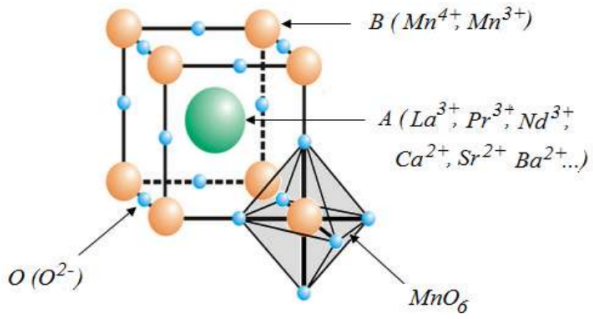

Figure 1.19: Ideal cubic Perovskite $AMnO_3$ structure.

The majority of ABO_3 compounds do not crystallize in the basic cubic lattice. Nevertheless, perovskite structure is flexible and can incorporate a considerable amount of vacancies and can be distorted in many cases leading to deformed structures such as; quadratic, monoclinic, triclinic, orthorhombic or rhombohedral. Most manganites having the ability to distort slightly and lose their cubic symmetry. Crystallographic distortions observed with respect to the cubic mesh come from atomic displacements and are usually explained by a change in the relative size of the ions or by electronic order phenomena of so called localized electrons or delocalized electrons. The most known manganite family is made up of perovskites with composition $La_{1-x}Ca_xMnO_3$. It has been shown that small deviations from the stoichiometry, such as lanthanum deficiency, causes large variations in magnetic properties of these compounds.

Computational and experimental studies have been reported on the magnetocaloric effect in different manganites materials. Thus, published studies covered many physical parameters aiming to improve as much as possible the magnetocaloric properties, namely, the Curie temperature (T_c), the maximum magnetic entropy change under low applied magnetic field that can be reached by permanent magnets, the adiabatic temperature change and the relative cooling power (RCP) which gives an indication of the cooling capacity of the implemented material in magnetic refrigerator. Table 1.1 below summarizes the magnetic properties of a large number of the La manganite family and their magnetocaloric properties.

Table 1.1: MCE parameters of different materials based La manganite family.

Cristalline Compound	T_c **K**	$\mu_0\Delta$**H T**	$\Delta\mathbf{S}_{max}$ **JKg^{-1}K^{-1}**	$\mathbf{RC}_{FWHM}$ **JKg^{-1}**	$\Delta\mathbf{T}_{ad}$ **K**	**Ref**
$La_{0.7}MnO_{3-\delta}$	290	1	1.32	-	-	[52]
$La_{0.8}Na_{0.2}MnO_3$	335	2	2.83	77	-	[53]
$La_{0.8}Na_{0.15}MnO_3$	320	2	2.98	78	-	[53]
$La_{0.8}Na_{0.1}MnO_3$	295	2	2.97	96	-	[53]
$La_{0.8}Na_{0.05}MnO_3$	260	2	3.48	80	-	[53]
$La_{0.925}Na_{0.075}MnO_3$	193	1	1.32	93	-	[54]
$La_{0.9}Na_{0.1}MnO_3$	218	1	1.53	91	-	[54]
$La_{0.927}Na_{0.072}Mn_{0.971}O_3$	193	1	1.3	89	-	[55]
$La_{0.901}Na_{0.099}Mn_{0.977}O_3$	220	1	1.52	87	-	[55]
$La_{0.935}Na_{0.165}MnO_3$	342	1	2.11	63	-	[54]
$La_{0.937}Na_{0.163}MnO_{2.99}$	343	1	2.11	63	-	[55]
$La_{0.8}Na_{0.2}MnO_3$	334	1	1.96	86	-	[54]
$La_{0.801}Na_{0.199}MnO_{2.97}$	334	1	2	90	-	[55]
$La_{0.95}Na_{0.05}MnO_3$	196	0.8	0.84	21.7	0.53	[56]
$La_{0.90}Na_{0.10}MnO_3$	298	0.8	2.18	28.2	2.09	[56]
$La_{0.85}Na_{0.15}MnO_3$	310	1	0.57	58	-	[57]
$La_{0.85}Na_{0.15}MnO_3$	300	1	0.55	48	-	[57]
$La_{0.922}K_{0.0.078}Mn_{0.965}O_3$	230	1.5	1.25	195	-	[55]
$La_{0.904}K_{0.096}Mn0.974O_3$	283	1.5	1.5	180	-	[55]
$La_{0.84}K_{0.16}Mn0.987O_3$	338	1.5	2.1	128	-	[55]
$La_{0.804}K_{0.196}Mn0.993O_3$	334	1.5	2.2	119	-	[55]
$La_{0.95}K_{0.05}MnO_3$	260	1	2.73	-	1.68	[56]

Continued on next page

Table 1.1 – continued from previous page

Cristalline Compound	T_c **K**	$\mu_0\Delta$**H T**	Δ**S**$_{max}$ **JKg**$^{-1}$**K**$^{-1}$	**RC**$_{FWHM}$ **JKg**$^{-1}$	Δ**T**$_{ad}$ **K**	**Ref**
$La_{0.90}K_{0.10}MnO_3$	287	1	2.74	-	1.79	[56]
$La_{0.85}K_{0.15}MnO_3$	310	1	3.00	-	2.08	[56]
$La_{0.9}K_{0.1}MnO_3$	271	1.1	1.42	40	-	[58]
$La_{0.85}K_{0.15}MnO_3$	324	1.1	1.81	42	-	[58]
$La_{0.825}K_{0.175}MnO_3$	333	1.1	1.24	35	-	[58]
$La_{0.95}K_{0.05}MnO_3$	186.3	0.05	0.033	-	0.0165	[59]
$La_{0.9}K_{0.1}MnO_3$	274.5	0.05	0.145	-	0.07	[59]
$La_{0.89}K_{0.11}MnO_3$	287.9	0.05	0.155	-	0.079	[59]
$La_{0.87}K_{0.13}MnO_3$	309.9	0.05	0.206	-	0.107	[59]
$La_{0.85}K_{0.15}MnO_3$	327.5	0.05	0.152	-	0.085	[59]
$La_{0.7}Ca_{0.3}MnO_3$	150	2	1.36	102	-	[60]
$La_{0.69}Ca_{0.29}MnO_3$	200	2	1.56	93	-	[60]
$La_{0.7}Ca_{0.29}MnO_3$	200	2	1.51	91		[60]
$La_{0.8}Ca_{0.2}MnO_3$	230	1.5	5.5	72	-	[55]
$La_{0.8}Ca_{0.2}MnO_3$	176	1.5	3.67	110	-	[20]
$La_{0.75}Ca_{0.25}MnO_3$	224	1.5	4.7	99		[55]
$La_{0.7}Ca_{0.3}MnO_3$	227	1/5	1.95/6.42	49	/4.8	[55]
$La_{0.67}Ca_{0.33}MnO_3$	260	1.5	4.3	47		[55]
$La_{0.67}Ca_{0.33}MnO_3$	259	3	2.6	114		[20]
$La_{0.67}Ca_{0.33}MnO_3$	252	5	2.06	175		[55]
$La_{0.67}Ca_{0.33}MnO_3$	267	3	6.4	134		[55]
$La_{0.6}Ca_{0.4}MnO_3$	263	3	5.0	135	2.1	[55]
$La_{0.55}Ca_{0.45}MnO_3$	238	1.5	1.9	68		[]
$La_{0.5}Ca_{0.5}MnO_3$	230	2	2.6	95		[61]

Continued on next page

Table 1.1 – continued from previous page

Cristalline Compound	T_c **K**	$\mu_0\Delta$**H T**	Δ**S**$_{max}$ **JKg**$^{-1}$**K**$^{-1}$	**RC**$_{FWHM}$ **JKg**$^{-1}$	Δ**T**$_{ad}$ **K**	**Ref**
$La_{0.5}Ca_{0.5}MnO_3$	240	2	0.75	95		[61]
$La_{0.7}Ca_{0.3}MnO_3$	252	2	2.2	55		[62]
$La_{0.7}Ca_{0.3}MnO_3$	190	2	0.45	36		[62]
$La_{0.67}Ca_{0.33}MnO_3$	267	1	0.84			[63]
$La_{0.65}Ca_{0.33}MnO_3$	277	1	2.78			[63]
$La_{0.61}Ca_{0.33}MnO_3$	281	1	2.33			[63]
$La_{0.57}Ca_{0.33}MnO_3$	283	1	1.99			[63]
$La_{0.8}Ca_{0.2}MnO_3$	183	2	2.23	112		[64]
$La_{0.8}Ca_{0.1}MnO_3$	179	2	2.06	104		[64]
$La_{0.7}Ca_{0.1}MnO_3$	247	2	5.75			[65]
$La_{0.87}Sr_{0.13}MnO_3$	197	5	5.8	232		[55]
$La_{0.845}Sr_{0.155}MnO_3$	234	7	6.6	396		[55]
$La_{0.84}Sr_{0.16}MnO_3$	244	5	5.85	240		[55]
$La_{0.88}Sr_{0.12}MnO_3$	152	7	6.0	372	2.5	[55]
$La_{0.865}Sr_{0.135}MnO_3$	200	7	4.4	330	2	[55]
$La_{0.845}Sr_{0.155}MnO_3$	235	7	6.7	670	3.5	[55]
$La_{0.815}Sr_{0.185}MnO_3$	280	7	7.1	533	4	[55]
$La_{0.8}Sr_{0.2}MnO_3$	305		7	7.9		[55]
$La_{0.75}Sr_{0.25}MnO_3$	340	1.5	1.5			[55]
$La_{0.65}Sr_{0.35}MnO_3$	305	1	2.12	106		[55]
$La_{0.67}Sr_{0.33}MnO_3$	348	5	1.69	211		[55]
$La_{0.67}Sr_{0.33}MnO_3$	370	1	1.5	41		[55]
$La_{0.8}Sr_{0.2}MnO_3$	287	2	1.7			[55]
$La_{0.7}Sr_{0.3}MnO_3$	365	5	4.44	128		[55]

Continued on next page

Table 1.1 – continued from previous page

Cristalline Compound	T_c **K**	$\mu_0\Delta$**H T**	Δ**S**$_{max}$ **JKg**$^{-1}$**K**$^{-1}$	**RC**$_{FWHM}$ **JKg**$^{-1}$	Δ**T**$_{ad}$ **K**	**Ref**
$La_{0.67}Sr_{0.33}MnO_3$	370	5	5.15		3.3	[55]
$La_{0.4}Pr_{0.3}Ca_{0.1}Sr_{0.2}MnO_3$	289	1.9	2.98		1.5	[66]
$La_{0.5}Pr_{0.2}Ca_{0.1}Sr_{0.2}MnO_3$	296	2	1.82			[67]
$La_{0.2}Pr_{0.5}Sr_{0.3}MnO_3$	299	1.8	1.95		1.2	[68]
$La_{0.4}Pr_{0.3}Sr_{0.3}MnO_3$	337	1.8	1.91		1.33	[68]
$La_{0.6}Ca_{0.4}MnO_3$	268	0.7	1.8		0.54	[69]
$La_{0.67}Ca_{0.33}MnO_3$	268	2.02	6.5		2.4	[70]
$La_{0.7}Ca_{0.15}Sr_{0.15}MnO_3$	338	2	0.925		1.26	[71]
$La_{0.7}Ba_{0.3}MnO_3$	336	1	1.6	36		[55]
$La_{0.67}Ba_{0.33}MnO_3$	292	5	1.48	161		[55]
$La_{0.67}Ba_{0.33}MnO_3$	337	1	2.7	68		[55]
$La_{0.67}Ba_{0.33}MnO_{2.98}$	312	1	2.6	65		[55]
$La_{0.67}Ba_{0.33}MnO_{2.95}$	300	1	2.55	69		[55]
$La_{0.67}Ba_{0.33}MnO_{2.92}$	275	1	1.8	90		[55]
$La_{0.67}Ba_{0.33}MnO_{2.9}$	268	1	1.7	94		[55]
$La_{0.95}Ag_{0.05}MnO_3$	214	1	1.1	44		[55]
$La_{0.8}Ag_{0.2}MnO_3$	278	1	3.4	41		[55]
$La_{0.8}Ag_{0.2}MnO_3$	300	1	2.4	32		[55]
$La_{0.78}Ag_{0.22}MnO_3$	306	1	2.9	38		[55]
$La_{0.75}Ag_{0.25}MnO_3$	306	1.52	45			[55]
$La_{0.7}Ag_{0.3}MnO_3$	306	1.35	33			[55]
$La_{0.9}Ag_{0.1}MnO_3$	293	2.6	2.8	92	1.4	[72]

Continued on next page

Table 1.1 – continued from previous page

Cristalline Compound	T_c **K**	$\mu_0\Delta$**H T**	Δ**S**$_{max}$ **JKg**$^{-1}$**K**$^{-1}$	**RC**$_{FWHM}$ **JKg**$^{-1}$	Δ**T**$_{ad}$ **K**	**Ref**
$La_{0.85}Ag_{0.15}MnO_3$	280	2.6	4.2	111	2.3	[72]
$La_{0.8}Ag_{0.2}MnO_3$	296	2.6			1.8	[72]
$La_{0.8}Ag_{0.15}MnO_3$	265	2.6	5.6	118	2.7	[72]
$La_{0.8}Ag_{0.1}MnO_3$	287	2.6	3.4	68	1.6	[72]
$La_{0.8}Cd_{0.2}MnO_3$	155	1.35	1.01	32		[55]
$La_{0.7}Cd_{0.3}MnO_3$	150	1.35	2.88	86		[55]
$La_{0.7}Cd_{0.3}MnO_3$	252	1	1.8			[73]
$La_{0.6}Cd_{0.4}MnO_3$	263	1	2.1			[73]
$La_{0.5}Cd_{0.5}MnO_3$	268	1	2.3			[73]
$La_{0.9}Te_{0.1}MnO_3$	242	1	1.49	34.5		[74]
$La_{0.9}Pb_{0.1}MnO_3$	235	1.35	0.65			[20]
$La_{0.8}Pb_{0.2}MnO_3$	310	1.35	1.3			[20]
$La_{0.7}Pb_{0.3}MnO_3$	358	1.35	1.53	53		[20]
$La_{0.6}Pb_{0.4}MnO_3$	360	1.35	0.87			[20]
$La_{0.5}Pb_{0.5}MnO_3$	355	1.35	0.81	31		[20]
$La_{0.9}Pb_{0.1}MnO_3$	160	1.5	0.53			[55]
$La_{0.8}Pb_{0.2}MnO_3$	294	1.5/2	1.22/	92/	/0.68	[55]
$La_{0.7}Pb_{0.3}MnO_3$	352	1.5/2	0.96	48/	/1.00	[55]
$La_{0.94}Bi_{0.06}MnO_3$	209	1	1.58			[75]
$La_{0.99}Bi_{0.01}MnO_3$	234	1	2.42	42		[76]
$La_{0.97}Bi_{0.03}MnO_3$	224	1	2.2	43		[76]
$La_{0.94}Bi_{0.06}MnO_3$	209	1	1.58	45		[76]

Continued on next page

Table 1.1 – continued from previous page

Cristalline Compound	T_c **K**	$\mu_0\Delta$**H T**	Δ**S**$_{max}$ **JKg**$^{-1}$**K**$^{-1}$	**RC**$_{FWHM}$ **JKg**$^{-1}$	Δ**T**$_{ad}$ **K**	**Ref**
$La_{0.9}Bi_{0.1}MnO_3$	198	1	1.5	46		[76]
$La_{0.8}Bi_{0.2}MnO_3$	149	1	0.79	40		[76]
$La_{0.5}Ca_0.4Li_{0.1}MnO_3$	250	3	4.16	140		[77]
$La_{0.7}Ca_{0.25}Li_{0.05}MnO_3$	217	2	6.63	109		[78]
$La_{0.7}Ca_{0.3}MnO_3$	234	2	7.03	106		[78]
$La_{0.7}Ca_{0.25}Na_{0.05}MnO_3$	254	2	4.98	99		[78]
$La_{0.7}Ca_{0.25}K_{0.05}MnO_3$	243	2	4.43	107		[78]
$La_{0.65}Ca_{0.30}Na_{0.05}MnO_3$		1/5	1.69/6.98	40/244		[79]
$La_{0.65}Ca_{0.25}Na_{0.10}MnO_3$		1/5	1.38/4.76	42/265		[79]
$La_{0.65}Ca_{0.20}Na_{0.15}MnO_3$		1/5	1.57/4.96	41/228		[79]
$La_{0.65}Ca_{0.15}Na_{0.20}MnO_3$		1/5	1.52/4.65	40/240		[79]
$La_{0.7}Ca_{0.25}Na_{0.05}MnO_3$	235	2	5.0	99		[78]
$La_{0.07}Ca_{0.27}Na_{0.03}MnO_3$	260	4	8.1	232		[80]
$La_{0.7}Ca_{0.24}Na_{0.06}MnO_3$	263	4	7.0	234		[80]
$La_{0.7}Ca_{0.21}Na_{0.09}MnO_3$	271	4	6.9	236		[80]
$La_{0.8}Ca_{0.2}MnO_3$	230	2	3.2	88		[81]
$La_{0.8}Ca_{0.15}Na_{0.05}MnO_3$	245	2	4.6	89		[81]
$La_{0.8}Na_{0.1}Ca_{0.1}MnO_3$	300	2	3.1	91		[81]
$La_{0.8}Ca_{0.05}Na_{0.15}MnO_3$	320	2	2.5	92		[81]
$La_{0.8}Na_{0.2}MnO_3$	330	2	2.3	89		[81]
$La_{0.7}Ca_{0.25}K_{0.05}MnO_3$	235	2	4.4	107		[78]
$La_{0.7}Ca_{0.3}MnO_3$	235	2	6.9	106		[78]
$La_{0.7}Ca_{0.25}K_{0.05}MnO_3$	270	2	3.95	88		[82]
$La_{0.7}Ca_{0.225}K_{0.075}MnO_3$	281	2	3.75	71		[82]

Continued on next page

Table 1.1 – continued from previous page

Cristalline Compound	T_c **K**	$\mu_0\Delta$**H T**	Δ**S**$_{max}$ **JKg**$^{-1}$**K**$^{-1}$	**RC**$_{FWHM}$ **JKg**$^{-1}$	Δ**T**$_{ad}$ **K**	**Ref**
$La_{0.7}Ca_{0.20}K_{0.10}MnO_3$	272	2	3.49	84		[82]
$La_{0.67}Ca_{0.33}MnO_3$	267	1	4.07			[83]
$La_{0.67}Ca_{0.31}Mg_{0.02}MnO_3$	237	1	3.24			[83]
$La_{0.67}Ca_{0.28}Mg_{0.05}MnO_3$	201	1	3.28			[83]
$La_{0.67}Ca_{0.23}Mg_{0.1}MnO_3$	109	1	1.38			[83]
$La_{0.67}Ca_{0.13}Mg_{0.2}MnO_3$	101	1	0.52			[83]
$La_{067.}Mg_{0.33}MnO_3$	96	1	0.41			[83]
$La_{0.75}Ca_{0.125}Sr_{0.125}MnO_3$	282	1.5	1.5	108		[55]
$La_{0.75}Ca_{0.1}Sr_{0.15}MnO_3$	325	1.5	2.85	72		[55]
$La_{0.75}Ca_{0.1}Sr_{0.175}MnO_3$	330	1.5	2.8	70		[55]
$La_{0.67}Ca_{0.3135}Sr_{0.0165}MnO_3$	275	1	3.26	71		[55]
$La_{0.67}Ca_{0.2805}Sr_{0.0495}MnO_3$	287	1	2.15	52		[55]
$La_{0.67}Ca_{0.2475}Sr_{0.0825}MnO_3$	300	1	1.8	54		[55]
$La_{0.67}Ca_{0.165}Sr_{0.165}MnO_3$	337	1	1.7	38		[55]
$La_{0.67}Ca_{0.0825}Sr_{0.2475}MnO_3$	366	1	1.65	37		[55]
$La_{0.72}Ca_{0.28}MnO_3$	190	1	0.62	10	0.26	[84]
$La_{0.72}(Ca_{0.5}Sr_{0.5})_{0.28}MnO_3$	270	1	2.56	36	1.13	[84]
$La_{0.72}(Ca_{0.25}Sr_{0.75})_{0.28}MnO_3$	333	1	1.80	38	0.97	[84]
$La_{0.72}(Ca_{0.25}Sr_{0.75})_{0.28}MnO_3$	350	1	1.57	58	0.85	[84]
$La_{0.72}Sr_{0.28}MnO_3$	364	1	1.76	35	1.06	[84]
$La_{0.7}Ca_{0.3}MnO_3$	258	1.35	6.5			[85]
$La_{0.7}(Ca_{0.95}Sr_{0.05})_{0.3}MnO_3$	263	1.35	0.62			[85]
$La_{0.7}$ $(Ca_{0.9}Sr_{0.1})_{0.3}MnO_3$	268	1.35	3.62			[85]
$La_{0.7}(Ca_{0.85}Sr_{0.15})_{0.3}MnO_3$	275	1.35	1.65			[85]

Continued on next page

Table 1.1 – continued from previous page

Cristalline Compound	T_c **K**	$\mu_0\Delta$**H T**	Δ**S**$_{max}$ **JKg**$^{-1}$**K**$^{-1}$	**RC**$_{FWHM}$ **JKg**$^{-1}$	Δ**T**$_{ad}$ **K**	**Ref**
$La_{0.7}(Ca_{0.8}Sr_{0.2})_{0.3}MnO_3$	282	1.35	1.81			[85]
$La_{0.7}(Ca_{0.75}Sr_{0.25})_{0.3}MnO_3$	293	1.35	5			[85]
$La_{0.7}Ca_{0.25}Sr_{0.05}MnO_3$	275	5	10.5	462		[55]
$La_{0.7}Ca_{0.2}Sr_{0.1}MnO_3$	308	5	7.45	374		[55]
$La_{0.7}Ca_{0.1}Sr_{0.2}MnO_3$	340	5	6.97	369		[55]
$La_{0.7}Ca_{0.05}Sr_{0.25}MnO_3$	341	5	6.86	364		[55]
$La_{0.6}Ca_{0.2}Sr_{0.2}MnO_3$	337	1	1.96	117		[55]
$La_{0.67}Ca_{0.2925}Sr_{0.0375}Mn_{1.05}O_3$	275	3.7	1.30			[86]
$La_{0.67}Ca_{0.285}Sr_{0.045}MnO_3$	282	3.5	1.17			[86]
$La_{0.7}Ca_{0.21}Ag_{0.09}MnO_3$	263	1	4.8			[87]
$La_{0.7}Ca_{0.3}MnO_3$	260	2	7.8	124		[55]
$La_{0.7}Ca_{0.275}Ba_{0.025}MnO_3$	260	2	6.4	109		[55]
$La_{0.7}Ca_{0.25}Ba_{0.05}MnO_3$	267	2	6.3	101		[55]
$La_{0.7}Ca_{0.225}Ba_{0.075}MnO_3$	268	2	4.1	90		[55]
$La_{0.7}Ca_{0.2}Ba_{0.1}MnO_3$	300	2	3.1	105		[55]
$La_{0.7}Ca_{0.06}Ba_{0.24}MnO_3$	298	1	1.85	45		[55]
$La_{0.7}Ca_{0.2}Ba_{0.1}MnO_3$	320	1	1.72	44		[55]
$La_{0.7}Ca_{0.2}Ba_{0.1}MnO_3$	281	2	3.82	86		[88]
$La_{0.7}Ca_{0.2}Ba_{0.1}MnO_3$	284	2	3.51	89		[88]
$La_{0.7}Ca_{0.2}Ba_{0.1}MnO_3$	286	2	2.94	103		[88]
$La_{0.7}Ca_{0.2}Ba_{0.1}MnO_3$	270	2	2.00	79		[88]
$La_{0.7}Ca_{0.2}Ba_{0.1}MnO_3$	263	2	0.92	68		[88]
$La_{0.7}Ca_{0.2}Ba_{0.1}MnO_3$	243	2	0.36	58		[88]

Continued on next page

Table 1.1 – continued from previous page

Cristalline Compound	T_c **K**	$\mu_0\Delta$**H T**	Δ**S**$_{max}$ **JKg**$^{-1}$**K**$^{-1}$	**RC**$_{FWHM}$ **JKg**$^{-1}$	Δ**T**$_{ad}$ **K**	**Ref**
$La_{0.6}Ca_{0.3}Pb_{0.1}MnO_3$	289	1.35	2.55	56		[20]
$La_{0.7}Ca_{0.2}Pb_{0.1}MnO_3$	295	1.35	2.53	45		[20]
$La_{0.7}Ca_{0.1}Pb_{0.2}MnO_3$	337	1.35	3.72	71		[20]
$La_{0.62}Ca_{0.33}Bi_{0.05}MnO_3$	248	1/2	3.5/5.3	53/125		[55]
$La_{0.6}Sr_{0.2}Ba_{0.2}MnO_3$	354	1	2.26	67		[55]
$La_{0.7}Sr_{0.25}Ba_{0.05}MnO_3$	342	1	0.94			[89]
$La_{0.7}Sr_{0.2}Ba_{0.1}MnO_3$	314	1	0.91			[89]
$La_{0.7}Sr_{0.15}Ba_{0.15}MnO_3$	266	1	0.59			[89]
$La_{0.7}Sr_{0.1}Ba_{0.2}MnO_3$	195	1	0.51			[89]
$La_{0.7}Bi_{0.3}MnO_3$	115	1	0.41			[89]
$La_{0.65}Bi_{0.05}Sr_{0.3}MnO_3$	353	5	5.02	216		[90]
$La_{0.6}Bi_{0.1}Sr_{0.3}MnO_3$	334	5	4.81	226		[90]
$La_{0.5}Bi_{0.2}Sr_{0.3}MnO_3$	296	5	4.21	251		[90]
$La_{0.4}Bi_{0.3}Sr_{0.3}MnO_3$	191	5	3.1	325		[90]
$La_{0.7}Ba_{0.25}Na_{0.05}MnO_3$	317	0.8	1.05	41	1.18	[91]
$La_{0.7}Ba_{0.2}Na_{0.1}MnO_3$	313	0.8	0.97	18	1.04	[91]
$La_{0.7}Ba_{0.15}Na_{0.15}MnO_3$	312	0.8	0.62	11	0.60	[91]
$La_{0.6}Ag_{0.15}K_{0.05}MnO_3$	300	1	1.79	43		[92]
$La_{0.8}Ag_{0.1}K_{0.1}MnO_3$	310	1	1.78	41		[92]
$La_{0.8}Ag_{0.05}K_{0.15}MnO_3$	330	1	1.14	49		[92]

Continued on next page

Table 1.1 – continued from previous page

Cristalline Compound	T_c **K**	$\mu_0\Delta$**H** **T**	Δ**S**$_{max}$ **JKg^{-1}K^{-1}**	**RC**$_{FWHM}$ **JKg^{-1}**	Δ**T**$_{ad}$ **K**	**Ref**
$La_{0.67}Ba_{0.18}Zn_{0.15}MnO_3$	260	5	3.39	224		[93]
$La_{0.67}Ba_{0.13}Zn_{0.2}MnO_3$	220	5	2.92	159		[93]
$La_{0.8}Cd_{0.15}K_{0.05}MnO_3$	260	2	2.6	47		[94]
$La_{0.8}Cd_{0.125}K_{0.075}MnO_3$	273	2	2.81	61		[94]
$La_{0.8}Cd_{0.1}K_{0.1}MnO_3$	282	2	3.25	63		[94]
$La_{0.8}Pb_{0.1}MnO_3$	201	1	0.43	34		[95]
$La_{0.8}Pb_{0.1}Na_{0.1}MnO_3$	247	1	0.68	32		[95]

1.4.3 Magnetic cooling systems

With the discovery of the giant magnetocaloric effect in 1997 [11], which was followed by a number of prototypes for magnetic refrigerators, magnetocaloric power generation has again become an interesting field of research. In addition, developing new materials and the possibility of making these materials in cascades (in order to amplify the temperature span) also led to new activities in magnetic power generation. This section is dedicated to magnetic refrigeration systems.

The magnetic field source is one of the essential components of magnetic refrigeration. The performance of a magnetic refrigeration system depends primarily on the magnetocaloric material and the magnetic field. Therefore, it is necessary to design structures generating magnetic fluxes with high density for magnetocaloric materials.

1.4.3.1 Magnetic field sources

There are several types of magnetic field source that can be used for magnetic refrigeration: We mention, electromagnets, superconducting coils and permanent magnets.

Electromagnets

The first idea that comes to mind for creating a variable magnetic field is the use of an electromagnet. Consider a magnetic circuit composed of a solenoid of N turns with a current of intensity I and a core of soft magnetic material of relative permeability μr and length lc. Induction in an air gap of length lg is deduced from Ampere's theorem and is expressed as:

$$B = \mu_0 N I \frac{1}{lc/r + lg} \tag{1.34}$$

The relative permeability of a soft material being very high (typically 1000 $\leq \mu r \leq$ 5000), we can neglect the first term of the denominator. Equation (4.5) is simplified:

$$B \approx \mu_0 N I \frac{1}{lg} \tag{1.35}$$

To obtain an induction of 1 T in an air gap of 30 mm, it is therefore necessary to generate arround 24000 Amperes turns. If we consider a current density in the coil j_S = 3 A·mm^{-2}, this corresponds to a section of 80 cm^2 and leads to joule losses of the order of 750 W. Such large losses would require a cooling system to compensate for the losses due to the joule effect within the core, which defeats the desired goal. This is why electromagnets are not generally used in magnetic refrigeration systems (and more generally, to create high inductions in large air gaps).

Superconducting coils

Superconducting coils easily create inductions greater than 10 T, and consume low energy once in their superconducting state. However, they must be cooled continuously to remain in the superconducting state and the size of refrigeration systems is very large, therefore incompatible with domestic applications or on-board systems.

Permanent magnets

Permanent magnets or hard magnetic materials retain their magnetization. These are permanent "magnets." Many ceramic ferrites are used to make inexpensive refrigerator magnets. A hard magnetic material does not lose its magnetic behavior easily [21]. The permanent magnet-based structures for which the flux density can be controlled by a mechanical operation are preferred over those using electromagnets or superconducting magnets since no electrical energy is consumed in the generation of magnetic field. The value of the induction depends on the remanent polarization of the magnets used as well as on the magnetic circuit in which they are placed. In everything that follows we will focus exclusively on permanent magnet field sources.

1.5 Conclusion

In this chapter we presented an introduction to the magnetic aspects of magnetic materials. Then, we described the magnetocaloric effect as an intrinsic property of magnetic materials, so we present its major role in the cold production by using the active magnetic regenerative refrigeration cycle. In addition, we discussed a list of desirable characteristics for the Selection of the Magnetocaloric Material. A brief review of some of the most common MCMs (Perovskites oxides) that exhibit a MCE close to room temperature were presented.

Chapter 2

Computational methods and Experimental techniques

2.1 Introduction

In this chapter, we will present the computational methods and the experimental techniques used during this thesis work: Density Functional Theory (DFT), Monte Carlo Simulation, Molecular field theory (MFT) different synthesis methods and the characterization techniques.

2.2 Density Functional Theory

2.2.1 Introduction to Density Functional Theory

Density functional theory (DFT) is one of the most commonly used quantum methods in the fields of solid-state physics and quantum chemistry for the determination of the physical and quantum quantities of a given system, in particular, systems containing a large number of electrons.

DFT was established on the basis of the theoretical formalism proposed by Pierre Hohenberg, Walter Kohn and Lu Sham in the mid-1960s [96–98]. The main goal of DFT is to solve the Schrödinger equation by using electron density as the base quantity for

calculations instead of the multielectronic wave function proposed by Hartree-Fock.

In this section, we will present the fundamentals and approximations of the density functional theory (DFT). First, it is necessary to define the equations involved in a system made of nuclei and electrons and leading to the development of the Kohn-Sham equation.

2.2.1.1 Schrödinger equation

The Schrödinger equation is the basic equation of theoretical solid state physics. Classical mechanics turns out to be insufficient, and quantum mechanics must be used, the objective of which is to solve the Schrödinger equation. this equation is fundamental to solve in order to describe the electronic structure of a system with several nuclei and electrons, it was established by Erwin Schrödinger in 1925, it is written in its time-independent and non-relativistic in the form [99, 100]:

$$\hat{H}\psi = E\psi \tag{2.1}$$

Where E is a constant equal to the energy level of the system, ψ is the wave function and $\hat{H}$ is the Hamiltonian of the system given by:

$$\hat{H} = -\frac{\hbar^2}{2m}\nabla^2 + \hat{V}(\vec{r}, t) \tag{2.2}$$

The first term corresponds to the kinetic energy, the second one to the potential.

The Hamiltonian H depends on the physical system described by the Schrödinger equation. For several well-known physical systems, such as the particle in a box, a harmonic oscillator, or in the case of the hydrogen atom, the Hamiltonian has a simple form, and the Schrödinger equation can be solved exactly. In the case of larger atoms, the electrons interact, which precludes analytical solutions. Solving a system with N electrons interaction in quantum mechanics is called the "multiple body" problem. The N body problem is the problem of determining the wave functions and energies of a system made up of N

electrons and M nuclei that form a physical system.

$$H_{total} = T_n + T_e + V_{nn} + V_{ne} + V_{ee} \tag{2.3}$$

For a system containing N electrons and M nuclei, the problem to be solved is a problem with (N + M) particles in mutual interaction. The solution of this problem is very complex and it is necessary to use simplifying approaches. The two levels of simplifications used are: Born-Oppenheimer approximation and Hartree and Hartree-Fock approximation.

2.2.1.2 Born-Oppenheimer approximation

All methods of solving the Schrödinger equation are based on this approximation, in which Born and Oppenheimer [101] assume that there is a large difference in mass between nuclei and electrons. Because of this, the movement of the nuclei relative to the electrons can be neglected and the nuclei will be considered as being frozen. Therefore, the kinetic energy of the nuclei becomes zero ($T_n = 0$) and the Coulomb energy due to the repulsion between nuclei becomes a constant (V_{nn}). The wave function is written as the product of two wave functions, one nuclear and the other electronic:

$$\psi(\vec{r}, \vec{R}) = \psi_n(\vec{R})\psi_e(\vec{r}, \vec{R}) \tag{2.4}$$

Which means that the Hamiltonian of the equation (2.4) can written as:

$$H_{total} = T_e + V_{ne} + V_{ee} \tag{2.5}$$

Although this approximation considerably reduces the degree of complexity of the Schrödinger equation. However, this approximation alone is not sufficient to solve the Schrödinger equation because of the complexity of the electron-electron interactions. This is why it is very often coupled with the Hartree approximation.

2.2.1.3 Hartree-Fock approximation

This approximation was first introduced by Hartree in 1928 [102]. These methods are widely used in quantum chemistry to study atoms and molecules. Hartree approximation, considers the multi-electron wave function as the product of single-particle (single-electron) functions, designated by the term "orbital". The wave function of the system is written as:

$$\psi(r_1, r_2, r_3, ..., r_N) = \psi_1(r_1).\psi_2(r_2).\psi_3(r_3).....\psi_N(r_N) \tag{2.6}$$

Hartree and Hartree-Fock consider that the electrons are independent and each electron evolves in an external field created by the other neighboring electrons. Thus, the Hartree approximation is a mean-field approximation replacing the complicated many-body problem by simple problems in a mean-field potential [102].

2.2.2 Principle of Density Functional Theory

The density functional theory (DFT), is based on the two theorems of Hohenberg and Kohn [103], which establish a functional relationship between the energy of the ground state and its electron density. This theory allows a great simplification of the solution of the Schrödinger equation. The first ideas in this direction were introduced in the works of Thomas and Fermi [96, 104]. The main goal of DFT is determining the ground-state properties of a given system composed of a fixed number of electrons interacting with the nuclei using only information about the electronic density ρ. So, we must first define what is the electronic density of the system to determine its ground state properties.

2.2.2.1 Hohenberg-Kohn theorems

Unlike the Hartree-Fock approach where the energy of the system is a function of the wave function ψ, Density Functional Theory expresses energy as a function of the electronic density.

The two theorems are as follows:

Theorem 1: *The total ground state energy of an interacting N-electron system in the presence of an external potential is a unique function of the electronic density ρ:*

$$E = E(\rho) \tag{2.7}$$

This theorem highlights a unique correspondence between the external potential and electronic density. Since the electronic density determines the number of electrons, it also uniquely determines the wave function and thus the electronic properties of the system.

Theorem 2: *The real ground state density is nothing else than the density that minimizes the energy of the system and all other properties are functional of the ground state density:*

$$E(\rho_0) = min(E(\rho)) \tag{2.8}$$

The main advantage of this theorem is the enormous simplification of the solution of the Schrödinger equation, because of the problem with 3N variables is reduced to a problem of a scalar function in 3-dimensional space.

2.2.2.2 Kohn-Sham equations

In 1965 Kohn and Sham developed a practical method to find the energy e of the ground state from the electron density [105].

Walter Kohn and Lu Sham have shown that the true density is given by the self-consistent solution of the set of Schrödinger-type single-particle equations, called the Kohn-Sham equations:

$$\{-\frac{1}{2}\nabla^2 + V_{KS}(r)\}\varphi_i(r) = \varepsilon_i\varphi_i(r) \tag{2.9}$$

$$\rho(r) = \sum_{ioccup} |\rho_i(r)|^2 \tag{2.10}$$

$$V_{KS}(r) = V_{ext}(r) + V_{XC}(r) + V_H(r) \tag{2.11}$$

Where:

$V_{ext}(r)$ is the external potential created by the nuclei.

$V_{XC}(r)$ is the potential of the exchange-correlation energy, given as:

$$V_{XC}(r) = \frac{\partial E_{XC}[\rho(r)]}{\partial \rho(r)} \tag{2.12}$$

$V_H(r)$ is the classical Hartree potential given as:

$$V_H(r) = \int \rho(r) \frac{1}{|r - r'|} \cdot dr' \tag{2.13}$$

The total energy of the system is obtained by solving the Kohn-Sham equations with the following equation:

$$E(r) = \sum_{ioccup} \varepsilon_i - \int \frac{\rho(r) \cdot \rho(r')}{|r - r'|} \cdot dr \cdot dr' + E_{XC}(\rho) \cdot \int V_{XC}(r)\rho(r) \cdot dr \tag{2.14}$$

The exact form of $E(r)$ is unknown. In order to calculate it, we need the help of approximation for the exchange-correlation term, which is the last term for which we don't know an expression in terms of density or orbitals. So the use of approximations is still necessary and for that we present here some approximations used in DFT.

Local Density Approximation (LDA):

The Local Density Approximation [106] is based on the uniform electron gas model and is the simplest approach to express the exchange-correlation energy. In this approximation, the charge density is assumed to vary slowly in each small volume (local density) that is modeled as a homogeneous electron gas. The LDA approximation assumes that the exchange-correlation term of the total energy of the ground state can be written according to the expression:

$$E_{XC}^{LDA}(\rho) = \int \rho(r) \cdot \varepsilon_{XC}^{hom}(\rho = \rho(r)) \cdot dr \tag{2.15}$$

Where $\varepsilon_{XC}^{hom}(\rho)$ is the exchange-correlation energy for a uniform density of an electron gas.

There is also a version of the LDA that allows electronic spin to be taken into account; it is the Local Spin Density Approximation (LSDA). The exchange-correlation energy E_{XC}^{LDA} become a function of the two spins (Up and down) densities and equation (2.15) becomes:

$$E_{XC}^{LSDA}(\rho\uparrow,\rho\downarrow) = \int \rho(r)\cdot\varepsilon_{XC}^{hom}(\rho\uparrow(r),\rho\downarrow(r))\cdot dr \tag{2.16}$$

Generalized Gradient Approximation (GGA): The generalized gradient approximation (GGA) aims to correct for defects in LDA. The main idea is to take into account the inhomogeneity of the electron density by introducing its first derivative $[\nabla\rho(\vec{r})]$ into the expression of the correlation exchange energy. The exchange-correlation energy is written in the following form:

$$E_{XC}^{GGA}[\rho(\vec{r})] = \int \rho(\vec{r})\cdot\varepsilon_{XC}[\rho(\vec{r}),|\nabla\rho(\vec{r})|]\cdot d\vec{r} \tag{2.17}$$

In which $\varepsilon_{XC}[\rho(\vec{r}),|\nabla\rho(\vec{r})|]$ represents the exchange-correlation energy dependent on the electronic density and its gradient.

In this part of chapter, we have described the main methods and approximations used to numerically solve the Schrödinger equation for a system of N electrons.

2.3 Monte Carlo simulation

2.3.1 Introduction

Condensed matter systems are well known to be treated in the context of statistical mechanics which has been designed primarily to calculate their properties. This branch of physics is based on a concept which considers that in a system the microscopic quantities closely reflect the macroscopic phenomena observed in this system [107]. The main constraint is the large number of particles in a condensed matter system which involves many problems related to the structure and type of interactions occurring in the system,

making it difficult to find concrete answers to all the questions. Thus, it is obvious that the answers provided by the analytical methods are only approximate answers. Therefore, simulation methods like MCS are numerical computing techniques that are now widely used as important complementary methods to further develop understanding of complex systems and phenomena in physics.

For several years, great efforts have been devoted to the study of magnetic properties and phase transitions of magnetic systems using various approximation techniques such as MFA [108], renormalization group [109], serial development [110] and MCS [111]. Among these techniques and others, MCS is recognized to give more precise results very close to those provided by exact solutions and compatible with the experimental results.

2.3.2 Basic concepts of Monte Carlo simulation

Monte Carlo simulation allows the estimation of the average of a physical quantity $\langle Q \rangle$, which can be given in the canonical system as:

$$\langle Q \rangle = \frac{\sum_i Q_i \exp(-\beta E_i)}{\sum_i \exp(-\beta E_i)} \tag{2.18}$$

Where $\exp(-\beta E_i)$ is the Boltzmann factor, that is, the probability density of the canonical ensemble.

$\beta = \frac{1}{K_B T}$ with K_B is the Boltzmann constant, T is the temperature of the system and E_i is the potential energy.

2.4 Theoretical Approach for MCE: Molecular Field Theory

2.4.1 Weiss mean field model

In this part we will present the theoretical approach of the magnetocaloric effect (EMC) based on the Molecular mean Field Theory(MFT). Magnetization, specific heat, isother-

mal magnetic entropy change and adiabatic temperature change are the main parameters that characterise magnetocaloric materials, these parameters must be calculated to quantify the cooling performances of such materials in magnetic refrigeration systems by simulation. Therefore, by using these models we can predict the needed parameters for the AMR cycle simulation. In addition, these models can be used to quantify the magnetocaloric properties of both first and second order magnetic phase transitions.

Weiss theory is based on the mean field approximation. It considers the field undergone by a particle within a system of N interacting particles is approximately the average of the fields created by the other particles. The here presented model named the Weiss-Debye in the model of the molecular field is applied in the case of absence of magneto-volume effects (second order transitions) where the valence electrons are localized, this is the case for example of alloys based on rare earth metals (4f), the magnetization of the magnetic material can be described using the function of Brillouin [18, 33, 112] given by:

$$\sigma = \frac{M}{M_0} = B_J(y) = \frac{2J+1}{2J}\coth\left(\frac{2J+1}{2J}y\right) - \frac{1}{2J}\coth\left(\frac{y}{2J}\right), \tag{2.19}$$

$$y = \frac{1}{T}\left[3T_C\left(\frac{J}{J+1}\right)\sigma + \frac{g_J\mu_B JB}{k}\right]. \tag{2.20}$$

with: σ : relative magnetization

M_0 : saturation magnetization)

$B_J(Y)$: Brillouin function

g_J : Landé factor

μB: Bohr magneton

J: total angular momentum

k: Boltzmann constant

The total angular momentum is determined from the saturation magnetization, ($M_0 = J * g_J * _B$).

The isothermal magnetic entropy as a function of the temperature and the magnetic

field can be calculated by using the expression for S_m as reported in the Smart model [33, 112]:

$$S_m = R.\left[ln\left(\frac{\sinh\left(\frac{2J+1}{2J}y\right)}{\sinh\left(\frac{y}{2J}\right)}\right) - yB_J(y)\right], \tag{2.21}$$

With R is the universal constant of ideal gases. Under a variation of magnetic field from B_I to B_F, the corresponding magnetic entropy change is given by the following relation:

$$\Delta S(T, \Delta B = B_F - B_I) = S_m(T, B_F) - S_m(T, B_I). \tag{2.22}$$

The adiabatic temperature change is determined from the total entropy which consists of three components, the magnetic entropy S_m, the electronic entropy (S_{el}) and the lattice entropy (S_l) (S = S_m + S_{el} + S_L). The electronic entropy is given by the following standard relation:

$$S_{el} = a_e T, \tag{2.23}$$

2.4.2 Debye model for phonons

The contribution of the crystal lattice can be described by the Debye model [33]. The energy of the phonons is calculated using the Planck distribution function. The mass entropy of the crystal lattice is then given by:

$$S_L = -3Rln\left[1 - exp\left(-\frac{T_D}{T}\right)\right] + 12R\left(\frac{T}{TD}\right)^3 \int_0^{\frac{T_D}{T}} \frac{x^3}{exp(x) - 1} dx, \tag{2.24}$$

T_D Presents the Debye temperature. For magnetic field variation of ΔB = B_F - B_I, the variation of the adiabatic temperature ΔT_{ad} is given by the following relation:

$$\Delta T_{ad}(T, \Delta B = B_F - B_I) = T_F(S_F) - T_I(S_I), \tag{2.25}$$

with S_F= S_I. In addition, for materials that exhibits a second order magnetic phase transition, by using the Weiss model, the adiabatic temperature change can be approached by:

$$\Delta T_{ad} = -\frac{T}{C_p}\Delta S. \tag{2.26}$$

Cp is the total specific heat ($C_P = C_m + C_{el} + C_L$) with the contribution of three components, magnetic, electronic and lattice specific heat. The magnetic specific heat is given by

$$C_m = T\frac{\delta S_m}{\delta T}, \tag{2.27}$$

while the specific heat related to the lattice vibrations is given by the Debye Model [33].

$$C_L = 9R\left(\frac{T}{T_D}\right)^3 \int_0^{\frac{T_D}{T}} \frac{x^4 e^x}{(e^x-1)^2} dx. \tag{2.28}$$

For the electronic specific heat ($S_e l = C_e l$), The isothermal magnetic entropy change can be found through the numerical form of the Maxwell relation [18].

$$\Delta S = \sum_i \frac{M_{i+1} - M_i}{T_{i+1} - T_i} \Delta B_i, \tag{2.29}$$

2.5 Synthesis methods

The synthesis of perovskites can be divided mainly into two categories of methods: The solid state reaction method and wet chemistry methods including sol gel and citrate gel methods. In this thesis, we have used different synthesis methods to prepare the manganites based (La-A-Ca)MnO_3 compounds and also LCMO/Mn_2O_3 composites. In the following, we describe every used synthesis method which are the solid state reaction, Sol gel and the modified Pechini Sol-gel.

2.5.1 Solid state reaction (SSR) method

The solid state reaction method, called also ceramic method, is widely used. It consists of mixing by grinding the appropriate metal oxides or carbonates in powder form and then calcinating at high temperature to allow interdiffusion of the cations. The chemical reaction occurs by solid-state diffusion of the ions, which is characterized by a slow kinetic rate. The degrees of mixing and powder particle sizes are of particular importance [113]. The solid-state reaction method, contains several steps as described in Figure 2.1. The

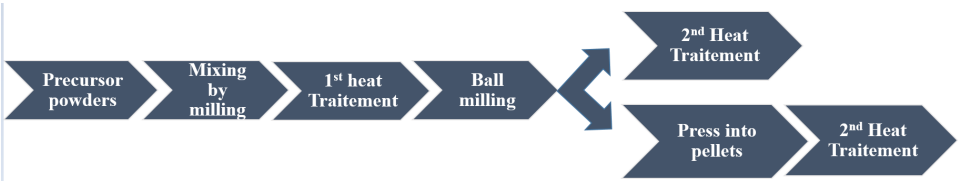

Figure 2.1: The solid state reaction route.

aim is to obtain, from a mixture of solid powder compounds, in stoichiometric proportions, a new product by an appropriate heat treatment. This technique is relatively inexpensive, simple, and it leads to acceptable results. Some drawbacks of this method that may be identified are high calcination and sintering temperatures, non-uniformity of particle size and shape, lack of reproducibility, multiphase character, and loss of stoichiometry.

2.5.2 Wet Chemistry methods

Wet chemistry methods differ from the solid state methods in that the starting materials are mixed to form a solution, which is then dried before the heat treatments. The recipes can vary in both methods and especially the heat treatment temperature, duration, and gas flow are parameters that vary greatly. The purity and the quality of obtained perovskites strongly depend on those variables. Usually used ingredients in wet chemistry methods are the nitric-acid-based method and citric-acid-based method. Stoichiometric amounts of starting ingredients are mixed with either of the acids forming a homogeneous solution.

2.5.2.1 Sol-Gel method

Sol-gel term refers to “solution-gelation”, where “sol” is a colloidal suspension of oligomers with few nanometers of diameter. The principle of this method is to develop a solid from a solution called ”sol” (suspension of colloidal particles in a liquid) to a solid state called ”gel”, which is a semi-rigid solid, where the solvent is trapped in the solid material, which can be colloidal (concentrated or polymeric sol).

The chemistry behind sol-gel method is based on hydrolysis and condensation of precursors dispersed in an organic solvent, or hydroxylated metal ions in aqueous solutions.

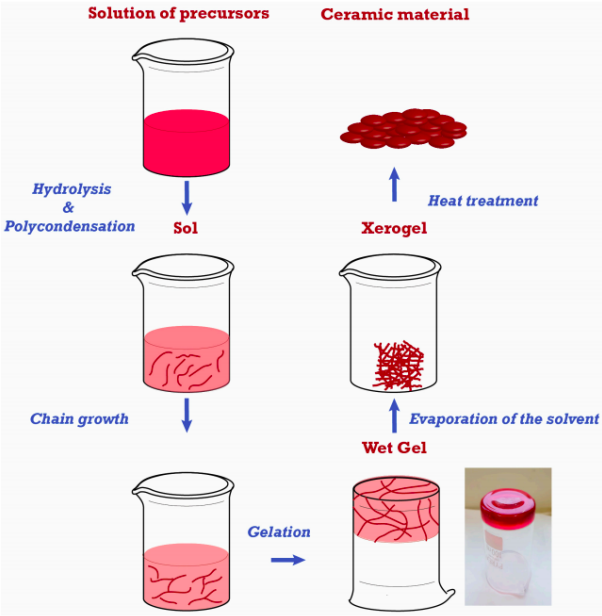

Figure 2.2: Sol-Gel process steps

The sol-gel technique allows the elaboration of various types of materials in different forms (powders, thin films, fibers...). This diversity made this method very attractive in different fields of research.

2.5.2.2 Modified Pechini sol gel

The fundamental idea behind the modified Pechini methods to reduce the mobility of different metal ions, which can be achieved by encircling stable metal-chelate complexes steadily by a growing polymer net. Immobilization of metalchelate complexes in such a rigid organic polymer net can reduce segregations of particular metals during the decomposition process of the polymer at high temperatures. The basic chemistry of this process is the dehydration reaction of a carboxylic acid and an alcohol. Citric acid and ethylene glycol are most widely employed in the Pechini process [113].

2.6 Characterization techniques

2.6.1 Thermogravimetric analysis (TGA)

Thermogravimetry is a technique for which the change in sample mass is measured as a function of time or temperature in a controlled atmosphere. The instrument is called a thermogravimetric analyzer (ATG) or a thermobalance. The measured variation could be a loss of mass in the case of vapor emission, such as, dehydration, decomposition, desorption, reduction or it could be a gain of mass in the case of adsorption, carbonation, oxidation. This method allows to evaluate the amount of hydroxide residues or organic matter existing in the samples as well as their evaporation temperature, so that we can fix an optimal annealing temperature for our samples.

In our thesis, the thermogravimetric analyses were performed using TGA Q500 instrument (see figure 2.3) at MAScIR laboratory with the following conditions:

- The used mass for each sample is between 10 and 30 mg
- Measurements were performed under inert gas (N2, Ar, He) to protect the sample from oxidation.
- The heating rate is 10 °C /min
- Temperature varies between 100 °C and 1000 °C.

Figure 2.3: Thermogravimetric analysis apparatus.

2.6.2 X-Ray diffraction (XRD)

A crystal structure of a crystalline material can be analyzed experimentally using x-ray diffraction (XRD) or electron diffraction techniques. X-ray diffractometry is an analytical technique based on the interaction of the X rays with the electron cloud of atoms in a material subjected to a monochromatic X-ray beam. It makes it possible to study crystallized materials and to obtain informations on the organization of matter, such as the crystal structure and the possible of existing parasitic phases. It also allows the measurement of lattice parameters, stresses, micro-stresses and the crystallite size.

Max von Laue (1879–1960) won the Nobel Prize in 1914 for his discovery related to the diffraction of x-rays by a crystal. William Henry Bragg (1862–1942) and his son William Lawrence Bragg (1890–1971) won the 1915 Nobel Prize for their contributions to XRD. the principle of this technique consists of a monochromatic and parallel X-ray beam striking a crystal is diffracted in a direction given by each of the families of the reticular planes or the beam is reinforced, when conditions satisfy Bragg's law,

$$Sin(\theta) = \frac{\lambda}{2d_{hkl}} \tag{2.30}$$

where the angle θ is half the angle between the diffracted beam and the original beam direction, λ is the wavelength of the x-rays, and d_{hkl} is the interplanar spacing between the planes that cause constructive reinforcement of the beam.

The diffractometer is an apparatus used to determine the angles at which diffraction occurs for powdered specimens; its features are represented schematically in Figure 2.4. As the counter moves at constant angular velocity, a recorder automatically plots the diffracted beam intensity (monitored by the counter) as a function of 2θ; 2θ is termed the diffraction angle, which is measured experimentally. In a diffractometer, a moving x-ray detector records the 2θ angles at which the beam is diffracted, giving a characteristic diffraction pattern (see Figure 2.6). If we know the wavelength of the x-rays, we can determine the interplanar spacings and, eventually, the identity of the planes that cause the diffraction. In an XRD instrument, x-rays are produced by bombarding a metal

target with a beam of high-energy electrons. Typically, x-rays emitted from copper have a wavelength λ=1.54060 $\mathring{A}$ (K-α1 line) are used.

In this work, Powder X-ray diffraction diagrams were made on a Bruker AXS diffractometer with Bragg-Brentano configuration at room temperature (Figure 2.4), the wavelength of the radiation used is that of the Kα line with Cu-Kα (λCu = 1.5407 $\mathring{A}$), the electron acceleration voltage is 40 KV, and the X-ray beam intensity is 75 mA. Diffractograms have been recorded at large angles ranging from 0.45 deg to 87 deg in 2θ, with a pitch of 0.1 deg.

Figure 2.4: Bruker D8 X-ray diffractometer.

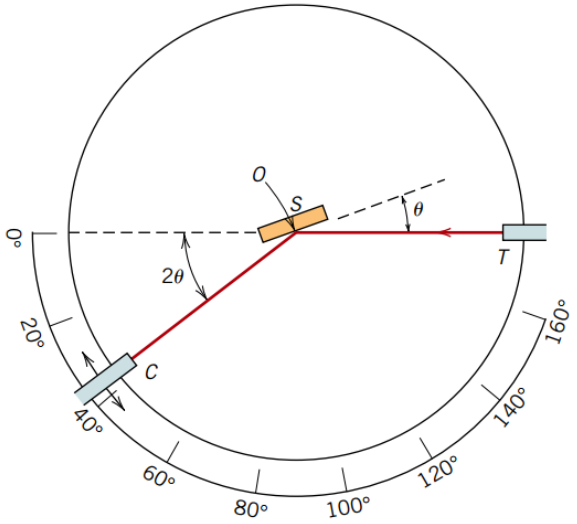

Figure 2.5: Schematic diagram of an x-ray diffractometer; T X-Ray source, S specimen, C detector, and O the axis around which the specimen and detector rotate.

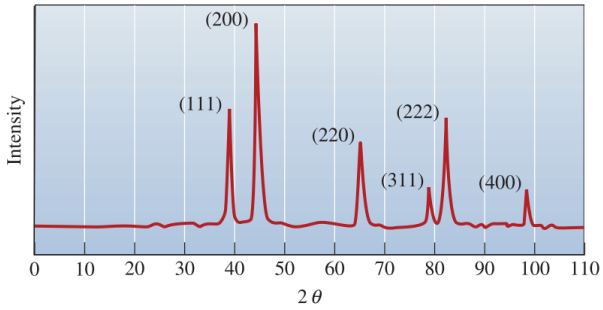

Figure 2.6: The diffraction pattern obtained from a sample of gold powder.

2.6.3 Scanning Electron Microscopy (SEM)

Morphological or microstructural characterization can be carried out either with the transmission electron microscope (TEM) or with the scanning electron microscope with high resolution (SEM-HR). The microstructural characterization of the samples was carried out with with both SEM and TEM microscopes.

The SEM Scanning Electron Microscope is a device that can quickly provide information on the morphology and chemical composition of a solid material. The SEM is coupled to an EDS (Energy Dispersive Spectrometry) microanalysis system. The surface of the sample is scanned by a beam of electrons accelerated at voltages generally between

10 and 30 kV which will interact with the primary radiation material. Many secondary radiations result from these electronic interactions that can be exploited with the help of appropriate detectors:

- Emission of secondary electrons
- Emission of backscattered electrons (without loss of energy)
- Emission of X photons, etc.

The exploitation of these emissions allows the observation of the morphology, topography and microstructure of the analyzed material, in addition to the qualitative and quantitative detection of the atomic elements present in the structure [114].

The SEM used in our work is an "FEI, Quanta FEG 450" electron microscope with an EDX detector. It is equipped with a column-integrated (In-lens) secondary electron (SE) detector for a clear topographic imaging and a backscattered electron (BSE) detector for compositional contract imaging, which allow simultaneous real-time imaging and mixing both signals (figure 2.7).

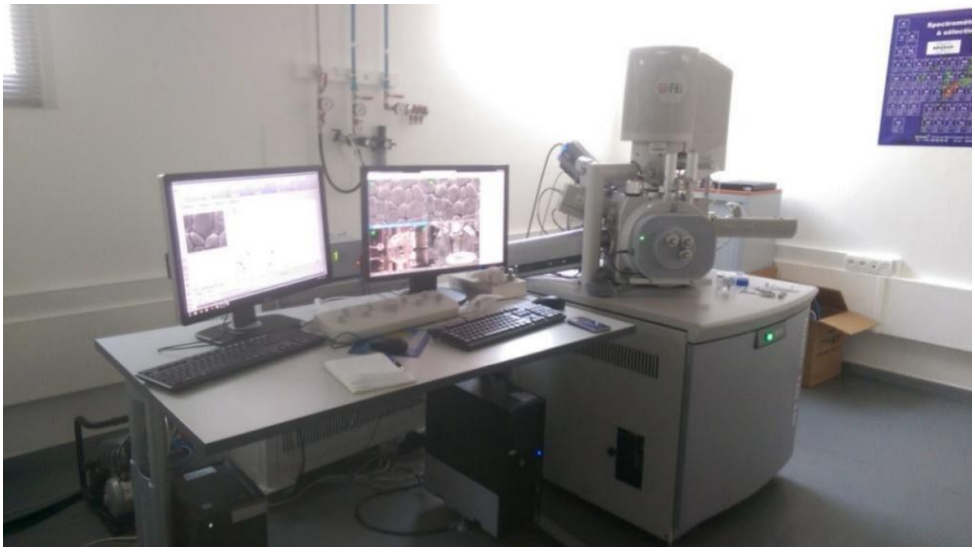

Figure 2.7: FEI Scanning Electron Microscope, Quanta FEG 450.

2.6.4 Transmission Electron Microscope (TEM)

Morphological or microstructural characterization can be carried out by using the transmission electron microscope (TEM) which allows the process of capturing images of very small nanoparticles ($\approx 10nm$).

A transmission electron microscope uses a beam of electrons instead of light, exploiting the wave-particle duality of electrons, with a resolution up to 0.1 nm. Is equipped with a source of electrons, electromagnetic lenses and an electron detector.

A very thin sample is placed on the electron path. An e beam is produced, accelerated, and then concentrated on the sample through the lenses. The beam passes through the sample which modifies it according to its shape and nature and prints its image to the beam. The beam is then enlarged by other lenses and detected, e.g., by fluorescence.

The scanning transmission microscope (TEM) (see figure 2.8). Here, the electron beam is focused at a particular point in the sample and not on the entire surface. The transmitted beam is detected. A sweep of the surface allows to visualize the further the magnified image of the sample. This technique makes it possible to visualize but also to identify the chemical nature of atoms in ultra-thin samples. The powder can only be observed under a microscope after dispersion. Only submicron particles can be observed under a microscope. This microscope works with an electron accelerating voltage of up to 120 kV. This type of device offers the possibility of working up to sizes of 0.35 nm.

Figure 2.8: Transmission Electron Microscopy.

2.6.5 Magnetic properties measurements system (SQUID-MPMS-XL7 magnetometer):

The study and optimization of the magnetic properties of perovskites constitute a large part of this thesis. Magnetic measurements were performed by MPMS-7XL magnetometer to determine the magnetic properties of the prepared samples. For this reason, we used the MPMS-XL7 magnetometer with SQUID (Superconducting Quantum Interference Device) from the company "Quantum Design" (figure 2.9). The main components of this magnetometer are:

- A superconducting solenoid to generate an intense magnetic field.
- A superconducting magnetic induction detection coil is located inside at the center of the magnet.
- A SQUID connected to the sensing coil (for magnetization measurement).
- A temperature control system.

The principle of this measurement is based on the displacement of the sample inside

the sensing coil by a vertical back and forth movement. The variations of the generated flux by the sample induce a current in the detection coil which is transmitted to the SQUID (Superconducting Quantum Interference Device). This is similar to a current to voltage converter and the voltage variations are then directly proportional to magnetic flux variations. The flow variations generated by the sample induce a current in the sensing coil which is transmitted to the SQUID.

The measurements obtained by this system give information about the magnetic reaction of the material subjected to magnetic fields and make it possible to characterize the magnetic properties of this material which are very dependent on the measurement conditions.

Figure 2.9: Superconducting Quantum Interference Device(SQUID) Magnetometry.

2.7 Conclusion

In this chapter, we have presented the different theoretical and experimental methods to determine the physical properties of magnetocaloric materials (Gd, $AlFe_2B_2$ and $La_{1-x}A_xCa_{0.4}MnO_3$) for their application as solid refrigerants in magnetic refrigeration

system. In particular, Density functional theory, Monte Carlo simulation and Molecular field theory. In addition to all the experimental techniques that allow the elaboration of these materials and the main characteristic measurements.

Part II

Contribution and results

Chapter 3

Magnetocaloric and Cooling Properties of the Intermetallic Compound $AlFe_2B_2$ in an AMR Cycle System

3.1 Introduction

The thermal energy derived from conventional techniques such as gas expansion system is no longer desirable because of their harmful effects on the environment, since the orientation towards clean and efficient technologies seems necessary. In this context, magnetic refrigeration based on the magnetocaloric effect (MCE) [31] is considered as a promising cooling technique that allows to fully eliminating the harmful synthetic refrigerant, usually used by standard refrigerators such as chlorofluorocarbons (CFCs), hydrofluorocarbons (HFCs) or hydrochlorofluorocarbons (HCFCs). In recent decades, new advanced solid magnetic refrigerants have been reported [18]. Some of among them were directly tested in functional magnetocaloric devices [48, 115, 116]. Also, following a parallel effort, innovative cooling devices have been built [2, 18]. It is worth noting that from a practical point of view, the suitable magnetocaloric material must exhibit a large MCE under

relatively low magnetic fields (< 2T) that can be reached via permanent magnets.

Giant magnetocaloric compounds near room temperature, such as $Gd_5Si_{4-x}Ge_x$ [11], $LaFe_{13-x}Si_x$ [117, 118],$Y_0.4Gd_{0.6}Co_2$ [119] and $MnFeP(As, Ge)$ [12] are the subject of current research and development. In this study, we report results to the intermetallic compound $AlFe_2B_2$. The most well known application of transition metal borides such as $Nd_2Fe_{14}B$ is their utilization as permanent magnets in several domains [120]. In this work, we are mainly interested by magnetothermal properties. Particularly, the $AlFe_2B_2$-Based compounds offer key advantages for application in magnetic refrigeration when compared with the reference gadolinium metal such as their low cost. In fact, for a large-scale commercialization of this emerging technology, the Gd is unfavorable because of rising prices of rare earths while the intermetallic $AlFe_2B_2$ is completely composed of abundant and affordable elements.

Significant theoretical and experimental studies were performed after 1969, when $AlFe_2B_2$ compound was synthetized by Jeitschko [121]. The orthorhombic structure, as well as the possibility of its ferromagnetic or paramagnetic characters, at room temperature, was identified in several reported studies [122, 123].

The intermetallic $AlFe_2B_2$ belongs to AlM_2B_2 (M=Fe, Mn, Cr) materials class. Combining theory and experiments Kadas et al. [124] have studied the phase stability of a group of nanolaminated materials AlM_2B_2 (M=Cr, Mn, Fe, Co, Ni). They found that compounds with M=Cr, Mn, Fe are stable phases, while compounds with M=Co, Ni are metastable. $AlFe_2B_2$ crystallizes in an orthorhombic structure (space group *Cmmm*, No 65) with two formulas in a unit cell (Z=2) and [a = 2.923(10) Å, b = 11.0337(14) Å, c = 2.8703(3) Å] as cell parameters reported in various studies as [125, 126]. Furthermore, the positions occupied by aluminum, iron and boron atoms are (0, 0, 0) (0, u, 0.5) (0, v, 0), respectively, with the inner parameters u=0.3540, v=0.2071 [127]. The structural, electronic and elastic properties of $AlFe_2B_2$, were studied, theoretically, by Cheng et al. [128]. However, the transition temperature T_c of $AlFe_2B_2$ compound was found to vary between 282 K and 320 K [122], according to Cedervall's study, the Curie temperature found is 299 K using a Mossbauer study on arc melted and annealed sample [129]. The

value of Fe magnetic moment is calculated to be 1.25 μ_B [127]. Additionally, a large magnetic entropy change of -4.1 J/Kg K and -7.7 J/Kg K was experimentally reported in this compound around its Curie point under an applied magnetic field of 2 T and 5 T respectively [123].

The objective of this study is to evaluate the magnetic and magnetocaloric properties of the transition metal boride $AlFe_2B_2$ in order to exploit them subsequently in a thermofluidics study using a numerical model based on the active magnetic regenerative refrigeration cycle (AMRR). This would enable us to get more insight about the performance of this material in functional magnetic refrigerators.

3.2 Computational details

3.2.1 First principles calculation (DFT)

The magnetic properties as well as the electronic structure of the $AlFe_2B_2$ compound were investigated using the density functional theory (DFT) on the basis of Korringa-Kohn-Rostoker coherent potential approximation (KKR-CPA) method, employing the local density approximation without and within self-interaction-corrected (LDA and LDA-SIC) code [128, 130, 131]. We use higher K-points number up to 500 in the irreducible part of the first Brillouin Zone. The relativistic effect has been considered using the scalar relativistic approximation. Moreover, the potential form, is approximately, given by the muffin tin model. The corresponding wave functions in the muffin-tin spheres have been expanded with the real harmonics up to l=2, where l is the angular momentum defined at different sites.

3.2.2 Monte Carlo simulation (MCs)

The Hamiltonian operator is given by:

$$H = -J_1 \sum_{<ij>} S_i S_j - J_2 \sum_{<ij>} S_i S_j - \Delta \sum_i S_i^2 - h \sum_i S_i, \tag{3.1}$$

where J_1 and J_2 are the exchange coupling interactions between the first and second near neighbors of the Fe atoms, respectively. S is the spin random variable which takes the values $\pm$ 1 and 0. Δ and h represent the crystal field and the external magnetic field applied on all the sites of the system. The exchange coupling interactions parameters (J_1, J_2) were calculated within the formalism derived by Lichtenstein given in details in Refs. [132, 133]. The magnetic properties are calculated using unit cell $40\times40\times40$ k-mesh. Our data were generated after 10^5 iterations per spin. The numerical results in term of magnetic and magnetocaloric properties are calculated using the following equations:

The total magnetization of the system is:

$$M = \frac{1}{N}\sum_i S_i \tag{3.2}$$

The magnetic specific heat is given by:

$$C_v = \beta^2 \left(< E^2 > - < E >^2 \right) \tag{3.3}$$

The total susceptibility is:

$$x = \beta \left(< M^2 > - < M >^2 \right), \tag{3.4}$$

where $\beta = \frac{1}{k_B T}$, and k_B is the Boltzmann constant which will be fixed at $k_B = 1$ in all the following numerical calculations.

The magnetic entropy change is:

$$\Delta S_m = \int_{h_i}^{h_f} \frac{\partial M}{\partial T} dh, \tag{3.5}$$

where $\frac{\partial M}{\partial T}$ is the thermal magnetization for a fixed magnetic field.The adiabatic temperature change can be approximated by:

$$\Delta T_{ad} = -T\frac{\Delta S_m}{C_v} \tag{3.6}$$

The relative cooling power (RCP) is given by:

$$RCP = \delta_{fwhm} \Delta S_m^{\mathrm{Max}}, \tag{3.7}$$

where δ_{fwhm} is the full width at half maximum of the ΔS_m curve.

3.2.3 AMR cycle model

The regenerator considered in this study is constituted of 18 parallel plates of the $AlFe_2B_2$ compound with 1mm thickness, 50mm length and 25mm width each. The plates are equidistant with an inter-space of about 0.1mm while the water is used as a heat transfer fluid. Based on the law of energy conservation, the main equations describing the heat transfer between the solid material and the carrier fluid in a 1D model are given by the following partial differential equations (PDE) [47]:

$$m_f C_f \left(T_f\right) \left(\frac{\partial T_f}{\partial t} + \dot{m}(t) \frac{\partial T_f}{\partial x} \right) = hS \left(T_s - T_f\right), \tag{3.8}$$

$$m_s C_s \frac{\partial T_s}{\partial t} + \lambda_s v \frac{\partial^2 T_s}{\partial x^2} = hS \left(T_f - T_s\right), \tag{3.9}$$

$$\dot{Q}_{HT}(x) = hA_{HT} \left(T_s - T_f\right), \tag{3.10}$$

where s and f in the subscript refer to the solid and the fluid, respectively; t is time; x design the spacial coordinate ($0 < x < L$); $T_f = T_f(x,t)$ denote the fluid temperature; $T_s = T_s(x,t)$ denote the regenerator solid temperature; ρ_s is the mass density of the solid; ρ_f is the mass density of the fluid. The heat capacity of the solid and the fluid are denoted by c_s and c_f, respectively; λ_s is the thermal conductivity of solid and λ_f is the fluid thermal conductivity; ν is the velocity of fluid.

The heat transfer between the solid and the fluid is described via a Nusselt number (Nu) calculated according to the empirical correlations corresponding to a laminar flow which is used to determine the convective heat transfer coefficient (h). The AMR cycle is

carried out following successive steps, in order to amplify the temperature span between the hot and cold sides:

1. Isentropic magnetization of the magnetocaloric material.
2. Hot flow at applied magnetic field: heat transfer fluid flows from the cold fluid reservoir to the hot fluid reservoir of the regenerator.
3. Isentropic demagnetization of the magnetocaloric material.
4. Cold flow at removed magnetic field: heat transfer fluid flows from the hot side to the cold side of the regenerator.

The magnetic field of 1T applied during the isentropic magnetization- demagnetization processes is implemented in the model within the following boundary conditions:

- during the magnetization step: $T = T_i + \Delta T_{ad}(T_i, \mu_0 H_i, \mu_0 H_f)$
- during the demagnetization step: $T = T_i - \Delta T_{ad}(T_i, \mu_0 H_i, \mu_0 H_f)$

where T_i is the initial temperature; H_i and H_f are the initial and final magnetic fields, respectively.

3.3 Results and discussion

3.3.1 Crystal structure and density of states

Based on the density functional theory (DFT) within the local density approximation (LDA), the obtained values of exchange coupling interactions and the crystal field for the intermetallic $AlFe_2B_2$ are $J1 = 17.05$ meV, $J2 = 71.71$ meV, $\Delta = 0.001$. The unit cell and atomic coordinate parameters for $AlFe_2B_2$ were taken from Ref. [121]. More details about the crystalline structure shown in Fig 3.1 for the $AlFe_2B_2$ compound are reported in Ref. [123]. The partial and total densities of state for $AlFe_2B_2$, as well as the contribution from the Fe 3d orbitals are illustrated in Fig. 3.2. The up and down densities of states refer to the majority (spin up) and minority (spin down) directions, respectively.

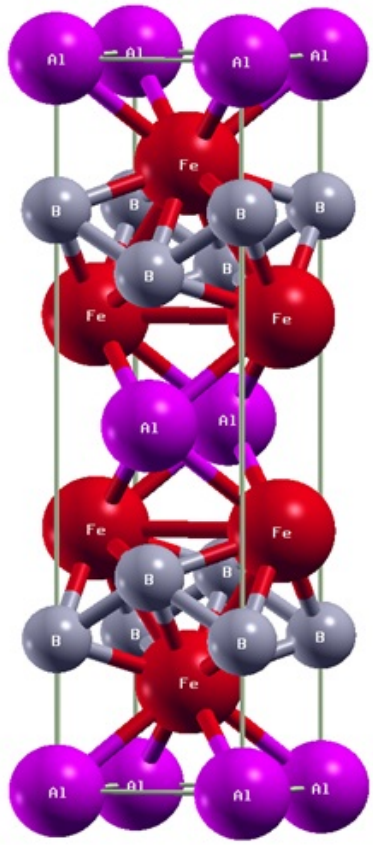

Figure 3.1: Crystalline structure of the $AlFe_2B_2$ compound.

The calculated saturation magnetization is 1.23 μ_B per Fe atom. This value is in good agreement with other theoretical results such as 1.25 μ_B published in Ref. [122]. Moreover, it is slightly larger than the experimental value reported (1.1μ_B) in Ref. [126]. On the other hand, the magnetic moments for Al and B atoms were found to be smaller when compared to Fe atoms. They were found to be only $-0.13\mu_B$ and $-0.14\mu_B$, respectively.

3.3.2 Magnetic and magnetocaloric properties

The magnetic moment and the exchange coupling interactions were determined using the first principles calculation as outlined in section 3.1 and then used to investigate the temperature dependence of magnetization, susceptibility, and specific heat of $AlFe_2B_2$ by MCs. As shown below in Fig 3.3, the spontaneous magnetization behavior indicates a ferromagnetic ordering in $AlFe_2B_2$ close to room temperature (T_C=292 K). In the same figure the temperature dependence of the heat capacity under zero magnetic fields in the temperature range 10-450 K is plotted. In the region of the magnetic phase transition, it

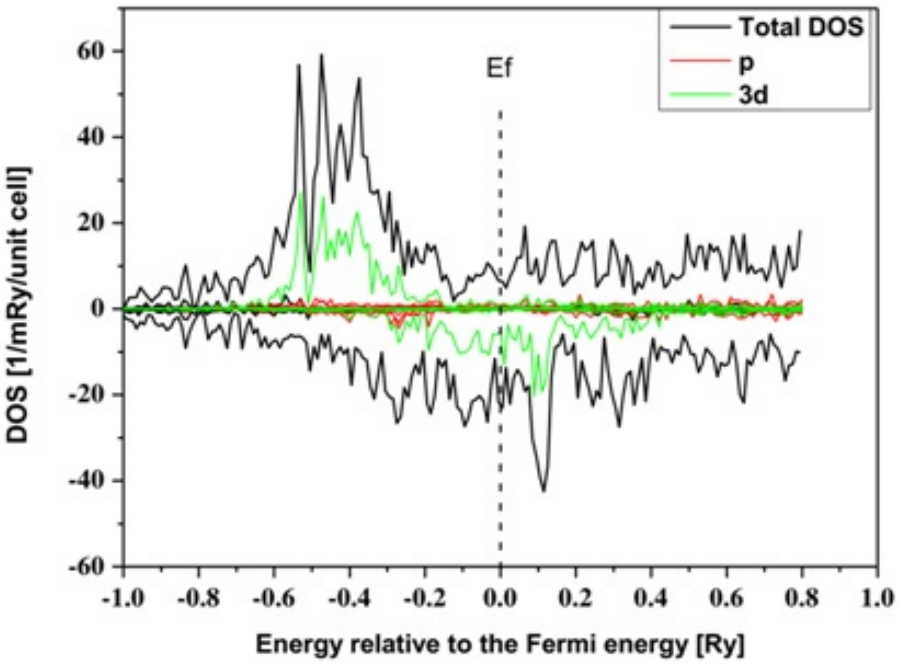

Figure 3.2: Total and partial densities of state (DOS) for $AlFe_2B_2$.

can be seen that the λ-type peak is well developed at the magnetic ordering temperature of 292 K, which assumes the second order transition at the Curie temperature. Also, the susceptibility is a characteristic λ-type peak near the Curie temperature.

Fig 3.4 illustrates the magnetic entropy changes as a function of temperature under some representative magnetic fields. It was calculated by using the numerical form of the Maxwell relation (eq. 3.11) [134] given by:

$$\Delta S_m(T, \Delta H) = \sum_i \frac{M_{i+1}\left(T_{i+1}, H\right) - M_i\left((T_i, H\right)}{T_{i+1} - T_i} \Delta H \tag{3.11}$$

All curves of (ΔS_m) exhibit a peak around its Curie temperature $(T_c = 292K)$ that is similar to the TC of gadolinium metal. Considerable magnetocaloric effect can be observed around this temperature. The peak values of $-\Delta S_m$ are 2.77 J/kgK, 6.02 J/kg K and 7.75 J/kgK under external magnetic fields of 1T, 3T and 5 T, respectively. These values are exploited to calculate the relative cooling power (RCP), which indicates the amount of heat transfer between hot and cold reservoirs of the refrigerator during an ideal thermodynamic cycle. Fig 3.5, shows the RCP values. It was found to be 70 J/kg, 301

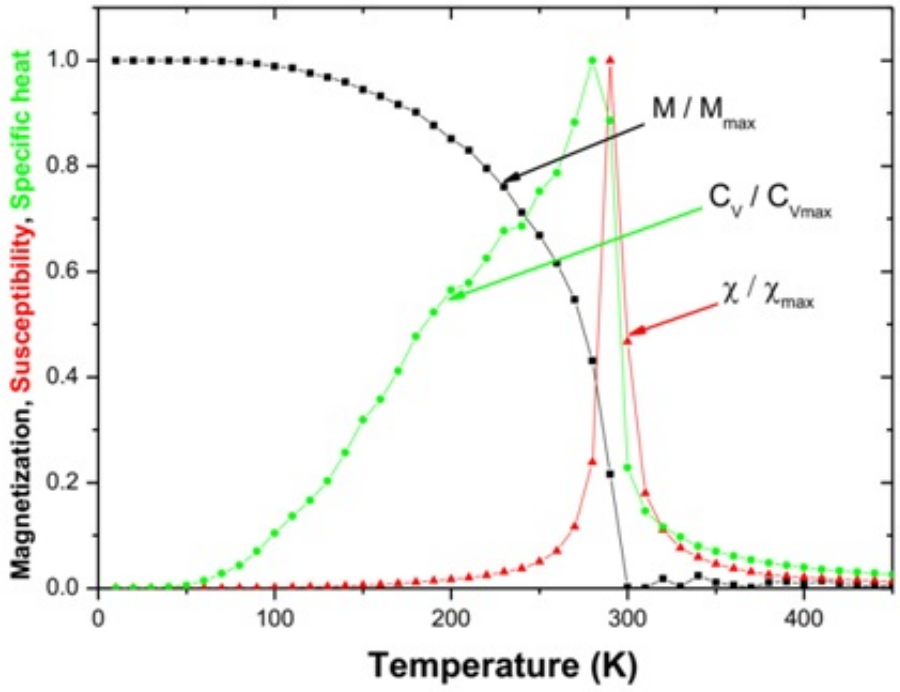

Figure 3.3: The temperature dependence of the magnetization, susceptibility, and the specific heat of $AlFe_2B_2$ compound, for a zero-external magnetic field, using MCs.

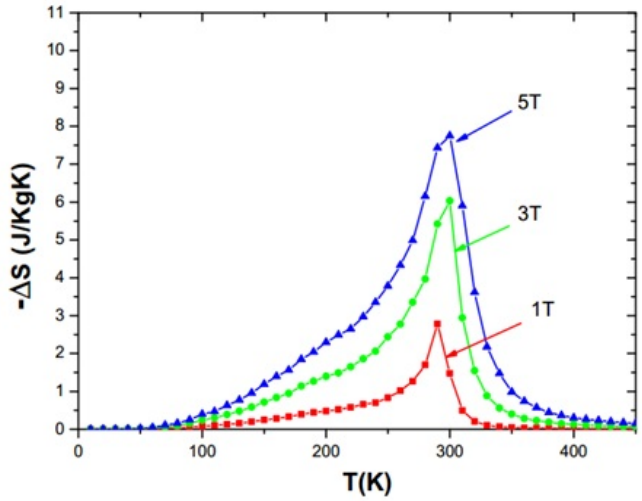

Figure 3.4: The magnetic entropy changes for the intermetallic $AlFe_2B_2$ as a function of temperature calculated under 1, 3 and 5 T, magnetic fields.

J/kg and 480 J/kg for 1, 3, and 5T, respectively.

The adiabatic temperature change is also an important parameter that clearly determines the temperature span in a magnetocaloric device. Fig 3.6 shows the temperature dependence of the adiabatic temperature change (ΔT_{ad}) under different external magnetic fields. It can be seen that (ΔT_{ad}) shows a peak around the $AlFe_2B_2$ transition temper-

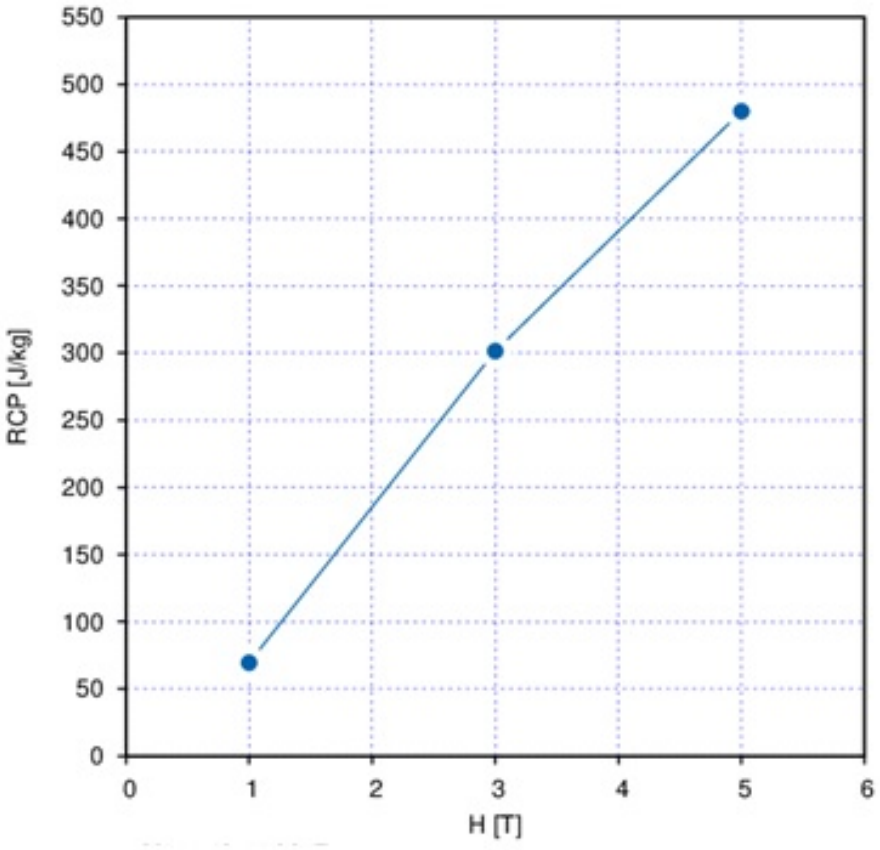

Figure 3.5: The relative cooling power as a function of field.

ature. The maximum values obtained under magnetic field changes of 1, 3 and 5 T are 0.96 K, 2.34 K and 3.74 K, respectively. As reported here, the $AlFe_2B_2$ compound unveils interesting levels of magnetocaloric effect in terms of both, the entropy and adiabatic temperature changes, being an interesting candidate for application in room-temperature magnetic refrigeration. In Table 3.1, we report a comparison between our calculations and early reported experimental data [123], good agreement can be observed.

3.3.3 Cooling properties

Regarding the cooling properties, two important parameters were investigated. The temperature span between cold and hot sources and the cooling power.

The value of the specific heat for $AlFe_2B_2$ compound at room temperature is equal to 115 J/mol K as reported in Ref. [123]. According to the results published in Ref. [135], the density of $AlFe_2B_2$ is equal to $5260 kg/m^3$. These parameters for $AlFe_2B_2$ have been

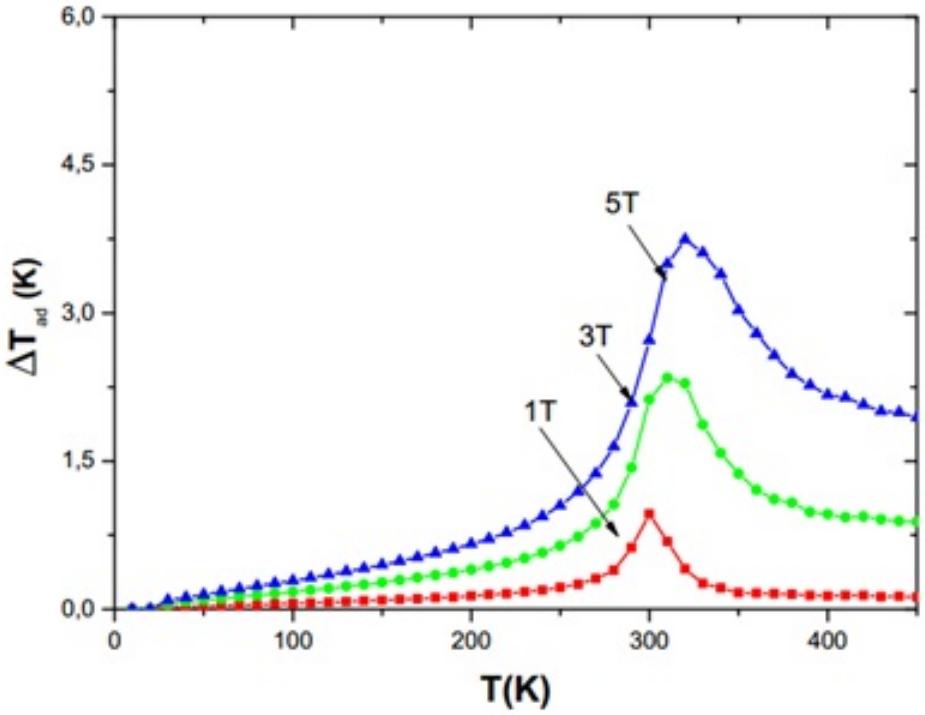

Figure 3.6: Temperature dependence of the adiabatic temperature change for $AlFe_2B_2$ compound under magnetic fields of 1T, 3T and 5T using Monte Carlo simulations.

implemented in 1D AMR-model, in addition of others described in computational details section.

At the beginning the solid material plates (Gd, $AlFe_2B_2$) and water are at ambient temperature (293 K), then the temperature of the hot source increases while the temperature of the cold source decreases after each cycle to reach their steady state after about 50 AMR cycles. It can be seen in Fig 3.7 that the maximum temperature span ($\Delta T_{span} = T_{Hot} - T_{Cold}$) obtained by numerical simulations after 50 cycles is $14°C$ for Gd and $9°C$ or $AlFe_2B_2$ for a 1 T-AMR operating frequency of 0.5 Hz. The temperature span of Gd is higher compared to the temperature span of $AlFe_2B_2$ metal. Nonetheless, it's worthy to note that the $AlFe_2B_2$ is composed of cheaper and abundant elements, which would compensate to its lower thermodynamic performance.

The cooling capacity $\dot{Q}_c$, is one of the cooling performance parameters of magnetocaloric devices, defined as the quantity of heat transferred per unit of time from the

cold side to the hot side, given by the following equation [136]:

$$\dot{Q}_c = \dot{m}(t)C_f(T_c - \overline{T_c}) \tag{3.12}$$

where:

$$\overline{T_c} = \frac{1}{\tau}\int_0^\tau T(x = L, t)dt \tag{3.13}$$

Table 3.1: Magnetic and magnetocaloric properties of the intermetallic $AlFe_2B_2$ in comparison with experimental results reported by (Tan et al., 2013).

Compound	Method	T_C, K	$-\Delta S_m, JKg^{-1}K^{-1}5T$	$\Delta T_{ad}, K5T$	RCP, $J\ Kg^{-1}5T$
$AlFe_2B_2$ Theoretically predicted	Monte Carlo simulation	292	7.7	3.74	480
$AlFe_2B_2$ [123]	Method A: Arc Melting	282	7.3	3.0	210
	Synthesis from Ga Flux	307	7.7		162

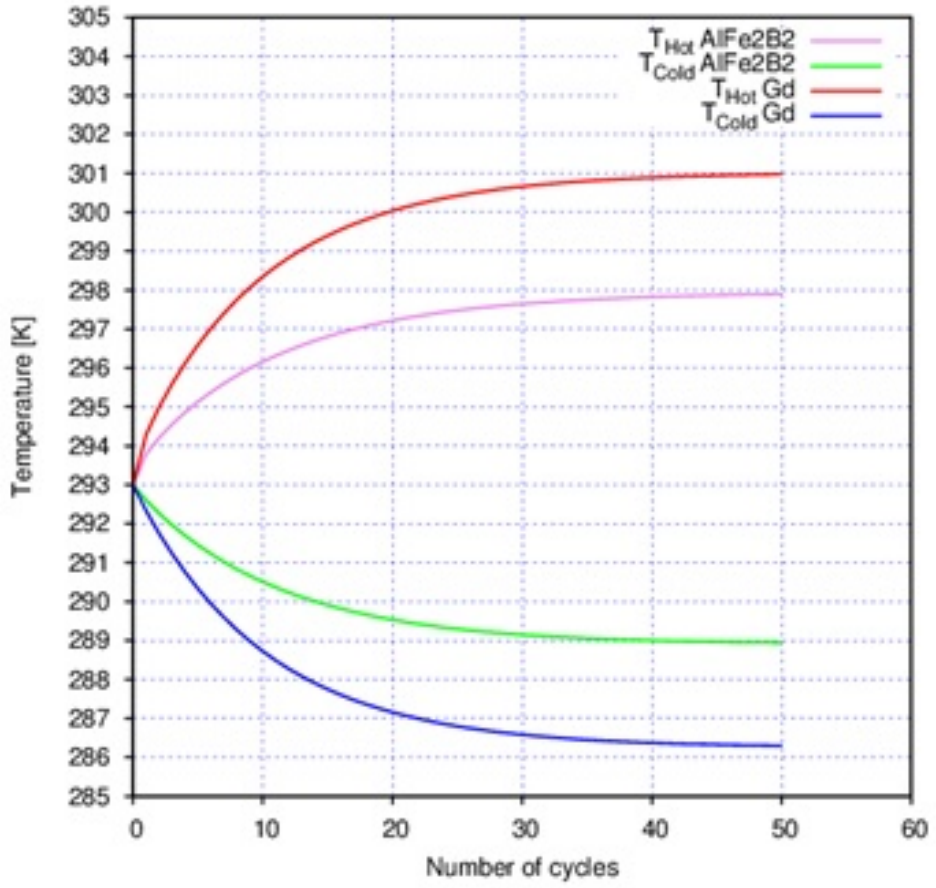

Figure 3.7: Temperature changes at the hot and the cold ends versus number of cycles for a 1 T-AMR-unit operation with both Gd and $AlFe_2B_2$ plates at the ambient temperature at a cycling frequency of f=0.5 Hz.

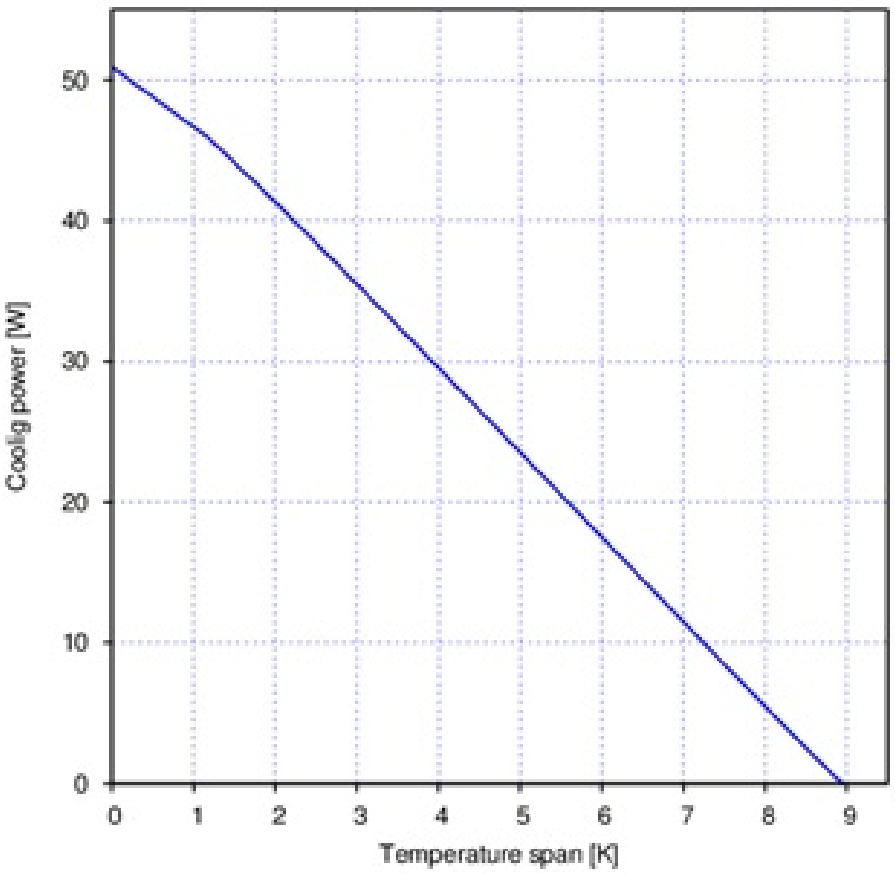

Figure 3.8: Cooling power vs. temperature span.

Fig 3.8 shows the temperature span ΔT_{span} dependence of the cooling capacity evolution ($\dot{Q}_c$) for the $AlFe_2B_2$ regenerator. The considered operating frequency is equal to 0.5 Hz, while the thermal load is applied in the cold source with T_c=289 K in the cold source. High cooling power $\dot{Q}_c$ occurs in low temperature span. The maximum reached $\dot{Q}_c$ is 52W for ΔT_{span}=0 K, while the device operating at a $\Delta T_{span,max}$ will not be able to support a heat load.

3.4 Conclusions

We have studied the magnetic, magnetocaloric and cooling properties of $AlFe_2B_2$. Results show that the second order magnetic phase transition of $AlFe_2B_2$ takes place at 292 K which is near room temperature. The isothermal magnetic entropy change and the

adiabatic temperature change of this compound are 7.75 J/kg K and 3.74 K, respectively, under a magnetic field of 5T these values are in good agreement with available experimental values. In contrast, the calculated relative cooling power (RCP) was found (480 J/kg) to largely exceed the reported experimental value in early works. On the other hand, the implementation of $AlFe_2B_2$ as a refrigerant in a 1T-AMR device would enable to generate a maximum no-load temperature span of about 10 K and a maximum cooling power of 50W for a low operating frequency of 0.5 Hz. We compared the cooling characteristics of both $AlFe_2B_2$ and gadolinium. It was found that, the cooling performance in term of temperature span between hot and cold sources (ΔT_{span}) and cooling capacity ($\dot{Q}_c$) are little lower for $AlFe_2B_2$ compared to those of gadolinium. Nevertheless, the $AlFe_2B_2$ based compounds are favorable because they consist of abundant light elements. The obtained results underline the promising applications in magnetic refrigeration of the $AlFe_2B_2$ intermetallic compound and its derivatives.

Appendix A. Supplementary data

Since ferromagnetism has been discovered within this material system a number of other studies have confirmed the ferromagnetic to paramagnetic phase transition. Supplementary data to this chapter can be found in the table bellow.

Table 3.2: MCE parameters reported for $AlFe_2B_2$.

Intermetallic Compound	T_c **K**	$\mu_0\Delta$**H** **T**	Δ**S**$_{max}$ **JKg**$^{-1}$**K**$^{-1}$	**RC**$_{FWHM}$ **JKg**$^{-1}$	Δ**T**$_{ad}$ **K**	**Ref**
$AlFe_2B_2$	292	5	7.7	480	3.74	[137]
$Al_2Fe_2B_2$	294	5	6.5			[138]
$Al_5Fe_3B_2$	274	2	2.8			[138]
$Al_3Fe_2B_2$	282	5	7.3			[123]
$Al_{1.5}Fe_2B_2$	285	5	4.5			[122]

Continued on next page

Table 3.2 – continued from previous page

Intermetallic Compound	T_c **K**	$\mu_0\Delta$**H T**	Δ**S**$_{max}$ **JKg**$^{-1}$**K**$^{-1}$	**RC**$_{FWHM}$ **JKg**$^{-1}$	Δ**T**$_{ad}$ **K**	**Ref**
$Al_{1.2}Fe_2B_2$	303	5	7.2			[125]
$AlFe_2B_2$	282	5	7.3	210	3.0	[123]
$AlFe_2B_2$	307	5	7.7	162		[123]
$Al_{1.2}Fe_2B_2$	272	2	2.7	64.8	1	[139]
$Al_1.15Ga_{0.05}Fe_2B_2$	282	2	3.67	69.73	1.3	[139]
$Al_{1.1}Ga_{0.1}Fe_2B_2$	290	2	4.42	57.46	1.4	[139]
$Al_{1.1}Ge_{0.1}Fe_2B_2$	291	2	5.18	62.16	1.74	[139]
$Al_{1.1}Ga_{0.05}Ge_{0.05}Fe_2B_2$	294	2	6.51	71.61	2.19	[139]
$AlFe_{1.975}Co_{0.025}B_2$	272	5	6.2			[140]
$AlFe_{1.925}Co_{0.075}B_2$	262	5	6			[140]
$AlFe_{1.875}Co_{0.125}B_2$	255	5	6			[140]

Chapter 4

A study of structural, magnetic, magnetocaloric and cooling properties of (1-x)$La_{0.6}Ca_{0.4}MnO_3$/xMn_2O_3 composite materials

4.1 Introduction

Global demand for energy grows continuously. The international energy agency-energy perspectives have analysed the strategy to reduce the global energy consumption and CO_2 emissions, and reported that the largest energy savings potential is in heating and cooling demands, due to building envelope improvements and the utilisation of energy efficient equipments [141]. As a response to these technological and environmental challenges, the orientation toward green technologies has become a necessity. Magnetic refrigeration based on the magnetocaloric effect (MCE) that is shown by certain magnetic materials is a very promising cooling technique that would enable us to partly overcome these environmental issues. In fact, this emerging technology operates without the harmful

chlorofluorocarbons or hydrochlorofluorocarbons fluids neither the compressor which may significantly contribute to the reduction of greenhouse gas emissions, the enhancement of energy efficiency while making the cooling devices more compact [142]. However, the design of appropriate materials is essential for the development of this emergent technology.

The topics of magnetocaloric materials and magnetic cooling systems were treated by numerous studies, with the aim to discover new magnetocaloric materials presenting high magnetocaloric effect (MCE) levels. Initially, the magnetocaloric materials used in the active magnetic regenerator (AMR) systems studies were the Gd and some related alloys such as GdTb, GdDy and GdEr [18, 143]. However, the use of such magnetic refrigerants is limited because of their high cost and weak chemical stability.

Recently, perovskite manganites of the general formula $La_{1-x}A_xMnO_3$, with $A = Sr, Ba, Ca...$have attracted much attention as working refrigerants in magnetic cooling applications because of their several advantages such as, low cost, easy preparation, grain size control via heat treatment, and high chemical stability [144–148]. In this work, we study one of the $La_{0.6}Ca_{0.4}MnO_3$ compounds that present rich magnetic and electronic properties leading to fascinating phenomena such as, the colossal magnetoresistance, and large magnetocaloric effects [149–152]. Mass of researches on Ca doping are devoted to $RMnO_3$. In $Ca_{0.85}R_{0.15}MnO_3$ (R = Sm, Dy) materials the Ca doping with larger R-ions (R=Sm, Dy) induces ferromagnetism through the interruption in the long range anti-ferromagnetic spin ordering of pristine $CaMnO_3$ and could exhibit different interesting phenomena like Griffiths phase, magneto-caloric effect and magnetic relaxation behavior [153, 154]. In the manganite $La_{0.6}Ca_{0.4}MnO_3$ the ratio La^{3+}/Ca^{2+} determines the oxidation state of Mn and thus the ratio Mn^{3+}(S=2)/Mn^{4+}(S=3/2) [155–157]. Usually, the physical properties of perovskites are driven by both superexchange and double exchange interactions between Mn^{3+} and Mn^{4+} that are mediated by oxygen atoms via the Mn^{3+}-O-Mn^{4+} bond and Mn^{3+}-O-Mn^{3+} bond [158–160]. In this way, the magnetic and magnetocaloric features of some oxides can be also tailored by mixing them with other secondary phases forming composite materials [81, 145, 161–163].

The $La_{1-x}Ca_xMnO_3$ with the perovskite structure can be considered as potential magnetocaloric candidates for applications in the temperature range between 250 and $300K$ [164]. Their curie temperature can be easily changed by doping the lanthanum and/or manganese sites [165]. According to Abir et al. $La_{0.6}Ca_{0.4}MnO_3$ perovskite material prepared by sol-gel method has a magnetic phase transition around $Tc = 260K$ and a maximum magnetic entropy change equal to $3.6J/kgK$ and a relative cooling power(RCP) of $141J/kg$ under the magnetic field change of $5T$ [166]. In another study, M. Nasri et al. have reported that $La_{0.6}Ca_{0.4}MnO_3$ material exhibits a magnetic entropy change of $5.8J/kgK$ and a RCP of $115J/kgK$ under $5T$ magnetic field [167]. Assoudi et al. have studied the effect of synthesis route on the structural, magnetic and magnetocaloric behaviors of $La_0.6Ca_0.3Ag_0.1MnO_3$, they have found that the compound elaborated by sol gel method exhibit larger magnetocaloric effect than that obtained by the solid state reaction technique [168].

On the other hand, only few studies have been dedicated to the improvement of $La_0.6Ca_0.4MnO_3$ magnetocaloric properties through composites approach [145, 162, 163, 167, 169]. M. Nasri et al. pointed out that (1-x)$La_{0.6}Ca_{0.4}MnO_3$/xCuO composites enables to improve the magnetoresistance properties, but results in a dramatic decrease of MCE when particularly increasing the CuO content [163]. Another compound of the general formula $La_0.70Ca_{0.30-x}Sr_xMnO_3$: Ag 10% has been studied by Jha et al. who unveiled that the addition of Ag improves the magnetocaloric properties, especially in terms of ΔS at $Tc = 300.5K$[162]. In addition Pal et al. [170] revealed that adding Ag in polycristalline colossal magnetoresistance-Ag nanocomposite can obtain large room temperature MR if Tc of the compound is near room temperature via the modification of the microstructural, electrical and magnetic inhomogeneties on the grains. Bhame et al. have studied the effect of LCMO/Mn_3O_4 composite to figure out whether an insulating secondary phase always enhance the low field magnetoresistance in manganites. They suggested accordingly that the diffusion of foreign cations (other than La, Ca, Mn) into the grain boundaries is a necessary tool to enhance the low field magnetoresistance in composites [169].

In this work, we study the impact of Mn_2O_3 secondary phase on the morphology, structure, and magnetic properties of $La_{0.6}Ca_{0.4}MnO_3$ material. The magnetocaloric features are also analysed in terms of magnetization and specific heat measurements.

In addition to the experimental work, We will present in the second part of this chapter a numerical analysis and performance parameters of $La_{0.6}Ca_{0.4}MnO_3$ perovskite manganite as active magnetocaloric material (MCM) in an active magnetic refrigeration cycle (AMR). This material displays a second-order phase transition at 260 K. The needed magnetocaloric parameters for the AMR model such as the adiabatic temperature (ΔTad) change and the heat capacity (Cp) of the solid material were taken from our experimental mesurements, while the thermodynamic performance are calculated according to the one-dimensional (1D) AMR model and, investigated as a function of frequencies and fluid flow rates.

4.2 Experimental details

The (1-x)$La_{0.6}Ca_{0.4}MnO_3$/xMn_2O_3 with 5 concentrations ($x = 0, 0.05, 0.1, 0.15, 0.20$) of Mn_2O_3 were prepared by the solid-state reaction method. First the precursors, La_2O_3, CaO, Mn_2O_3 and MnO_2 powders were ground and mixed in the stoichiometric ratios and then calcinated in air at 900 °C for $12h$. A final sintering was carried out at 1200 °C for $24h$ with intermediate grinding. Later, MnO was mixed with calcined $LCMO$ in different mole ratio and the grinded mixture was again annealed at 900 °C for about $2h$ to avoid any diffusion. The obtained mixtures were re-ground, mixed, pressed into pellets, and then sintered at 1200 °C for $2h$ in air. Samples were compacted to cylindrical pellets in thickness of $0.4mm$ and in diameter of $13mm$ under $10MPa$ of pressure by using a mechanical press (MTI 100 T, with a maximum pressure of $100MPa$). The crystalline structure of prepared samples was checked by X-ray diffraction. In order to identify the distribution and size of particles in the obtained composites, measurements of samples using scanning electron microscopy (SEM) analysis is performed, (MEB, FEI, Quanta $FEG450$) instrument was used. SEM-EDS conditions were set with a spot at 6.0 and a high voltage at $15Kv$, the SEM analysis is carried out under high vacuum. Mag-

netic measurements were performed using the Magnetic Properties Measurement System ($MPMS - SQUID$). Heat capacity measurements were carried out using the physical properties measurement system ($PPMS$) in a temperature range going from 5 to $300K$.

4.3 Computational details

4.3.1 AMR cycle model

The thermo-physical characteristics of $La_{0.6}Ca_{0.4}MnO_3$ around its curie temperature (260 K) and water are assumed to be constants and were taken from our experimental results. They are given in table 4.1. The mentioned MCE value (1.1 K) of $La_{0.6}Ca_{0.4}MnO_3$ in Table 4.1 corresponds to a magnetic field of 1 T that is easily accessible via permanent magnets.

Symbol	Parameter (Unit)	Value	
		Water	$La_{0.6}Ca_{0.4}MnO_3$
δ	Thickness (mm)	0.1	1
L	Length of the bed regenerator (mm)	50	50
I_{ea}	Equivalent cell width of the regenerator (mm)	525	525
λ	Thermal conductivity (w/m.K)	0.59	-
ρ	Volume density (kg/m^3)	1000	5940
C_p	Specific heat (J/Kg.K)	4185	640
μ	Dynamic viscosity (Kg/m.s)	0.001	-
MCE	Magnetocaloric effect (K)	-	1.1
$\dot{m(t)}$	Flow rate (ml/s)	3	-

Table 4.1: Geometrical and thermo-physical parameters of water and $La_{0.6}Ca_{0.4}MnO_3$ used in simulations.

4.3.2 Description of the regenerator and working cycle

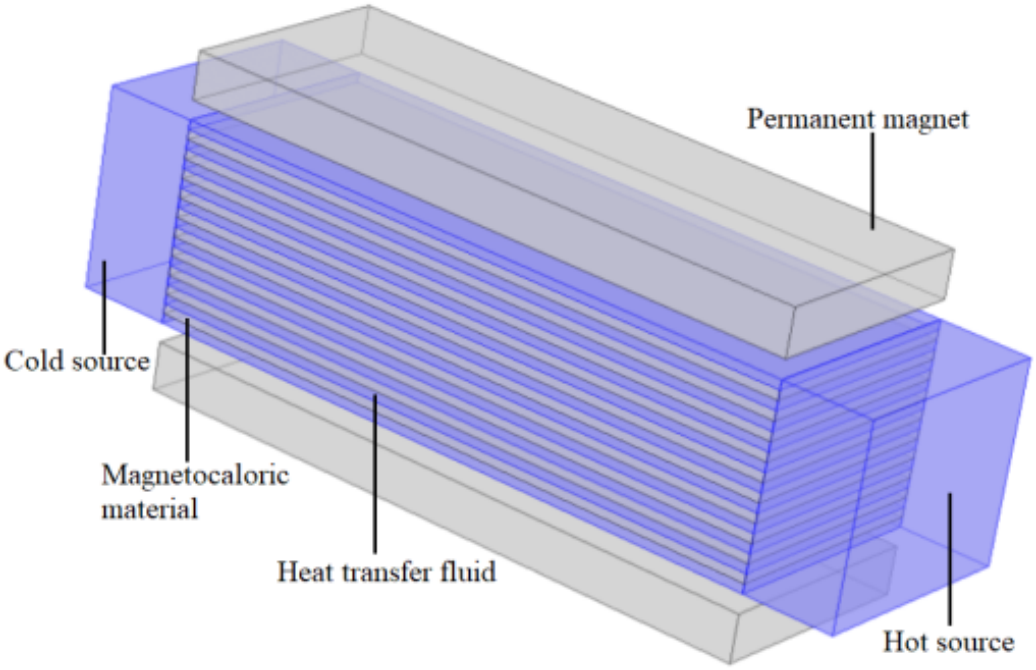

Figure 4.1: Parallel plates of MCM stacked in the regenerator. The MCM is in gray and the fluid channels in blue

The considered regenerator in this study is shown in Figure 4.1. It is constituted of 18 parallel plates of the magnetocaloric material $La_{0.6}Ca_{0.4}MnO_3$ with 1 mm thickness, 50 mm length and 25 mm width each. The plates are equidistant with an inter-space of about 0.1 mm while the water is used as a heat transfer fluid. The regenerator experiences several AMR cycles where each cycle breaks up into four steps:

1. Isentropic magnetization of the magnetocaloric material.
2. Heat evacuation under constant applied magnetic field: heat transfer fluid flows from the cold side to the hot side of the regenerator.
3. Isentropic demagnetization of the magnetocaloric material.
4. Fridges recuperation under zero magnetic field: heat transfer fluid flows from the hot side to the cold side of the regenerator.

As the adiabatic temperature change of magnetocaloric materials (MCMs) is not enough to achieve refrigeration, it is necessary that the regenerator experience several AMR cycles. Thus, the temperature span between the hot and cold sources of the regenerator is continuously increased, to finally reach a steady state in which:

$$|Tc_k - Tc_{k-1}| < \varepsilon\varepsilon = 0.00005K \tag{4.1}$$

Tc_k - Tc_{k-1} represents the difference between the reached cold temperature (Tc_k) and the previous cold temperature (Tc_{k-1}).

4.3.2.1 Governing equations

Based on the law of energy conservation, the main equations describing the heat transfer between a solid material and a carrier fluid in 1D model are given by the following partial differential equations (PDE):

$$\rho_s C_s \frac{\partial T_s}{\partial t} = \frac{\partial}{\partial X}\left(\lambda_s \frac{\partial T_s}{\partial X}\right) + \dot{Q}_{MCE} + \dot{Q}_{loss} + \dot{Q}_{HT} \tag{4.2}$$

$$\rho_f C_f \left(\frac{\partial T_f}{\partial t} + u_x \frac{\partial T_f}{\partial X}\right) = \frac{\partial}{\partial X}\left(\lambda_f \frac{\partial T_f}{\partial X}\right) + \dot{Q}_{loss} - \dot{Q}_{HT} \tag{4.3}$$

where s and f subscripts are referred to the solid (MCM) and the fluid, respectively. t is time; x is a spatial coordinate (0¡x¡L); Tf=T_f (x,t) denotes the fluid temperature; Ts=T_s (x,t) is the regenerator solid temperature; ρ_s is the mass density of the solid and ρ_f is the mass density of the fluid. The heat capacity of the solid and the fluid are denoted by c_s and c_f, respectively. λ_s is the thermal conductivity of the solid and λ_f is the fluid thermal conductivity; u_x is the velocity of the fluid; $\dot{Q}_{MCE}$ is the internal heat generation term; $\dot{Q}_{loss}$s represents the thermal losses; $\dot{Q}_{HT}$ T denotes the heat transfer flux between the solid and the fluid in the bed regenerator. The term $\dot{Q}_{MCE}$E in the Eq. (4.4) represent the internal heat flux generated during the interaction between the magnetic field and the

magnetocaloric material can be calculated by using the Eq. (4.4):

$$\dot{Q}_{MCE} = \rho_s C_p, s(H,T)\frac{\Delta T_{ad}(H,T)}{dt} \tag{4.4}$$

Where c_p, s(H,T) and ΔT_{ad}(H,T) represents the specific heat and the adiabatic temperature change of the solid material, which depend on the applied magnetic field and temperature. These values can be measured experimentally or calculated by using the mean field theory, [171] or by using Monte carlo simulations as reported in [172]. In this study the $\dot{Q}_{MCE}$ term is implemented in the model by applying directly the adiabatic temperature change to the solid during the processes of magnetization and demagnetization.

The term $\dot{Q}_{HT}$ in the Eq. (4.2) and Eq. (4.3) represents the heat exchanges by convection between a fluid in motion on a plate and this latter. It can be expressed by a convective heat transfer coefficient h. The heat transfer rate $\dot{Q}_{MCE}$T can be expressed as:

$$\dot{Q}_{HT} = hA_{HT}(T_s - T_f) \tag{4.5}$$

where A_{HT} is the wetted area per unit cell of the solid material. The convective heat transfer coefficient is calculated according to the empirical Nusselt-Reynolds correlations corresponding to a laminar flow.

4.4 Results and discussion

4.4.1 Structural properties

Figure 4.2 displays the XRD patterns of composite samples for $x = 0, 0.05, 0.1$ and 0.2 of Mn_2O_3. Slight peaks of the minor secondary phase Mn_2O_3 were detected as indicated by blue asterisk $(*)$. The absence of any peak in the X-ray data of MnO indicates on its transformation into Mn_2O_3 and is caused by the oxidation of manganese (II) oxide used at first as the insulating phase, under air and temperature conditions according to the following chemical reaction $2MnO + \frac{1}{2}O_2 \rightarrow Mn_2O_3$ [173, 174]. The $La_0.6Ca_0.4MnO_3$

and Mn_2O_3 are indexed in the orthorhombic structure with Pnma space groupe ($N = 62$) and cubic structure with $Ia - 3(N206)$, respectively.

Figure 4.3 shows the superposition of the observed (Red) and the calculated (Blue) XRD patterns for ($x = 0.2$) sample. The line just below the patterns correspond to the difference, and the bars at the bottom are the Bragg positions. The refinement of cell parameters was done in the orthorhombic system with Pnma space group confirming the presence of all the identified characteristic peaks. The lattice parameters and the average crystallite size calculated using Rietveld refinement with Topas Software (built in TOPAS V4.2 of BRUKER AXS), are listed in table 4.2 slight deviation between the lattice parameters of both phases is observed for all samples. The crystallites size (not to be confused with the grain/particle size) is found to decrease slightly with Mn_2O_3 concentration. It is reduced from ($\sim 35nm$) to ($\sim 24nm$) when varying x from 0 to 0.2 respectively. In total, two phases were used in the results of the quantitative analysis with TOPAS. Through the X-ray diffractograms, it was possible to quantify the phase ratio amount for $x = 0.2$ composition and we have found 85.61% for LCMO and 14.39% for Mn_2O_3, these values are different from the theoretical ones which confirm that small amount of Mn_2O_3 has dissolved in the structure of manganite.

	Lattice parameters						Crystallite size	
	a (Å)		b (Å)	c (Å)	V (Å^3)		D (nm)	
Sample	LCMO	Mn_2O_3	LCMO	LCMO	LCMO	Mn_2O_3	LCMO	Mn_2O_3
x=0.00	5.447	-	7.6755	5.4619	228.25	-	35	-
x=0.05	5.4562	9.457	7.6895	5.4756	229.73	845.78	32	121
x=0.10	5.4309	9.409	7.6568	5.4535	226.78	832.97	36	116
x=0.15	5.4281	9.406	7.6453	5.4520	226.26	832.17	23	77.8
x=0.20	5.4465	9.430	7.6683	5.4654	228.27	838.56	24	84.5

Table 4.2: Rietveld refined lattice parameters, unit cell volume and crystallite size for (1-x)$La_{0.6}Ca_{0.4}MnO_3$/xMn_2O_3, (x = 0, 5, 10, 15 and 20 %) calculated using Topas software

The morphology of all composite are examined using the scanning electronic microscope

(SEM) and EDAX analyses as shown in (fig 4.4) for $x = 0, 0.05, 0.1 and 0.2$. We can observe a microcrystalline structure that is characterized by various shapes. The pure compound LCMO appears to be agglomerated ($x = 0$) with an average grain size of about $1.3m$. However, the $LCMO/Mn_2O_3$ composite ($x = 0.2$) shows similar morphologies with less agglomeration and greater grain size, of roughly $4.3m$. The observed increase in particle size in the case of the composite with $x = 0.2$ compared to the particle size of parent LCMO powder can be explained by the presence of the minor phase that occupies the grain boundaries for the composite as shown in (fig.4.5) and/or due to the last step in the composite preparation.

In order to confirm the presence of monovalent elements and the cationic stoichiometry, EDS spectrum (Energy Dispersive Spectrometry) has been carried out at several spots on the surface (Figure 4.4). The EDS analysis indicating the cationic compositions of samples ($x = 0, 0.05, 0.1, 0.2$). We can first notice that all samples contain all the expected chemical elements La, Ca and Mn without any additional impurity or lost element during the sintering process.

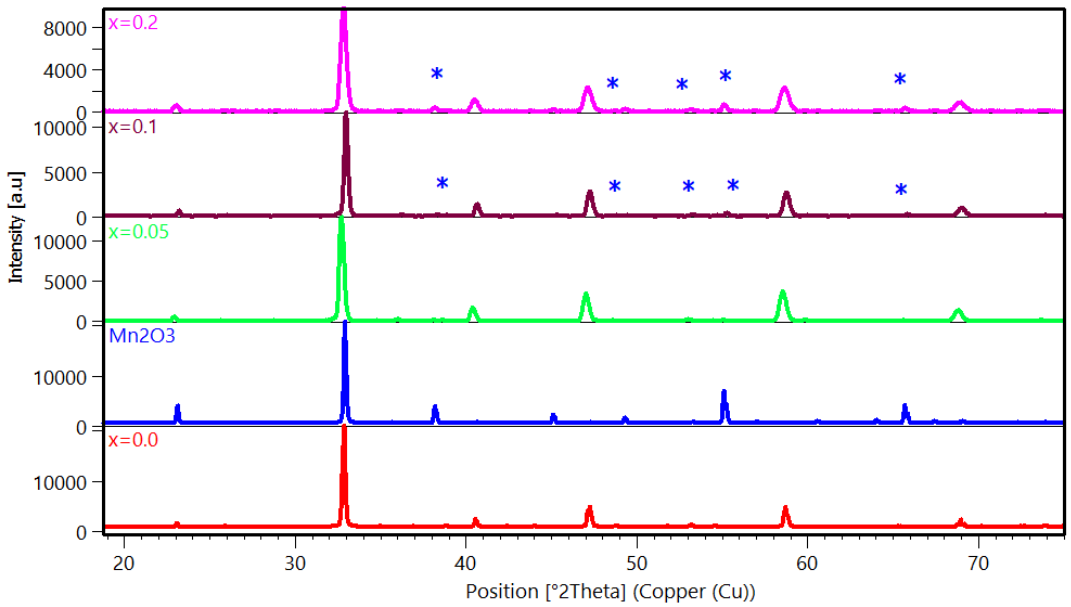

Figure 4.2: XRD patterns of $LCMO/\ Mn_2O_3$ composite. Blue asterisk indicate peaks of Mn_2O_3 for $x = 0.1, 0.2$ samples.

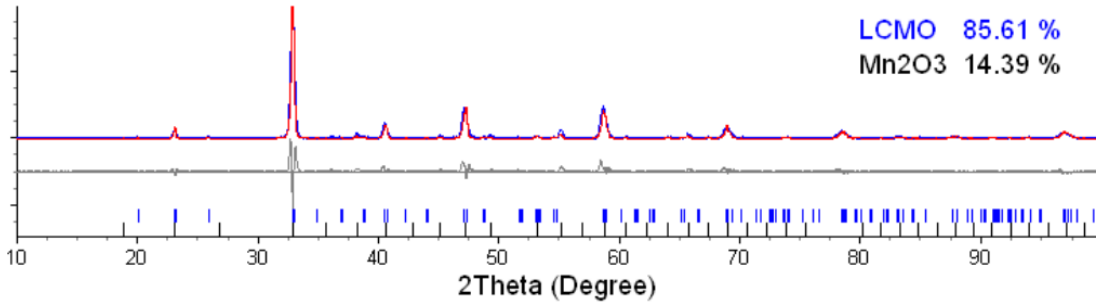

Figure 4.3: Reitveld refined XRD patterns of the $LCMO/\ Mn_2O_3$ for x=0.2 using Topas software.

	Lattice parameters						Crystallite size	
	a (Å)		b (Å)	c (Å)	V (Å^3)		D (nm)	
Sample	LCMO	Mn_2O_3	LCMO	LCMO	LCMO	Mn_2O_3	LCMO	Mn_2O_3
x=0.00	5.447	-	7.6755	5.4619	228.25	-	35	-
x=0.05	5.4562	9.457	7.6895	5.4756	229.73	845.78	32	121
x=0.10	5.4309	9.409	7.6568	5.4535	226.78	832.97	36	116
x=0.15	5.4281	9.406	7.6453	5.4520	226.26	832.17	23	77.8
x=0.20	5.4465	9.430	7.6683	5.4654	228.27	838.56	24	84.5

Table 4.3: Rietveld refined lattice parameters, unit cell volume and crystallite size for (1-x)$La_{0.6}Ca_{0.4}MnO_3$/xMn_2O_3, (x = 0, 5, 10, 15 and 20 %) calculated using Topas software

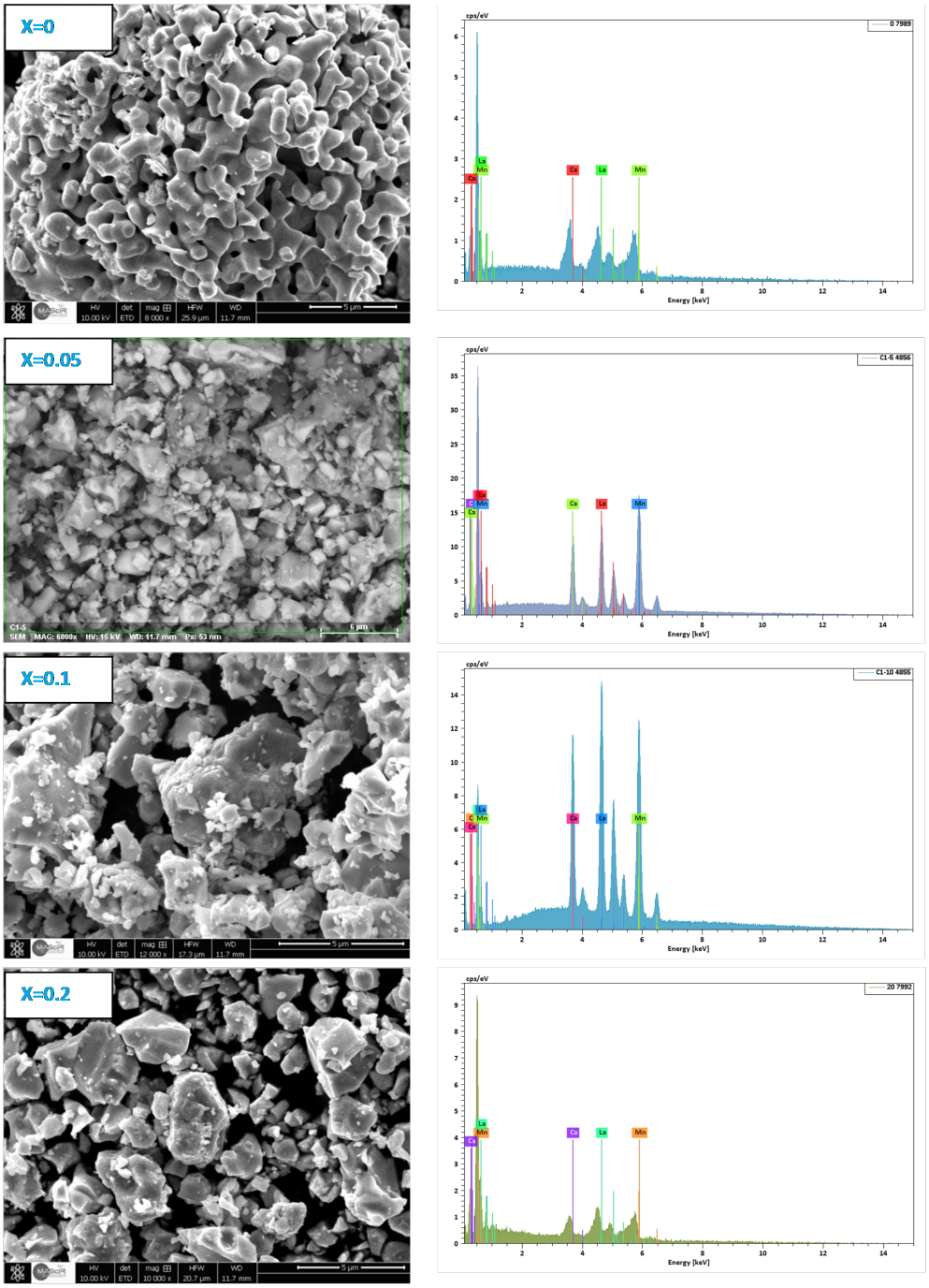

Figure 4.4: SEM images and EDAX analyses of (1-x)$La_{0.6}Ca_{0.4}MnO_3$/xMn_2O_3 for $x = 0, 0.05, 0.1$ and 0.2.

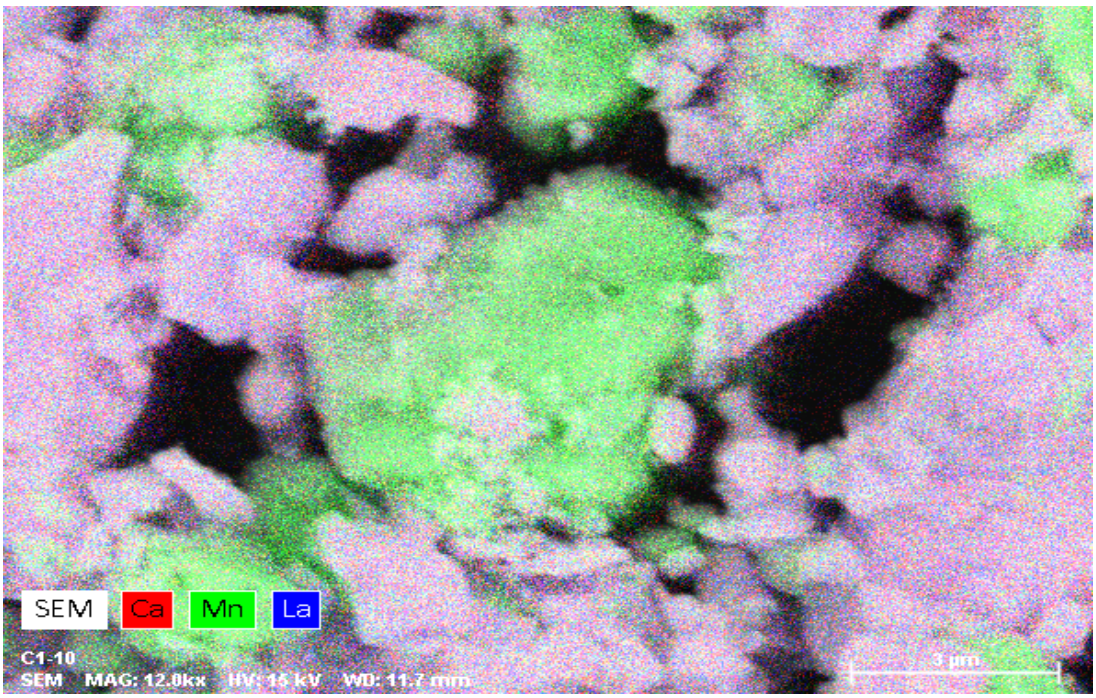

Figure 4.5: Scanning electron micrographs of (1-x)$La_{0.6}Ca_{0.4}MnO_3$/xMn_2O_3 showing the cations distribution for x=0.1.

4.4.2 Magnetic and magnetocaloric properties

Thermomagnetic measurements as a function of temperature for the parent LCMO and $LCMO/Mn_2O_3$ composites were performed under $500Oe$ applied magnetic field (Fig 4.6).

According to fig 4.6 all the samples display a second order like ferromagnetic-paramagnetic phase transition. As shown, the evolution of dM/dT versus temperature (T) indicates that the Curie temperature is around $260K$ for all the here studied compounds, being similar to that reported in Bohigas et al. [151] for LCMO. The insulating phase Mn_2O_3 has no impact on the LCMO magnetic phase transition. A similar behaviour was previously pointed out by Huang et al. [145] in the $LCMO - Ag$ composite. We observed a slight decrease of magnetization M with Mn_2O_3 concentration. In this way, Craus et al. [175] argues that there is a strong correlation between the structure dimensionality and magnetic features, which explain the change observed in magnetic properties with the microstructure in the case of competing phases in manganites. We mention that authors

have used an important techniques for investigating the microstructure and the magnetic properties of $La_{0.5}Pr_{0.2}Pb_{0.3} - xSrxMnO_3$ manganites are small-angle scattering (SAS, neutrons and X-rays) techniques.

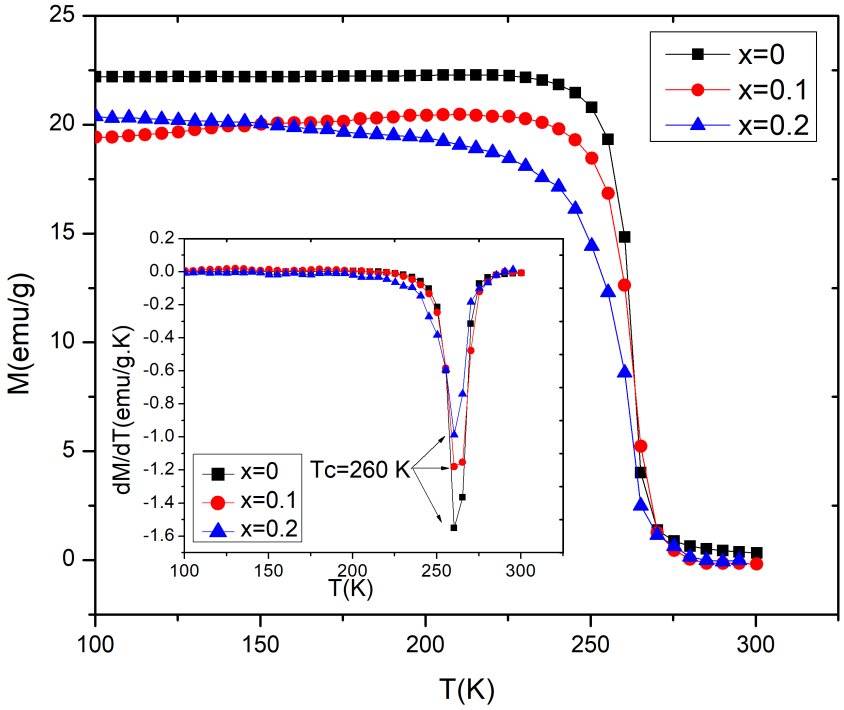

Figure 4.6: Temperature dependence of magnetization measured at $\mu_0 H$=0.05T for (1-x)$La_{0.6}Ca_{0.4}MnO_3$/xMn_2O_3 ($0 \leq x \leq 0.2$) samples. The inset shows the dM/dT curves for $x = 0, 0.1, 0.2$.

Fig 4.7 shows isothermal magnetization measurements magnetic isotherms reported for the mother compound and the composites with $x = 0.1, 0.2$ in the temperature range between 180 and 300K. M–H curves indicate that the magnetization of the samples increases rapidly at low fields and tends to saturate under sufficiently high magnetic fields particularly at low temperatures. Hence, the linear behavior of isotherms ($T < Tc$) in high field indicates the presence of mean-field interactions [176]. Aiming to confirm the nature of the magnetic phase transition exhibited by the here studied materials (first or second order) we plot in figure 4.8 the so called Arrot plots ($\mu_0 H/M$ dependence of M^2) in the temperature range around the Curie point. All the curves exhibit a positive slope

indicating that our composites ($x = 0, 0.1, 0.2$) display a second order magnetic phase transition type in accordance with Banerjee criteria [177].

The intersections of the linear extrapolation line (for high-magnetic field parts) of the Arrot plots with the vertical axis ($T < Tc$) and with horizontal axis ($T > Tc$) allows to obtain the values of the spontaneous magnetization $M_{Sp}(T)$ as well as the inverse magnetic susceptibility $\chi^{(}-1)(T)$, respectively [178]. T_C can be determined accurately since the isotherms at this temperature pass through the origin. At $T < TC$, the ferromagnetic materials produce a spontaneous magnetization $M_S(T)$. Thus, the insets of figure 4.8 show the temperature dependence of the spontaneous magnetization and the inverse of the magnetic susceptibility evolution versus temperature for $x = 0, 0.1and, 0.2$. Obviously, the $M_Sp(T)$ becomes larger, when temperature decreases, suggesting that the system is approaching a spin ordering state at lower temperature. For the composites with $x = 0.1$ and 0.2, the temperature variation of spontaneous magnetization confirms the coexistence of two magnetic phases, which is revealed by the drastic change in the value of spontaneous magnetization and the distinct change in the slope of the curve observed at approximately $210K$.

On the other hand, these samples show a linear inverse susceptibility behavior in the paramagnetic phase ($T > TC$) indicating that the Curie–Weiss law is well satisfied. Besides, in this context, the second-order magnetic phase transition near the Curie point is characterized by three critical exponents, β (related to the spontaneous magnetization), γ (associated with the initial magnetic susceptibility), and δ (dependent on the critical magnetization isotherm). The three exponents are connected through Widom scaling relation,$\delta = 1 + \gamma/\beta$, allowing a simple determination of δ from the known values of β and γ [168, 179]. The critical exponents were calculated by using the Kouvel Fisher (KF) method according to equations 4.6 and 4.7.

$$\frac{M_S(T)}{dM_s(T)/dT} = \frac{T - T_c}{\beta}, \tag{4.6}$$

$$\frac{\chi^{-1}(T)}{d\chi(T)/dT} = \frac{T - T_c}{\gamma} \tag{4.7}$$

This method propose that the quantities $\frac{M_S(T)}{dM_s(T)/dT}$ and $\frac{\chi^{-1}(T)}{d\chi(T)/dT}$ plotted versus temperature yield straight lines with slopes $\frac{1}{\beta}$ and $\frac{1}{\gamma}$, respectively [180]. The critical exponents, obtained in a wide variety of FM material systems, can be grouped into a few well known universal classes [179], such as the mean field (MF) model ($\beta = 0.5$, $\gamma = 1.0$ and $\delta = 3.0$), $3D$ Heisenberg ($3DH$) model ($\beta = 0.365$, $\gamma = 1.386$ and $\delta = 4.80$), 3D Ising ($3DI$) model ($\beta = 0.325$, $\gamma = 1.241$ and $\delta = 4.82$) and the tricritical mean field model ($\beta = 0.25$, $\gamma = 1.0$ and $\delta = 5.0$). In our case the estimated values were found to be $\beta = 0.24 + -0.02$, $\gamma = 1.12 + -0.02$ and $\delta = 5.1 + -0.02$ or the mother compound ($La_{0.6}Ca_{0.4}MnO_3$) indicating that the observed ferromagnetic phase transition in the present material can be approximately understood with the tricritical mean field model. On the other hand, the obtained results of critical exponents are in agreement with those published by Zhang et al.[179]. These results point out that the mother compound ($La_{0.6}Ca_{0.4}MnO_3$) show the existence of the tricritical point that sets a boundary between first order and second-order magnetic phase transition.

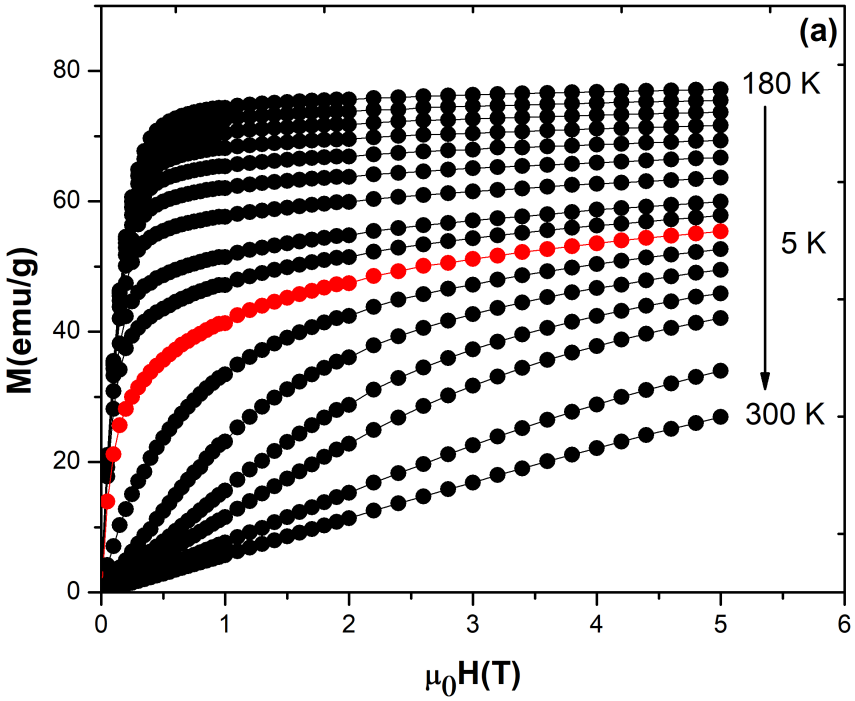
(a)
180 K
5 K
300 K
M(emu/g)
μ_0H(T)
0
20
40
60
80
0
1
2
3
4
5
6

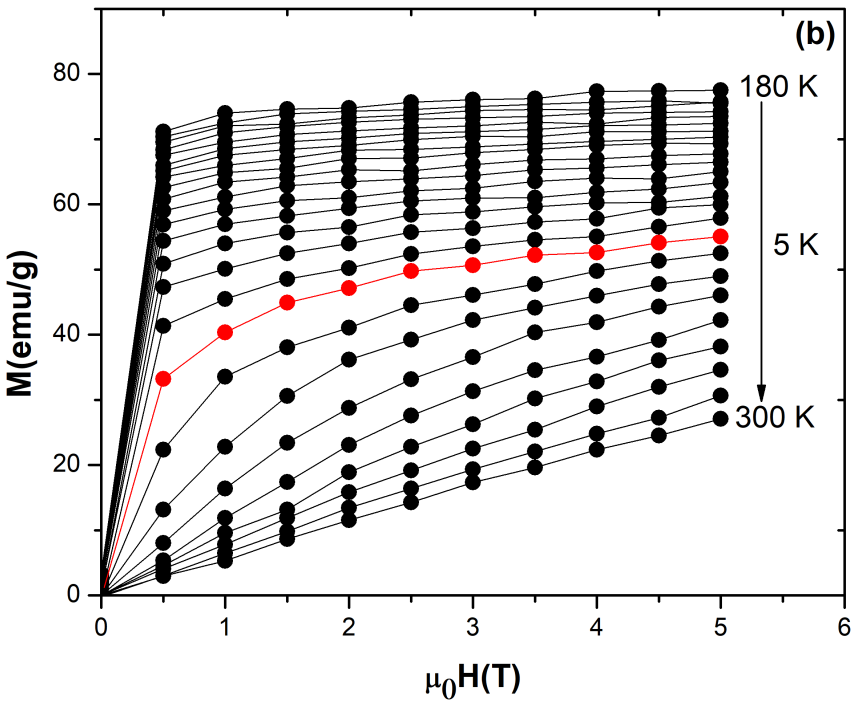
(b)
180 K
5 K
300 K
M(emu/g)
μ_0H(T)
0
20
40
60
80
0
1
2
3
4
5
6

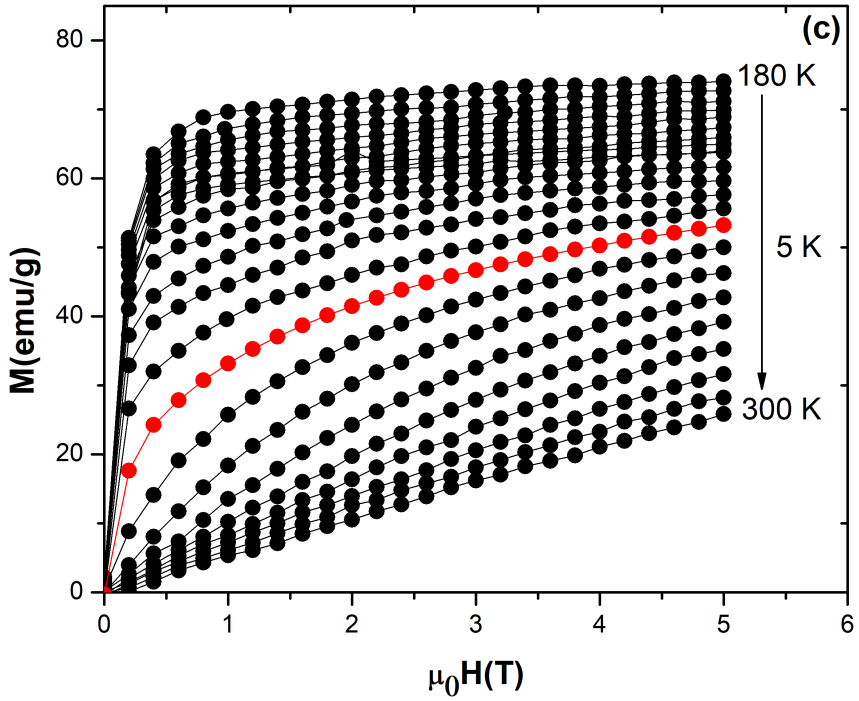

Figure 4.7: Scanning electron micrographs of (1-x)$La_{0.6}Ca_{0.4}MnO_3$/xMn_2O_3 showing the cations distribution for x=0.1

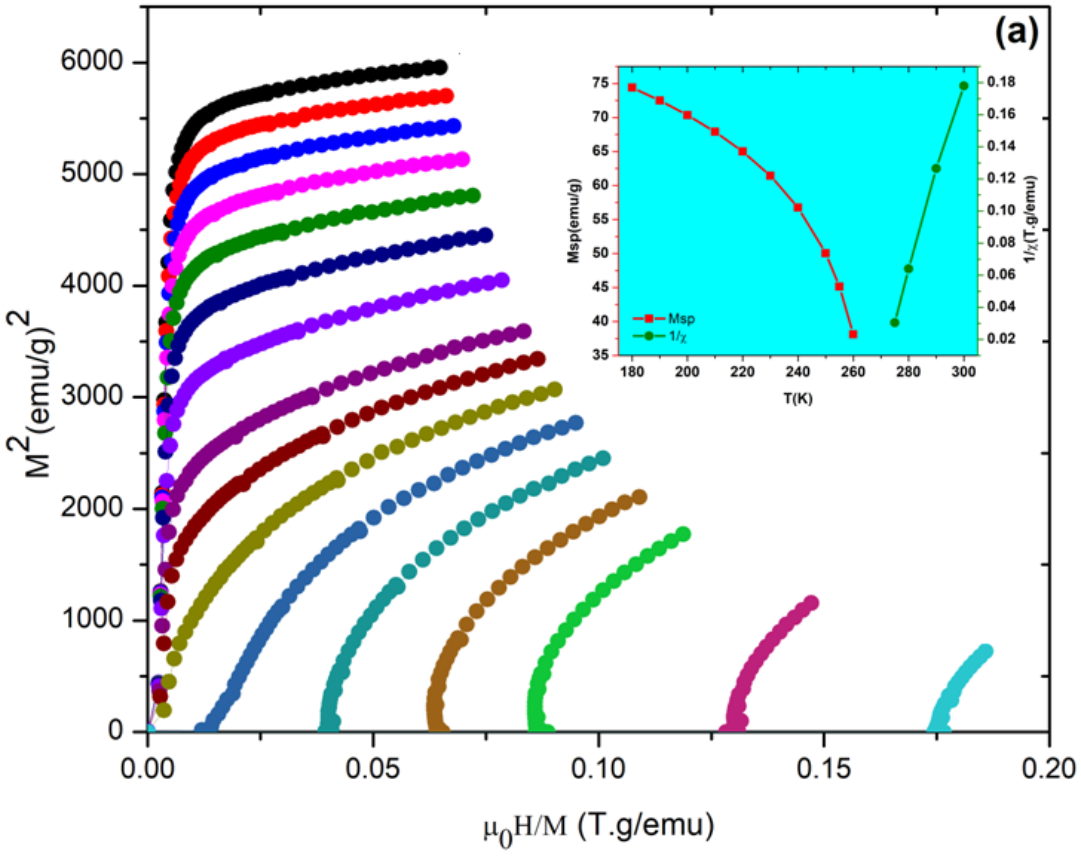
(a)
M^2(emu/g)^2
μ_0H/M (T.g/emu)
Msp(emu/g)
1/χ(T.g/emu)
T(K)
Msp
1/χ

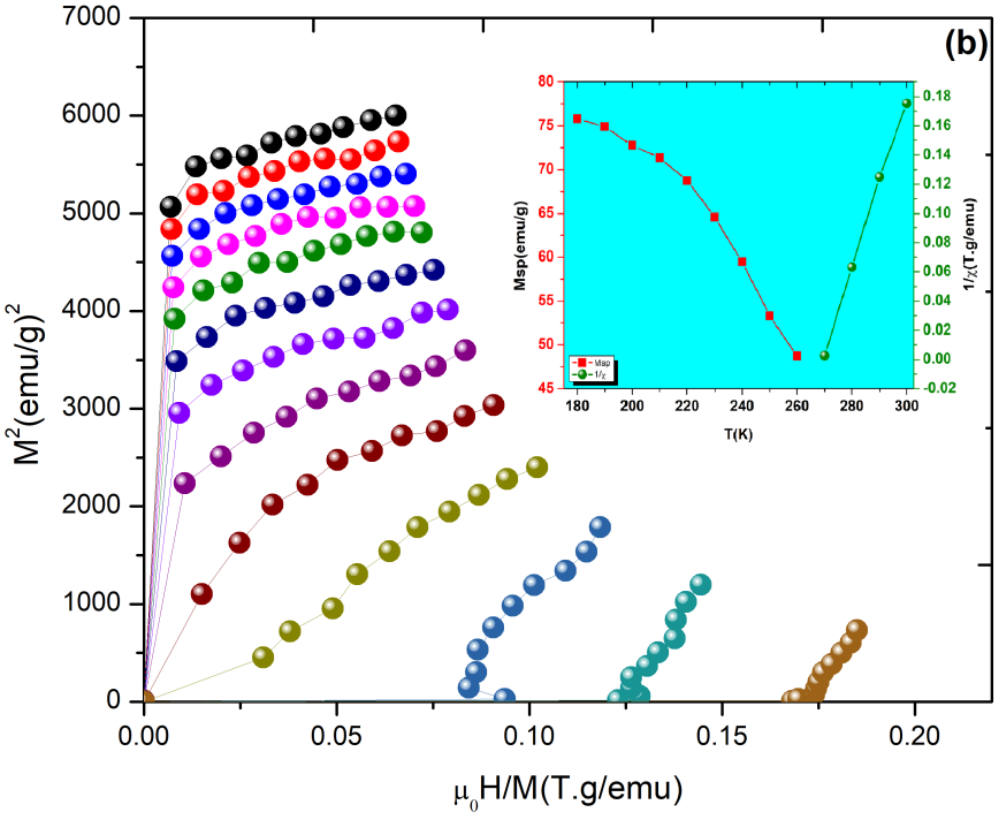
(b)
M^2(emu/g)^2
μ_0H/M(T.g/emu)
Msp(emu/g)
1/χ(T.g/emu)
T(K)

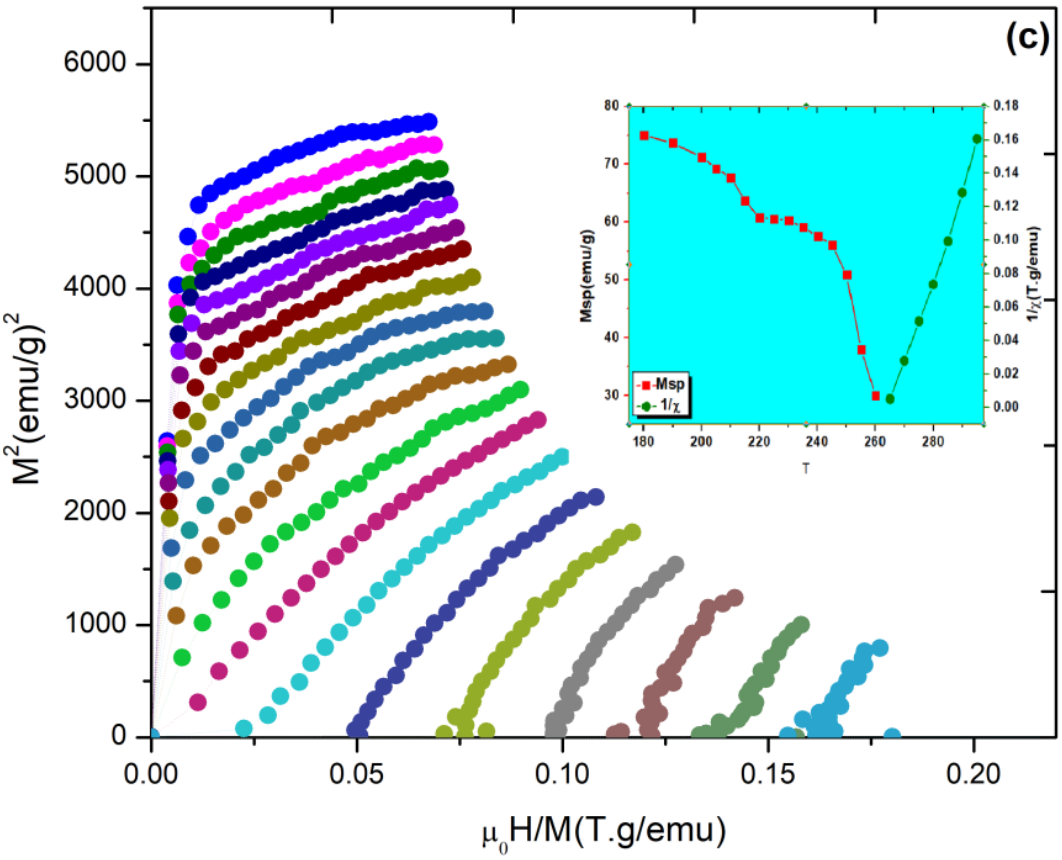

Figure 4.8: M^2 versus $\mu_0 H/M$ isotherms (Arrot's curves). The inset is the temperature dependence of the spontaneous magnetization Msp and $\frac{1}{\chi}$ for (1-x)$La_{0.6}Ca_{0.4}MnO_3$/xMn_2O_3 composites (a) $x = 0$, (b) $x = 0.1$, (c) $x = 0.2$.

[H]

Figure 4.9 illustrates the magnetic entropy change ΔS_m as a function of temperature under different applied magnetic fields ($\mu_0 H = 1, 2, 3, 4$ and $5T$). ΔS_m is derived from magnetic isotherms using the numerical integral of the well-known Maxwell relation given by:

$$\Delta S_m(T, \Delta H) = \sum_i \frac{M_{i+1}(T_{i+1,H}) - M_i(T_i, H)}{T_{i+1} - T_i} \Delta H, \tag{4.8}$$

where M_i and M_{i+1} are the magnetization values at temperatures T_i and T_{i+1}, respectively, under an applied field H. All ΔS_m curves exhibit maximum values around T_c and decreases when moving away from the transition for all composites. The maximum value increases with increasing the applied magnetic field. On the other hand, the maximum value of (1-x)$La_{0.6}Ca_{0.4}MnO_3$/xMn_2O_3 magnetic entropy change is found to decrease

slightly with the further increasing of Mn_2O_3 amount. Under a magnetic field changing from 0 to $5T$, the maximum ΔS_m values are found to be $5.87, 5.33, 5.21$ for $x = 0, 0.1$ and 0.2respectively.

We note that the width of magnetic entropy change curves is broad for all composite due to the second-order nature of the magnetic phase transition.

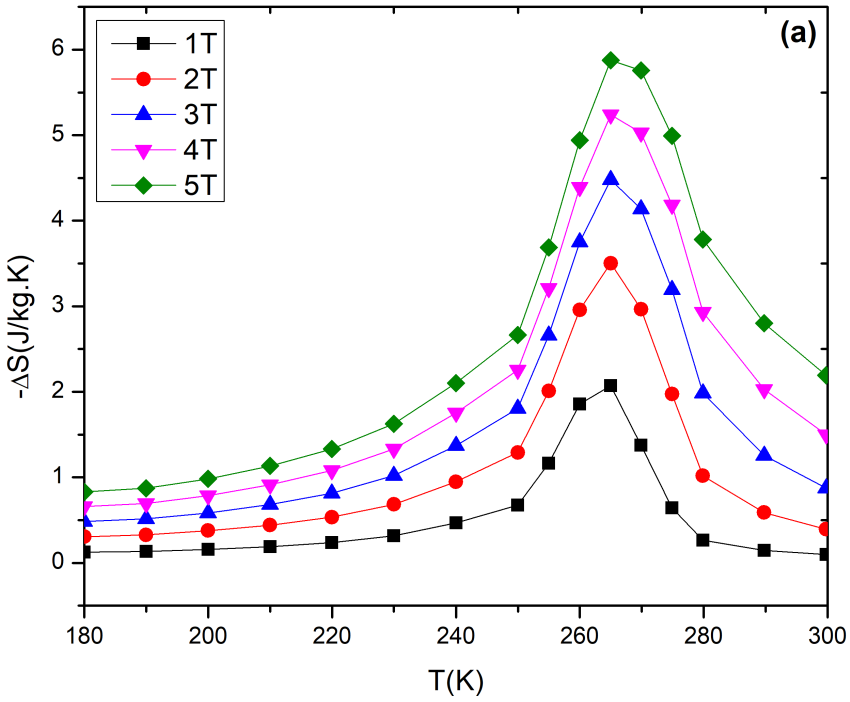

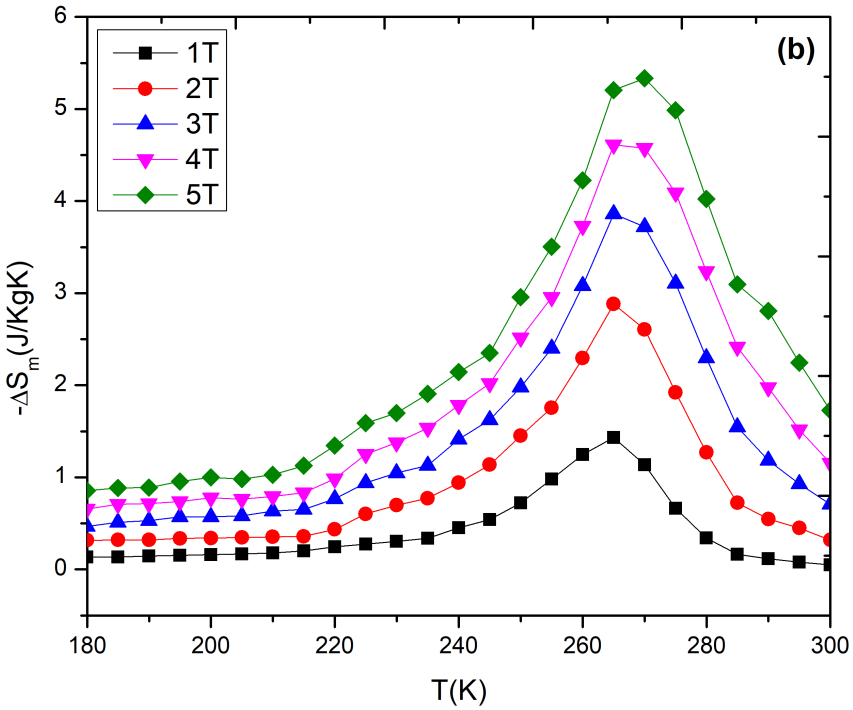
(b)
1T
2T
3T
4T
5T
-ΔS_m (J/KgK)
T(K)
0
1
2
3
4
5
6
180
200
220
240
260
280
300

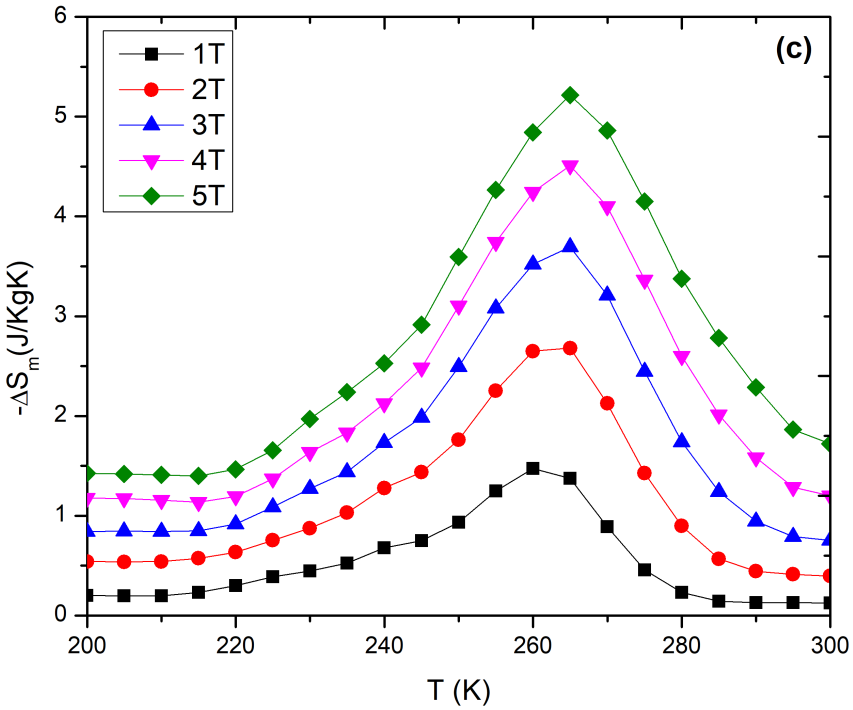

Figure 4.9: The magnetic entropy change as a function of temperature for different applied magnetic fields for (1-x)$La_{0.6}Ca_{0.4}MnO_3$/xMn_2O_3 composites (a) $x = 0, (b)x = 0.1, (c)x = 0.2$.

The magnetocaloric effect is usually characterized by three main quantities, namely, magnetic entropy change ΔS_m, adiabatic temperature change ΔT_{ad}, and the relative cooling power (RCP) suggested in the past by Gschneidner and Pecharsky as a figure of merit [181] which consider not only the value of ΔS_m, but also the width of its profile as a function of temperature. The relative cooling power is the parameter that evaluates the cooling efficiency of the solid refrigerant [159]. In other word it measures the heat amount that can be transferred by the magnetic refrigerant material between the hot and cold sides during an AMR cycle. Hence, larger RCP values combined with large entropy changes lead to better cooling performance of magnetocaloric devices. We obtained the relative cooling power (Eq. 4.9) by multiplying the maximum value of magnetic entropy

change by the full width at half maximum of ΔS_m -$m(T)$ curve as follow:

$$RCP = \delta_{(TFWHM)} {\Delta S_m}^{Max}, \tag{4.9}$$

Where $\delta_{(TFWHM)}$ is the full width at half maximum of the ΔS_m curve. The RCP as a function of magnetic field is shown in Figure 4.10. The RCP increases with the magnetic field and reaches 235 J/kg for $x = 0.2$ in the magnetic field change of $5T$ to largely exceed the reported experimental value reported by M. Nasri et al. and A. Nasri et al. [163, 166] in $La_{0.6}Ca_{0.4}MnO_3$ under similar magnetic field change. It's worth noting that, the RCP are greatly enhanced ($upto22\%$) in the composite sample with $x = 0.2$ ($146J/kg$ under $3.2kOe$) compared to that shown by the mother compound ($RCP = 120J/kg$) Figure 4.11.This could probably attributed to the increase of particles size and the exchange coupling interaction generated by the minor phase Mn_2O_3 of the composite.

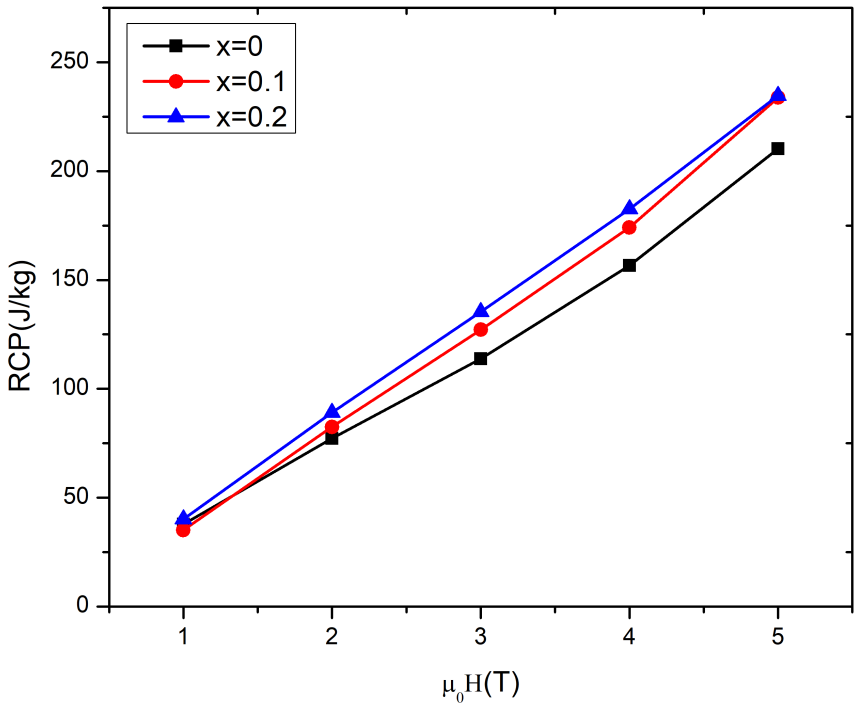

Figure 4.10: Magnetic field dependence of RCP reported for $LCMO/Mn_2O_3$composites.

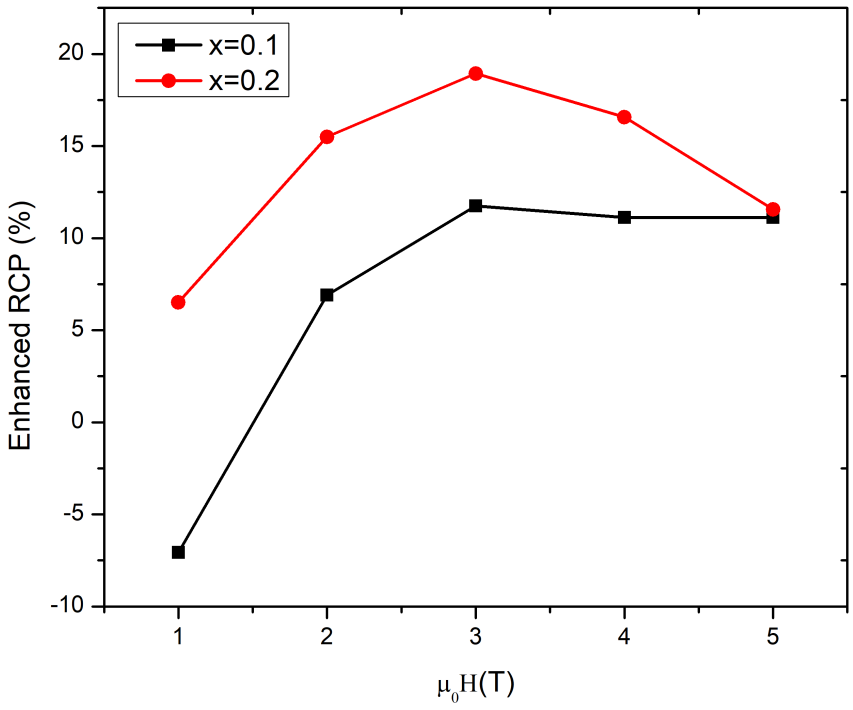

Figure 4.11: Enhanced RCP for $x = 0.1$ and 0.2.

The specific heat is an important parameter that plays a key role in the determination of magnetocaloric materials properties. It measures the ability of the solid material to capture and stock the heat and cold during the magnetization and demagnetization processes. Considering the equation below (Eq. 4.10) that give an accepted approximation for the adiabatic temperature change,

$$\Delta T_{ad} = -\Delta S \frac{T}{C_p}, \tag{4.10}$$

Where ΔS is the entropy change and C_p is the total specific heat. Larger MCE (ΔT_{ad}) can be obtained for materials with both, high magnetic entropy change and lower total heat capacity [18]. In this way, Akiko et al. have found by comparing the LaFeSiH with Gd performance in a magnetic cooling device, that $La(Fe_{0.86}Si_{0.14})_{13}H_{1.2}$ generates moderate temperature spans on account to its large specific heat [182]. The temperature dependence of specific heat was carried out for the here studied composites by using the

PPMS facility. The obtained data are displayed in figure 4.12 for zero magnetic field. As expected, all C_p curves exhibit a peak around the samples Curie temperature. The total specific heat decreases slightly with increasing the Mn_2O_3 content. The mother compound LCMO exhibit the highest heat capacity value around the curie temperature of about $632 J/kgK$, while it is 618 and $596 J/kgK$ for $x = 0.1, 0.15$, respectively. According to V. Ovsyannikov et al, the transition observed below $50K$ indicates a weak thermal hysteresis that is characteristic for a first-order transition having a sizable structural component [183].

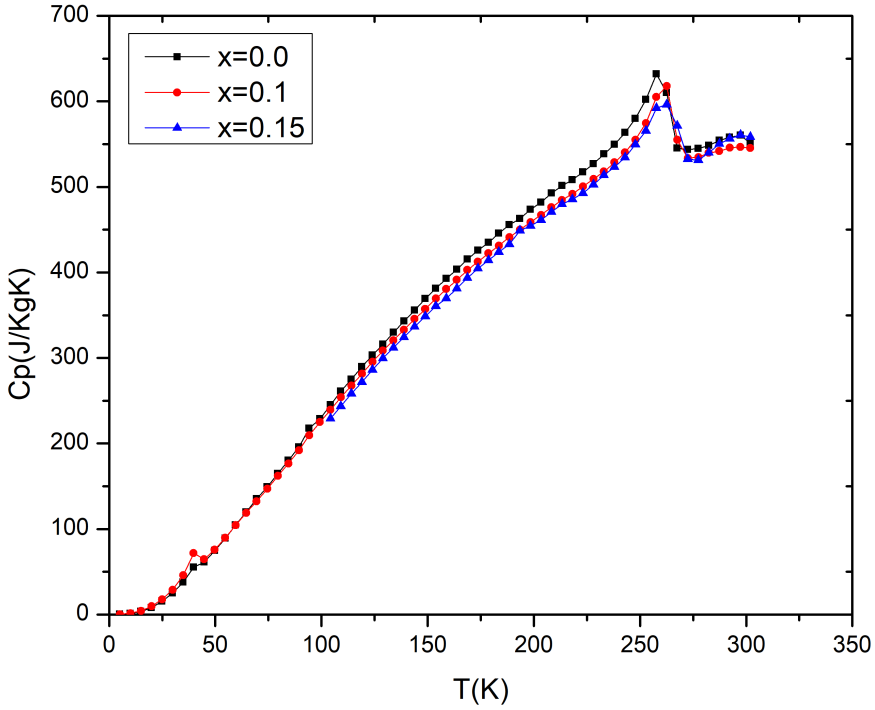

Figure 4.12: The specific heat of some selected $La_{0.6}Ca_{0.4}MnO_3/Mn_2O_3$ composites as a function of temperature measured under zero magnetic field.

The measurement of the adiabatic temperature change ΔT_{ad} adcould be directly performed by using a system of thermocouples or indirectly evaluated by using the heat and magnetization measurements [155, 184]. In our case we have used the latter to estimate ΔT_{ad} based on (Eq. 4.10). As shown in figure 4.13, ΔT_{ad} that maximises around TC are found to be roughly $0.7K$ and $1K$ for $x = 0$ and 0.1 respectively in the moderate field

change of $1T$.

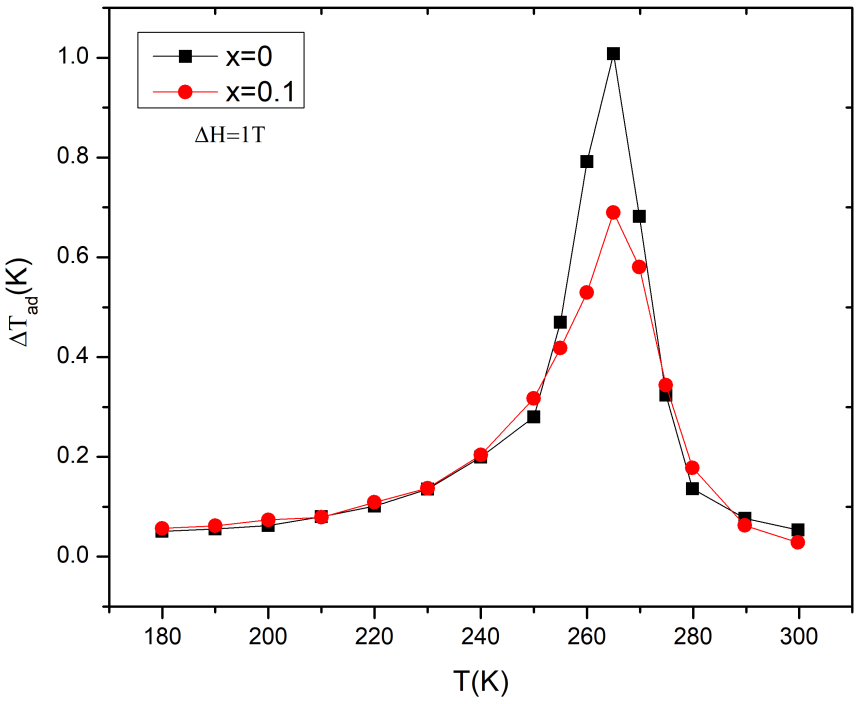

Figure 4.13: Temperature dependence of adiabatic temperature change for (1-x)$La_{0.6}Ca_{0.4}MnO_3$/xMn_2O_3 (with $x = 0$ and 0.1) under $1T$ magnetic field.

A comparison between our experimental measurements and other reported experimental results are summarized in table 4.4.

Compound	**Method**	**Tc, K**	**ΔS_{max}, $JKg^{-1}K^{-1}$ 5T**	**FWHM, K**	**ΔT_{ad}, K 5T**	**RCP, JKg^{-1} 5T**	**Ref**
$La_{0.6}Ca_{0.4}MnO_3$	SOl gel	260	3.66	38.52	-	141.98	[166]
$La_{0.6}Ca_{0.4}MnO_3$/xMn_2O_3							
x=0.0			5.87	35.38	1	210	
x=0.1	SSR	260	5.33	43.50	0.7	234	This Work
x=0.2			5.21	45	-	235	
$La_{0.6}Ca_{0.4}MnO_3$/xCuO							
x=0.00			5.8	37.06	-	215	
x=0.07	SSR	260	5.3	39.24	-	208	[163]
x=0.18			4.9	38.77	-	190	

Table 4.4: Magnetic and magnetocaloric properties of (1-x)$La_{0.6}Ca_{0.4}MnO_3$/xMn_2O_3 compared with those reported in recent published works.

4.4.3 Cooling properties

The $La_{0.6}Ca_{0.4}MnO_3$ material is used as refrigerant while the heat transfer is carried out by using water. A magnetic field of 1 T that can be produced by simply using permanent magnets is considered in the calculations.

According to the results published in [151], the value of the specific heat for $La_{0.6}Ca_{0.4}MnO_3$ compound at 260 K is equal to 640 J/Kg K, and the density is equal to 5940 kg/m3. These parameters for this magnetocaloric material have been implemented in 1D AMR-model, in addition of others described in computational details section. At the beginning the solid material plates and water are at (260 K), then the temperature of the hot source increases while the temperature of the cold source decreases after each cycle to reach their steady state after about 80 AMR cycles. It can be seen in Fig 4.14 that the maximum temperature span ($\Delta T_{span} = T_{Hot} - T_{Cold}$) obtained by numerical simulations after 80 cycles is 11°C for $La_{0.6}Ca_{0.4}MnO_3$ for a 1 T-AMR operating frequency of 0.5 Hz.

The temperature span shown in (Fig 4.14) between the cold and hot sources, the cooling capacity (Fig 4.16) and the coefficient of performance (Fig 4.17) are crucial parameters for a thermodynamic evaluation of magnetic refrigerators. (Fig 4.15) shows several no-load temperature gradients that are induced in the $La_{0.6}Ca_{0.4}MnO_3$ plates along the direction of the carrier fluid flow. It can be observed that initially the solid is at the temperature (T_i = 260 K), then the thermal gradient increases gradually to reach 11 °C at the steady state after 80 cycles, for a Reynolds number Re equal to 8600.

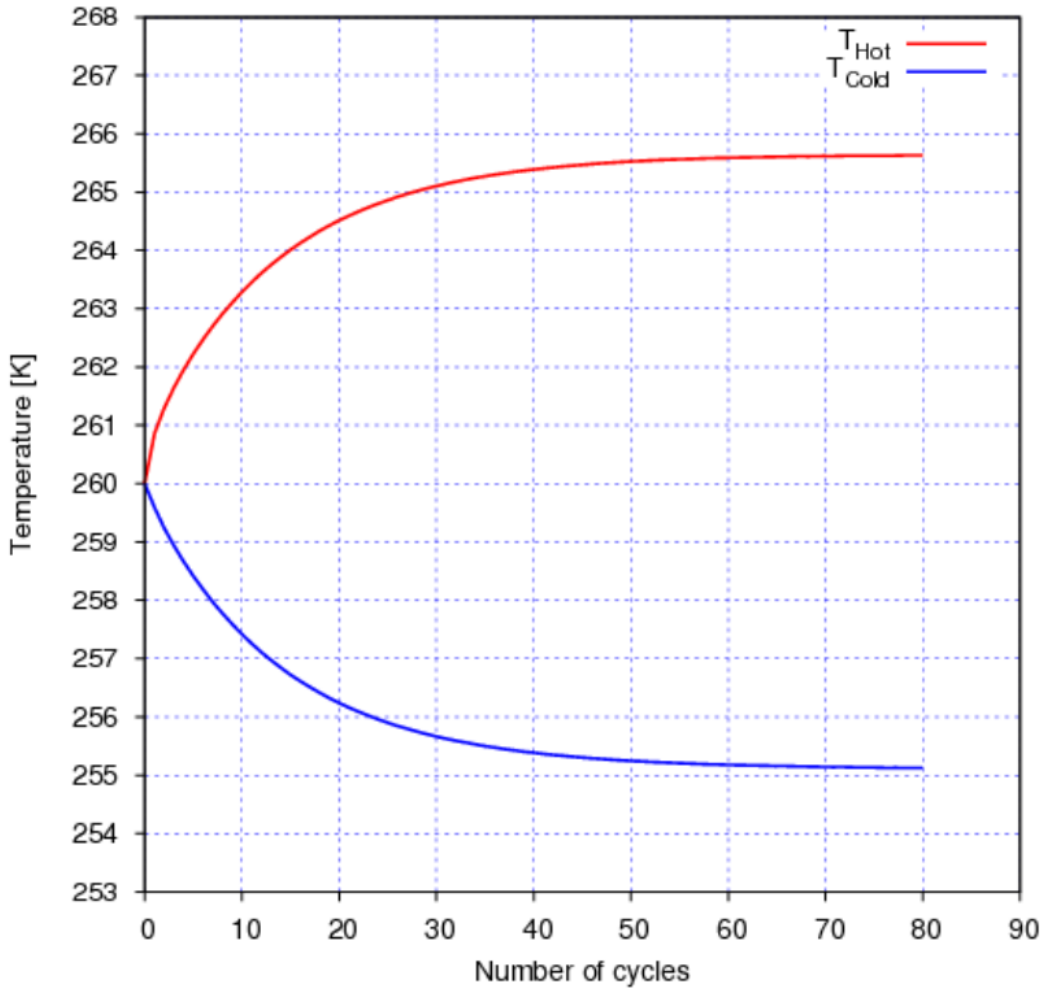

Figure 4.14: Temperature span between hot and cold sides of the regenerator

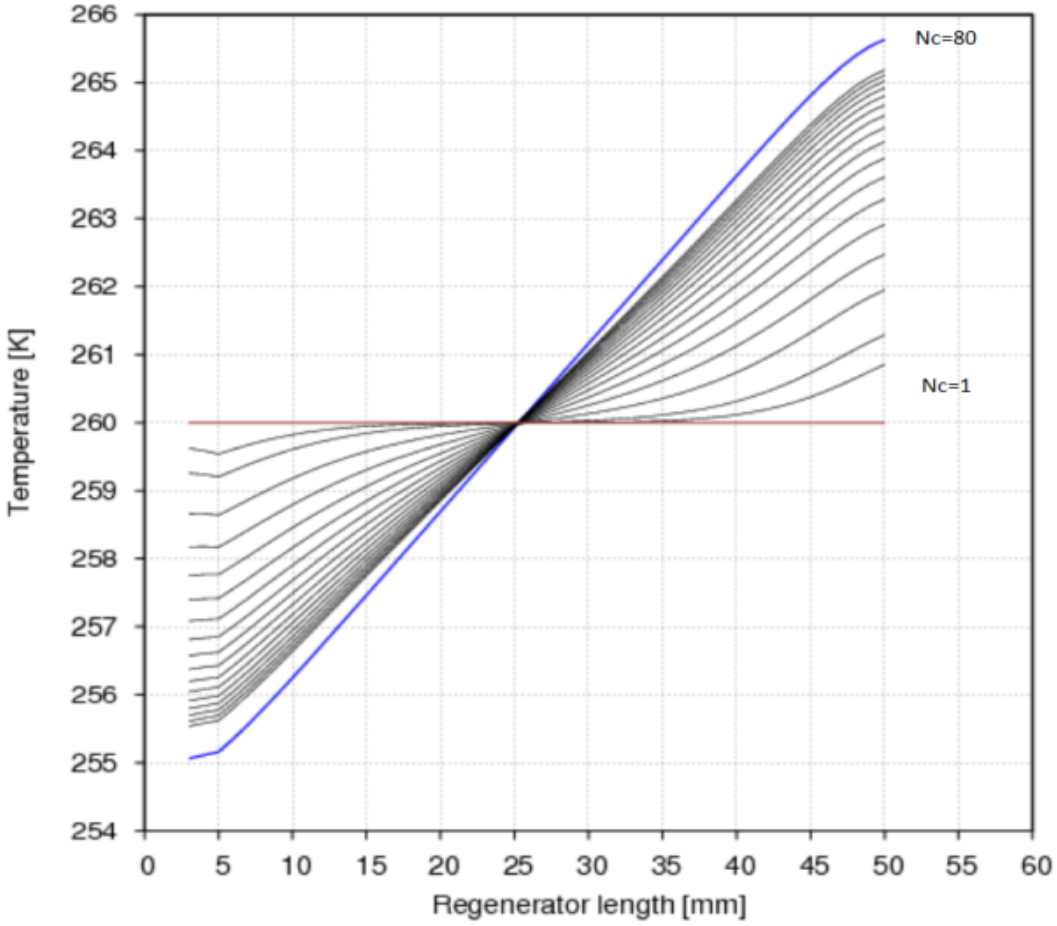

Figure 4.15: Temperature span between hot and cold sides of the regenerator

The cooling capacity $\dot{Q}_c$, is one of the cooling performance parameters of magnetocaloric devices, defined as the quantity of heat transferred per unit of time from the cold side to the hot side, given by the following Eq. (4.11).

$$Q_c = \frac{1}{\tau} \int_0^{\tau} \dot{m}(t) C_f \left(T_c - T(x = L, t)\right) dt \tag{4.11}$$

The coefficient of performance is calculated according to Eq. (4.12):

$$COP = \frac{Q_c}{(Q_h - Q_c) + W_{pump}} \tag{4.12}$$

Where,Q_H is the rejected heat calculated by:

$$Q_h = \frac{1}{\tau} \int_0^{\tau} \dot{m}(t) C_f \left(T(x = 0, t) - T_H\right) dt \tag{4.13}$$

$$W_{pump} = \frac{m(\dot{t})\Delta p}{\rho_f \zeta} \tag{4.14}$$

Where

$$\Delta p = \frac{96}{Re}\rho_f \frac{L_f}{D_H}\frac{u^2}{2} \tag{4.15}$$

In the above equations, τ is the cycle time, W_{pump} is the pumping power calculated using the pressure drop and the mass flow rate, u is the velocity of the fluid.

Fig 4.16 shows the temperature span ΔT_{span} dependence of the cooling capacity evolution ($\dot{Q}_c$) for the $La_{0.6}Ca_{0.4}MnO_3$ regenerator. The considered operating frequency is equal to 0.5 Hz, while the thermal load applied in the cold source is Tc=255 K. High cooling power $\dot{Q}_c$ results in low temperature spans. The maximum cooling power $\dot{Q}_c$ reached is 62 W for ΔT_{span}=0 K, while the device operating at a $\Delta T_{span,max}$ will not be able to support a heat load, the best performance was found for a fluid flow of 3 ml/s and low operating frequency of 0.5 Hz. As shown in (Fig. 4.17) the (COP) coefficient of performance obtained was around 0.5 at 10 K temperature span.

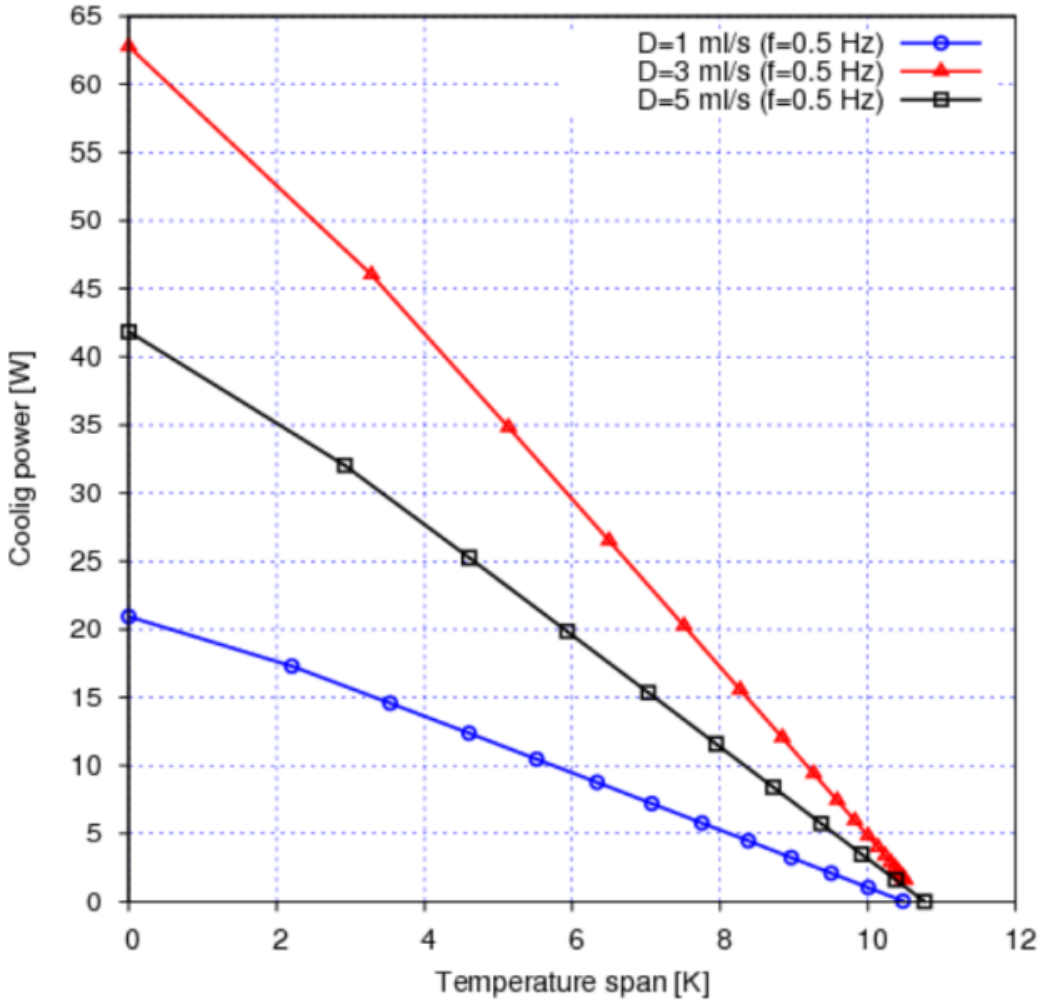

Figure 4.16: Cooling power vs. temperature span

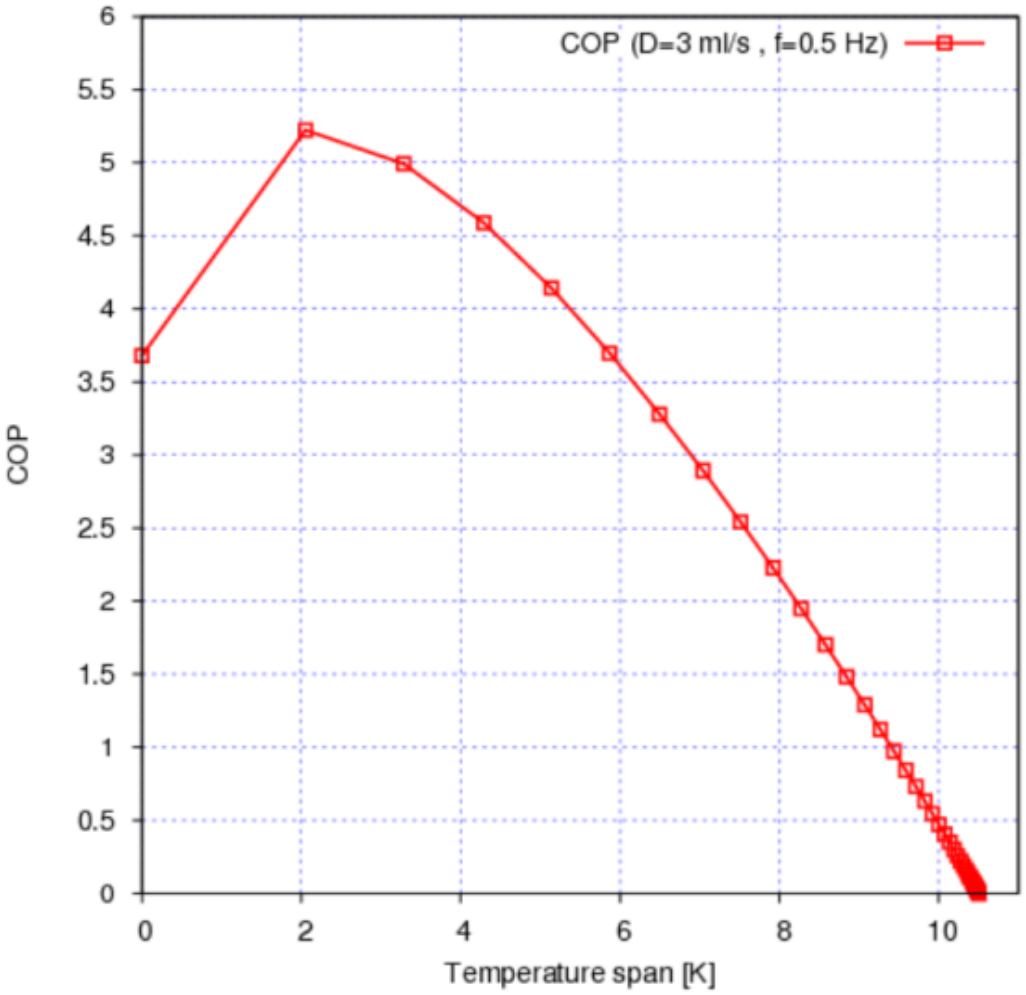

Figure 4.17: COP vs. temperature span

4.5 Conclusion

In this chapter, we have presented a combined experimental and numerical investigation of the structural, magnetic, magnetocaloric and cooling properties of the magnetocaloric material $La_{0.6}Ca_{0.4}MnO_3$.

The first part of this chapter was devoted to the study of the structural, magnetic and magnetocaloric properties of (1-x)$La_{0.6}Ca_{0.4}MnO_3$/xMn_2O_3 using experimental investigation. We explored the (1-x)$La_{0.6}Ca_{0.4}MnO_3$/xMn_2O_3 composite materials with the aim to enhance their magnetocaloric properties and refrigerant cooling power. The investigated (1-x)$La_{0.6}Ca_{0.4}MnO_3$/xMn_2O_3composites show a second order magnetic phase transition taking place at $260K$. In fact, the insertion of the Mn_2O_3 secondary phase has no impact

on the Curie point. On the other hand, a slight decrease in magnetic entropy change ΔS_m and in specific heat C_P values was observed when increasing the Mn_2O_3 concentration around T_C. The maximum generated entropy changes in the magnetic field variation of $5T$ are $5.87, 5.33$ and $5.21 J/kgK$ for $x = 0, 0.1$ and 0.2 respectively. In contrast, it is found that with 20% of Mn_2O_3 in the composite, the RCP can be markedly enhanced by more than 20% without affecting the Curie temperature. However, the origin of such enhancement remains not understood, opening the way for further investigations. In addition, the here studied materials exhibits better magnetocaloric features when compared to those of similar compounds early reported in the literature. Finally, these findings suggest that the addition of Mn_2O_3 could be useful for the enhancement of the LCMO refrigerant capacity.

The obtained experimental magnetocaloric properties in term of ΔT_{ad} and C_p results have been used within the 1D-AMR numerical model in order to investigate the cooling properties of the mother compound $La_{0.6}Ca_{0.4}MnO_3$. We have reported preliminary numerical simulations that discuss the thermodynamic performance of a reciprocating magnetic cooling machine using $La_{0.6}Ca_{0.4}MnO_3$ as the solid refrigerant. We particularly found that the no load temperature span between the hot and cold ends of the magnetocaloric devices is about 11°C for 0.1 mm thickness because it strongly depends on the gap between the magnetocaloric material plates, the cooling capacity obtained is about 62 W, and a coefficient of performance (COP) of about 0.5 at 10 K temperature span. What remains now is to experimentally validate these obtained results. For this purpose, the development of a magnetic cooling prototype is in progress and its experimental performance will be communicated in the future. And to overcome the low value of MCE of these materials and achieve better performances, it is necessary to combine different magnetocaloric materials with different values of Tc in the regenerator in order to obtain a temperature span as large as possible.

Chapter 5

The magnetic refrigeration test device

5.1 Introduction

This chapter concerns the realization of an experimental prototype of the magnetocaloric effect. Following the first magnetic refrigeration demonstrator developed at MAScIR, work on these devices continued with a new system which is discussed in this chapter. The first version of the system was realized by Dr. Khadija Al maalam [185]. We performed a second version within the framework of this thesis; the realization has been completed. The objective of the work on this prototype was to realize a complete magnetic refrigeration system in order to examine the performance of different magnetocaloric materials in direct application. As will be seen in this chapter, the operation and performance of such a system are governed by a large number of factors that are very closely related with each other. As the entire system is not easily modeled numerically, it is essential to build the device physically. This, in order to reveal the problems and quantify their influences. One of the guides for the design of this system, in addition to the simplicity of implementation, was to try to obtain sufficient induction in the active material during the magnetization phase while keeping a low induction during the demagnetization phase.

A magnetic refrigeration test device has been built. The device allows variation and control of many important experimental parameters, such as the type of heat transfer fluid, the movement of the heat transfer fluid, the frequency of the refrigeration cycle. A 1D-dimensional numerical model has previously been implemented in order to help in the optimization of the design of a refrigeration test device.

5.2 Magnetic field source

The magnetic field source is one of the essential components of magnetic refrigeration. The performance of a magnetic refrigeration system depends primarily on the magnetocaloric material and the magnetic field. Therefore, it is necessary to design structures generating magnetic fluxes with high density for magnetocaloric materials.

There are several types of magnetic field source that can be used for magnetic refrigeration: We mention, electromagnets, superconducting coils and permanent magnets. we will focus exclusively on permanent magnet field sources. A number of permanent magnets structures have been proposed for magnetic refrigeration systems. We can classify these structures in three categories:

- Simple magnetic circuits, composed of permanent magnets and soft materials.
- Halbach type assemblies (single or double, open or closed).
- complex magnetic structures.

The permanent magnet-based structures are preferred over those using electromagnets or superconducting magnets since no electrical energy is consumed in the generation of magnetic field. Bjork et al.[186] compared a variety of magnet designs and suggested that desirable magnetic flux distribution is obtained from the modified Halbach cylinder. The concept of Halbach design is to assemble pieces of permanent magnets for stronger magnetic fields in the air gap with minimal flux leakage outside the assembly [187]. The Halbach arrays have been used in motors and other electromagnetic devices [188]. To implement in magnetic refrigerators, regions of weaker magnetic field are also needed for

the demagnetization of magnetocaloric materials in the air gap. The abrupt transition between strong and weak fields in the air gap is achieved by modifying the Halbach design [189].

5.3 Regenerator (Active material)

Gadolinium, the reference magnetocaloric material was used as active material thanks to its magnetocaloric properties at room temperature and also for its mechanical properties which allow obtaining different geometries. The regenerator is formed of gadolinium (plates) 70 mm long, 25 mm wide and 1 mm thick. The bed regenerator has a rectangular form containing both the magnetocaloric material and the heat transfet fluid. Based on the results of the thermal modeling of the AMRR cycle, the gap between plate and Gd plate is 0.3 mm and the corresponding height is equal to 23.7 mm. So we used 18 Gadolinium plates separated by an internal gap of 0.3 mm allowing the fluid circulation.

Two options are possible to obtain the reciprocating movement of the device, either by moving the Halbach cylinder, or the cylinder containing the magnetocaloric material. In both cases pneumatic cylinder is necessary to manage the reciprocating movement. The experimental setup of the whole system that illustrated schematically in figure 5.1 involves the following major elements:

- Active Magnetic Regenerator structure.
- Power supply system.
- Measuring instruments. Active Magnetic Regenerator Structure The primary components of the Active Magnetic Regenerator structure are the:
- The cylindrical enclosure housing of the regenerator.
- Inert magnetocaloric material plates.
- Heat transfer fluid system.

5.4 The Heat Transfer Fluid System

The heat transfer fluid flows through the channels between the regenerator plates. A 20 mm long plastic flow guide plates placed on each side of the Gd plates in the direction of the flow to ensure laminar flow in the channels. The guide plates inserted and placed inside the cylindrical enclosure housing that connected with the Perspex tubes at both ends. Perspex tube is a kind of polymers durable to high temperature, and stable chemically. The Perspex tube has an outer and inner diameter of 40 mm and 34 mm respectively, machined with an internal screw 34 mm for 12 mm long at open end. This design used to connect and fix the (PVC) housing cylinder ends' surrounding the regenerator block, and to holds the pistons that used to pushed stream of fluid. Taphelon washers used with all connect to prevent any leak. The whole experimental close-up drawing, cylindrical enclosure housing design is shown in figure 5.1.

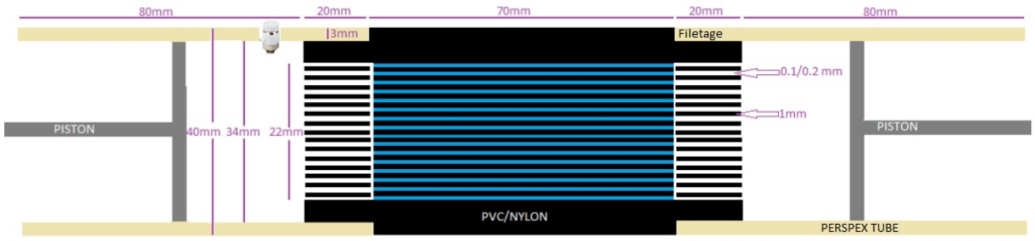

Figure 5.1: AMR cycle

5.5 Measuring Instruments

Temperature measurement system consists of three thermocouples wire, type "T" (Copper Constantan) with a small diameter about (0.3 mm). This type of thermocouples used to reduce the time constant of each thermocouple accurately to measure transient behavior of the plate and fluid temperature. These thermocouples were distributed at various locations on Active Magnetic Regenerator to measure temperature at these places. Figure 5.2. show the thermocouples used in the experimental setup.

Figure 5.2: Thermocouple type T used in the experimental setup.

5.6 Practical realization of the reciprocating prototype

We were based on the simple structure of the first demonstrator developed at MAScIR to design a similar system with some modifications to improve its technical aspect. Figure 5.3 shows the general view of the device developed within our center Materials and Nanomaterials at MAScIR Foundation.

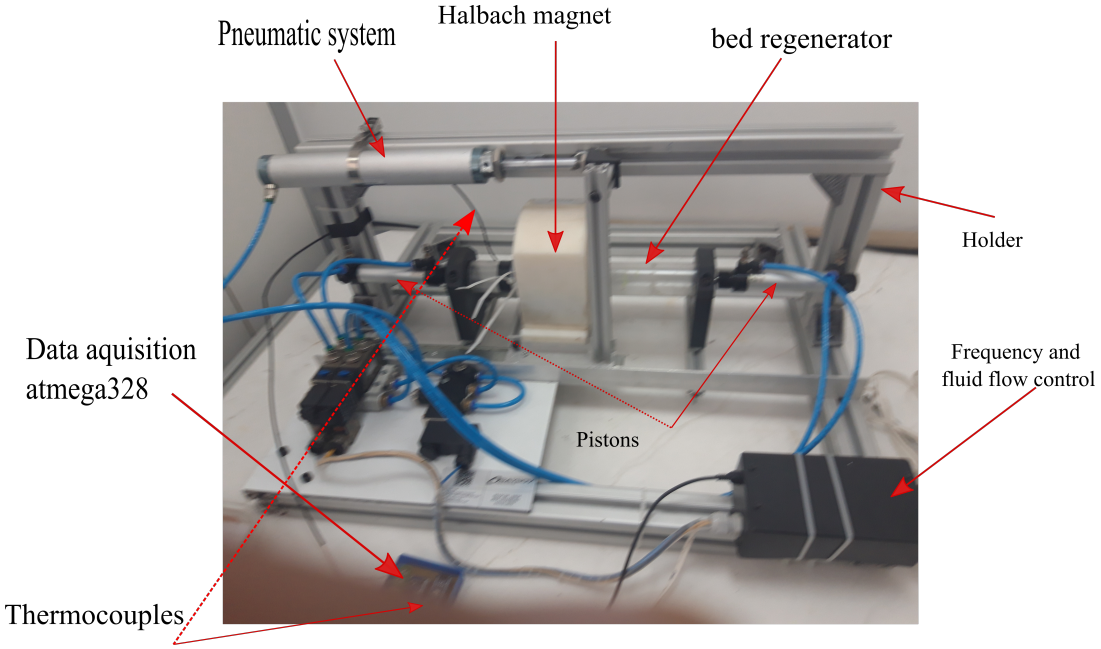

Figure 5.3: General view of the linear magnetic refrigeration prototype.

5.7 Computational details

5.7.1 Magnetic study by finite elements

Configurations of permanent magnets that produce a strong homogeneous field in a confined region of space and a very weak field elsewhere are useful in many applications such as magnetic cooling applications [190]. For the design of this device, numerical simulations were made to model the magnetic behavior of the halbach cylinder. The results of this study are detailed here. This work was done with the finite element electromagnetic simulation software Comsol Multiphysics. In this part of thesis the two dimensional Halbach cylinder will be investigated in greater detail, and the flux density will be computed for different configurations.

The Halbach cylinder can be characterized by three parameters: the internal and external radii, r_{in} and r_{ex}, respectively, and the length, L. In our case The source of the magnetic field is a Halbach cylinder. It is a structure composed of an assembly of permanent magnets (Nd-Fe-B) creating an intense magnetic field entirely confined inside the cylinder.

Figure 5.4 shows the principle of Halbach cylinder used in our device. Each part with specific direction of magnetization. These directions are indicated for each segment of the permanent magnet. there is 90 deg ° between the magnetization of two successive sectors (black arrows). We performed simulation for this configuration to calculate the produced field and its distribution inside the cylinder. Figure 5.5 shows a photograph of the Halbach cylinder used and the dimensions of the latter. This cylinder has a Length of 74mm, an inner diameter of 43mm and an outer diameter of 100mm. The magnetization in the thickness of the cylinder is given by the expression:

$$M(\vec{\theta}) = M(sin(k.\theta)\vec{u_r} - cos(k.\theta)\vec{u_\theta}) \tag{5.1}$$

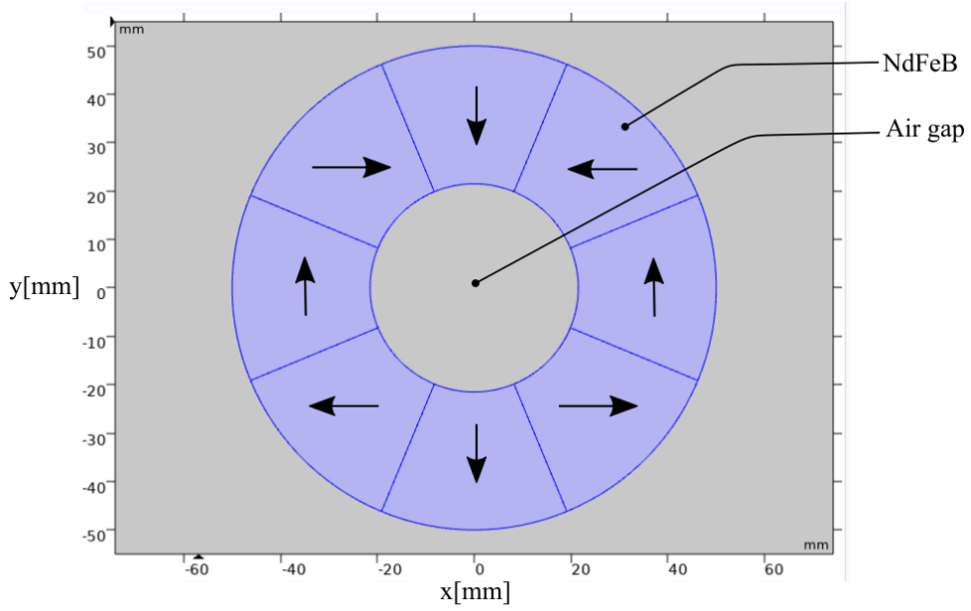

Figure 5.4: Geometry of Halbach cylinder of 8 permanent magnets used for magnetic simulations.

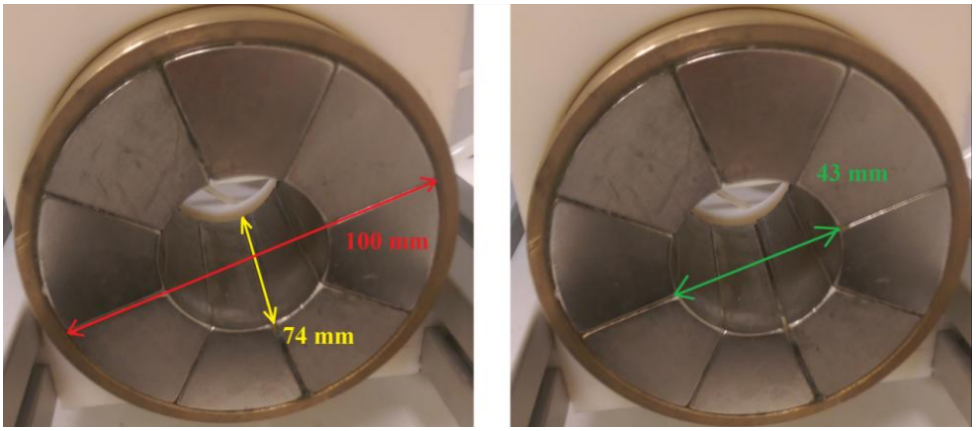

Figure 5.5: Photograph of the Halbach cylinder used in the developped prototype

5.7.1.1 Conditions for simulation

The here studied structure is in two dimensions, the thickness of the structure is equal to 1 m. The remanent flux density of permanent magnetic NdFeB of $1.42T$ is in different directions by separating vectors along the x and y axis, the relative permeability is $\mu = 1.05$. The element size of the mesh is set to normal in the beginning. View of the mesh performed for finite element modeling of the magnet is shown in figure 5.6.

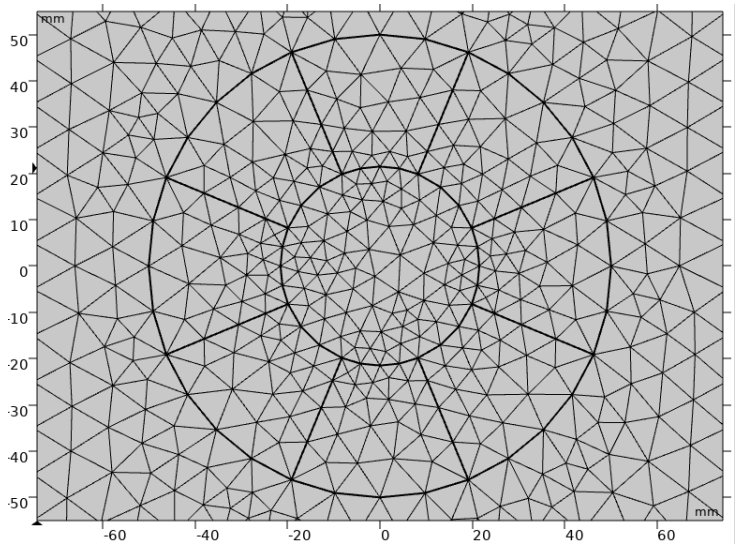

Figure 5.6: View of the mesh performed for finite element modeling of the Halbach

5.7.2 The numerical AMR model

An important tool in the optimization of any magnetic refrigeration device is a comprehensive and flexible numerical model. This may help in predicting the effect of a proposed alteration of the operation of the device as well as physical changes to the device. It also allows parameter optimizations to be performed consistently and efficiently.

The device presented in the following is a linear design, relying on the active magnetic regenerator AMR cycle.

The first part of this chapter is devoted specifically to present our 1D transient numerical model. The numerical model solves the mass and momentum equations for the flow of the heat transfer fluid and the coupled heat transfer equations for the temperatures in the regenerator and in the fluid. The only inputs to the model are the physical properties of the modeled materials.

For that we have used the implicit finite difference as a numerical solution to simulate the AMR cycle and implemented using Fortran programming language. And the flowchart of the algorithm used is given in the Appendix B at the ending of this chapter.

The thermo-physical characteristics of the gadolinium and water at reference temperature (298 K) are assumed constants; they are given in (Table 5.1). It's worthy to note that the classical values of gadolinium were taken from literature data published in

[44, 48, 191], and the MCE value (1.45 K) of gadolinium mentioned in the table correspond to a permanent magnetic source with an induction field of 1 T.

Symbol	Parameter (Unit)	Value	
		Water	Gadolinium
δ	Thickness (mm)	0.1	1
L	Length of the bed regenerator (mm)	50	50
I_{ea}	Equivalent cell width of the regenerator (mm)	525	525
λ	Thermal conductivity (w/m.K)	0.59	10.05
ρ	Volume density (kg/m^3)	1000	7800
C_p	Specific heat (J/Kg.K)	4185	240
μ	Dynamic viscosity (Kg/m.s)	0.001	-
MCE	Magnetocaloric effect (K)	-	1.45
$\dot{m}(t)$	Flow rate (ml/s)	3	-

Table 5.1: Geometrical and thermo-physical parameters of water and Gadolinium used in simulation.

5.7.2.1 Description of the regenerator and working cycle

The regenerator considered in this study is shown in "Fig 5.7" The bed regenerator is constituted of 21 parallel plates made of gadolinium used as the refrigerant with 1 mm thickness, 50 mm length and 25 mm width each. The plates are equidistant with an inter-space of about 0.1 mm where water flows as a heat transfer fluid.

The system undergoes the AMR thermodynamic cycle realized by combining the magnetocaloric material and the heat transfer fluid, functioning as a regenerator, which used for achieving very low temperature in cold source. The alternative movement of fluid is ensured by a controlled hydraulic system, the latter consists of a pump and two pistons driven in opposite directions. The AMR cycle is carried out by the following successive steps:

1. Isentropic magnetization of the magnetocaloric material.

2. Hot blow at applied magnetic field: heat transfer fluid flows from the cold fluid reservoir to the hot fluid reservoir of the regenerator.

3. Isentropic demagnetization of the magnetocaloric material.

4. Cold blow at removed magnetic field: heat transfer fluid flows from the hot side to the cold side of the regenerator.

As the adiabatic temperature difference of MCMs (MagnetoCaloric materials) is very low, a single stage of AMR cycle is inefficient and impractical, for this reason the four process of AMR cycle must be repeated as a strategy to enhance the temperature span known by AMRR cycle, this technique was first used by Barclay in 1982 [1]. Thus, the temperature span between both hot and cold sources of regenerators is increased. for this reason, single cycle is not recommended. In such cases, the four processes are reproduced several times in practice until a permanent state is reached, namely Tck – Tck-1¡ ε (ε=0.00005K). Where Tck – Tck-1 represent the difference between the cold temperature (Tck) of the current cycle and the cold temperature (Tck-1) of the previous cycle.

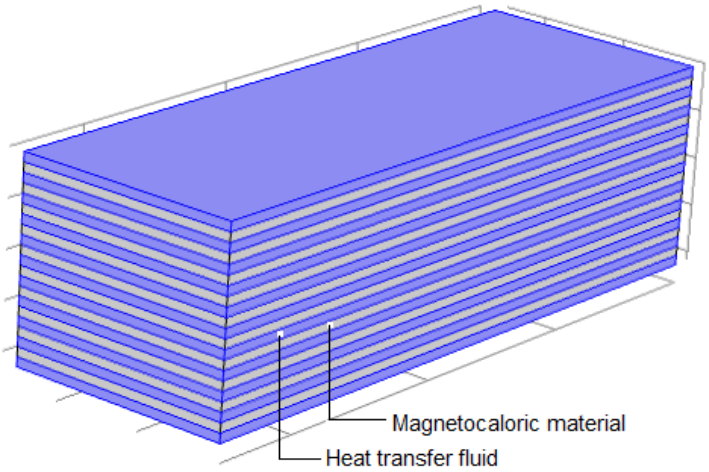

Figure 5.7: Parallel plate regenerator. The MCM is in gray and the fluid channels in blue.

5.7.2.2 Governing equations

Based on the law of energy conservation, the main equations describing heat transfer in a solid material and thermal fluid in 1D model are given by the following partial

differential equations (PDE):

$$\rho_s C_s \frac{\partial T_s}{\partial t} = \frac{\partial}{\partial X}\left(\lambda_s \frac{\partial T_s}{\partial X}\right) + \dot{Q}_{MCE} + \dot{Q}_{loss} + \dot{Q}_{HT} \tag{5.2}$$

$$\rho_f C_f \left(\frac{\partial T_f}{\partial t} + u_x \frac{\partial T_f}{\partial X}\right) = \frac{\partial}{\partial X}\left(\lambda_f \frac{\partial T_f}{\partial X}\right) + \dot{Q}_{loss} - \dot{Q}_{HT} \tag{5.3}$$

Where s and f in the subscript are referred to solid and fluid, respectively; t is time; x design spacial coordinate ($0 < x < L$); $Tf = Tf(x,t)$ denote the fluid temperature; Ts=T(x,t) denote the regenerator solid temperature; ρ_s is the mass density of solid; ρ_f is the mass density of fluid; the heat capacity of solid and fluid are denoted by C_s,and C_f respectively; λ_s is the thermal conductivity of solid and λ_f is the fluid thermal conductivity; u_x is the velocity of fluid; $QMCE$ is the internal heat generation term; $Qloss$ represent the thermal losses; QHT denote the heat transfer flux between solid and fluid in the bed regenerator. Moreover, for simplification, the next assumptions were adopted:

- The fluid is incompressible, and its velocity remains constant, also the fluid flow within the bed regenerator is fully developed.
- The external wall of the system is perfectly thermally insulated which insure no thermal losses (adiabatic conditions). Also, the perfect sealing is considered, which leads to no-flow leakage through the system.
- Conjugate heat transfer through the regenerator is considered, by conduction in the solid and convection in the fluid, although the radiation heat transfer is negligible.
- The axial conduction heat transfer in the solid is negligible, because the metal wall is very thin.
- The interface solid-fluid is thermally perfect, it means that no thermal contact resistance because roughness of the solid material is low.

The term Q_{MCE} in the equation (5.4) represent the internal heat flux generated during the interaction between magnetic field and magnetocaloric material can be calculated by

using this equation:

$$\dot{Q}_{MCE} = \rho_s C_p, s(H,T)\frac{\Delta T_{ad}(H,T)}{dt} \tag{5.4}$$

Where Cp,s (H,T) and ΔT_{ad}(H,T) represents the specific heat and the adiabatic temperature change of the solid material named magnetocaloric properties, which depends on the magnetic field applied and varies with temperature. these values can be calculated by using the mean field theory, (see Balli et al., 2007) [171], or by experimental measurement. Then "Fig 5.8" show the heat capacity curves of gadolinium and the adiabatic temperature is deduced from the latter and it's shown in "Fig 5.9". The expression of adiabatic temperature change can be approached by:

$$\Delta T_{ad} = -\frac{T}{C_p}\Delta S \tag{5.5}$$

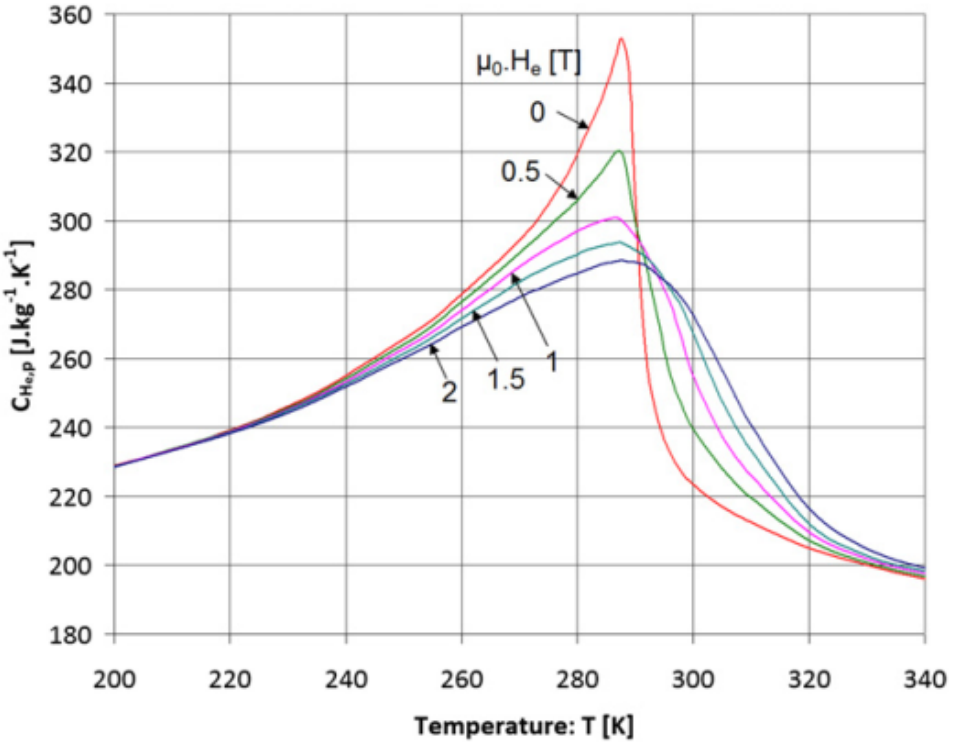

Figure 5.8: Heat capacity of Gadolinium used for the one-dimensional model

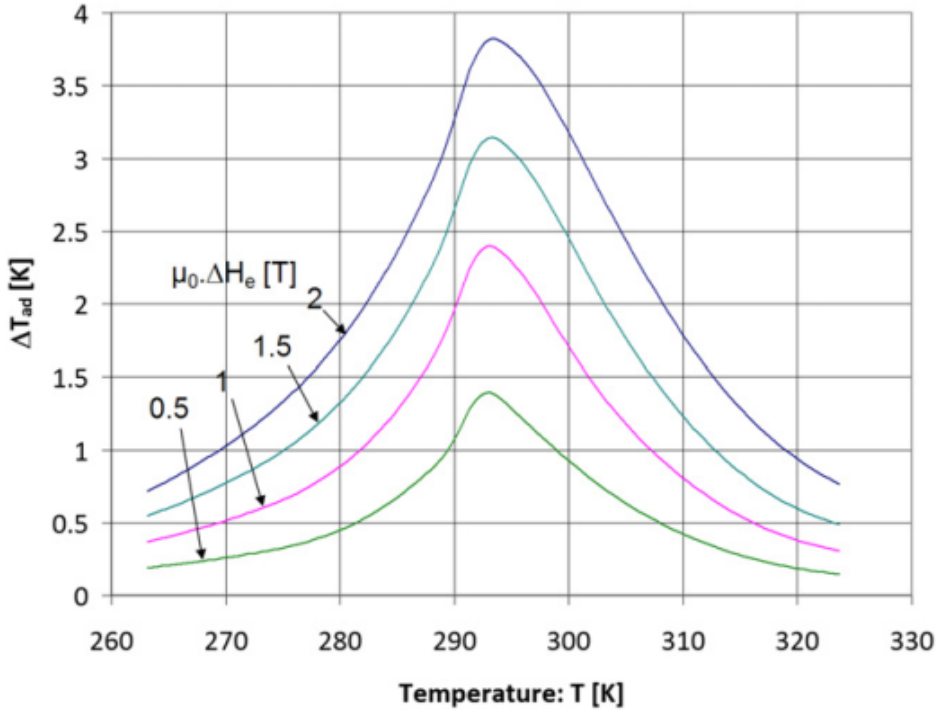

Figure 5.9: Adiabatic temperature change deducated from the heat capacity

It is clear from equation (5.5) that, larger MCE (ΔT_{ad}) of materials correspond to low specific heat and high entropy change.

The term Q_{HT} in the equation (5.2) and (5.3) represent the heat exchanges by convection between a fluid in motion on a wall and this latter, it can be expressed by a convective heat transfer coefficient h. The heat transfer rate Q_{HT} can be expressed as: The heat transfer rate $\dot{Q}_{MCE}$ can be expressed as:

$$\dot{Q}_{HT} = hA_{HT}(T_s - T_f) \tag{5.6}$$

where A_{HT} is the wetted area per unit cell of the solid material. The convective heat transfer coefficient is calculated according to empirical Nusselt-Reynolds correlations corresponding for fully developed laminar flow given in [192]. Reynolds number is defined as $Re = \rho u D_h/\mu$, and Prandtl number is defined as $Pr = \mu C_f/\lambda$.

$$Nu = \frac{hD_h}{\lambda} \tag{5.7}$$

$$Pr > 0.7 \qquad Nu = \frac{hD_h}{\lambda} = CRe^m Pr^{0.31} \tag{5.8}$$

$$Pr < 0.7 \qquad Nu = \frac{hD_h}{\lambda} = CRe^m \tag{5.9}$$

Where C and m are empirical constants given in the table 5.2.

Re	C	M
$1 < Re < 4$	0.891	0.33
$4 < Re < 40$	0.821	0.385
$40 < Re < 4.10^3$	0.615	0.446
$4.10^3 < Re < 4.10^4$	0.174	0.618
$4.10^4 < Re < 4.10^5$	0.024	0.805

Table 5.2: empirical constants C and M.

5.7.2.3 Initial and boundary condition

First the bed regenerator is considered in thermal equilibrium with the ambient, then the fluid and solid are initialized at a constant temperature: $T(x, t = 0) = T_{amb} = 293K$. To include the MCE of solid material in the AMR model. The magnetization/demagnetization phenomena created by a permanent magnet is modeled through the following boundary conditions:

- during the magnetization step: $T = T_i + \Delta T_{ad}(T_i, \mu_0 H_i, \mu_0 H_f)$

- during the demagnetization step: $T = T_i - \Delta T_{ad}(T_i, \mu_0 H_i, \mu_0 H_f)$

where Ti is the initial temperature; Hi and Hf are the initial and final magnetic field respectively. The processes of cold and hot blow can be simulated through the following boundary conditions:

- Hot blow: the coolant flows from the cold reservoir to the hot one, then it enters the bed regenerator with the temperature of the cold reservoir, Tf (x=0, t) = T_{cold};

- Cold blow: The coolant enters the bed regenerator with the hot tank temperature, Tf (x=L, t) = T_{hot};

Based on the assumptions cited in the section 2.2. The temperature span between cold and hot sources given by $\Delta T_{source} * N = T_{Hot} - T_{Cold}$ (N is the number of stages). The cooling capacity $\dot{Q}_c$, is one of the cooling performance parameters of magnetocaloric devices, defined as the quantity of heat transferred per unit of time from the cold side to the hot side, given by the following equation:

$$Q_c = \frac{1}{\tau} \int_0^{\tau} \dot{m}(t) C_f \left(T_c - T(x = L, t)\right) dt \tag{5.10}$$

5.8 Results and discussion

5.8.1 Magnetic field analysis

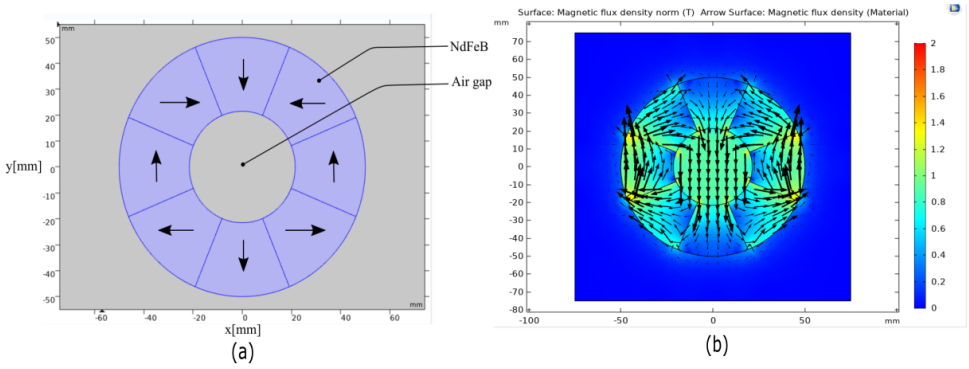

Figure 5.10: (a) Geometry of Halbach cylinder of 8 permanent magnets, (b) distribution of magnetic flux simulated by COMSOL.

It is clear from the result of simulation (figure 5.10(b)) that the Halbach cylinder structure concentrates the magnetic flux within the center of cylinder but there are still a large flux leakage outside the magnetic assembly by such configurations. Based on the gradient colors, the induction is around 1 T at the core of the Halbach.

5.8.2 Cooling performance

The temperature span between cold and hot sources, cooling capacity and the coefficient of performance are the main parameters to investigate the energetic performance of the regenerators. The magnetocaloric material used is gadolinium, the heat transfer fluid is water and the magnetic field generated by the permanent magnet is 1 Tesla.

"Fig 5.11" shows the No load temperature gradient along the solid material, when both sources are not exposed to any temperature or power. It can be observed that initially the solid is at ambient temperature (Ti=293 K). Then the thermal gradient increases gradually after 50 cycles, in a case of Reynolds number equal to 12000. At the end of the cycle, the temperature gradient has stabilized at 13°C the profiles obtained are in good agreement qualitatively with those obtained by Chen et al. (1994) with experimental data [193].

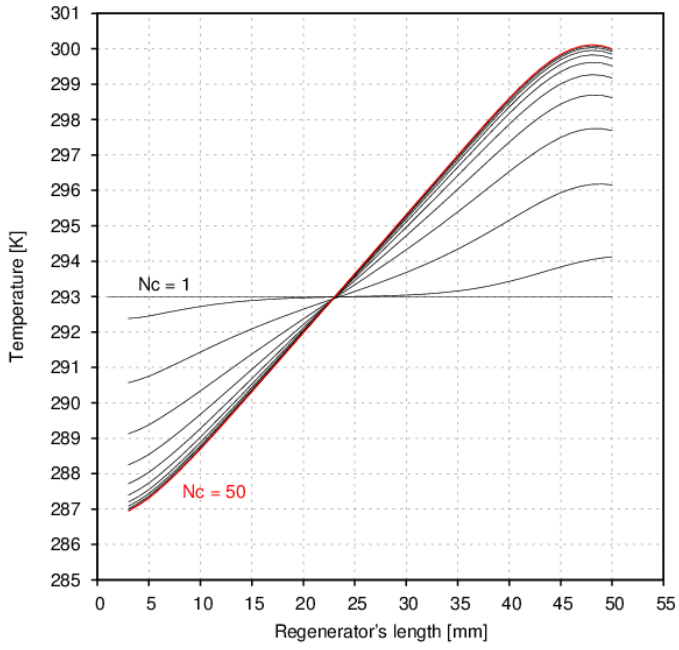

Figure 5.11: No-Load temperature gradient along the solid material

"Fig. 5.12" shows the temperature evolution of both sides of the regenerator hot and cold with no heat exchangers. The observed temperature fluctuations represent the change

of the process that is taking place, starting by magnetization followed by the hot flow then demagnetization step followed by the cold flow. It can be seen clearly that the two curves pass through a transitory regime that lasts 50s and then the regenerator enter gradually into the permanent regime. From this curve, we have obtained the temperature evolution at the end of each cycle showed in "Fig 5.13"

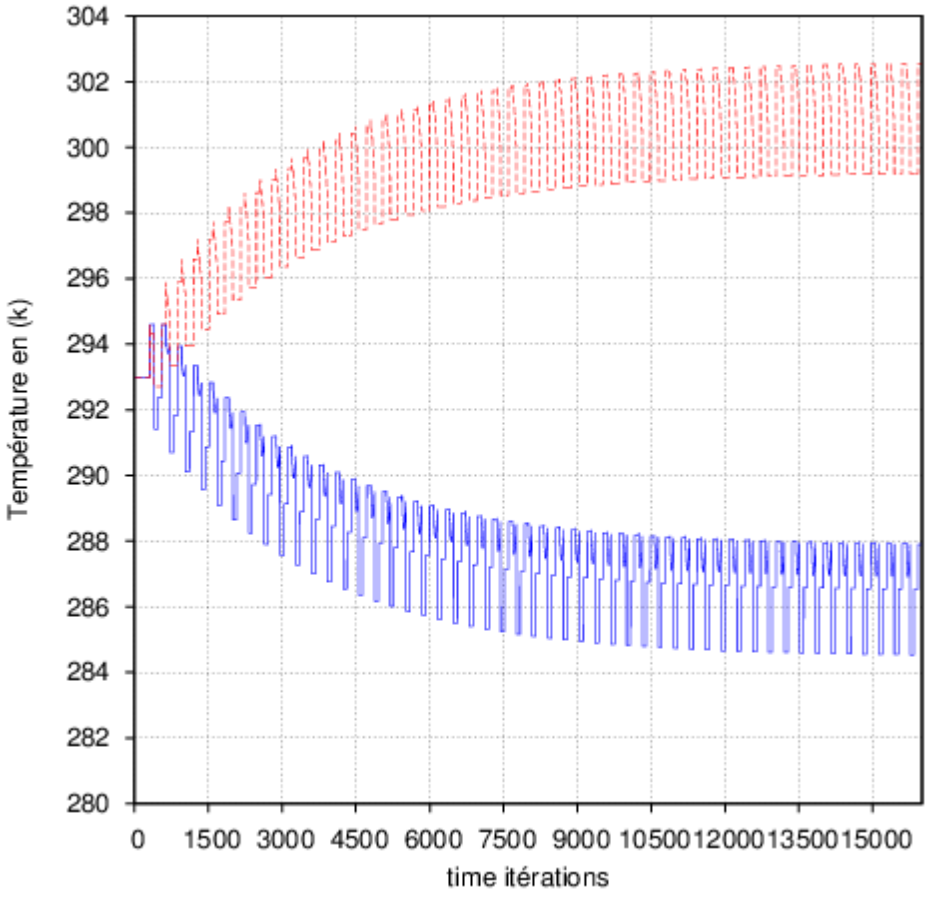

Figure 5.12: Time evolution of Temperature of both sides within the regenerator

"Fig 5.13" shows the temperature evolution computed in both sides versus number of cycles. At the beginning the gadolinium plates and water are initially at constant temperature (293 K), then the temperature of hot source increase while the temperature of cold source decrease during the evolution of cycles. It can be seen that The maximum temperature span obtained by numerical simulation at the end of 50 cycle is 13°C. this value depends on the cycle operating conditions, for this case the temperature span is predicted for operating frequency equal to 0.5 Hz, the parameter which determine the working speed of system.

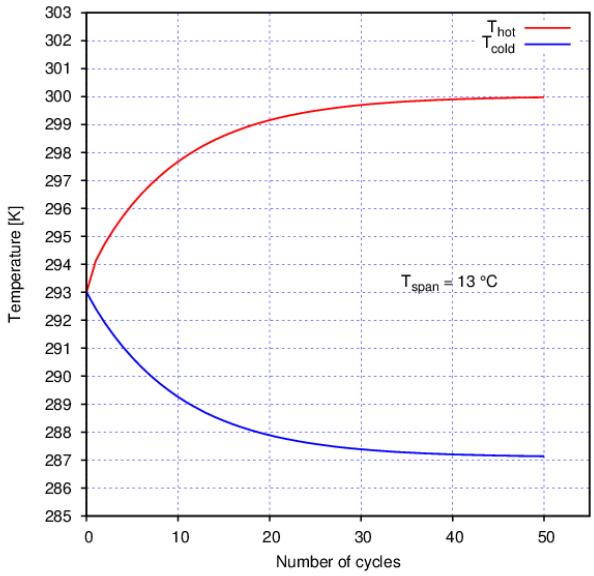

Figure 5.13: temperature evolution versus number of cycles

In order to optimize the system geometry, the influence of micro-channels thickness on the no load temperature span has been simulated and it was found through simulation results shown in "Fig 5.14". It can be seen that the temperature span between the both sources decrease when the thickness of fluid increase, so the optimum microchannels thickness is around 0.1 and 0.3 mm.

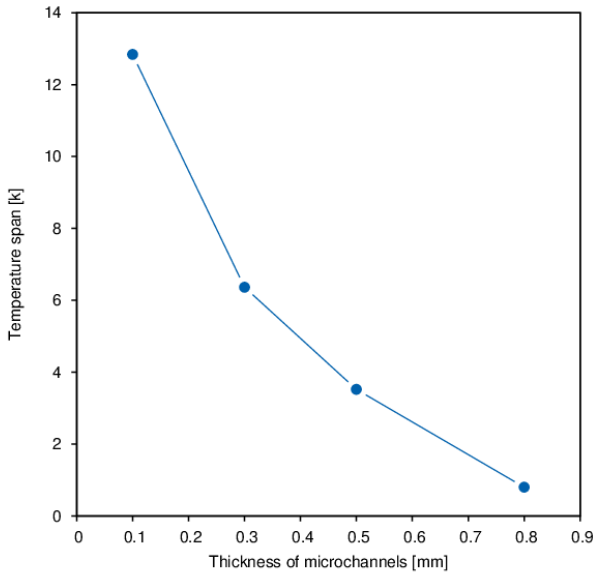

Figure 5.14: Effect of the thickness of the fluid on the difference of T.

The energy supplied by the system is an essential quantity. The energy provided by the magnetocaloric material for each cycle is expressed as:

$$Q_s^{Magnetization} = m_s C_s \sum_{i=2}^{Nt} \sum_{i=1}^{Nx} \delta_{i,j}^{Magnetization} \tag{5.11}$$

$$Q_s^{Demagnetization} = m_s C_s \sum_{i=2}^{Nt} \sum_{i=1}^{Nx} \delta_{i,j}^{Demagnetization} \tag{5.12}$$

Where Δ(i,j) represents the temperature difference between two successive instants for a point marked by the index j. “Fig 5.15” gives the profile of this energy. The red curve corresponds to what we call the hot energy produced during the magnetization phase. Similarly, the blue curve corresponds to the cold energy produced during the demagnetization phase.

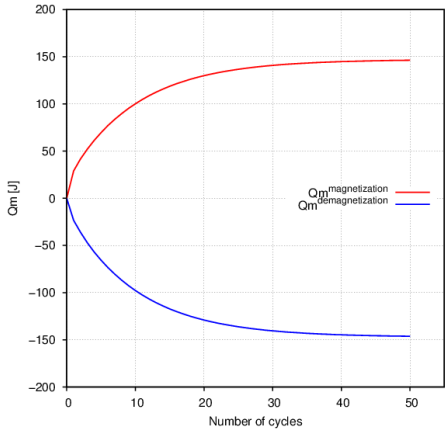

Figure 5.15: Profile of the energy produced by the magnetocaloric material

5.8.3 conclusion

Working on the prototype of magnetic refrigeration allowed us to forge a first experience on a complete magnetic refrigeration system. Numerous scientific, technical and practical difficulties were revealed during its realization. We discovered the problem linked to the coupling of magnetic and thermal phenomena. The operating temperature has a great influence on the quantities obtained by the simulations such as induction in the material or the torque, by the dependence of the magnetic permeability of the active material on temperature. The work on this prototype also showed the difficulties in terms of mechanical assembly. The goal being to have the strongest possible field variation, this leads to large amplitude force variations.

Appendix B. Flowchart of the numerical model of AMR cycle.

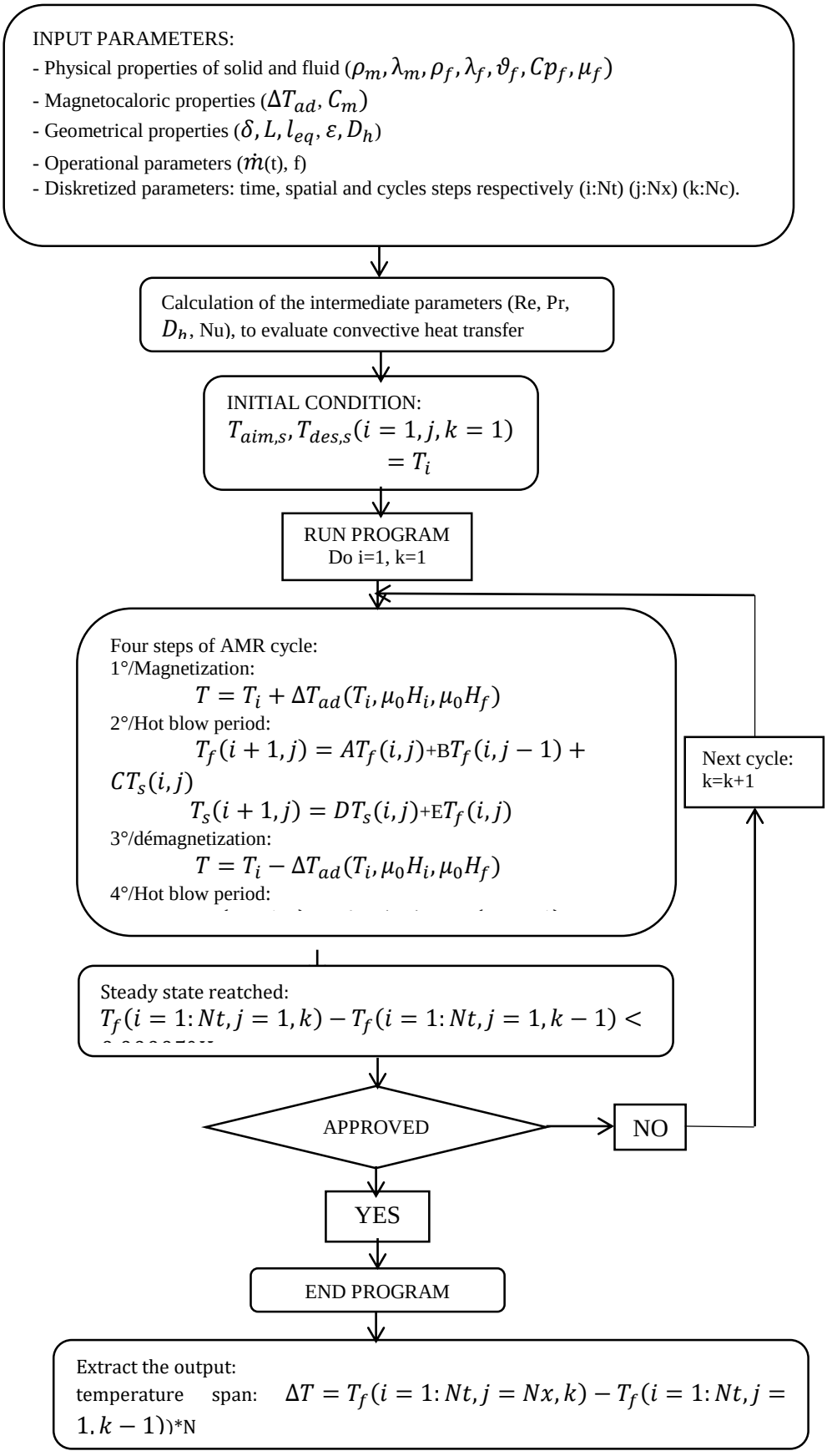

Flowchart of the AMR cycle numerical model.

General conclusion

Make progress and understand the physical process of magnetic refrigeration, requires a combination of several areas of research, starting with the characterization of giant materials to the numerical modeling of heat and mass transfer, in addition to the development of prototype design with its magnetic source. The results given along this dissertation can be summarized in three major parts.

In the first part, we report a detailed theoretical study dealing with the magnetic and thermal features of the intermetallic compound $AlFe_2B_2$ close to room temperature. The magnetocaloric properties in terms of both adiabatic temperature (ΔT_{ad}) and magnetic entropy (ΔS_{mag}) changes were determined using the Monte Carlo approach, while the thermodynamic performances were simulated according to the active magnetic refrigeration (AMR) model. $AlFe_2B_2$ based compounds are favorable because they consist of abundant light elements. The obtained results underline the promising applications in magnetic refrigeration of the $AlFe_2B_2$ intermetallic compound and its derivatives. Furthermore, our findings suggest new approach to provide a complete study from magnetocaloric effect to the application phase by using numerical tools.

In the second part, Perovskites manganites have been considered as promising candidates to replace intermetallic alloys for magnetic cooling applications. The challenge for perovskites manganites is that they do not simultaneously exhibit high magnetic entropy change and high adiabatic temperature change. The main objective of this part of thesis was the combination of experimental and numerical simulation to investigate the structural, magnetic, magnetocaloric and cooling properties of new composite based manganite. In this sense Perovskite manganite (1-x)$La_{0.6}Ca_{0.4}MnO_3$/xMn_2O_3 ($x = 0, 0.05, 0.1, 0.15, 0.20$) composites were prepared by solid state reaction method. X-ray diffraction measurements were used to confirm the crystal structure and the average crystallite size of samples. Their magnetic, magnetocaloric and heat capacity properties display a second order magnetic phase transition at $260K$. The maximum magnetic entropy change was found to be 5.33 J/kgK for $x = 0.1$ of Mn_2O_3 under $5T$. The relative cooling power (RCP) was found ($235J/kg$) to largely exceed the reported experimental

values in early works for similar materials. In addition, the RCP of the mother alloy is enhanced by more than 20% under $32kOe$ without affecting the Curie temperature that remains approximately constant around $260K$. Our results suggest that the addition of Mn_2O_3 could be useful for the enhancement of the LCMO refrigerant capacity without affecting the Curie temperature.

The third part of this thesis outline the work carried out on the study of magnetic refrigeration systems. To make the link with research on magnetocaloric materials, this system will make it possible to test these materials in real conditions and to study the influencing parameters. It is a linear system whose field is created by permanent magnets in the form of a halbach cylinder.

Appendix A

The Effect of PEG additive on the morphology and magnetocaloric properties in $La_{0.6}Ca_{0.4}MnO_3$.

The present appendix present the magnetic and magnetocaloric properties of the $La_{0,6}Ca_{0.4}MnO_3$. Perovskite manganite $La_{0,6}Ca_{0.4}MnO_3$ Nanomaterials were prepared by a modified Pechini sol– gel process followed by high temperature sintering. Polyethylene glycol (PEG-4000) was used to control the particle size and morphology of the materials. X-ray diffraction measurements were used to confirm the crystal structure of samples. Their magnetic, magnetocaloric display a second order magnetic phase transition around 190 K. The maximum magnetic entropy change was found to be 2.3 J/kg K under 3T. The relative cooling power (RCP) was found (135 J/kg).

A.0.1 Material preparation structural Characterization

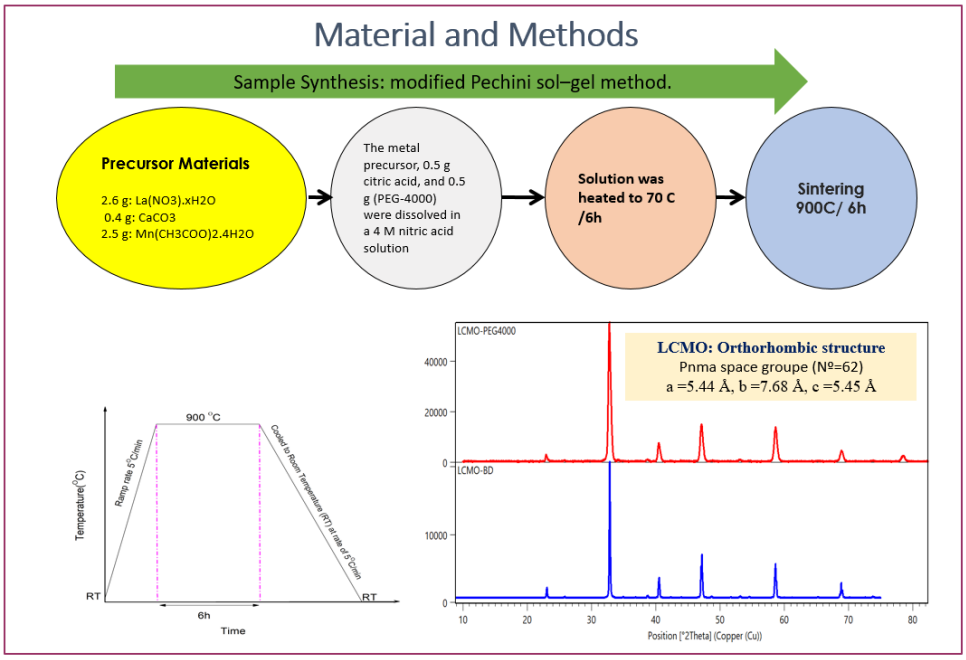

Figure A.1: Material preparation and structural Characterization

A.0.2 Structural Characterization: Morphology and composition

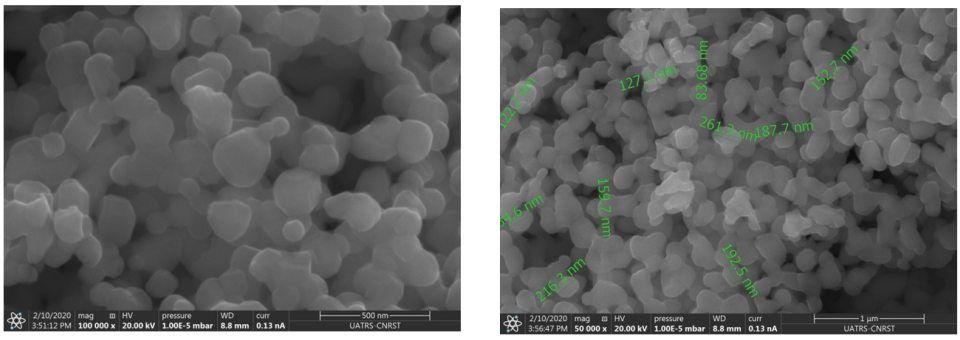

Figure A.2: SEM and TEM micrographs of particles at different magnifications synthesized using PEG 4000.

A.0.3 Magnetic and magnetocaloric properties

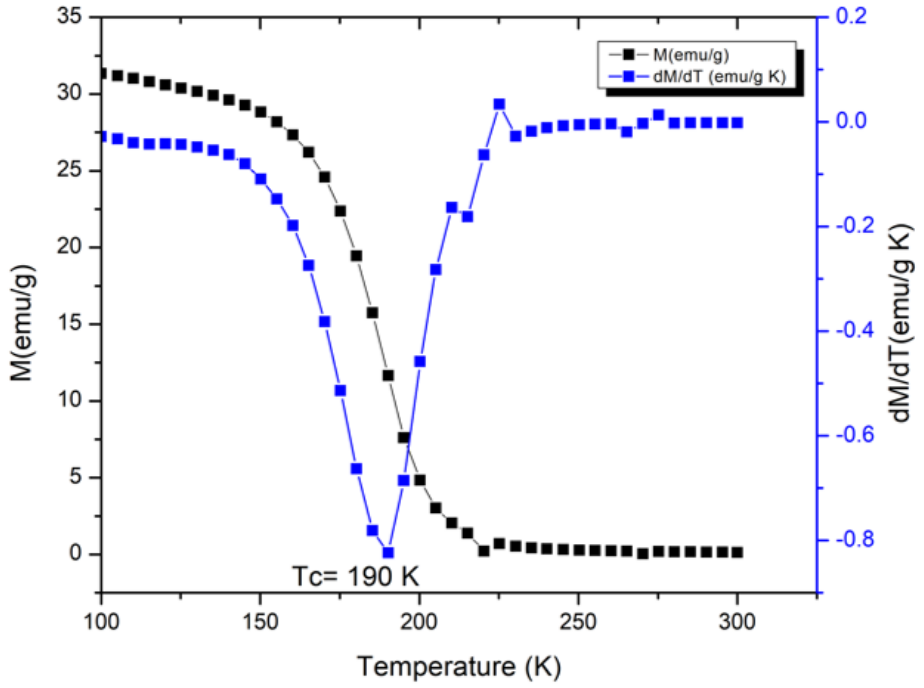

Figure A.3: M-T curve for the synthesized LCMO at 500 Oe applied field

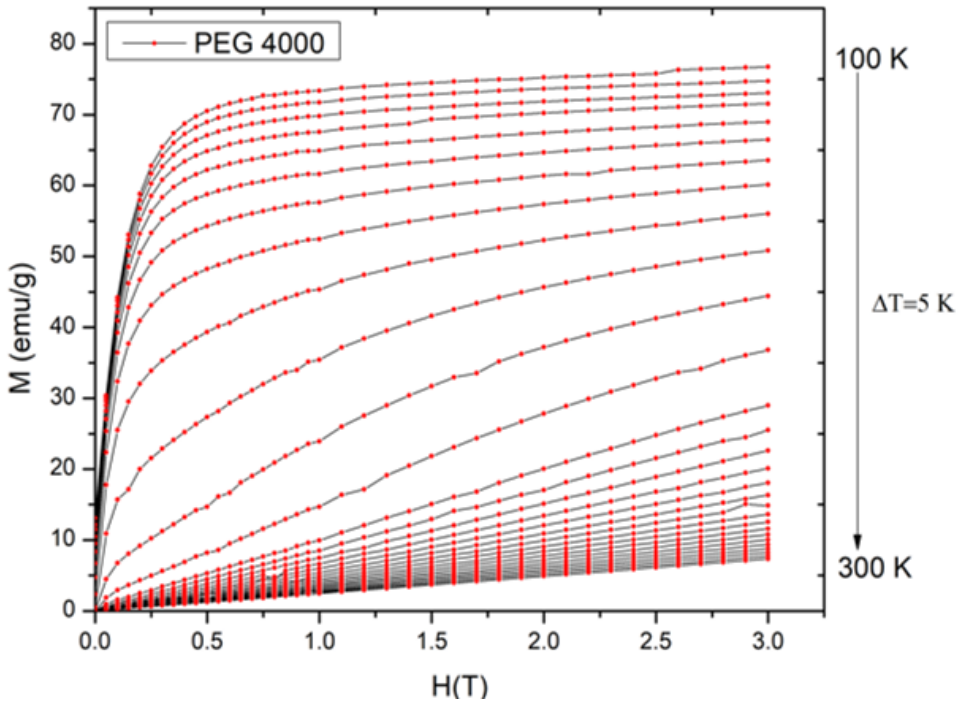

Figure A.4: Isothermal magnetization (M–H) measured from 100 to 300 K, LCMO-PEG 4000

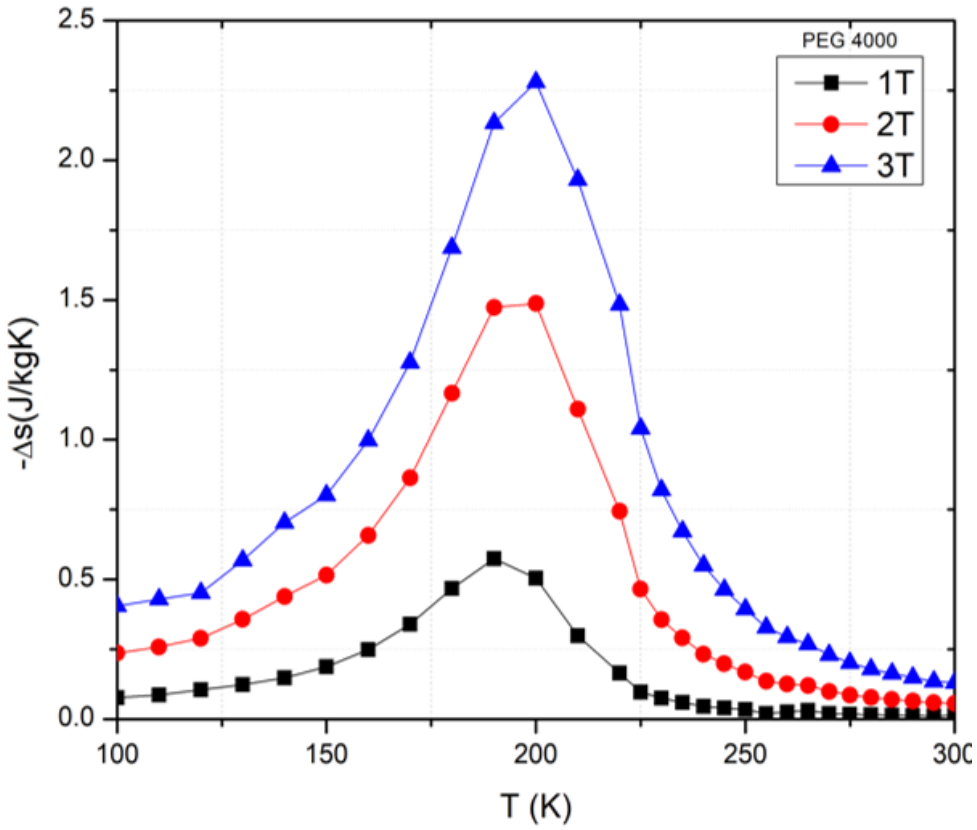

Figure A.5: Temperature dependence of the magnetic entropy change change for LCMO-PEG4000 calculated at various external field

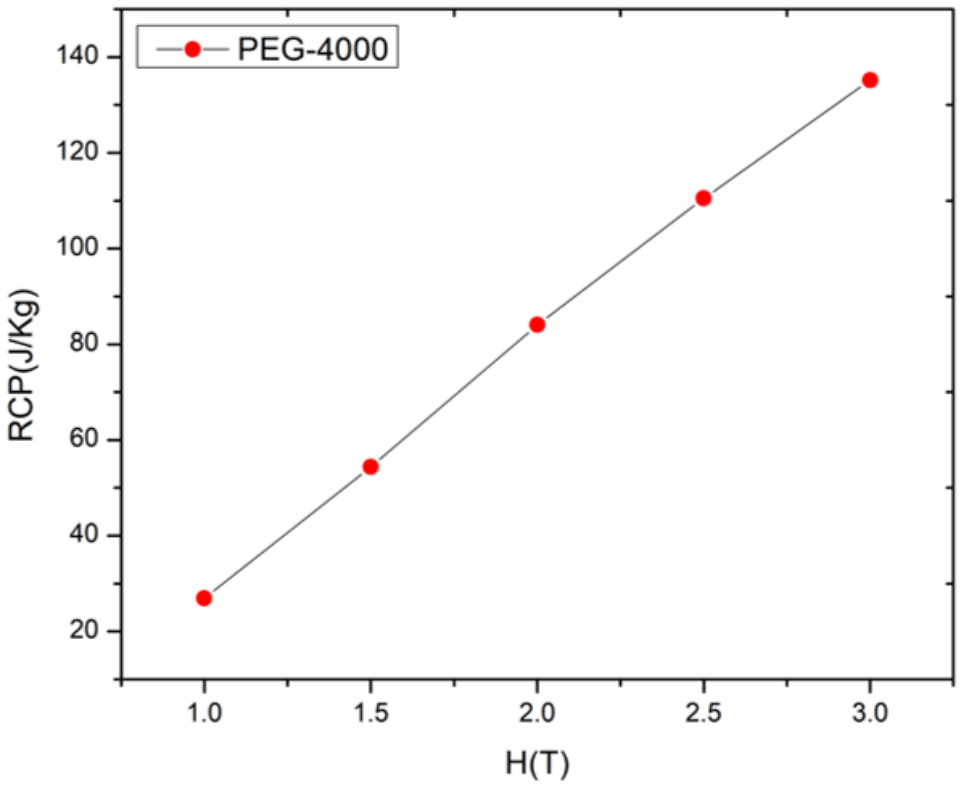

Figure A.6: The calculated RCP values for LCMO-PEG4000

A.0.4 Conclusion

In summary, magnetocaloric properties were obtained for La0.6Ca0.4MnO3 via a modified sol–gel method. In this study, PEG-4000 was shown to control morphology and magnetocaloric properties of the LCMO Nanomaterials. The structure and morphology were investigated using XRD, TEM and SEM. Magnetic measurements revealed that the nanoparticles undergo a second order magnetic transition with the PM–FM transition. The maximum change in magnetic entropy was found to be 2.3 J/kgK at 190 K, the relative cooling power (RCP) that is used to evaluate magnetic refrigeration properties was determined to be 135 J/kg for a field change of 0–3 T.

Appendix B

Magnetic, magnetocaloric of rare earth (R= Eu, Pr) doped perovskite manganites $La_{0.5}R_{0.1}Ca_{0.4}MnO_3$

The present appendix present the magnetic and magnetocaloric properties of the $La_{0.5}R_{0.1}Ca_{0.4}MnO_3$ (R=La, Eu, Pr). Perovskite manganite $La_{0.5}R_{0.1}Ca_{0.4}MnO_3$ (R=La, Eu, Pr) Nanomaterials were prepared by solid state reaction.

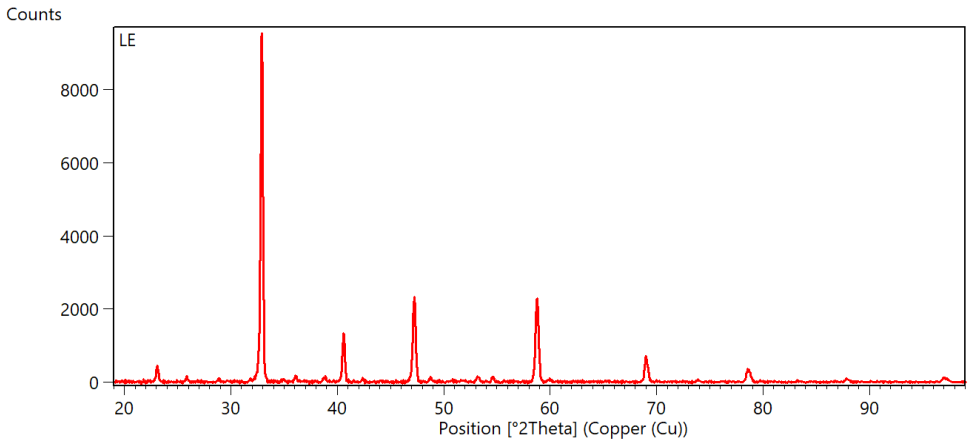

Figure B.1: XRD patterns LECMO

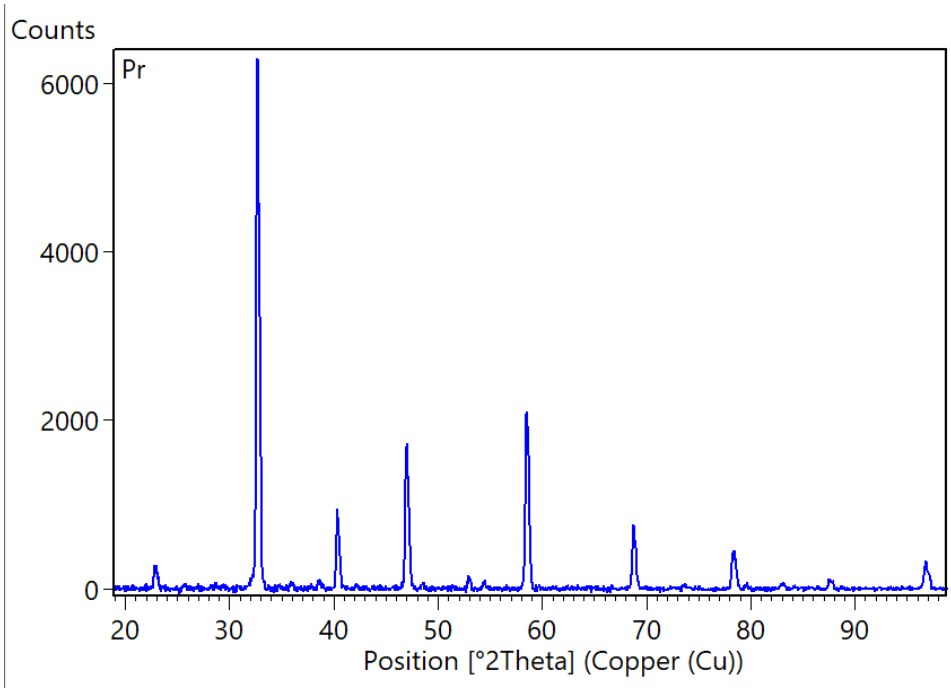

Figure B.2: XRD patterns LPCMO

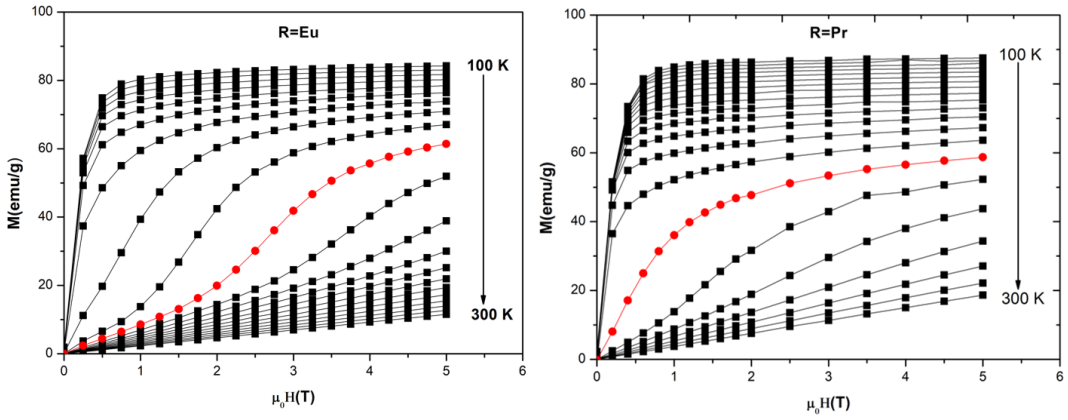

Figure B.3: Isothermal magnetization (M–H) measured from 100 to 300 K for LECMO (R=Eu) and LPCMO (R=Pr)

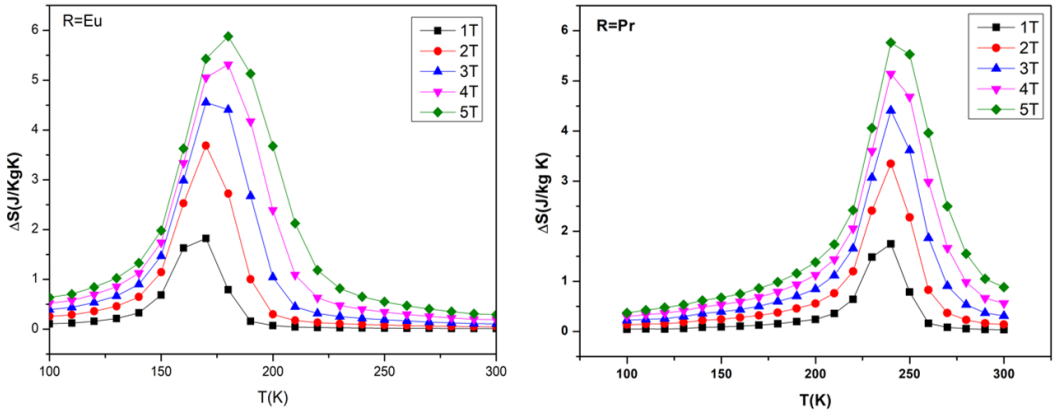

Figure B.4: Magnetic entropy change for LECMO (R=Eu) and LPCMO (R=Pr)

Bibliography

[1] J. Barclay and W. Steyert, "Active magnetic regenerator-uspatent 4332135," 1982.

[2] A. Kitanovski, J. Tušek, U. Tomc, U. Plaznik, M. Ožbolt, and A. Poredoš, "Magnetocaloric energy conversion, green energy and technology," *Cham, Switzerland: Springer International Publishing*, 2015.

[3] T. Gottschall, K. P. Skokov, M. Fries, A. Taubel, I. Radulov, F. Scheibel, D. Benke, S. Riegg, and O. Gutfleisch, "Making a cool choice: The materials library of magnetic refrigeration," *Advanced Energy Materials*, vol. 9, no. 34, p. 1901322, 2019.

[4] D. Rowe, "Thermoelectrics, an environmentally-friendly source of electrical power," *Renewable energy*, vol. 16, no. 1-4, pp. 1251–1256, 1999.

[5] S. L. Garrett and T. J. Hofler, "Thermoacoustic refrigeration," 1991.

[6] A. Allouhi, T. Kousksou, A. Jamil, and Y. Zeraouli, "Modeling of a thermal adsorber powered by solar energy for refrigeration applications," *Energy*, vol. 75, pp. 589–596, 2014.

[7] J. Shi, D. Han, Z. Li, L. Yang, S.-G. Lu, Z. Zhong, J. Chen, Q. Zhang, and X. Qian, "Electrocaloric cooling materials and devices for zero-global-warming-potential, high-efficiency refrigeration," *Joule*, vol. 3, no. 5, pp. 1200–1225, 2019.

[8] F. Bruederlin, L. Bumke, C. Chluba, H. Ossmer, E. Quandt, and M. Kohl, "Elastocaloric cooling on the miniature scale: a review on materials and device engineering," *Energy Technology*, vol. 6, no. 8, pp. 1588–1604, 2018.

[9] T. Gottschall, A. Gràcia-Condal, M. Fries, A. Taubel, L. Pfeuffer, L. Mañosa, A. Planes, K. P. Skokov, and O. Gutfleisch, "A multicaloric cooling cycle that exploits thermal hysteresis," *Nature Materials*, vol. 17, no. 10, pp. 929–934, 2018.

[10] A. Kitanovski, "Energy applications of magnetocaloric materials," *Advanced Energy Materials*, vol. 10, no. 10, p. 1903741, 2020.

[11] V. Pecharsky and K. Gschneidner Jr, "Effect of alloying on the giant magnetocaloric effect of gd5 (si2ge2)," *Journal of Magnetism and Magnetic Materials*, vol. 167, no. 3, pp. L179–L184, 1997.

[12] O. Tegus, E. Brück, K. Buschow, and F. De Boer, "Transition-metal-based magnetic refrigerants for room-temperature applications," *Nature*, vol. 415, no. 6868, pp. 150–152, 2002.

[13] H. Wada and Y. Tanabe, "Giant magnetocaloric effect of mnas 1- x sb x," *Applied physics letters*, vol. 79, no. 20, pp. 3302–3304, 2001.

[14] F. Wang, Y.-F. Chen, G.-J. Wang, and B.-G. Shen, "The effect of mn substitution in lafe11. 7si1. 3 compound on the magnetic properties and magnetic entropy changes," *Journal of Physics D: Applied Physics*, vol. 36, no. 1, p. 1, 2002.

[15] A. Fujita, S. Fujieda, Y. Hasegawa, and K. Fukamichi, "Itinerant-electron metamagnetic transition and large magnetocaloric effects in la (fe x si 1- x) 13 compounds and their hydrides," *Physical Review B*, vol. 67, no. 10, p. 104416, 2003.

[16] F.-x. Hu, B.-g. Shen, J.-r. Sun, G.-j. Wang, and Z.-h. Cheng, "Very large magnetic entropy change near room temperature in lafe 11.2 co 0.7 si 1.1," *Applied Physics Letters*, vol. 80, no. 5, pp. 826–828, 2002.

[17] M. Balli, D. Fruchart, and D. Gignoux, "Optimization of la (fe, co) 13- xsix based compounds for magnetic refrigeration," *Journal of Physics: Condensed Matter*, vol. 19, no. 23, p. 236230, 2007.

[18] M. Balli, S. Jandl, P. Fournier, and A. Kedous-Lebouc, "Advanced materials for magnetic cooling: Fundamentals and practical aspects," *Applied Physics Reviews*, vol. 4, no. 2, 2017.

[19] T. Krenke, E. Duman, M. Acet, E. F. Wassermann, X. Moya, L. Mañosa, and A. Planes, "Inverse magnetocaloric effect in ferromagnetic ni–mn–sn alloys," *Nature materials*, vol. 4, no. 6, pp. 450–454, 2005.

[20] M.-H. Phan and S.-C. Yu, "Review of the magnetocaloric effect in manganite materials," *Journal of Magnetism and Magnetic Materials*, vol. 308, no. 2, pp. 325–340, 2007.

[21] M. C. Flemings, "Materials Science and Engineering - Its Past and Its Future.," *Transactions of the Iron and Steel Institute of Japan*, vol. 26, no. 2, pp. 93–100, 1986.

[22] M. C. Flemings and W. Callister, "Materials science and engineering: An introduction (2nd edition)," *Materials & Design*, vol. 26, no. 2, p. 59, 1991.

[23] L. Néel, "Some new results on antiferromagnetism and ferromagnetism," *Reviews of Modern Physics*, vol. 25, no. 1, p. 58, 1953.

[24] D. C. Jiles and D. L. Atherton, "Theory of ferromagnetic hysteresis," *Journal of magnetism and magnetic materials*, vol. 61, no. 1-2, pp. 48–60, 1986.

[25] E. Wohlfarth, "Hard magnetic materials," *Advances in physics*, vol. 8, no. 30, pp. 87–224, 1959.

[26] A. Inoue and F. Kong, "Soft magnetic materials," 2020.

[27] R. Hadimani, Y. Melikhov, J. Snyder, and D. Jiles, "Determination of curie temperature by arrott plot technique in gd5(sixge1x)4 for x¿0.575," *Journal of Magnetism and Magnetic Materials*, vol. 320, no. 20, pp. e696 – e698, 2008. Proceedings of the 18th International Symposium on Soft Magnetic Materials.

[28] A. Arrott, "Criterion for ferromagnetism from observations of magnetic isotherms," *Physical Review*, vol. 108, no. 6, p. 1394, 1957.

[29] H. M. Rietveld, "A profile refinement method for nuclear and magnetic structures," *Journal of applied Crystallography*, vol. 2, no. 2, pp. 65–71, 1969.

[30] R. M'Nassri, "Élaboration et caractérisations physiques des manganites à effet magnetocalorique.," 2013.

[31] P. Weiss and A. Piccard, "Le phénomène magnétocalorique," 1917.

[32] E. Warburg, "Magnetische untersuchungen," *Annalen der Physik*, vol. 249, no. 5, pp. 141–164, 1881.

[33] A. M. Tishin and Y. I. Spichkin, *The magnetocaloric effect and its applications*. CRC Press, 2016.

[34] P. Weiss and R. Forrer, "Aimantation et phénomène magnétocalorique du nickel," *AnPh*, vol. 10, no. 5, pp. 153–213, 1925.

[35] V. Pecharsky and K. Gschneidner Jr, "Some common misconceptions concerning magnetic refrigerant materials," *Journal of Applied Physics*, vol. 90, no. 9, pp. 4614–4622, 2001.

[36] A. Tishin, "Magnetocaloric effect in strong magnetic fields," *Cryogenics*, vol. 30, no. 2, pp. 127–136, 1990.

[37] O. Sari, M. Balli, G. Trottet, P. Bonhote, P. Egolf, C. Muller, J. Heitzler, and S. Bour, "Initial results of a test-bed magnetic refrigeration machine with practical running conditions," 2009.

[38] V. K. Pecharsky and K. A. Gschneidner Jr, "Giant magnetocaloric effect in gd 5 (si 2 ge 2)," *Physical review letters*, vol. 78, no. 23, p. 4494, 1997.

[39] J. Tušek, A. Kitanovski, I. Prebil, and A. Poredoš, "Dynamic operation of an active magnetic regenerator (amr): numerical optimization of a packed-bed amr," *International Journal of Refrigeration*, vol. 34, no. 6, pp. 1507–1517, 2011.

[40] J. Roudaut, A. Kedous-Lebouc, J.-P. Yonnet, and C. Muller, "Numerical analysis of an active magnetic regenerator," *International journal of refrigeration*, vol. 34, no. 8, pp. 1797–1804, 2011.

[41] T. F. Petersen, N. Pryds, A. Smith, J. Hattel, H. Schmidt, and H.-J. H. Knudsen, "Two-dimensional mathematical model of a reciprocating room-temperature active magnetic regenerator," *International Journal of Refrigeration*, vol. 31, no. 3, pp. 432–443, 2008.

[42] P. Nikkola, C. Mahmed, M. Balli, and O. Sari, "1d model of an active magnetic regenerator," *International journal of refrigeration*, vol. 37, pp. 43–50, 2014.

[43] K. Engelbrecht, J. Tušek, K. K. Nielsen, A. Kitanovski, C. R. Bahl, and A. Poredoš, "Improved modelling of a parallel plate active magnetic regenerator," *Journal of Physics D: Applied Physics*, vol. 46, no. 25, p. 255002, 2013.

[44] H. Bouchekara and M. Nahas, "Magnetic refrigeration technology at room temperature," in *Trends in Electromagnetism-From Fundamentals to Applications*, InTech, 2012.

[45] C. Aprea, A. Greco, A. Maiorino, and C. Masselli, "A two-dimensional investigation about magnetocaloric regenerator design: parallel plates or packed bed?," in *Journal of Physics: Conference Series*, vol. 796, p. 012018, IOP Publishing, 2017.

[46] T. F. Petersen, K. Engelbrecht, C. R. Bahl, B. Elmegaard, N. Pryds, and A. Smith, "Comparison between a 1d and a 2d numerical model of an active magnetic regenerative refrigerator," *Journal of Physics D: Applied Physics*, vol. 41, no. 10, p. 105002, 2008.

[47] K. K. Nielsen, J. Tusek, K. Engelbrecht, S. Schopfer, A. Kitanovski, C. R. H. Bahl, A. Smith, N. Pryds, and A. Poredos, "Review on numerical modeling of active magnetic regenerators for room temperature applications," *International Journal of Refrigeration*, vol. 34, no. 3, pp. 603–616, 2011.

[48] U. Legait, F. Guillou, A. Kedous-Lebouc, V. Hardy, and M. Almanza, "An experimental comparison of four magnetocaloric regenerators using three different materials," *International Journal of Refrigeration*, vol. 37, pp. 147–155, 2014.

[49] J. Tušek, A. Kitanovski, S. Zupan, I. Prebil, and A. Poredoš, "A comprehensive experimental analysis of gadolinium active magnetic regenerators," *Applied Thermal Engineering*, vol. 53, no. 1, pp. 57–66, 2013.

[50] J. R. Gómez, R. F. Garcia, J. C. Carril, and M. R. Gómez, "A review of room temperature linear reciprocating magnetic refrigerators," *Renewable and Sustainable Energy Reviews*, vol. 21, pp. 1–12, 2013.

[51] A. Tishin, "Handbook of magnetic materials," *Noth Holland: Amstendam*, vol. 12, 1999.

[52] Z. Wang, Q. Xu, J. Sun, J. Pan, and H. Zhang, "Room temperature magnetocaloric effect of la-deficient bulk perovskite manganite la0. 7mno3- δ," *Physica B: Condensed Matter*, vol. 406, no. 8, pp. 1436–1440, 2011.

[53] M. Wali, R. Skini, M. Khlifi, E. Dhahri, and E. Hlil, "A giant magnetocaloric effect with a tunable temperature transition close to room temperature in na-deficient la 0.8 na 0.2- x x mno 3 manganites," *Dalton Transactions*, vol. 44, no. 28, pp. 12796–12803, 2015.

[54] W. Zhong, W. Chen, W. Ding, N. Zhang, Y. Du, and Q. Yan, "Magnetocaloric properties of na-substituted perovskite-type manganese oxides," *Solid state communications*, vol. 106, no. 1, pp. 55–58, 1998.

[55] V. Franco, J. Blázquez, J. Ipus, J. Law, L. Moreno-Ramírez, and A. Conde, "Magnetocaloric effect: From materials research to refrigeration devices," *Progress in Materials Science*, vol. 93, pp. 112–232, 2018.

[56] S. Das and T. Dey, "Magnetic entropy change in polycrystalline la1- xkxmno3 perovskites," *Journal of alloys and compounds*, vol. 440, no. 1-2, pp. 30–35, 2007.

[57] Y. Regaieg, L. Sicard, J. Monnier, M. Koubaa, S. Ammar-Merah, and A. Cheikhrouhou, "Magnetic and magnetocaloric properties of la0. 85 (na1- xkx) 0.15 mno3 ceramics produced by reactive spark plasma sintering," *Journal of Applied Physics*, vol. 115, no. 17, p. 17A917, 2014.

[58] I. Kamilov, A. Gamzatov, A. Batdalov, A. Mankevich, and I. Korsakov, "Heat capacity and magnetocaloric properties of la 1- x k x mno 3 manganites," *Physics of the Solid State*, vol. 52, no. 4, pp. 789–793, 2010.

[59] A. Aliev, A. Gamzatov, A. Batdalov, A. Mankevich, and I. Korsakov, "Magnetocaloric properties of la 1- x kxmno 3 manganites," *Journal of Experimental and Theoretical Physics*, vol. 112, no. 3, pp. 460–468, 2011.

[60] J. Makni-Chakroun, W. Cheikhrouhou-Koubaa, M. Koubaa, and A. Cheikhrouhou, "Impact of a small amount of vacancy in both lanthanum and calcium on the physical properties of nanocrystalline la0. 7ca0. 3mno3 manganite," *Journal of Alloys and Compounds*, vol. 650, pp. 421–429, 2015.

[61] M. Pekala, V. Drozd, J.-F. Fagnard, and P. Vanderbemden, "Magnetocaloric effect in nano-and polycrystalline manganites la0. 5ca0. 5mno3," *Journal of alloys and compounds*, vol. 507, pp. 350–355, 2010.

[62] M. Pekala, V. Drozd, J.-F. Fagnard, P. Vanderbemden, and M. Ausloos, "Magnetocaloric effect in nano-and polycrystalline manganite *la_{0.7}ca_{0.3}mno_3*," *arXiv preprint arXiv:0710.5705*, 2007.

[63] D. Hou, Y. Bai, J. Xu, G. Tang, and X. Nie, "Magnetic entropy change in la0. 67-xca0. 33mno3," *Journal of alloys and compounds*, vol. 384, no. 1-2, pp. 62–66, 2004.

[64] M. Khlifi, M. Bejar, O. E. Sadek, E. Dhahri, M. Ahmed, and E. Hlil, "Structural, magnetic and magnetocaloric properties of the lanthanum deficient in la0. 8ca0. 2- x xmno3 (x= 0–0.20) manganites oxides," *Journal of alloys and compounds*, vol. 509, no. 27, pp. 7410–7415, 2011.

[65] R. Skini, A. Omri, M. Khlifi, E. Dhahri, and E. Hlil, "Large magnetocaloric effect in lanthanum-deficiency manganites la0. 8- x xca0. 2mno3 (0.00 x 0.20) with a first-order magnetic phase transition," *Journal of magnetism and magnetic materials*, vol. 364, pp. 5–10, 2014.

[66] S. Ghorai, R. Skini, D. Hedlund, P. Ström, and P. Svedlindh, "Field induced crossover in critical behaviour and direct measurement of the magnetocaloric properties of la 0.4 pr 0.3 ca 0.1 sr 0.2 mno 3," *Scientific Reports*, vol. 10, no. 1, pp. 1–13, 2020.

[67] R. Skini, S. Ghorai, P. Ström, S. Ivanov, D. Primetzhofer, and P. Svedlindh, "Large room temperature relative cooling power in la0. 5pr0. 2ca0. 1sr0. 2mno3," *Journal of Alloys and Compounds*, vol. 827, p. 154292, 2020.

[68] A. Gamzatov, A. Aliev, P. Yen, K. Hau, K. E. Kamaludinova, T. Thanh, N. Dung, and S.-C. Yu, "Magnetocaloric effect in la0. 7- xprxsr0. 3mno3 manganites: Direct and indirect measurements," *Journal of Magnetism and Magnetic Materials*, vol. 474, pp. 477–481, 2019.

[69] A. Dinesen, S. Linderoth, and S. Mørup, "Direct and indirect measurement of the magnetocaloric effect in a la0. 6ca0. 4mno3 ceramic perovskite," *Journal of magnetism and magnetic materials*, vol. 253, no. 1-2, pp. 28–34, 2002.

[70] G. Lin, Q. Wei, and J. Zhang, "Direct measurement of the magnetocaloric effect in la0. 67ca0. 33mno3," *Journal of magnetism and magnetic materials*, vol. 300, no. 2, pp. 392–396, 2006.

[71] K. Riahi, I. Messaoui, A. Ezaami, F. Cugini, M. Solzi, W. Cheikhrouhou-Koubaa, and A. Cheikhrouhou, "Adiabatic temperature change, magnetic entropy change and critical behavior near the ferromagnetic–paramagnetic phase transition in la0. 7 (ca, sr) 0.3 mno3 perovskite," *Phase Transitions*, vol. 91, no. 7, pp. 691–702, 2018.

[72] I. Kamilov, A. Gamzatov, A. Aliev, A. Batdalov, A. Aliverdiev, S. B. Abdulvagidov, O. Melnikov, O. Y. Gorbenko, and A. Kaul, "Magnetocaloric effect in la1- xagymno3

(y x): direct and indirect measurements," *Journal of Physics D: Applied Physics*, vol. 40, no. 15, p. 4413, 2007.

[73] J. Dhahri, A. Dhahri, M. Oumezzine, E. Dhahri, M. Said, and H. Vincent, "Magnetocaloric properties of cd-substituted perovskite-type manganese oxides," *Journal of alloys and compounds*, vol. 467, no. 1-2, pp. 44–47, 2009.

[74] J. Yang, Y. Lee, and Y. Li, "Magnetocaloric effect of electron-doped manganite la 0.9 te 0.1 mn o 3," *Journal of Applied Physics*, vol. 102, no. 3, p. 033913, 2007.

[75] T. Izgi, V. Kolat, N. Bayri, H. Gencer, and S. Atalay, "Structural, magnetic and magnetocaloric properties of the compound la0. 94bi0. 06mno3," *Journal of magnetism and magnetic materials*, vol. 372, pp. 112–116, 2014.

[76] V. S. Kolat, S. Atalay, T. Izgi, H. Gencer, and N. Bayri, "Structural, magnetic, and magnetocaloric properties of la 1- x bi x mno 3 (x= 0.01, 0.03, 0.06, 0.1, 0.2) compounds," *Metallurgical and Materials Transactions A*, vol. 46, no. 6, pp. 2591–2597, 2015.

[77] R. Li, W. Tong, L. Pi, and Y. Zhang, "Coexistence of large magnetoresistance and magnetocaloric effect in monovalent doped manganite la0. 5ca0. 4li0. 1mno3," *Journal of magnetism and magnetic materials*, vol. 355, pp. 276–281, 2014.

[78] C. Hao, B. Zhao, Y. Huang, G. Kuang, and Y. Sun, "A-site-disorder-dependent magnetocaloric properties in the mono-valent-metal doped la0. 7ca0. 3mno3 manganites," *Journal of Alloys and Compounds*, vol. 509, no. 19, pp. 5877–5881, 2011.

[79] A. A.-B. Ammar, W. Cheikhrouhou-Koubaa, M. Koubaa, S. Nowak, H. Lecoq, L. Sicard, S. Ammar, and A. Cheikhrouhou, "Effect of sodium substitution on the physical properties of sol–gel made la0. 65ca0. 35mno3 ceramics," *Materials Chemistry and Physics*, vol. 148, no. 3, pp. 751–758, 2014.

[80] T. Ho, N. Dang, T.-L. Phan, D. Yang, B. Lee, and S. Yu, "Magnetic and magnetocaloric properties in la0. 7ca0. 3- xnaxmno3 exhibiting first-order and second-order

magnetic phase transitions," *Journal of Alloys and Compounds*, vol. 676, pp. 305–312, 2016.

[81] S. C. Maatar, R. M'Nassri, W. C. Koubaa, M. Koubaa, and A. Cheikhrouhou, "Structural, magnetic and magnetocaloric properties of la0.8Ca0.2-xNaxMnO3 manganites (00.2)," *Journal of Solid State Chemistry*, vol. 225, pp. 83–88, 2015.

[82] M. Bejar, R. Dhahri, E. Dhahri, M. Balli, and E. K. Hlil, "Large magnetic entropy change at room temperature in La0.7Ca0.3-xKxMnO3," *Journal of Alloys and Compounds*, vol. 442, no. 1-2 SPEC. ISS., pp. 136–138, 2007.

[83] V. Kolat, U. Esturk, T. Izgi, H. Gencer, and S. Atalay, "The structural, magnetic and magnetocaloric properties of la0. 67ca0. 33- xmgxmno3 (x= 0, 0.02, 0.05, 0.1, 0.2, 0.33) compounds," *Journal of Alloys and Compounds*, vol. 628, pp. 1–8, 2015.

[84] M. Gutiérrez, J. Olivares, I. Betancourt, and F. Morales, "Structural and magnetic properties of la 0.72 (ca 1- x sr x) 0.28 mno 3 (x= 0 to 1) manganites," *Journal of Materials Research*, vol. 24, no. 4, pp. 1585–1589, 2009.

[85] M. Islam, D. Hanh, F. Khan, M. Hakim, D. Minh, N. Hoang, N. Hai, and N. Chau, "Giant magneto-caloric effect around room temperature at moderate low field variation in la0. 7 (ca1- xsrx) 0.3 mno3 perovskites," *Physica B: Condensed Matter*, vol. 404, no. 16, pp. 2495–2498, 2009.

[86] C. R. Bahl, D. Velazquez, K. K. Nielsen, K. Engelbrecht, K. B. Andersen, R. Bulatova, and N. Pryds, "High performance magnetocaloric perovskites for magnetic refrigeration," *Applied Physics Letters*, vol. 100, no. 12, p. 121905, 2012.

[87] A. Coşkun, E. Taşarkuyu, A. Irmak, and S. Aktürk, "High magnetic entropy change in la0. 70ca0. 21ag0. 09mno3 compound," *Journal of Alloys and Compounds*, vol. 669, pp. 217–223, 2016.

[88] W. Tang, W. Lu, X. Luo, B. Wang, X. Zhu, W. Song, Z. Yang, and Y. Sun, "Size-induced changes of structural, magnetic and magnetocaloric properties of la0. 7ca0. 2ba0. 1mno3," *Physica B: Condensed Matter*, vol. 405, no. 12, pp. 2733–2741, 2010.

[89] N. Nedelko, S. Lewinska, A. Pashchenko, I. Radelytskyi, R. Diduszko, E. Zubov, W. Lisowski, J. Sobczak, K. Dyakonov, A. Ślawska-Waniewska, *et al.*, "Magnetic properties and magnetocaloric effect in la0. 7sr0. 3- xbixmno3 manganites," *Journal of Alloys and Compounds*, vol. 640, pp. 433–439, 2015.

[90] S. Barik and R. Mahendiran, "Effect of bi doping on magnetic and magnetocaloric properties of la 0.7- x bi x sr 0.3 mno 3 (0 x 0.4)," *Journal of Applied Physics*, vol. 107, no. 9, p. 093906, 2010.

[91] S. Das and T. Dey, "Above room temperature magnetocaloric properties of la0. 7ba0. 3- znazmno3 compounds," *Materials Chemistry and Physics*, vol. 108, no. 2-3, pp. 220–226, 2008.

[92] Y. Regaieg, M. Koubaa, W. C. Koubaa, A. Cheikhrouhou, L. Sicard, S. Ammar-Merah, and F. Herbst, "Structure and magnetocaloric properties of la0. 8ag0. 2-xkxmno3 perovskite manganites," *Materials Chemistry and Physics*, vol. 132, no. 2-3, pp. 839–845, 2012.

[93] A. Zaidi, Z. Mohamed, J. Dhahri, E. Hlil, T. Alharbi, and M. Zaïdi, "Structural, magnetic and magnetocaloric properties of polycrystalline la 0.67 ba 0.33- x zn x mno 3 (x= 0.15 and 0.2) manganites," *Applied Physics A*, vol. 122, no. 4, p. 421, 2016.

[94] A. Dhahri, J. Dhahri, and E. Dhahri, "Effect of potassium doping on physical properties of perovskites la0. 8cd0. 2- xkxmno3," *Journal of alloys and compounds*, vol. 489, no. 1, pp. 9–12, 2010.

[95] A. Tozri, E. Dhahri, and E. Hlil, "Magnetic transition and magnetic entropy changes of la0. 8pb0. 1mno3 and la0. 8pb0. 1na0. 1mno3," *Materials Letters*, vol. 64, no. 19, pp. 2138–2141, 2010.

[96] L. H. Thomas, "The calculation of atomic fields," *Mathematical Proceedings of the Cambridge Philosophical Society*, vol. 23, no. 5, p. 542–548, 1927.

[97] W. Kohn and L. J. Sham, "Self-consistent equations including exchange and correlation effects," *Phys. Rev.*, vol. 140, pp. A1133–A1138, Nov 1965.

[98] D. Shechtman, I. Blech, D. Gratias, and J. W. Cahn, "Metallic phase with long-range orientational order and no translational symmetry," *Phys. Rev. Lett.*, vol. 53, pp. 1951–1953, Nov 1984.

[99] J. M. Seminario, "An introduction to density functional theory in chemistry," in *Modern Density Functional Theory* (J. Seminario and P. Politzer, eds.), vol. 2 of *Theoretical and Computational Chemistry*, pp. 1 – 27, Elsevier, 1995.

[100] C. Daniel, "Density functional theories and coordination chemistry," in *Reference Module in Chemistry, Molecular Sciences and Chemical Engineering*, Elsevier, 2020.

[101] M. Born and R. Oppenheimer, "Zur quantentheorie der molekeln," *Annalen der physik*, vol. 389, no. 20, pp. 457–484, 1927.

[102] H. J. Schnitzer, "Hartree approximation in relativistic field theory," *Phys. Rev. D*, vol. 10, pp. 2042–2046, Sep 1974.

[103] P. Hohenberg and W. Kohn, "Density functional theory (dft)," *Phys. Rev*, vol. 136, p. B864, 1964.

[104] E. H. Lieb and B. Simon, "The thomas-fermi theory of atoms, molecules and solids," *Advances in Mathematics*, vol. 23, no. 1, pp. 22 – 116, 1977.

[105] W. Kohn and L. J. Sham, "Self-consistent equations including exchange and correlation effects," *Physical review*, vol. 140, no. 4A, p. A1133, 1965.

[106] S. Kurth, M. Marques, M. Lüders, and E. K. U. Gross, "Local density approximation for superconductors," *Phys. Rev. Lett.*, vol. 83, pp. 2628–2631, Sep 1999.

[107] S. S. A. Naji, "A theoretical study on physical properties of 2d hexagonal nanostructured materials," 2014.

[108] J. M. Yeomans, *Statistical mechanics of phase transitions*. Clarendon Press, 1992.

[109] K. G. Wilson, "Renormalization group and critical phenomena. i. renormalization group and the kadanoff scaling picture," *Physical review B*, vol. 4, no. 9, p. 3174, 1971.

[110] J. Oitmaa, "High temperature series expansions for griffiths' model of 3he-4he mixtures," *Physics Letters A*, vol. 33, no. 4, pp. 230–231, 1970.

[111] K. Binder, D. Heermann, L. Roelofs, A. J. Mallinckrodt, and S. McKay, "Monte carlo simulation in statistical physics," *Computers in Physics*, vol. 7, no. 2, pp. 156–157, 1993.

[112] N. De Oliveira and P. Von Ranke, "Theoretical aspects of the magnetocaloric effect," *Physics Reports*, vol. 489, no. 4-5, pp. 89–159, 2010.

[113] S. Ivanov, "Multiferroic complex metal oxides: Main features of preparation, structure, and properties," in *Science and Technology of Atomic, Molecular, Condensed Matter & Biological Systems*, vol. 2, pp. 163–238, Elsevier, 2012.

[114] L. Reimer, "Scanning electron microscopy: Physics of image formation and microanalysis, second edition," *Measurement Science and Technology*, vol. 11, pp. 1826–1826, nov 2000.

[115] M. Balli, O. Sari, L. Zamni, C. Mahmed, and J. Forchelet, "Implementation of la (fe, co) 13- xsix materials in magnetic refrigerators: Practical aspects," *Materials Science and Engineering: B*, vol. 177, no. 8, pp. 629–634, 2012.

[116] J. Tušek, A. Kitanovski, S. Zupan, I. Prebil, and A. Poredoš, "A comprehensive experimental analysis of gadolinium active magnetic regenerators," *Applied Thermal Engineering*, vol. 53, no. 1, pp. 57–66, 2013.

[117] J. Liu, J. Moore, K. Skokov, M. Krautz, K. Löwe, A. Barcza, M. Katter, and O. Gutfleisch, "Exploring la (fe, si) 13-based magnetic refrigerants towards application," *Scripta Materialia*, vol. 67, no. 6, pp. 584–589, 2012.

[118] M. Phejar, V. Paul-Boncour, and L. Bessais, "Structural and magnetic properties of magnetocaloric lafe13–xsix compounds synthesized by high energy ball-milling," *Intermetallics*, vol. 18, no. 12, pp. 2301–2307, 2010.

[119] N. Pierunek, Z. Śniadecki, M. Werwiński, B. Wasilewski, V. Franco, and B. Idzikowski, "Normal and inverse magnetocaloric effects in structurally disordered laves phase y1-xgdxco2 (0 x 1) compounds," *Journal of Alloys and Compounds*, vol. 702, pp. 258–265, 2017.

[120] J. Herbst and J. Croat, "Neodymium-iron-boron permanent magnets," *Journal of magnetism and magnetic materials*, vol. 100, no. 1-3, pp. 57–78, 1991.

[121] W. Jeitschko, "The crystal structure of fe2alb2," *Acta Crystallographica Section B: Structural Crystallography and Crystal Chemistry*, vol. 25, no. 1, pp. 163–165, 1969.

[122] J. Cedervall, M. S. Andersson, T. Sarkar, E. K. Delczeg-Czirjak, L. Bergqvist, T. C. Hansen, P. Beran, P. Nordblad, and M. Sahlberg, "Magnetic structure of the magnetocaloric compound alfe2b2," *Journal of Alloys and Compounds*, vol. 664, pp. 784–791, 2016.

[123] X. Tan, P. Chai, C. M. Thompson, and M. Shatruk, "Magnetocaloric effect in alfe2b2: toward magnetic refrigerants from earth-abundant elements," *Journal of the American Chemical Society*, vol. 135, no. 25, pp. 9553–9557, 2013.

[124] K. Kádas, D. Iuşan, J. Hellsvik, J. Cedervall, P. Berastegui, M. Sahlberg, U. Jansson, and O. Eriksson, "Alm2b2 (m= cr, mn, fe, co, ni): a group of nanolaminated materials," *Journal of Physics: Condensed Matter*, vol. 29, no. 15, p. 155402, 2017.

[125] Q. Du, G. Chen, W. Yang, Z. Song, M. Hua, H. Du, C. Wang, S. Liu, J. Han, Y. Zhang, *et al.*, "Magnetic properties of alfe2b2 and cemn2si2 synthesized by melt spinning of stoichiometric compositions," *Japanese Journal of Applied Physics*, vol. 54, no. 5, p. 053003, 2015.

[126] M. ElMassalami, D. d. S. Oliveira, and H. Takeya, "On the ferromagnetism of

alfe2b2," *Journal of magnetism and magnetic materials*, vol. 323, no. 16, pp. 2133–2136, 2011.

[127] P. Chai, S. A. Stoian, X. Tan, P. A. Dube, and M. Shatruk, "Investigation of magnetic properties and electronic structure of layered-structure borides alt2b2 (t= fe, mn, cr) and alfe2–xmnxb2," *Journal of Solid State Chemistry*, vol. 224, pp. 52–61, 2015.

[128] M. Toyoda, H. Akai, K. Sato, and H. Katayama-Yoshida, "Electronic structures of (zn, tm) o (tm: V, cr, mn, fe, co, and ni) in the self-interaction-corrected calculations," *Physica B: Condensed Matter*, vol. 376, pp. 647–650, 2006.

[129] J. Cedervall, L. Häggström, T. Ericsson, and M. Sahlberg, "Mössbauer study of the magnetocaloric compound alfe 2 b 2," *Hyperfine Interactions*, vol. 237, no. 1, pp. 1–8, 2016.

[130] H. Akai. http://sham.phys.sci.osaka-u.ac.jp/kkr/.

[131] A. W. V.L. Mouruzzi, J.F. Janak, "Calculated properties of metals," *Pergramon, New York*, 1998.

[132] A. I. Liechtenstein, M. Katsnelson, V. Antropov, and V. Gubanov, "Local spin density functional approach to the theory of exchange interactions in ferromagnetic metals and alloys," *Journal of Magnetism and Magnetic Materials*, vol. 67, no. 1, pp. 65–74, 1987.

[133] A. Liechtenstein, M. Katsnelson, and V. Gubanov, "Exchange interactions and spin-wave stiffness in ferromagnetic metals," *Journal of Physics F: Metal Physics*, vol. 14, no. 7, p. L125, 1984.

[134] L. Li, D. Huo, Z. Qian, and K. Nishimura, "Study of the critical behaviour and magnetocaloric effect in dyfeal," *Intermetallics*, vol. 46, pp. 231–235, 2014.

[135] S. Hirt, F. Yuan, Y. Mozharivskyj, and H. Hillebrecht, "Alfe2–x co x b2 (x= 0–0.30): Tc tuning through co substitution for a promising magnetocaloric material realized

by spark plasma sintering," *Inorganic chemistry*, vol. 55, no. 19, pp. 9677–9684, 2016.

[136] Y. Chiba, A. Smaili, C. Mahmed, M. Balli, and O. Sari, "Thermal investigations of an experimental active magnetic regenerative refrigerator operating near room temperature," *International journal of refrigeration*, vol. 37, pp. 36–42, 2014.

[137] A. El Boukili, N. Tahiri, E. Salmani, H. Ez-Zahraouy, M. Hamedoun, A. Benyoussef, M. Balli, and O. Mounkachi, "Magnetocaloric and cooling properties of the intermetallic compound alfe2b2 in an amr cycle system," *Intermetallics*, vol. 104, pp. 84–89, 2019.

[138] J. Lee, M. Song, K. Cho, B. Cho, and C. Nam, "Magnetocaloric properties of alfe 2 b 2 including paramagnetic impurities of al 13 fe 4," *Journal of the Korean Physical Society*, vol. 73, no. 10, pp. 1555–1560, 2018.

[139] R. Barua, B. Lejeune, B. Jensen, L. Ke, R. McCallum, M. Kramer, and L. Lewis, "Enhanced room-temperature magnetocaloric effect and tunable magnetic response in ga-and ge-substituted alfe2b2," *Journal of Alloys and Compounds*, vol. 777, pp. 1030–1038, 2019.

[140] B. T. Lejeune, *Composition-Lattice Interactions in Ternary Transition-Metal Boride Ferromagnetic Systems*. PhD thesis, Northeastern University, 2019.

[141] C. Energy and T. Transformations, *Energy Technology Perspectives 2017*. 2017.

[142] C. Zimm, A. Jastrab, A. Sternberg, V. Pecharsky, K. Gschneidner, M. Osborne, and I. Anderson, "Description and performance of a near-room temperature magnetic refrigerator," in *Advances in cryogenic engineering*, pp. 1759–1766, Springer, 1998.

[143] B. Yu, M. Liu, P. W. Egolf, and A. Kitanovski, "A review of magnetic refrigerator and heat pump prototypes built before the year 2010," *International Journal of Refrigeration*, vol. 33, no. 6, pp. 1029–1060, 2010.

[144] R. M'Nassri, N. C. Boudjada, and A. Cheikhrouhou, "Nearly constant magnetic entropy change involving the enhancement of refrigerant capacity in (La0.6Ba0.2Sr0.2MnO3)1-x/(Co2O3)x composite," *Ceramics International*, vol. 42, no. 6, pp. 7447–7454, 2016.

[145] Y. H. Huang, C. H. Yan, F. Luo, W. Song, Z. M. Wang, and C. S. Liao, "Large enhancement in room-temperature magnetoresistance and dramatic decrease in resistivity in La0.7Ca0.3MnO3-Ag composites," *Applied Physics Letters*, vol. 81, no. 1, pp. 76–78, 2002.

[146] A. Mleiki, R. M'nassri, W. Cheikhrouhou-Koubaa, A. Cheikhrouhou, and E. K. Hlil, "Structural characterization, magnetic, magnetocaloric properties and critical behavior in lacunar La0.5Eu0.2Ba0.20.1MnO3 nanoparticles," *Journal of Alloys and Compounds*, vol. 727, pp. 1203–1212, 2017.

[147] S. Estemirova, V. Mitrofanov, S. Uporov, and G. Kozhina, "Structural and magnetic properties, magnetocaloric effect in (La 0.7 Pr 0.3) 0.8 Sr 0.2 Mn 0.9 Ti 0.1 O 3±δ (δ=0.03, 0.02, 0.03)," *Journal of Alloys and Compounds*, vol. 751, pp. 96–106, 2018.

[148] H. Baaziz, A. Tozri, E. Dhahri, and E. K. Hlil, "Magnetocaloric properties of La0.67Sr0.33MnO3 tunable by particle size and dimensionality," *Chemical Physics Letters*, vol. 691, pp. 355–359, 2018.

[149] P. T. Phong, N. V. Khiem, N. V. Dai, D. H. Manh, L. V. Hong, and N. X. Phuc, "Low-field magnetoresistance of (1 - x)La0.7Ca0.3MnO3 + xAg composites," *Journal of Alloys and Compounds*, vol. 484, no. 1-2, pp. 12–16, 2009.

[150] M. H. Phan, S. C. Yu, N. H. Hur, and Y. H. Jeong, "Large magnetocaloric effect in a La0.7Ca0.3MnO 3 single crystal," *Journal of Applied Physics*, vol. 96, no. 2, pp. 1154–1158, 2004.

[151] X. Bohigas, J. Tejada, M. L. Marínez-Sarrión, S. Tripp, and R. Black, "Magnetic and calorimetric measurements on the magnetocaloric effect in La0.6Ca0.4MnO3," *Journal of Magnetism and Magnetic Materials*, vol. 208, no. 1, pp. 85–92, 2000.

[152] V. Moshnyaga, B. Damaschke, O. Shapoval, A. Belenchuk, J. Faupel, O. I. Lebedev, J. Verbeeck, G. Van Tendeloo, M. Mücksch, V. Tsurkan, R. Tidecks, and K. Samwer, "Structural phase transition at the percolation threshold in epitaxial (La0.7Ca0.3MnO3)1-x: (MgO)x nanocomposite films," *Nature Materials*, vol. 2, no. 4, pp. 247–252, 2003.

[153] R. Nag, B. Sarkar, and S. Pal, "Griffiths phase and magnetocaloric behaviour in electron doped Ca0.85Sm0.15MnO3," *Journal of Alloys and Compounds*, vol. 749, pp. 385–390, 2018.

[154] R. Nag, B. Sarkar, and S. Pal, "Magnetic field dependence of Griffith phase and magnetocaloric effect in Ca0.85Dy0.15MnO3," *Journal of Magnetism and Magnetic Materials*, vol. 449, pp. 21–24, 2018.

[155] R. M. Nassri, "Élaboration et Caractérisations physiques des manganites à effet magnetocalorique . To cite this version : HAL Id : tel-01560653 Elaboration et Caractérisations Physiques des Manganites à Effet Magnétocalorique," 2017.

[156] E. G. Vrieland, "The activity and selectivity of Mn3+ and Mn4+ in lanthanum calcium manganites for the oxidation of ammonia," *Journal of Catalysis*, vol. 32, no. 3, pp. 415–428, 1974.

[157] H. Y. Hwang, S. W. Cheong, P. G. Radaelli, M. Marezio, and B. Batlogg, "Lattice effects on the magnetoresistance in doped LaMnO3," *Physical Review Letters*, vol. 75, no. 5, pp. 914–917, 1995.

[158] S. Yahyaoui, S. Kallel, and H. T. Diep, "Magnetic properties of perovskites La0.7Sr0.3 Mn 0.73+ Mn 0.3-x4+ TixO3: Monte Carlo simulation versus experiments," *Journal of Magnetism and Magnetic Materials*, vol. 416, pp. 441–448, 2016.

[159] M. H. Tsui, D. T. Dryer, A. A. El-Gendy, and E. E. Carpenter, "Enhanced near room temperature magnetocaloric effect in La0.6Ca0.4MnO3 for magnetic refrigeration application," *RSC Advances*, vol. 7, no. 74, pp. 46589–46593, 2017.

[160] P. Schiffer, A. P. Ramirez, W. Bao, and S. W. Cheong, "Low temperature magnetoresistance and the magnetic phase diagram of La1-xCaxMnO3," *Physical Review Letters*, vol. 75, no. 18, pp. 3336–3339, 1995.

[161] M. A. Hamad, "Magnetocaloric effect in La0.7Sr0.3MnO3/Ta2O5 composites," *Journal of Advanced Ceramics*, vol. 2, no. 3, pp. 213–217, 2013.

[162] R. Jha, S. K. Singh, A. Kumar, and V. P. Awana, "Room temperature magnetic entropy change and magnetoresistance in La 0.70(Ca 0.30-xSr x)MnO 3:Ag 10% (x=0.0-0.10)," *Journal of Magnetism and Magnetic Materials*, vol. 324, no. 18, pp. 2849–2853, 2012.

[163] M. Nasri, J. Khelifi, M. Triki, E. Dhahri, and E. K. Hlil, "Impact of CuO phase on magnetocaloric and magnetotransport properties of La0.6Ca0.4MnO3 ceramic composites," *Journal of Alloys and Compounds*, vol. 678, pp. 427–433, 2016.

[164] V. M. Andrade, R. J. Vivas, S. S. Pedro, J. C. Tedesco, A. L. Rossi, A. A. Coelho, D. L. Rocco, and M. S. Reis, "Magnetic and magnetocaloric properties of La0.6Ca0.4MnO3 tunable by particle size and dimensionality," *Acta Materialia*, vol. 102, pp. 49–55, 2016.

[165] A. Gómez, E. Chavarriaga, I. Supelano, C. A. Parra, and O. Morán, "Tuning the magnetocaloric properties of La0.7Ca0.3MnO3 manganites through Ni-doping," *Physics Letters, Section A: General, Atomic and Solid State Physics*, vol. 382, no. 13, pp. 911–919, 2018.

[166] A. Nasri, S. Zouari, M. Ellouze, E. K. Hlil, and F. Elhalouani, "X-ray diffraction, magnetic and magnetocaloric properties of La0.6Ca0.4Mn1xFexO3 (0 x 0.3) manganites prepared by the sol-gel method," *European Physical Journal Plus*, vol. 129, no. 8, pp. 1–10, 2014.

[167] M. Nasri, M. Triki, E. Dhahri, and E. K. Hlil, "Critical behavior in Sr-doped manganites La0.6Ca 0.4-xSrxMnO3," *Journal of Alloys and Compounds*, vol. 546, pp. 84–91, 2013.

[168] N. Assoudi, I. Walha, K. Nouri, E. Dhahri, and L. Bessais, "Effect of synthesis route on structural, magnetic and magnetocaloric aspects and critical behavior of La0.6Ca0.3Ag0.1MnO3," *Journal of Alloys and Compounds*, vol. 753, pp. 282–291, 2018.

[169] S. D. Bhame, J. F. Fagnard, M. Pekala, P. Vanderbemden, and B. Vertruyen, "La 0.7Ca 0.3MnO 3 / Mn 3O 4 composites: Does an insulating secondary phase always enhance the low field magnetoresistance of manganites," *Journal of Applied Physics*, vol. 111, no. 6, pp. 0–4, 2012.

[170] S. Pal, A. Banerjee, S. Chatterjee, A. K. Nigam, B. K. Chaudhuri, and H. D. Yang, "Transport and magnetic properties of La0.7Pb 0.3Mno3+ x Ag (x = 0-20 wt%) nanocomposites," *Journal of Applied Physics*, vol. 94, no. 5, pp. 3485–3491, 2003.

[171] M. Balli, *Etude structurale et magnétique en vue de la mise en oeuvre de nouveaux matériaux à effet magnétocalorique géant.* PhD thesis, 2007.

[172] A. El Boukili, N. Tahiri, E. Salmani, H. Ez-Zahraouy, M. Hamedoun, A. Benyoussef, M. Balli, and O. Mounkachi, "Magnetocaloric and cooling properties of the intermetallic compound alfe2b2 in an amr cycle system," *Intermetallics*, vol. 104, pp. 84–89, 2019.

[173] H. Xu, Z. Qu, S. Zhao, J. Mei, F. Quan, and N. Yan, "Different crystal-forms of one-dimensional mno2 nanomaterials for the catalytic oxidation and adsorption of elemental mercury," *Journal of hazardous materials*, vol. 299, pp. 86–93, 2015.

[174] F. E. Sesen, "Practical reduction of manganese oxide," *Journal of Chemical Technology and Applications*, vol. 01, no. 01, pp. 3–4, 2017.

[175] M. L. Craus, A. K. Islamov, E. M. Anitas, N. Cornei, and D. Luca, "Microstructural, magnetic and transport properties of La 0.5Pr0.2Pb0.3-xSrx MnO3 manganites," *Journal of Alloys and Compounds*, vol. 592, pp. 121–126, 2014.

[176] A. Selmi, R. M'nassri, W. Cheikhrouhou-Koubaa, N. C. Boudjada, and

A. Cheikhrouhou, "Influence of transition metal doping (fe, co, ni and cr) on magnetic and magnetocaloric properties of pr0. 7ca0. 3mno3 manganites," *Ceramics International*, vol. 41, no. 8, pp. 10177–10184, 2015.

[177] B. K. Banerjee, "On a generalised approach to first and second order magnetic transitions," 1964.

[178] M. Deschizeaux and G. Develey, "Équation magnétique d'état du gadolinium au voisinage du point de curie," *Journal de Physique*, vol. 32, no. 4, pp. 319–323, 1971.

[179] P. Zhang, P. Lampen, T. Phan, S. Yu, T. Thanh, N. Dan, V. Lam, H. Srikanth, and M. Phan, "Influence of magnetic field on critical behavior near a first order transition in optimally doped manganites: the case of la1- xcaxmno3 (0.2 x 0.4)," *Journal of magnetism and magnetic materials*, vol. 348, pp. 146–153, 2013.

[180] W. P. Labora, "p=1. 37 (&0. 04).," vol. 136, no. 6, 1964.

[181] V. K. Pecharsky, V. K. Pecharsky, K. A. Gschneidner, K. A. Gschneidner, A. O. Pecharsky, and A. M. Tishin, "Thermodynamics of the magnetocaloric effect," *Physical Review B - Condensed Matter and Materials Physics*, vol. 64, no. 14, pp. 1444061–14440613, 2001.

[182] A. T. Saito, T. Kobayashi, H. Fukuda, R. Arai, and H. Nakago, "Cooling Properties of Gd Alloys and La(Fe,Si)13-Based Compounds in Active Magnetic Refrigeration for Environmentally-Friendly Cooling Systems," *International Journal of Environmental Science and Development*, vol. 7, no. 5, pp. 335–339, 2016.

[183] S. V. Ovsyannikov, A. M. Abakumov, A. A. Tsirlin, W. Schnelle, R. Egoavil, J. Verbeeck, G. V. Tendeloo, K. V. Glazyrin, M. Hanfland, and L. Dubrovinsky, "Angewandte Communications Perovskite-like Mn 2 O 3 : A Path to New Manganites **," vol. 201208553, no. 278510, pp. 1494–1498, 2013.

[184] S. K. Çetin, M. Acet, M. Güneş, A. Ekicibil, and M. Farle, "Magnetocaloric effect in (La1-xSmx)0.67Pb0.33MnO3 (0 x 0.3) manganites near room temperature," *Journal of Alloys and Compounds*, vol. 650, pp. 285–294, 2015.

[185] K. E. MAALAM, "Propriétés magnétocaloriques des matériaux composites $(la_{0.7-x}nd_x)sr_{0.3}mno_3$/cuo, de l'élaboration à l'application de la réfrigération magnétique," 2016.

[186] R. Bjørk, K. K. Nielsen, C. R. Bahl, A. Smith, and A. C. Wulff, "Comparing superconducting and permanent magnets for magnetic refrigeration," *AIP Advances*, vol. 6, no. 5, p. 056205, 2016.

[187] K. Halbach, "Design of permanent multipole magnets with oriented rare earth cobalt material," *Nuclear instruments and methods*, vol. 169, no. 1, pp. 1–10, 1980.

[188] H. Li, W. Liu, and B. Li, "A sensing system of the halbach array permanent magnet spherical motor based on 3-d hall sensor," *Journal of Electrical Engineering & Technology*, vol. 13, no. 1, pp. 352–361, 2018.

[189] R. Bjørk, C. R. H. Bahl, A. Smith, D. Christensen, and N. Pryds, "An optimized magnet for magnetic refrigeration," *Journal of Magnetism and Magnetic Materials*, vol. 322, no. 21, pp. 3324–3328, 2010.

[190] R. Bjørk, C. R. H. Bahl, A. Smith, and N. Pryds, "Optimization and improvement of halbach cylinder design," *Journal of Applied Physics*, vol. 104, no. 1, p. 013910, 2008.

[191] S. Y. Dan'Kov, A. Tishin, V. Pecharsky, K. Gschneidner, *et al.*, "Magnetic phase transitions and the magnetothermal properties of gadolinium," *Physical Review B*, vol. 57, no. 6, p. 3478, 1998.

[192] F. Allab, *Etude et Conception D'un Dispositif De Refrigeration Magnetique Base Sur L'effet Magnetocalorique Geant*. PhD thesis, 2008.

[193] D. Chen, R. Murphy, V. Mei, F. Chen, J. Lue, and M. Lubell, "Performance analysis of reciprocating regenerative magnetic heat pumping," *STIN*, vol. 94, p. 35683, 1994.

Intermetallics 104 (2019) 84–89

Contents lists available at ScienceDirect

Intermetallics

journal homepage: www.elsevier.com/locate/intermet

Magnetocaloric and cooling properties of the intermetallic compound $AlFe_2B_2$ in an AMR cycle system

A. El Boukili[a,b,*], N. Tahiri[a], E. Salmani[a], H. Ez-Zahraouy[a,**], M. Hamedoun[b], A. Benyoussef[a,b,c], M. Balli[d], O. Mounkachi[a,***]

[a] Laboratory of Condensed Matter and Interdisciplinary Sciences, Faculty of Sciences-Mohammed V University in Rabat, P.O.Box 1014, Rabat, Morocco
[b] Materials and Nanomaterials Center, MAScIR Foundation, B.P. 10100, Rabat, Morocco
[c] Hassan II Academy of Science and Technology, Rabat, Morocco
[d] Institut Quantique, Université de Sherbrooke, J1K 2R1 Quebec, Canada

ARTICLE INFO

Keywords:
Magnetic refrigeration
Solid refrigerants
$AlFe_2B_2$ based compounds
AMR cycle
Heat transfer
Monte Carlo simulation
ab initio calculations

ABSTRACT

In this work, we report a detailed theoretical study dealing with the magnetic and thermal features of the intermetallic compound $AlFe_2B_2$ close to room temperature. The magnetocaloric properties in terms of both adiabatic temperature (ΔT_{ad}) and magnetic entropy (ΔS_{mag}) changes were determined using the Monte Carlo approach, while the thermodynamic performances were simulated according to the active magnetic refrigeration (AMR) model. Under a magnetic field changing from 0 to 5 T, the ΔS_{mag} and ΔT_{ad} reach maximum values of 7.75 J/kg K and 3.74 K close to 290 K, respectively, being in good agreement with previously reported experimental values. In contrast, the calculated relative cooling power (RCP) was found (480 J/kg) to largely exceed the reported experimental value in early works. On the other hand, the implementation of $AlFe_2B_2$ as a refrigerant in a 1T-AMR device would enable to generate a maximum no-load temperature span of about 10 K and a maximum cooling power of 50 W for a low operating frequency of 0.5 Hz. These findings unveil that the relatively cheaper $AlFe_2B_2$ compound and its derivatives could be a promising alternative to the rare earth-based alloys in magnetic refrigeration.

1. Introduction

The thermal energy derived from conventional techniques such as gas expansion system is no longer desirable because of their harmful effects on the environment, since the orientation towards clean and efficient technologies seems necessary. In this context, magnetic refrigeration based on the magnetocaloric effect (MCE) [1] is considered as a promising cooling technique that allows to fully eliminating the harmful synthetic refrigerant, usually used by standard refrigerators such as chlorofluorocarbons (CFCs), hydrofluorocarbons (HFCs) or hydrochlorofluorocarbons (HCFCs). In recent decades, new advanced solid magnetic refrigerants have been reported [2]. Some of among them were directly tested in functional magnetocaloric devices [3–5]. Also, following a parallel effort, innovative cooling devices have been built [2,6]. It is worth noting that from a practical point of view, the suitable magnetocaloric material must exhibit a large MCE under relatively low magnetic fields (< 2 T) that can be reached via permanent magnets.

Giant magnetocaloric compounds near room temperature, such as $Gd_5Si_{4-x}Ge_x$ [7], $LaFe_{13-x}Si_x$ [8,9], $Y_{0.4}Gd_{0.6}Co_2$ [10] and MnFeP(As, Ge) [11] are the subject of current research and development. In this study, we report results to the intermetallic compound $AlFe_2B_2$. The most well known application of transition metal borides such as $Nd_2Fe_{14}B$ is their utilization as permanent magnets in several domains [12]. In this paper, we are mainly interested by magnetothermal properties. Particularly, the $AlFe_2B_2$-Based compounds offer key advantages for application in magnetic refrigeration when compared with the reference gadolinium metal such as their low cost. In fact, for a large-scale commercialization

* Corresponding author. Laboratory of Condensed Matter and Interdisciplinary Sciences, Faculty of sciences-Mohammed V University in Rabat, P.O.Box 1014, Rabat, Morocco.
** Corresponding author. Laboratory of Condensed Matter and Interdisciplinary Sciences, Faculty of sciences-Mohammed V University in Rabat, P.O.Box 1014, Rabat, Morocco.
*** Corresponding author. Laboratory of Condensed Matter and Interdisciplinary Sciences, Faculty of sciences-Mohammed V University in Rabat, P.O.Box 1014, Rabat, Morocco.
E-mail addresses: elboukiliaicha@gmail.com (A. El Boukili), ezahamid@fsr.ac.ma (H. Ez-Zahraouy), o.mounkachi@gmail.com (O. Mounkachi).

https://doi.org/10.1016/j.intermet.2018.10.025
Received 6 March 2018; Received in revised form 9 August 2018; Accepted 30 October 2018
Available online 08 November 2018

Journal of Alloys and Compounds 859 (2020) 158392

Contents lists available at ScienceDirect

Journal of Alloys and Compounds

journal homepage: www.elsevier.com/locate/jalcom

A study of structural, magnetic and magnetocaloric properties of (1−x) $La_{0.6}Ca_{0.4}MnO_3/xMn_2O_3$ composite materials

A. El Boukili[a,b,*], O. Mounkachi[a], M. Hamedoun[b], P. Lachkar[c], E.K. Hlil[c], A. Benyoussef[d], M. Balli[e], H. Ez-Zahraouy[a]

[a] LaMCScI Laboratory, B.P. 1014, Faculty of science. Mohammed V University in Rabat, Morocco
[b] Materials and Nanomaterials Center, MAScIR Foundation, BP 10100 Rabat, Morocco
[c] Univ. Grenoble Alpes, CNRS, Grenoble INP, Institut Néel, 38000 Grenoble, France
[d] Hassan II Academy of Science and Technology, Rabat, Morocco
[e] AMEEC Team, LERMA, College of Engineering & Architecture, International University of Rabat, Parc Technopolis, Rocade de Rabat, Salé 11100, Morocco

ARTICLE INFO

Article history:
Received 29 June 2020
Received in revised form 24 November 2020
Accepted 15 December 2020
Available online 18 December 2020

Keywords:
Composites
Magnetic properties
Magnetocaloric effect
Refrigeration applications

ABSTRACT

Perovskite manganite (1−x)$La_{0.6}Ca_{0.4}MnO_3/xMn_2O_3$ (x = 0, 0.05. 0.1, 0.15, 0.20) composites were prepared by solid state reaction method. X-ray diffraction measurements were used to confirm the crystal structure and the average crystallite size of the samples. Their magnetic, magnetocaloric and heat capacity properties display a presence of second order magnetic phase transition at 260 K. The maximum magnetic entropy change was found to be 5.33 J/kgK for x = 0.1 of Mn_2O_3 under 5 T. The relative cooling power (RCP) was found (235 J/kg) to largely exceed that reported in early works for a similar family of materials. In addition, the RCP of the mother alloy is enhanced by more than 20% under 32 kOe without affecting the Curie temperature that remains approximately constant close to 260 K. Our results suggest that the addition of Mn_2O_3 could be useful for the enhancement of the LCMO refrigerant capacity without affecting the Curie temperature.

1. Introduction

Global demand for energy grows continuously. The international energy agency-energy perspectives have analysed the strategy to reduce the global energy consumption and CO_2 emissions, and reported that the largest energy savings potential is in heating and cooling demands, due to building envelope improvements and the utilization of energy efficient equipments [1]. As a response to these technological and environmental challenges, the orientation toward green technologies has become a necessity. Magnetic refrigeration based on the magnetocaloric effect (MCE) that is shown by certain magnetic materials is a very promising cooling technique that would enable partly overcome these environmental issues. In fact, this emerging technology operates without the harmful chlorofluorocarbons or hydrochlorofluorocarbons fluids neither the compressor which may significantly contribute to the reduction of greenhouse gas emissions, the enhancement of energy efficiency while making the cooling devices more compact [2]. However, the design of appropriate materials is essential for the development of this emergent technology.

The topics of magnetocaloric materials and magnetic cooling systems were a subject of numerous studies, with the aim to discover new magnetocaloric materials presenting high magnetocaloric effect (MCE) levels. Initially, the magnetocaloric materials used in the active magnetic regenerator (AMR) systems studies were the Gd and some related alloys such as GdTb, GdDy and GdEr [3,4]. However, the use of such magnetic refrigerants is limited because of their high cost and weak chemical stability.

Recently, perovskite manganites of the general formula $La_{1-x}A_xMnO_3$, with A = Sr, Ba, Ca. have attracted much attention as working refrigerants in magnetic cooling applications because of their several advantages such as, low cost, easy preparation, grain size control via heat treatment, and high chemical stability [5–9]. In this work, we study one of the $La_{1-x}Ca_xMnO_3$ compounds that present rich magnetic and electronic properties leading to fascinating phenomena such as, the colossal magnetoresistance, and large magnetocaloric effects [10–13]. Many studies on Ca doping are devoted to $RMnO_3$. In $Ca_{0.85}R_{0.15}MnO_3$ (R = Sm, Dy) materials the Ca replacement by larger R-ions (R=Sm, Dy) induces ferromagnetism

* Corresponding author at: LaMCScI Laboratory, B.P. 1014, Faculty of science. Mohammed V University in Rabat, Morocco.
E-mail addresses: elboukiliaicha@gmail.com, aicha.elboukili@um5s.net.ma (A. El Boukili).

https://doi.org/10.1016/j.jallcom.2020.158392
0925-8388/

Manuscript ID: 1768
DOI: 10.18462/iir.icr.2019.1768

Numerical investigation of cooling properties of $La_{0.6}Ca_{0.4}MnO_3$ in an active magnetic regenerator system

A. El Boukili[(a,b,*)], H. Ez-Zahraouy[(a)], M. Hamedoun[(b)], A. Benyoussef[(a,b,c)], M. Balli[(d,e)], O. Mounkachi[(a)]

[(a)]LaMCScI Laboratory, B.P. 1014, Faculty of science-Mohammed V University, Rabat, Morocco.
[(b)] Materials and Nanomaterials Center, MAScIR Foundation, B.P. 10100-Rabat, Morocco.
[(c)] Hassan II Academy of Science and Technology, Rabat, Morocco.
[(d)]LERMA, ECINE, International University of Rabat, Parc Technopolis, Rocade de Rabat-Salé, 11100, Morocco.
[(e)]Institut Quantique & Département de Physique, Université de Sherbrooke, 2500 Boulevard de l'Université, J1K 2R1, Québec, Canada.

ABSTRACT

In this work, we report a numerical analysis and performance parameters of $La_{0.6}Ca_{0.4}MnO_3$ perovskite manganite as active magnetocaloric material (MCM) in an active magnetic refrigeration cycle (AMR). This material displays a second-order phase transition at 260 K. The needed magnetocaloric parameters for the AMR model such the adiabatic temperature (ΔT_{ad}) change and the heat capacity (Cp) of the solid material were taken from previous studies, while the thermodynamic performance are calculated according to the one-dimensional (1D) AMR model and, investigated as a function of frequencies and fluid flow rates. The implementation of $La_{0.6}Ca_{0.4}MnO_3$ material as a refrigerant in a 1T-AMR device would enable to generate a maximum no-load temperature span of about 11 K, a maximum cooling power of 62 W and a coefficient of performance of 0.5 at 10 K temperature span for a low operating frequency of 0.5 Hz.
Keywords: Magnetic Refrigeration, Cooling properties, Heat Transfer, AMR Cycle, COP, Magnetocaloric Material.

1. INTRODUCTION

Refrigeration is vital in a wide variety of applications such as building, transportation and food preservation. However, until today the traditional cooling technologies that are based on the compression-relaxation of some synthetic refrigerants remain as one of the biggest sources of greenhouse gases (GHG) emissions. On the other hand, the conventional refrigeration markedly enhances the electric energy consumption on account of its lower thermodynamic efficiency, being indirectly responsible for atmospheric pollutants emissions. In contrast, the magnetic refrigeration which is based on the magnetocaloric effect (MCE) seems to be an interesting alternative because of its potential high efficiency as well as the absence of the harmful CFCs and HFCs gases usually present in conventional refrigerators (Balli et al., 2017). The magnetic materials (ferromagnets and paramagnets) heat up in the presence of magnetic field and cool down when the magnetic field is removed. Usually the MCE presents its maximum in the magnetic phase transition region and can be amplified in functional devices by using the AMR thermodynamic cycles (Kitanovski et al., 2015).

Since the experimental discovery of the MCE in a sample of Ni by (Weiss and Picard, 1917), several experimental and theoretical research works were devoted to the investigation of magnetocaloric materials and understanding the mechanisms behind their magnetic and thermal features. For example, (Tishin, 1990, 2003) used the molecular field theory (MFT) to quantify the crucial thermo-physical properties such as specific heat (Cp) adiabatic temperature change (ΔT_{ad}) and entropy change (ΔS) of several rare earth and transition metal elements (Gd, Tb, Dy, Ho, Er, Tm, Fe, Ni, Co). It should be noted that the gadolinium metal which is a reference for magnetocaloric materials is widely used in magnetic refrigeration because of its excellent

Numerical Optimization of the Energetic Performance of a Near Room Temperature Magnetic Refrigerator

A. El Boukili [1,2], H. Ez-Zahraouy [2, *], M. Hamedoun [1], A. Benyoussef [1,2,3], M. Balli [4], O. Mounkachi [1, *]

[1] Materials and Nanomaterials Center, MAScIR Foundation, B.P. 10100-Rabat, Morocco.
[2] LaMCScI Laboratory, B.P. 1014, Faculty of science-Mohammed V University, Rabat, Morocco.
[3] Hassan II Academy of Science and Technology, Rabat, Morocco.
[4] University of Applied Sciences of Western Switzerland, Avenue des sports 20, 1400 Yverdon-Les-Bains, Switzerland.
[*] ezahamid@fsr.ac.ma , o.mounkachi@mascir.com , elboukiliaicha@gmail.com

Abstract— **The present work reports numerical study of a linear reciprocating magnetic refrigerator operating at room temperature. The model's geometry considers parallel plates of Magneto-caloric Materials used as a refrigerant, separated by microchannels of water as a heat transfer fluid. To investigate the energetic performance of our magnetic cooling system, the temperature span between cold and hot sides of the bed regenerator and the coefficient of performance (COP) of the device were evaluated. Furthermore, numerical predictions are also exploited to optimize the controlling parameters such as, mass flow rate, the operation frequency of the magnetic refrigerator, by studying their effects on the characteristics of the heat transfer and fluid flow within the bed regenerator.**

Keywords-component; Magnetic refrigeration, Active Magnetic Regenerator, energetic performance, environment, heat transfer, Numerical modeling.

I. INTRODUCTION

Refrigeration process is in continuous development. But until today, the traditional technique based on the refrigerant compression, remains the dominant technique with high yield as a second biggest source of greenhouse gas emissions after electricity, and significant responsible of huge increase of energy consumption. As stated by the international energy agency (IEA), the overall world electricity consumption of 2016 is estimated at 23816 TWh, of which 67% is produced from fossil fuels [1]. In this spirit, we noticed the enhanced interest of the researchers to innovate new clean technologies for cold production, such as: Thermoelectric refrigeration named the Peltier effect [2], Thermoacoustic [3], Adsorption cooling system [4], and Magnetic cooling [5].

Nowadays, magnetic cooling attracts more interest, due to its several advantages compared to the conventional heating and cooling systems such as high theoretical efficiency and environmental safety. The latter consists in exploiting the magnetocaloric effect of some magnetic materials, which exhibits a giant magnetocaloric effect, by using the entropy variation of these specific materials (gadolinium and some of its alloys) submitted to a magnetic field [6]. Hence, these magnetic materials heat up when applying a magnetic field and cool down when the magnetic field is removed. This effect is greatest around the transition temperature and can be exploited to make a thermal-cycle known by AMR cycle, and equivalent to conventional thermodynamic cycle of compression and expansion of a gas.

Significant research studies, both experimental and theoretical, has been carried out on the use of magnetocaloric effect for refrigeration after 1917 [7] when Weiss and Picard discovered a reversible heating of a nickel sample observed near its curie temperature of (354°C) when the sample was exposed to a magnetic field, this discovery is called a “novel magnetocaloric phenomenon”. On theoretical works, we found Tishin [8,9] who used the molecular field theory (MFT) to quantify the crucial thermo-physical properties cp, ΔT_{ad}, ΔS of magnetocaloric materials, that exhibit both first and second order magnetic phase transitions (Gd, Tb, Dy, Ho, Er, Tm, Fe, Ni, Co) used as a refrigerant by magnetic cooling devices. It should be noted that One of the problems of existing MCMs is the adiabatic temperature change (ΔT_{ad}) or magnetocaloric effect (MCE) limit. ΔT_{ad} of gadolinium under 1Tesla magnetic field is around 3 K and 9 K under 5 Tesla magnetic field, for this reason research orients itself to find new magnetic materials which exhibits a giant magnetocaloric effect, with large MCE chiefly at induction fields close to 2 T and close to room temperature [10], with large entropy change as well as large adiabatic temperature change that offers the promise to surmount the gadolinium powders used in the current rotary refrigerator as $Gd_5(SiGe_2)$ [11].

978-1-5386-2847-8/17/$31.00 ©2017 IEEE

Résumé

La conversion d'énergie magnétocalorique est une technologie de production de froid basée sur l'effet magnétocalorique (EMC). Ce dernier est un phénomène physique qui se traduit par le refroidissement ou l'échauffement de certains matériaux sous l'action d'un champ magnétique. L'objectif de la présente thèse vise à estimer le potentiel d'application de ce phénomène dans la technologie de la réfrigération magnétique.

Ce travail est divisé en deux parties. La première partie concernait l'étude de la physique de l'(EMC) et les résultats expérimentaux et théoriques obtenus pour deux familles de matériaux. Ainsi, des composés à effet magnétocalorique géant de formule $AlFe_2B_2$ et des oxydes de type manganite ($La_{1-x}A_xCa_{0,4}MnO_3$) ont été explorés en ce qui concerne leurs propriétés structurales, magnétiques et magnétocalorique, ainsi que leur utilisation comme source d'énergie dans les dispositifs de réfrigération magnétique. Les propriétés thermomagnétiques du réfrigérant solide ont été déterminées en utilisant la théorie du champ moléculaire et des simulations de Monte Carlo ainsi que par des mesures expérimentales. La deuxième partie est axée sur le développement d'un modèle numérique 1D pour optimiser le système de régénérateur magnétique actif. Ce modèle permet de calculer et simuler le fonctionnement du cycle de réfrigération magnétique actif (AMR) afin de prédire les performances thermiques du cycle et par conséquent de contribuer à la compréhension du couplage magnétothermique complexe entre le fluide caloporteur et l'effet magnétocalorique de réfrigérant solide dans un dispositif magnétique.

Mots-clés: Réfrigération magnétique, Matériaux à effet magnétocalorique géant, Source de champ à aimants permanents, Réfrigération magnétique à régénération active (AMRR).

Abstract

Magnetocaloric energy conversion is a cooling technology based on the magnetocaloric effect (MCE). The latter is a physical phenomenon which results in the cooling or heating of certain materials under the action of a magnetic field. The objective of the present thesis aims to estimate the potential of application of this phenomenon in magnetic refrigeration technology.

This work is divided in two parts. The first part involved the study of the MCE physics and the experimental and theoretical results obtained for two different material families. Thus, compounds with a giant magnetocaloric effect with the formula $AlFe_2B_2$ and manganite ($La_{1-x}A_xCa_{0,4}MnO_3$) were explored in regard to their structural, magnetic and magnetocaloric effect properties, as well as for use as the energy source in magnetic refrigeration devices. The thermomagnetic properties of the solid refrigerant have been determined by using the Mean field theory and Monte Carlo simulations as well as by experimental measurements. The second part is focused on developing a 1D numerical model to optimize the active magnetic regenerator system. This model is used to calculate and simulate the operation of active magnetic refrigeration cycle (AMR) in order to predict thermal performances of the cycle and consequently to contribute to the comprehension of the complex magneto-thermal coupling between the carrier fluid and the magnetocaloric effect of solid refrigerant in the magnetic device.

Keywords: Magnetic refrigeration, Magnetocaloric effect, Permanent magnets field source, Active magnetic regenerative regenerator system (AMRR).